LARGE INELASTIC DEFORMATION OF GLASSY POLYMERS

by

MARY CUNNINGHAM BOYCE

B.S., Eng. Sci. and Mech., Virginia Polytechnic Institute and State University (1981)

S.M., Mech. Eng., Massachusetts Institute of Technology (1983)

SUBMITTED IN PARTIAL FULFILLMENT

OF THE REQUIREMENTS FOR THE

DEGREE OF

DOCTOR OF PHILOSOPHY

IN MECHANICAL ENGINEERING

at the

MASSACHUSETTS INSTITUTE OF TECHNOLOGY

December 1986

Signature of Author____

Department of Mechanical Engineering
December 17, 1986

Certified by_

Professor David M. Parks
Thesis Supervisor

Accepted by_____

Professor Ain Ants Sonin, Chairman
Departmental Committee on Graduate Studies

Large Inelastic Deformation of Glassy Polymers

by

Mary C. Boyce

Submitted to the Department of Mechanical Engineering
on December 17,1986 in partial fulfillment of the
requirements for the Degree of Doctor of Philosophy in
Mechanical Engineering

Abstract

Glassy polymers constitute a large class of engineering solids. In order to successfully analyze the warm (near the glass transition temperature) mechanical processes by which many glassy polymeric products are manufactured, as well as to ascertain the resulting products' response to service life loading conditions, a constitutive law that properly accounts for the large, inelastic deformation behavior of these materials is required. Such behavior is known to exhibit rate, temperature, and pressure dependent yield, as well as true strain softening and hardening after yield. This thesis work develops a constitutive model based on the macromolecular structure of these materials and the micromechanism of plastic flow which encompasses the above dependencies. The model is numerically integrated and incorporated into an existing finite element code in order to enable the analysis of real boundary value problems involving inhomogeneous deformation. The model is then used in the numerical simulation of a real forming process - the hydrostatic extrusion of polymethylmethacrylate. Manufactured polymeric products generally contain residual texture, i.e. preferred directions of orientation. The effect of such texture on subsequent inelastic behavior is also examined.

Thesis Supervisor: Dr. David M. Parks

Title: Associate Professor of Mechanical Engineering

Acknowledgments

I would like to express my gratitude to Professors David M. Parks and Ali S. Argon for their support and guidance during my four+ years at MIT, and also for giving me the opportunity to work on this particular research topic. I thank Professor Robert Cohen for participating on my thesis committee. I would also like to thank the Mechanics of Materials research group as a whole for creating a pleasant, good-humored working environment. It definitely made the many hours, days, weeks, etc., etc. of research and problem sets bearable, and, actually, a lot of fun. I must also extend my appreciation to Mary Toscano for the many cups of coffee and, without whom, things probably wouldn't get done - at least not on time.

I am grateful to the Data General Corporation for their donation of the MV10000 computer which made most of the numerical work possible. I thank Hibbitt, Karlson, and Sorenson, Inc. for the use of the finite element computer program ABAQUS. I also thank the Solid Mechanics division of the National Science Foundation for funding this research under grant .

Finally, I especially thank my husband, Duncan, (and our son, Matthew), and my parents for their love, support, and encouragement throughout my studies.

Contents

PREFACE

Industrial and commercial products manufactured from glassy polymers are done so primarily by warm mechanical processes such as extrusion, drawing, blow moulding, and calendering. These processes usually produce a textured solid. The design of the actual process necessary to create a particular product can be an expensive trial and error procedure. This is because the material behavior of glassy polymers at large deformations is not yet well characterized or understood. It is therefore of interest to quantify the large inelastic deformation behavior of these materials in order to better predict the development of texture and residual stresses under various processing conditions as well as to ascertain the effect of this texture on the inelastic behavior of the resulting product during its typical operating conditions.

The following chapters and appendices of this thesis will discuss the development, numerical implementation, and practical application of a constitutive model describing the large inelastic deformation of glassy polymers. In Chapter One, the development of a physically based constitutive model which describes the large inelastic deformation of initially isotropic glassy polymers is detailed. This model properly accounts for such characteristics as the rate, pressure, and temperature dependence of yield, as well as the occurrence of true strain softening and hardening after yield. Chapter Two will give an example of a standard industrial polymer process, hydrostatic extrusion, analyzed with this model. The results of this analysis are compared with documented experimental results. Chapter Three will discuss the incorporation of the effect of pre-orientation into the model. An analysis of a preoriented solid is then conducted where the effect of orientation on the initiation of such localization phenomena as shear banding is examined. There will also be three appendices: the first will discuss the numerical

implementation of the model into a finite element code; the second will discuss the finite strain kinematics of this model and its application to the single crystal problem; the third will be a simple heat transfer analysis determining the exit temperature profile of the extrudate of Chapter Two. Finally, the concluding chapter will summarize this work as well as discuss its value and suggest future avenues of related research.

Chapter 1

CONSTITUTIVE MODEL

1.1 Background

The development of the constitutive model is begun by first defining exactly what is meant by a glassy polymer and then by identifying the general response of such glassy polymers to loading via their true stress-strain curves. A plot of the log of the elastic modulus of these materials vs temperature (Figure 1.1a) generally exhibits a drop of several orders of magnitude at a specific temperature termed the glass transition temperature, Θ_g. This temperature may also be obtained from a plot of specific volume as a function of temperature (Figure 1.1b) and for a reference rate of measurement is a material property. An amorphous polymer is considered glassy at temperatures below its Θ_g and "rubbery" at temperatures above its Θ_g. The difference in the response of the material to loading when in the glassy and rubbery regimes is schematically illustrated in the true stress-stretch curves of Figure 1.2. When the material is at a temperature $\Theta > \Theta_g$, i.e. in the rubbery regime, the material behaves as a nonlinear elastic solid. In the glassy regime, i.e at $\Theta < \Theta_g$, the initially isotropic solid exhibits a linear elastic response followed by yielding. The initial yielding of the material is known to depend on pressure, strain rate, and temperature. After yielding, the material may

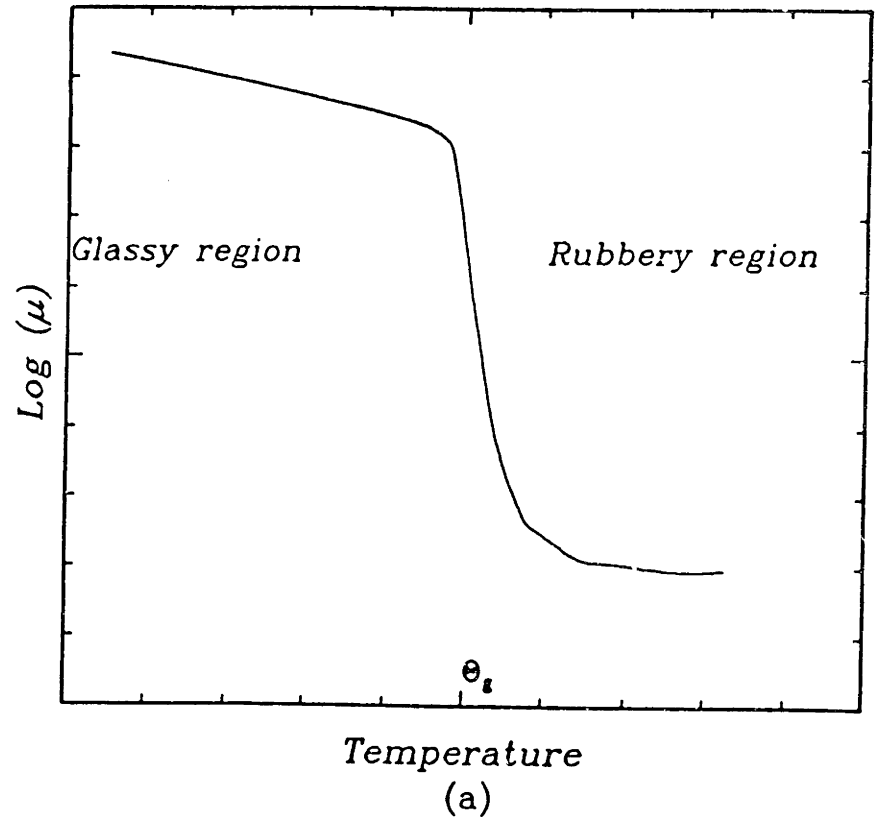

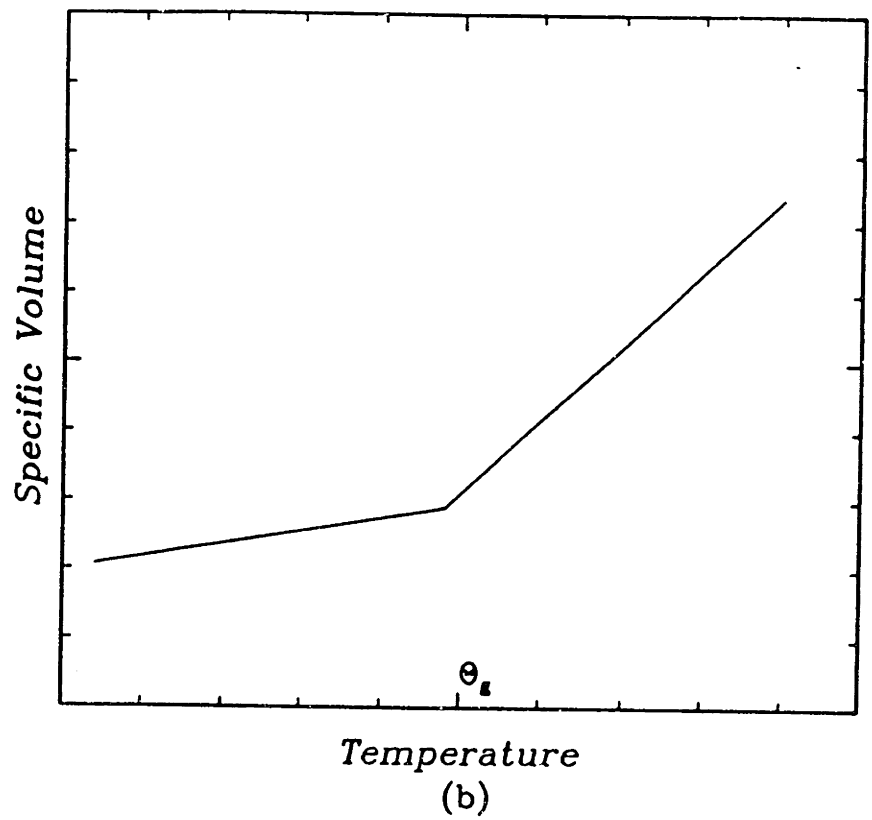

Figure 1.1. Schematic of the elastic shear modulus (a) and specific volume (b) of an amorphous polymer as a function of temperature. The amorphous polymer is considered glassy below the glass transition temperature, Θ_g, and rubbery above Θ_g.

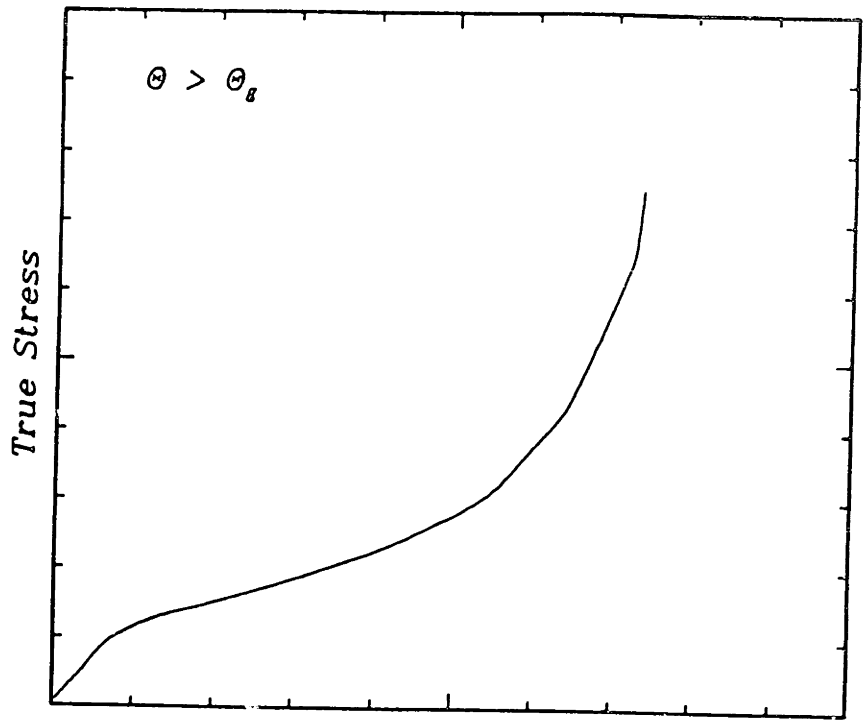

(a)

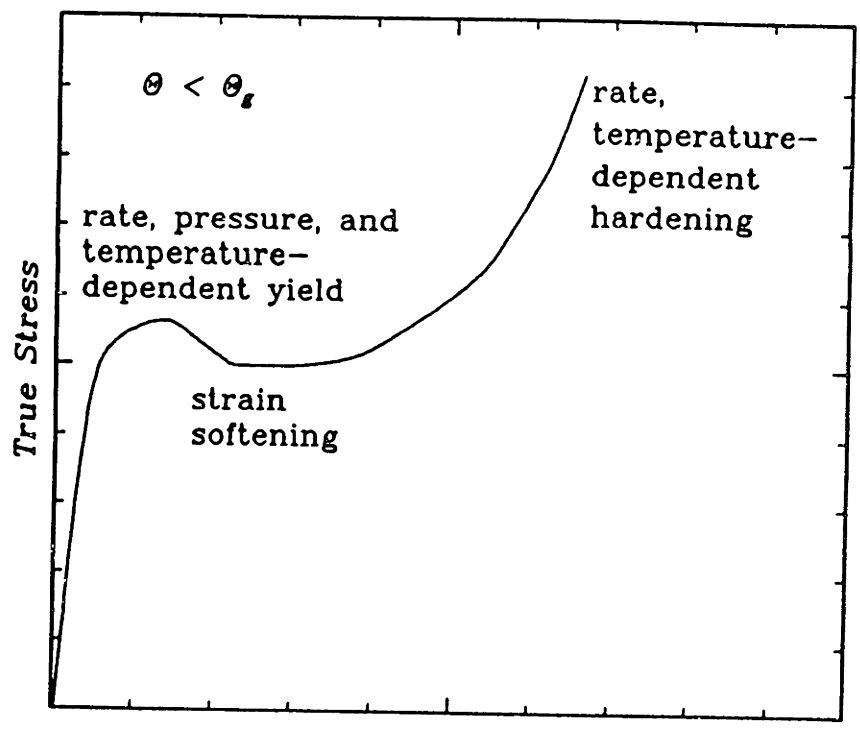

(b)

Figure 1.2. Schematic of the true stress–stretch relationship for an amorphous polymer (a) above the glass transition temperature, Θ_g, and (b) below Θ_g.

possess the response of true strain softening. This is a drop in the true stress with plastic straining and is the global response to small-scale inhomogeneous deformation such as shear banding. As larger strains are approached, the material strain hardens. In this chapter, a physically-based constitutive law is developed which models these traits of the inelastic behavior of glassy polymers at finite strains.

It has been previously documented that a glassy polymer must overcome two physically distinct sources of resistance before large strain inelastic flow may occur [1, 2]. Below the glass transition temperature, Θ_g, prior to initial yield, the material must be stressed to exceed its intermolecular resistance to segment rotation. Once the material begins to flow, molecular alignment occurs, altering the configurational entropy of the material. This is the second source of deformation resistance. Haward and Thackray [1] have modelled these resistances in 1-D using an Eyring dashpot to represent the intermolecular resistance and a Langevin spring (as derived from a non-Gaussian statistical mechanics theory of rubber elasticity [23]) to represent the entropic resistance. Argon [2] developed a micro-mechanical model describing the rate-dependent intermolecular resistance and suggested that the subsequent hardening was due to entropic resistance resulting from molecular alignment. Parks, Argon and Bagepalli [4] later extended these models to incorporate full 3-D effects. In this case, the intermolecular resistance was taken to be constant, and therefore modelled as ideally plastic. The entropic resistance was modelled as suggested by Argon and by Haward and Thackray. This material description yields a back stress tensor which has a unique correspondence to the inelastic distortion in the polymer. The inelastic extension ratios describe the texture developed in the material. This constitutive model could be broken into two distinct parts: the elastic, ideally plastic response and the entropic hardening response.

Here, the Parks, et al. 3-D model is extended to include the effects of rate, pressure, true strain softening, and temperature on the plastic resistance. The incorporation of these effects will enable the realistic simulation of forming processes (Chapter Two), as well as other boundary value problems of inhomogeneous deformation. The finite strain kinematics that were used here are those followed by Parks, et al. as originally detailed by Fardshisheh and Onat [4]. These are reviewed below for completeness. Experiments necessary for the systematic identification of material constants used in the material model are identified. The constants for one such amorphous polymer, polymethylmethacrylate (PMMA), are determined from experimental data found in the literature.

1.2 Three Dimensional Constitutive Model

The constitutive model begins with an overview of the kinematic formulation used to appropriately account for finite strain effects. The modelling of the physics of this class of material is then discussed. This begins with the assumption that the plastic resistance to flow may be decomposed into two parts as previously described: the intermolecular resistance to segment rotation and the entropic resistance to molecular alignment (Figure 1.3). The intermolecular resistance model begins with the rate-dependent micromechanical model developed by Argon [2], which is subsequently modified to include additional effects on yielding which, previously, had not been specifically accounted for in the model. The 3-D entropic resistance is modelled by the Wang and Guth [5] non-Gaussian statistical mechanics network model of rubber elasticity.

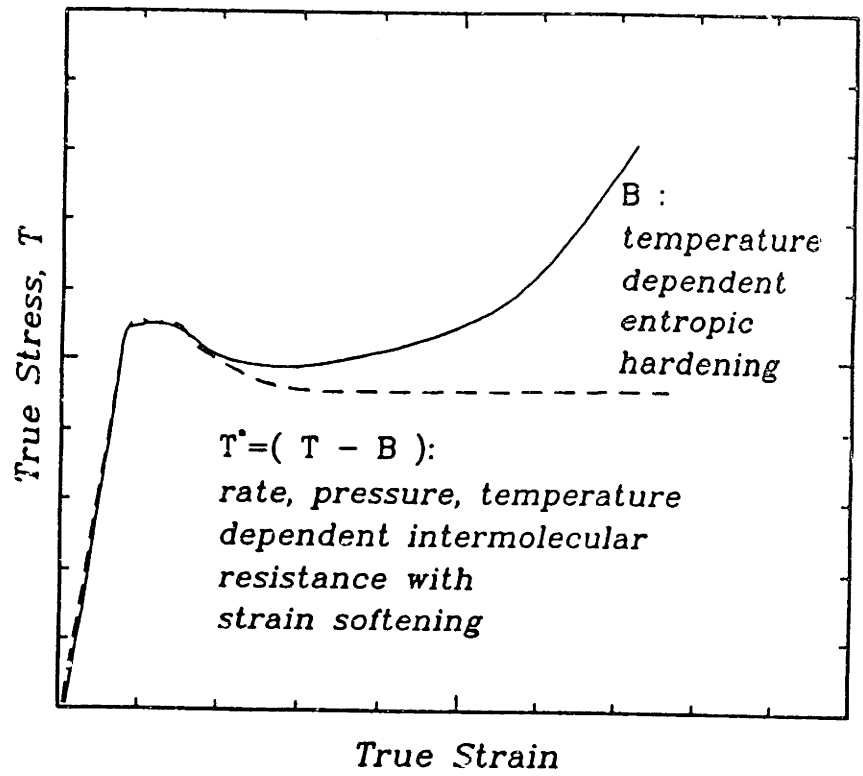

Figure 1.3. Schematic of the model for the stress–strain behavior of a glassy polymer.

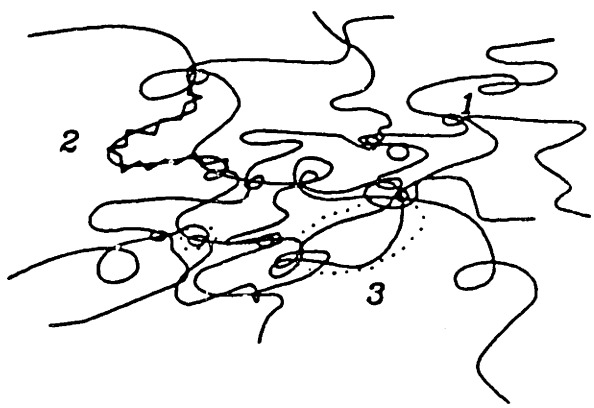

1. *physical entanglement*
2. *N rigid links between entanglements*
3. *intermolecular interaction*

Figure 1.4. Schematic of amorphous polymer.

1.2.1 Kinematics of Finite Strain

The finite strain formulation begins with a description of the deformed body *via* its deformation gradient, $\mathbf{F} = \nabla_{\mathbf{X}}\mathbf{x}$, where $\mathbf{X}$ represents the reference position and $\mathbf{x}$ the current position of a material point. For the polymers under consideration here, the reference configuration is the isotropic state of the material consisting of randomly oriented molecular chains (Figure 1.4). We assume that, during plastic flow, these molecules deform affinely on a scale larger than the strain-producing, rotating molecular segments. The deformation gradient is multiplicatively decomposed into elastic and plastic components [39], $\mathbf{F} = \mathbf{F}^e\mathbf{F}^p$. The plastic deformation gradient, $\mathbf{F}^p$, represents the configuration obtained by complete elastic unloading to a stress free state, and physically indicates the degree of permanent molecular orientation existing in the material. The deformation gradient may also be expressed as the product of the elastic stretch, the rotation, and the plastic stretch: $\mathbf{F} = \mathbf{V}^e\mathbf{R}\mathbf{U}^p$. The elasticity and/or plasticity of the rotation tensor is indeterminate. We may decompose $\mathbf{R}$ into the products of elastic and plastic components, $\mathbf{R} = \mathbf{R}^e\mathbf{R}^p$, where $\mathbf{F}^e = \mathbf{V}^e\mathbf{R}^e = \mathbf{R}^e\mathbf{U}^e$ and $\mathbf{F}^p = \mathbf{R}^p\mathbf{U}^p = \mathbf{V}^p\mathbf{R}^p$ via the polar decomposition theorem. If we choose $\mathbf{R} = \mathbf{R}^p$ and $\mathbf{R}^e = \mathbf{1}$, we are lumping all rotation effects into the affine plastic deformation response of the material. This results in a symmetric and, therefore, unique elastic deformation gradient, $\mathbf{F}^{eT} = \mathbf{F}^e$. Also, the tensorial resistance associated with the inelastic deformation may be computed in an already rotated configuration (see section 1.2.3). If we choose $\mathbf{R} = \mathbf{R}^e$ and $\mathbf{R}^p = \mathbf{1}$, $\mathbf{F}^e$ will be unique, but the tensorial resistance to flow will have to be rotated when used in future calculations. Here, we take $\mathbf{R} = \mathbf{R}^p$ and $\mathbf{R}^e = \mathbf{1}$. This will also simplify the rate kinematics as will be shown below. It is also assumed that plastic flow is an incompressible process, thereby requiring $det\mathbf{F}^p = 1$.

The rate-kinematics are now examined beginning with the velocity gradient, $\mathbb{L}$, which is given by:

$$\mathbf{L} = \nabla_{\mathbf{x}}\mathbf{v} = \dot{\mathbf{F}}\mathbf{F}^{-1} = \mathbf{D} + \mathbf{W}, \tag{1.1}$$

where $\mathbf{D}$, the rate of deformation, is the symmetric portion of $\mathbf{L}$; and $\mathbb{W}$, the spin, is the anti-symmetric portion of $\mathbf{L}$. The following expression for the velocity gradient is obtained after incorporating the product decomposition of the deformation gradient:

$$\mathbf{L} = \dot{\mathbf{F}}^e\mathbf{F}^{e^{-1}} + \mathbf{F}^e\mathbf{L}^p\mathbf{F}^{e^{-1}}, \tag{1.2}$$

$$\text{where, } \mathbf{L}^p = \dot{\mathbf{F}}^p\mathbf{F}^{p^{-1}} = \mathbf{D}^p + \mathbf{W}^p. \tag{1.3}$$

The tensor $\mathbf{L}^p$ is called the "plastic" velocity gradient. The tensor $\mathbf{D}^p$ describes the rate of change of shape of the unloaded configuration $\mathbf{F}^p$. Due to the symmetry of $\mathbb{F}^e$, it is easily shown that $\mathbf{W}^p$ is uniquely defined by $\mathbf{W}$, $\mathbf{D} + \mathbf{D}^p$, and $\mathbf{F}^e$, and therefore may not be constitutively prescribed. $\mathbf{W}^p$ is given by:

$$\mathbf{W}^p = \mathbf{W} - \mathcal{W}\left[\mathbf{D} + \mathbf{D}^p\right], \tag{1.4}$$

where $\mathcal{W}$ is a fourth order tensor, defined in reference 3, which is a function of $\mathbb{F}^e$ only, and is of the order of the elastic strain. Had we not chosen $\mathbf{F}^e$ to be symmetric, it is probable that $\mathbf{W}^p$ would have had to somehow be "constitutively" defined. This would alter the integration of these equations (Appendix A), but should not affect the overall solution because the choice of $\mathbf{R} = \mathbf{R}^p$ rather than $\mathbf{R} = \mathbf{R}^e$ is, in principle, arbitrary for this material. However, it does warrant further investigation in future research. We must constitutively prescribe a rate of plastic shape change, $\hat{\mathbf{D}}^p$, for the material which is either in the loaded configuration given by $\mathbf{F}$, or the unloaded configuration given by $\mathbf{F}^p$. The configuration does not need to be defined at this point. By arguments

of isotropic representation theorems [40, 44], the rate of plastic shape change may be expressed as:

$$\hat{\mathbf{D}}^p = \sum_i \phi_i \mathbf{Z}_i, \tag{1.5}$$

where the coefficients ϕ_i are a function of the irreducible set of scalar invariants for an anisotropically hardening material:

$$[tr\mathbf{T}^*, tr(\mathbf{T}^*)^2, tr(\mathbf{T}^*)^3, tr\mathbf{B}, tr\mathbf{B}^2, tr\mathbf{B}^3, tr\mathbf{T}^*\mathbf{B}, tr(\mathbf{T}^*)^2\mathbf{B}, tr\mathbf{T}^*\mathbf{B}^2, tr(\mathbf{T}^*)^2\mathbf{B}^2]. \tag{1.6}$$

The tensor $\mathbf{T}^*$ is the driving stress state, which is schematically shown in 1-D in Figure 1.3, and is given in the continuum by:

$$\mathbf{T}^* = \mathbf{T} - \frac{1}{J}\mathbf{F}^e\mathbf{B}\mathbf{F}^e, \tag{1.7}$$

where: $\mathbf{B}$ is the back stress tensor due to entropic hardening, which will be constitutively defined below; J is the volume change given by $det\mathbf{F}^e$, and $\mathbf{T}$ is the Cauchy stress tensor. The tensors $\mathbf{Z}_i$ are given by the functionally irreducible set of tensors:

$$[\mathbf{I}, \mathbf{T}^*, (\mathbf{T}^*)^2, \mathbf{B}, \mathbf{B}^2, \mathbf{B}\mathbf{T}^* + \mathbf{T}^*\mathbf{B}, (\mathbf{T}^*)^2\mathbf{B} + \mathbf{B}(\mathbf{T}^*)^2, \mathbf{T}^*\mathbf{B}^2 + \mathbf{B}^2\mathbf{T}^*, (\mathbf{T}^*)^2\mathbf{B}^2 + \mathbf{B}^2(\mathbf{T}^*)^2] \tag{1.8}$$

For a first approximation, we take the reduced case of:

$$\hat{\mathbf{D}}^p = \phi_1\mathbf{I} + \phi_2\mathbf{T}^* + \phi_3\mathbf{B}. \tag{1.9}$$

Assuming plastic incompressibility and zero plastic straining at zero effective equivalent stress (see sections 1.2.2 and 1.2.5) results in:

$$\hat{\mathbf{D}}^p = \phi_2(\mathbf{T}^*)', \tag{1.10}$$

where ϕ_2 is proportional to the plastic shear strain rate for which a physically-based constitutive model is developed in later sections. The question of whether this expression applies to the loaded or unloaded configuration is not easily resolved. The

unloaded and loaded configurations differ by an elastic stretch, $\mathbb{F}^e = (\mathbb{F}^e)^T$. The rate of plastic shape change is given by $\mathbf{D}^p = sym[\mathbf{L}^p]$ in the unloaded configuration, and $\bar{\mathbf{D}}^p = sym[\mathbf{F}^e\mathbf{L}^p(\mathbf{F}^e)^{-1}]$ in the loaded configuration. Therefore, for the case of a rigid-"plastic" material, $\mathbf{D}^p = \bar{\mathbf{D}}^p = \hat{\mathbf{D}}^p$. When the material exhibits an elastic response, the difference between $\bar{\mathbf{D}}^p$ and $\mathbf{D}^p$ will be of the order of the elastic strain which we assume to be small. It has also been shown by Onat that a thermodynamic analysis suggests a flow rule of the sort:

$$\tilde{\mathbf{D}}^p = \dot{\tilde{\gamma}}^p(\mathbf{T} - \mathbf{B}^*)', \tag{1.11}$$

$$\mathbf{D}^p = \frac{1}{2}[\mathbf{F}^e\tilde{\mathbf{D}}^p(\mathbf{F}^e)^{-1} + (\mathbf{F}^e)^{-1}\tilde{\mathbf{D}}^p\mathbf{F}^e], \tag{1.12}$$

where $\mathbf{B}^* = \frac{1}{2}\frac{1}{J}[\mathbf{F}^e\mathbf{B}(\mathbf{F}^e)^{-1} + (\mathbf{F}^e)^{-1}\mathbf{B}\mathbf{F}^e]$. Again, for the rigid case, $\tilde{\mathbf{D}}^p = \mathbf{D}^p = \bar{\mathbf{D}}^p = \hat{\mathbf{D}}^p$, and, including elasticity, the differences will be of the order of the elastic strain. It seems unlikely that such differences are experimentally measurable. Here, we take $\mathbf{D}^p = \hat{\mathbf{D}}^p$, or:

$$\mathbf{D}^p = \dot{\gamma}^p\mathbf{N}, \tag{1.13}$$

$$\mathbf{N} = \frac{1}{\sqrt{2}\tau}\mathbf{T}^{*\prime}, \tag{1.14}$$

$$\tau = [\frac{1}{2}(\mathbf{T}^{*\prime})^2]^{\frac{1}{2}}. \tag{1.15}$$

The Cauchy stress tensor is taken to be uniquely defined by the elastic modulus tensor acting upon the natural logarithm of the elastic deformation gradient:

$$\mathbf{T} = \frac{1}{J}\mathcal{L}^e[ln\mathbf{F}^e], \tag{1.16}$$

where, the isotropic elastic moduli are given by:

$$\mathcal{L}^e = 2\mu I + (K - \frac{2}{3}\mu)\mathbf{I} \otimes \mathbf{I}, \tag{1.17}$$

where μ is the shear modulus, K is the bulk modulus, and I and $\mathbf{I}$ are the fourth and second order identity tensors respectively. It is noted that isotropic elasticity is taken to hold for all time since the magnitude effects of developing elastic anisotropy in glassy polymers is small [24] especially in the overall solution of a problem involving large strain plasticity.

In order to demonstrate its wider applicability, the basic finite strain formulation employed here has also been used to analyze the problem of single crystal deformation, which has previously been analyzed in the context of a different finite strain plasticity formulation [41]. This is done in Appendix B where the results are also compared with the other formulation. With the description of the kinematics and the constitutive connection between stress and elastic deformation complete, we now move on to the development of a constitutive law for the plastic strain rate, $\dot{\gamma}^p$, and the back stress tensor, $\mathbf{B}$, already mentioned in this section.

1.2.2 Intermolecular Resistance: Rate and Temperature Dependence

At temperatures below the glass transition temperature of an amorphous polymer, it is assumed that plastic flow and subsequent molecular chain alignment does not commence until the intermolecular resistance of the material to segment rotation has been overcome. This deformation resistance is due to the restriction imposed on molecular chain motion due to neighboring chains (Figure 1.4). Flow commences once the free energy barrier to molecular mobility is overcome through the thermally activated rotation of these segments under stress. Argon [2] has derived an expression for the free energy change, ΔG^*, necessary to produce segment rotation based on a double-kink model of a chain segment rotating against the elastic impedance of surrounding chains which are modelled as an equivalent elastic medium (Figure 1.5):

$$\Delta G^* = \frac{3\pi\mu\omega^2 a^3}{16(1-\nu)}\left[1 - \left(\frac{\tau}{\frac{.077\mu}{1-\nu}}\right)^{\frac{5}{6}}\right]. \tag{1.18}$$

The corresponding plastic strain rate is given by[1]:

$$\dot{\gamma}^p = \dot{\gamma}_0 exp\left(-\frac{\Delta G^*}{k\Theta}\right). \tag{1.19}$$

The material properties in these expressions include the shear modulus, $\mu(\Theta)$[2]; Poisson's ratio, $\nu(\Theta)$; the net angle of rotation, ω, of the molecular segment between the initial configuration and the activated configuration, ω; the mean molecular radius, a; and the pre-exponential shear strain rate factor, $\dot{\gamma}_0$. The absolute temperature is given by Θ, and k is Boltzmann's constant. These values may be consolidated as follows, let:

[1]This form is appropriate at the plastic limit. It can be generalised, if desired, for the low stress limit by subtracting from it a term representing the "reverse flux" of configurations to obtain a hyperbolic sine dependence on stress.

[2]The shear modulus is also dependent on strain rate through distributed anelastic processes. This dependence will be ignored here.

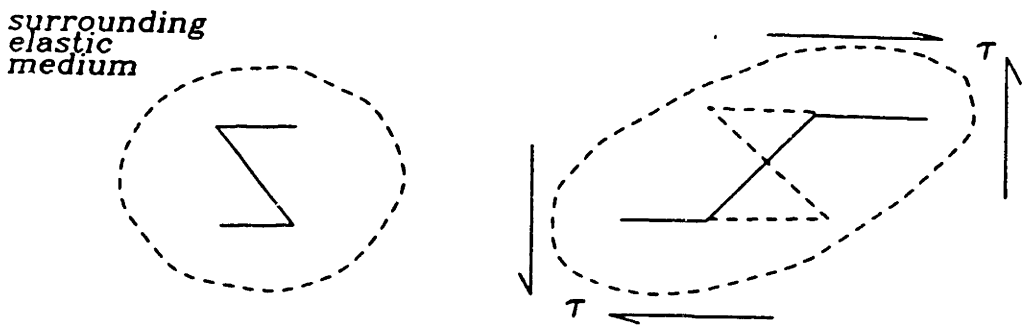

Figure 1.5. Argon double--kink model of the intermolecular resistance.

$$s_0 \equiv \frac{0.077\mu}{1-\nu}, \tag{1.20}$$

$$A \equiv \frac{39\pi\omega^2 a^3}{16k}. \tag{1.21}$$

Equation (1.12) may then be rewritten as:

$$\dot{\gamma}^p = \dot{\gamma}_0 exp\left[-\frac{As_0}{\Theta}\left(1-\left(\frac{\tau}{s_0}\right)^{\frac{5}{6}}\right)\right], \tag{1.22}$$

or, alternatively as:

$$\tau = s_0\left[1-\frac{\Theta}{As_0}ln\left(\frac{\dot{\gamma}_0}{\dot{\gamma}^p}\right)\right]^{\frac{6}{5}}. \tag{1.23}$$

It is noted that as the temperature approaches absolute zero, τ approaches s_0 if non-negligible plastic strain rates are to be sustained. Therefore, s_0 may be termed the athermal shear yield strength of the material.

The rate and temperature dependence of the intermolecular shear resistance of the material are described by equation (1.23), where s_0 is also implicitly a function of temperature because of the temperature dependence of the elastic moduli. This expression will be used later as the basic building block for the incorporation of pressure and strain softening effects. However, having introduced the intermolecular resistance, it is now important to complete the picture of the total deformation resistance with a description of the second component, the entropic resistance.

1.2.3 Entropic Resistance

The modelling of the entropic resistance was previously reported by Parks, et al. [3] and is briefly summarized below. The basic macromolecular structure of isotropic glassy polymers consists of randomly oriented molecular chains connected by physical entanglements (Figure 1.4). As these polymers are stretched, and once the intermolecular

resistance has been overcome, the chains begin to orient themselves in an affine manner. If these materials with high molecular weight ($\bar{M}_W > 10^5$) have been permanently deformed below Θ_g, and subsequently heated to a temperature above Θ_g (i.e., the rubbery region) without constraint, the isotropic structure and macroscopic shape are fully recovered(see Figure 1.6). These and related observations motivate our modelling of the orientation hardening in these materials by the statistical mechanics network models of rubber elasticity [23]. Therefore, the entropic resistance is determined by finding the external stress state resulting when the material is stretched at temperatures above Θ_g, i.e. the "rubbery" regime, and assuming that this state represents an internal resistance which is "locked" in the material, i.e. not recoverable, at temperatures below Θ_g. Our internal variables, B_i, or principal back stress components, are defined by this state and are uniquely related to the texture or "locked-in" plastic stretches, $V^p{}_i$ in the glassy regime. The stress state is found by beginning with the expression for the Helmholtz free energy, F:

$$F = U - \Theta S, \tag{1.24}$$

where U is the internal energy of the material, S is the configurational entropy of the material, and Θ is the absolute temperature of the system. The internal energy of the system may be further decomposed into intermolecular and intramolecular components. The intermolecular component, as described earlier, is due to resistance to chain mobility imposed by surrounding chains; while the intramolecular component is due to resistance imposed by the chain itself, e.g. from its own bulky side groups and energy barriers between different isomeric states. Well below Θ_g, the intermolecular component is usually the more dominant of the two. The case of isothermal deformation is now examined and it is seen that the change in the Helmholtz free energy, ΔF, is:

Material Response

1. After unloading at $\Theta \leq \Theta_g$

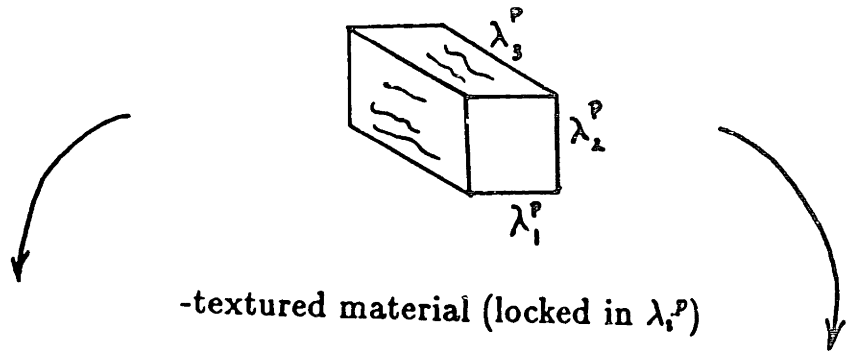

-textured material (locked in λ_i^p)

2a. Subsequently heat to $\Theta \geq \Theta_g$ without constraint

2b. Heat to $\Theta \geq \Theta_g$ constraining shape

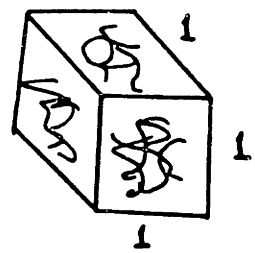

-return to isotropic state

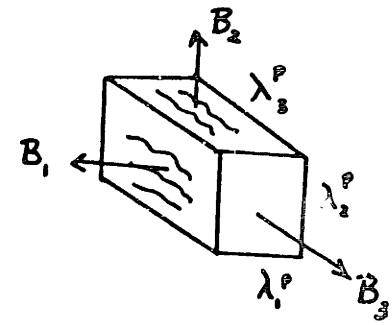

-external tractions (Back Stresses) must be applied to retain texture

Figure 1.6. Physical description of the back stresses in principal stress space, where λ_i^p represent the principal stretches; B_i represent the principal back stresses.

$$\Delta F = \Delta U_{inter} + \Delta U_{intra} - \Theta \Delta S. \tag{1.25}$$

The external stresses are equal to the gradient in the Helmholtz free energy, ΔF, with respect to the corresponding strain. In the rubbery regime, changes in the intermolecular (and often in the intramolecular energy) are negligible compared to the change in the configurational entropy which is large due to the orienting of the chains. Therefore, these energy changes may be neglected in the determination of the external stresses at temperatures above Θ_g. In the adaptation of these results to the material in the glassy regime, the resulting principal back stress components, B_i, are accordingly related to the gradient of the entropy change with respect to the principal plastic stretch, $V^p{}_i$, in that tensorial direction[3]:

$$B_i = -\Theta V^p{}_i \frac{\partial \Delta S}{\partial V^p{}_i}. \tag{1.26}$$

The Wang and Guth non-Gaussian statistical mechanics network model [5] is used to describe the change in entropy. This model accounts for the orientation effects up to large stretches, properly describing the "locking" of these materials which is induced by network constraints. At low stretch ratios, this model reduces to the more standard Gaussian statistical mechanics model of rubber elasticity [23]. After incorporation of the Wang and Guth network model into equation (1.26), a detailed expression for the back stress in terms of specific molecular characteristics is obtained:

$$B_i = C^R \frac{\sqrt{N}}{3} \left[V_i^P \mathcal{L}^{-1}\left(\frac{V_i^P}{\sqrt{N}}\right) - \frac{1}{3}\sum_{j=1}^{3} V_j^P \mathcal{L}^{-1}\left(\frac{V_j^P}{\sqrt{N}}\right) \right], \tag{1.27}$$

[3]It may be argued that a configurational entropy model for temperatures above Θ_g, where different configurational states can be freely sampled by thermal fluctuations, should not be applicable below Θ_g, where configurations are frozen-in. However, in amorphous polymers, if for each state of deformation below Θ_g, an excursion to a temperature above Θ_g is taken, the material will return to its original state of maximum entropy. Therefore, the Wang and Guth model adopted here is considered a very good measure of the back stress.

where: N is the number of rigid chain links between entanglements; C^R is essentially the rubbery modulus which is equal to $nk\Theta$; where n is the number of chains per unit volume; k is Boltzmann's constant; and $\mathcal{L}$ is the Langevin function defined by:

$$\mathcal{L}(\beta_i) = coth(\beta_i) - \frac{1}{\beta_i} = \frac{V_i^p}{\sqrt{N}}, \tag{1.28}$$

with the inverse given by $\mathcal{L}^{-1}(\frac{V_i^p}{\sqrt{N}}) = \beta_i$. The temperature dependence of the back stress enters the model through the rubbery modulus C^R. As will be discussed below, it is also worth noting that experiments indicate that strain rate affects the back stress of some amorphous polymers at very large deformations, but then only at sufficiently high temperatures and very low strain rates. This is indicative of some relaxation phenomenon, possibly due to entanglement drift produced by reptation at large stretches and over longer periods of time. This effect is not modelled here, but is discussed in a later section. It should not have a significant influence on most forming processes which are usually conducted at moderate to high strain rates ($\dot{\gamma} \geq 0.01 sec^{-1}$).

Operationally, the back stress tensor, $\mathbf{B}$, is computed by noting that it is coaxial with the left plastic stretch tensor, $\mathbf{V}^p$, which is determined from the polar decomposition of the plastic deformation gradient, $\mathbf{F}^p$:

$$\mathbf{F}^p = \mathbf{R}^p\mathbf{U}^p = \mathbf{V}^p\mathbf{R}^p. \tag{1.29}$$

The principal components, $V^p{}_i$, and axes of $\mathbf{V}^p$ are then found and the associated B_i are calculated from equation (1.27). The back stress tensor $\mathbf{B}$ is then found by rotating the diagonal tensor consisting of elements B_i to the unloaded configuration $\mathbb{F}^p$ from the eigen space of $\mathbf{V}^p$. We note here that if we had chosen $\mathbf{R}^p = \mathbf{1}$ and $\mathbf{R} = \mathbb{R}^e$, then $\mathbf{F}^p = \mathbf{U}^p$. The resulting principal components of the back stress tensor, B_i, would be identical, but the tensor would be coaxial with $\mathbf{U}^p$ not $\mathbf{V}^p$. We could call this tensor

$\mathbf{B}_{U^p}$. In future calculations, such as determining the driving stress state $\mathbf{T}^{*\prime}$ (equation 1.4), $\mathbf{B}_{U^p}$ would have to be rotated by $\mathbf{R} = \mathbf{R}^e$ to obtain $\mathbf{B}$: $\mathbf{B} = \mathbf{R}\mathbf{B}_{U^p}\mathbf{R}^T$. This is one of the reasons for having chosen $\mathbf{R} = \mathbf{R}^p$ and $\mathbf{R}^e = \mathbf{1}$ in section 1.2.1.

1.2.4 Intermolecular Resistance: Softening and Pressure Dependence

As mentioned previously, the yield and post-yield behavior of glassy polymers exhibit pressure dependence and true strain softening, as well as rate and temperature dependence. Temperature and rate effects have already been modelled. It is now of interest to model the effects of strain softening and pressure on the intermolecular resistance. The expression for this resistance, equation (1.23), will now be modified to incorporate these effects. The intermolecular resistance is now interpreted as the effective equivalent shear stress, τ, present at a material point:

$$\tau = \left[\frac{1}{2} tr\left(\mathbf{T}^{*\prime 2}\right)\right]^{\frac{1}{2}}, \qquad (1.30)$$

where $\mathbf{T}^{*\prime}$ is the driving stress state defined earlier.

Strain softening is the term given to the drop in true stress with strain upon initiation of deformation, which is characteristic of many polymers, whether amorphous or semi-crystalline. Other materials, including granular solids, also exhibit this behavior. Softening is invariably accompanied by inhomogenous deformation on small scale in the form of shear banding. We incorporate softening into the constitutive law for $\dot{\gamma}^p$ by modifying the athermal yield strength, s_0, of the material as plastic straining occurs. We assume that as the material begins to undergo plastic deformation, there is some average restructuring of the molecular chains in the "flowing state" that causes an actual fall in the athermal shear resistance of the material. This assumption is motivated

by examining experiments on companion polycarbonate (PC) samples which have been given different heat treatments and, therefore, different initial structures. Under identical testing conditions, these test specimens initially yield at different stress levels and subsequently soften to approximately the same level [6]. In particular, PC quenched from Θ_g will yield at a low stress level and show little softening. On the other hand, if this same material is first annealed somewhat below Θ_g, it will yield at a much higher stress level and subsequently soften until it reaches the lower stress level at which its quenched companion flows. This strength level is thought to be associated with a "preferred" structure being reached during plastic straining, possibly due to the attainment of a local flow dilatation, i.e. increased local free volume, associated with the shear banding on a small scale. That this is indeed so has been established in amorphous metallic alloys [17].

In order to construct an evolution equation for the athermal shear resistance, s_0, certain characteristics of strain softening are identified by examining stress-strain curves. Such curves [7, 12, 13] indicate that softening is dependent on plastic strain rate, temperature, and structure. We define the total yield drop to be the difference between the peak stress prior to softening and the lowest stress level reached subsequent to plastic flow. In general, this drop depends on the strain rate and temperature. The rate of the drop depends on the structure and strain rate. The following phenomenological softening evolution equation encompasses most of the above dependencies:

$$\dot{s} = h\left(1 - \frac{s}{s_{ss}(\Theta, \dot{\gamma}^p)}\right)\dot{\gamma}^p, \tag{1.31}$$

where the quantity s is the current athermal deformation resistance of the material indicating the current state of the structure. The initial structure is represented by the value of s at the upper yield point, s_0; h is the slope of the yield drop with respect to

plastic strain; s_{ss} is the value s reaches at steady state, i.e. the "preferred" structure, and, as indicated, s_{ss} may depend on temperature and strain rate.

The instantaneous elastic shear modulus, μ, is a fundamental scaling factor of the intermolecular resistance, as can be inferred from equation (1.20). Therefore, a decrease in the intermolecular resistance with plastic straining must be accompanied by a decrease in the elastic shear modulus. We may hypothesize that this reduction in μ is indeed the basic cause of the effect in the localization zone. At the flow state, the steady state flow dilatation results in a decreased intermolecular interaction that reduces the shear modulus of the material in the flow state (possibly by only 10%) which then lowers the athermal flow resistance by a corresponding amount. The effect on the plastic flow of the material is large as seen in the amount of strain softening exhibited by glassy polymers. However, the effect on the large strain response of the solid is negligible.

Amorphous polymers are also known to age under certain pressure and temperature conditions. In these materials, aging apparently leads to the recovery of the initial resistance s_0 after some time. Thus, after aging, the yield stress increases with no additional plastic straining. The aging of polyvinylchloride (PVC) under sustained load is discussed in reference [7]. When this material is taken past yield in tension, partially unloaded and held for some time at a stress level insufficient to further propagate the neck, and then reloaded, an initial increase in the yield stress is observed. However, when unloaded to zero load and then reloaded, no increase is observed. The holding times were not given. This is indicative of aging in PVC. This aging phenomenon was also observed by Kramer [50] in nylon where he concluded that the stress caused better interchain packing in the amorphous regions of the nylon. This suggests our

assumption that aging increases the athermal shear resistance of the polymer. For future applications, equation (1.31) may be generalized to include aging:

$$\dot{s} = h\left(1 - \frac{s}{s_{ss}}\right)\dot{\gamma}^p + a(s, \Theta, p), \tag{1.32}$$

where the function a represents the rate of aging which is presumed to depend on the current structure, s, the temperature, Θ, and the hydrostatic pressure, $p = -\frac{1}{3}tr(\mathbb{T})$. The rate of aging tends to increase as the temperature, Θ, approaches Θ_g as demonstrated by the results of annealling. Currently, for most amorphous polymers, more experimental data is required before an appropriate function for a may be determined. In this current application, it will not be included.

The peak shear yield strength of amorphous polymers has been found to be essentially linearly dependent upon pressure for moderately large hydrostatic stresses. This has been shown experimentally by comparing the peak yield stress in compression at constant strain rate with that in tension as well as by superposing pressure on various tests [8,9,10]. This dependence may be linearized in the rate-independent case as:

$$\tau_y = \tau_{y0}\left(1 + \alpha\frac{p}{\tau_{y0}}\right), \tag{1.33}$$

where: τ_{y0} is the peak shear yield strength at zero pressure level; p is the hydrostatic pressure; α is the pressure coefficient, and τ_y is the shear yield strength under pressure. The pressure dependence of the effective equivalent shear stress necessary to sustain (visco-)plastic strain rate $\dot{\gamma}^p$ may be similarly obtained by once again modifying the expression for the athermal shear resistance, s. To this end, we introduce the parameter $\tilde{s}$, dependent on pressure as well as the evolving athermal shear resistance s:

$$\tilde{s} = s\left(1 + \alpha\frac{p}{s}\right). \tag{1.34}$$

In applications, this parameter, the "effective" athermal shear resistance, will be used in equation (1.15) rather than s_0, to provide a constitutive law for $\dot{\gamma}^p$ which accounts for the effects of temperature, pressure, rate and strain softening:

$$\dot{\gamma}^p = \dot{\gamma}_0 exp\left[-\frac{A\tilde{s}}{\Theta}\left(1-\left(\frac{\tau}{\tilde{s}}\right)^{\frac{5}{6}}\right)\right]. \tag{1.35}$$

This law for the rate of plastic straining is incorporated into equation (1.13) of the 3-D continuum model providing $\mathbf{D}^p$, the rate of plastic deformation.

1.2.5 Secondary Relaxation Effects: Entanglement Drift

Experiments indicate that strain rate and temperature affect the back stress of some amorphous polymers at very large deformations but only at sufficiently high temperatures and very low strain rates. This is indicative of the occurance of additional material relaxation due to entanglement drift at large stretches when given an appropriate amount of time or a high enough temperature.

The strain rate effect is apparent in the Hope, et al [12] stress-strain data for PMMA which is at fixed temperature and over several decades of strain rate. Here the slope of the stress-strain curves (Figure 1.7) for the lower strain rates is notably lower than those of the higher strain rate curves at large stretches. This suggests that an additional relaxation process such as entanglement drift is occurring in the material, thereby increasing the number of rigid links between entanglements, N, or the effective locking stretch, which simultaneously decreases the rubbery modulus, C^R, by decreasing the molecular chain density, n. A change in the chain density is inversely related to a change in the number of rigid links between entanglements due to the conservation of the total number of rigid links in a material sample, nN. Therefore, any increase in the number of rigid links between entanglements due to entanglement

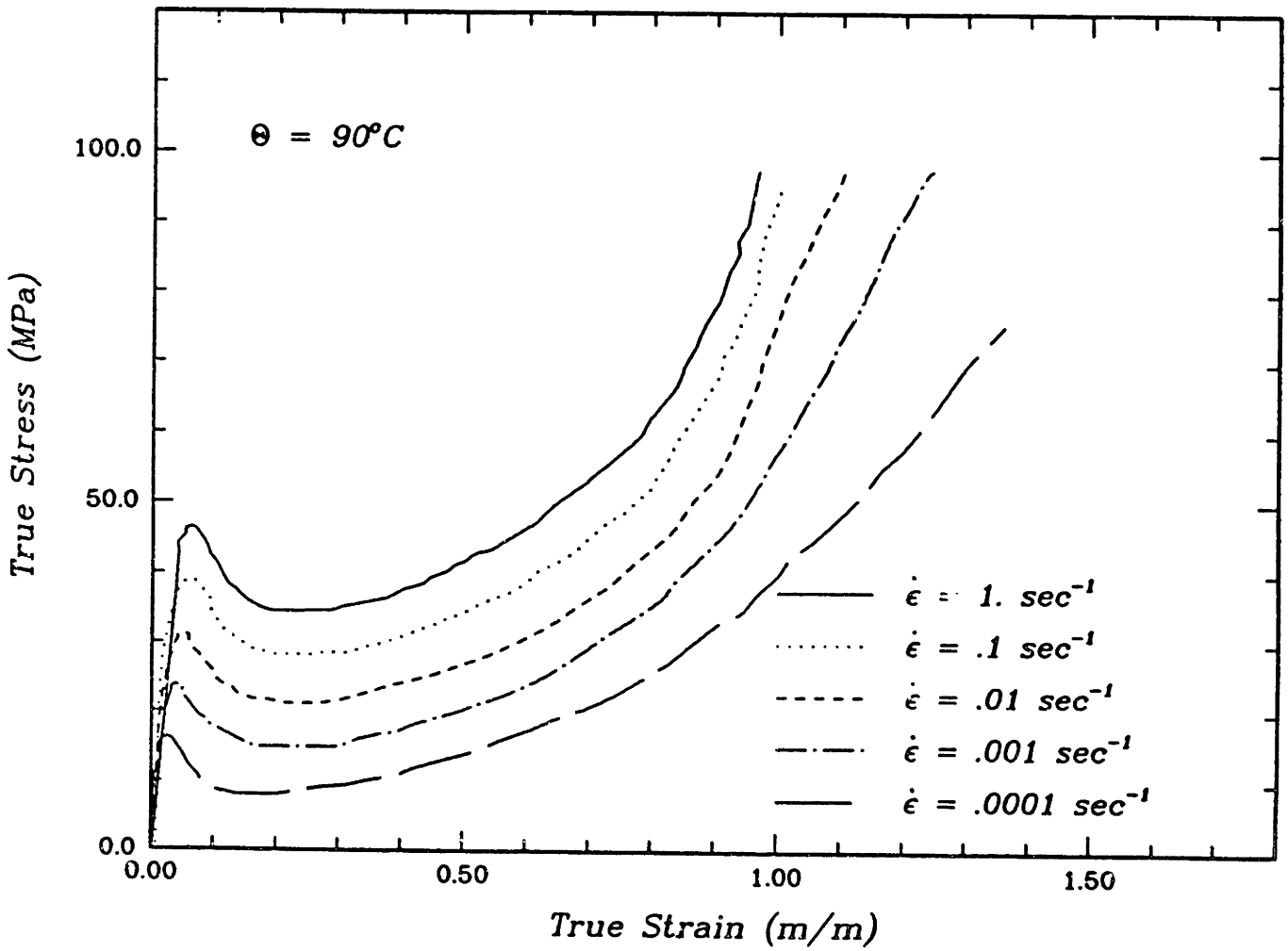

Figure 1.7. Tensile true stress–strain–strain rate curves for PMMA at 90°C, [12].

drift must be accompanied by a decrease in the overall chain density because the average length of a chain has increased, thus decreasing the number of chains in the material sample. These changes in the macromolecular structure of the material have the experimentally observable effect of decreasing the back stress at any particular value of imposed stretch.

The temperature effect is apparent in the Kahar [15] analysis of birefringence data where he determines the molecular chain density at various temperatures above and below the glass transition temperature for PMMA. This data is given in Table 1.1. A slight decrease in n occurs with increasing temperature before $\Theta_g = 110°C$ is reached and after which a dramatic decrease in n occurs. This results in a lower C^R which, as discussed earlier, is equal to $nk\Theta$.

A similar relaxation phenomenon has been observed in vulcanized rubber by Rivlin and Thomas [18]. They proposed modelling this behavior with the Green and Tobolsky [19] modification to the James and Guth [20] non-Gaussian statistical mechanics model of rubber elasticity. This modification essentially states that when the material is in a deformed state, the chain density and the number of rigid segments (our rigid links) between crosslinks (our entanglements) changes such that a two-network system develops. This suggests that only portions of the material are relaxing and these portions relax to a new and fixed number of rigid segments between crosslinks, thereby creating a second network which coexists with the original network. The relaxation occurs such that the density of rigid segments in the material is preserved. This model gives a simple but physically realistic picture of what may actually be occuring in the material. This model is simple in the sense that there are probably many coexisting networks in the material, rather than just two. The model also does not account for

TABLE 1.1

PMMA Chain Density [15]

Temperature Θ (^oC)	Chain Density n $\cdot 10^{-26}$ (m^{-3})
50	15.1
90	8.4
100	6.4
116.5	2.4

the evolution of the material to this new state of two fixed coexisting networks. Here, we propose a phenomenological model of this relaxation process where the effect of the development of coexisting networks which contain different numbers of rigid links between entanglements is averaged into a single network model which contains an evolving N such that the rate of change of N may be functionally represented as:

$$\dot{N} = f\left(\tau^B, \Theta, N\right). \tag{1.36}$$

where N is taken to depend on the equivalent back stress, $\tau^B = \sqrt{\frac{1}{2}\mathbf{B}\cdot\mathbf{B}}$, the absolute temperature, and the current number of links between entanglements. We note that τ^B is itself dependent on V_i^p, Θ, N, and n, but consider $\dot{N}$ to also be explicitly dependent on Θ and N. A specific function for $\dot{N}$ is proposed in the next paragraph. The initial conditions are taken to be N_0 and n_0 giving $n_0 N_0$ as the density of rigid links in the material. Therefore, if N represents the newly evolved average number of links between entanglements, then the corresponding current chain density is given by $n = \frac{N_0}{N} n_0$. This model does not explicitly contain the physical picture of different coexisting networks within the material as does the Rivlin-Thomas model; however, it does represent the average, relaxed state of the material and accounts for the evolution of this state.

Since we are considering N to be evolving because of entanglement drift, we may view the function f, to be derivable from a viscous dashpot formulation, where $\dot{N}$ is given by:

$$\dot{N} = \frac{1}{\eta(\Theta)}\tau^B, \tag{1.37}$$

where $\eta(\Theta)$ is a temperature dependent viscosity-like term with dimensions of stress-time. This rate is proportional to the relaxation creep rate of the material, $\dot{\gamma}^c$, i.e. $\dot{\gamma}^c \propto \dot{N}$. In one dimension, we can express the total strain rate as the sum of its elastic, plastic, and creep components:

$$\dot{\gamma} = \dot{\gamma}^e + \dot{\gamma}^p + \dot{\gamma}^c. \tag{1.38}$$

In order to generalize this to three dimensions, the creep rate must be mod 97a tensorial direction. Since the driving stress state for this relaxation phenomenon is the back stress, the tensorial direction must be the normalized back stress tensor. We now consider the tensor $\mathbf{D}^p$ to represent the rate of permanent deformation in the material. Therefore, the expression for $\mathbf{D}^p$ must be modified to include this additional relaxation phenomenon and becomes:

$$\mathbf{D}^p = \dot{\gamma}^p \mathbf{N} + \dot{\gamma}^c \frac{1}{\sqrt{2\tau^B}} \mathbf{B}. \tag{1.39}$$

This proposed function for the evolution of N, although simple, encompasses the observed effects of both strain rate and temperature on the back stress. The effect of strain rate is appropriately accounted for by noting that at high rates of deformation the first term of equation (1.39) dominates the second term and, therefore, there will not be enough real time for any significant evolution of N. At lower strain rates, the two terms in equation (1.39) will be of the same order of magnitude, and enough time will elapse for N to evolve and have a marked impact on the back stress. The effect of temperature on this relaxation is taken into account through the temperature dependent viscosity term which decreases with decreasing temperature in a manner similar to the temperature dependence of the elastic modulus which exhibits a gradual drop before Θ_g and a large drop in the Θ_g region. Therefore, at temperatures near Θ_g, $\dot{\gamma}^c$ would become of order $\dot{\gamma}^p$ and N would have enough time to evolve and significantly impact the back stress.

This proposed phenomenological model for the relaxation of amorphous polymers due to entanglement drift qualitatively accounts for the experimentally observed tendencies in the behavior of these materials at large stretches. This model has not been

numerically incorporated into the constitutive model described earlier where both C^R and N are taken to be constant. The implementation of this relaxation effect into the current numerical model would be complicated because we now have an evolving C^R and N, as well as a more complicated (no longer associative) constitutive law for $\mathbf{D}^p$. However, the basic framework of the numerical integration and overall FORTRAN program would remain essentially intact.

1.2.6 Additional Temperature Effects

Here, we briefly note that temperature may also be "evolving" during deformation. At high strain rates, adiabatic heating may have a significant impact on the material response. In this case, plastic dissipation would result in a rate of change of temperature $\dot{\Theta} = \frac{\omega}{\rho c} tr[\mathbf{T}^{*\prime}\mathbf{D}^p]$. Here, ρ is the density of the material, c is the specific heat, and ω is the fraction of heat dissipated. The plastic working term due to the back stress $tr[\mathbf{B}\mathbf{D}^p]$ is not dissipative but stored in the material due to the locked in orientation.

Another limiting case is the case of isothermal deformation where $\dot{\Theta} = 0$. In general, thermo-mechanical coupling should be considered where Θ may be both a loading parameter as well evoloving due to adiabatic heating, and the thermal properties of the material must be considered. In this thesis work, we take temperature to be a specified parameter of current state.

1.3 Summary of Model

For completeness, the basic equations necessary to implement this constitutive model, with the exclusion of the secondary relaxation effects, are summarized below:

Elastic-Plastic Decomposition of the Deformation Gradient:

$$\mathbf{F} = \mathbf{F}^e\mathbf{F}^p; \tag{1.40}$$

$$\mathbf{F}^{e^T} = \mathbf{F}^e; \tag{1.41}$$

Polar Decomposition of the Plastic Deformation Gradient:

$$\mathbf{F}^p = \mathbf{V}^p\mathbf{R}^p; \tag{1.42}$$

Cauchy Stress Tensor:

$$\mathbf{T} = \frac{1}{J}\mathcal{L}^e\left[ln\mathbf{F}^e\right]; \tag{1.43}$$

Driving Stress Tensor:

$$\mathbf{T}^* = \mathbf{T} - \frac{1}{J}\mathbf{F}^e\mathbf{B}\mathbf{F}^e; \tag{1.44}$$

Principal Components of the Back Stress Tensor:

$$B_i = C^R\frac{\sqrt{N}}{3}\left[V_i^p\mathcal{L}^{-1}\left(\frac{V_i^p}{\sqrt{N}}\right) - \frac{1}{3}\sum_{j=1}^{3}V_j^p\mathcal{L}^{-1}\left(\frac{V_j^p}{\sqrt{N}}\right)\right]. \tag{1.45}$$

Rate of Deformation referred to the Unloaded Configuration:

$$\mathbf{D}^p = \dot{\gamma}^p\mathbf{N}; \tag{1.46}$$

Plastic Spin:

$$\mathbf{W}^p = \mathbf{W} - \mathcal{W}\left[\mathbf{D} + \mathbf{D}^p\right]; \tag{1.47}$$

Rate of Plastic Straining:

$$\dot{\gamma}^p = \dot{\gamma}_0 exp\left[-\frac{A\tilde{s}}{\Theta}\left(1 - \left(\frac{\tau}{\tilde{s}}\right)^{\frac{k}{q}}\right)\right]; \tag{1.48}$$

Initial Value of the Athermal Shear Resistance:

$$s_0 = \frac{0.077\mu}{1-\nu}; \tag{1.49}$$

Evolution Equation for the Athermal Shear Resistance:

$$\dot{s} = h\left(1 - \frac{s}{s_{ss}(\Theta, \dot{\gamma}^p)}\right)\dot{\gamma}^p; \tag{1.50}$$

Pressure Dependence of the Effective Athermal Shear Resistance:

$$\tilde{s} = s + \alpha p. \tag{1.51}$$

All quantities used here have been defined earlier in the paper.

In order to facilitate the solving of boundary value problems for inhomogeneous deformation, this constitutive model has been numerically integrated and incorporated into the finite element code ABAQUS [16] (see Appendix A). The integration of these equations, while complex, can be simplified to some extent by considering the temperature and deformation range of the boundary value problems for which this model is primarily applicable. Most forming processes on glassy polymers are conducted near Θ_g where plastic flow occurs at relatively low stress levels resulting in very small elastic strains. For the example to be considered in the next section, the magnitude of the elastic strains, ϵ^e, is approximately given by:

$$\epsilon^e \cong \frac{\sigma_y}{E} \cong \frac{30MPa}{2000MPa} \cong 0.015. \tag{1.52}$$

This magnitude is negligible when we consider deformation processes where the plastic strain will be as great, and often greater than 1.0. Neglecting terms of order ϵ^e simplifies the governing equations of the problem. This is observed by noting the following relevant approximations:

$$\mathbf{W}^p \cong \mathbf{W}; \tag{1.53}$$

$$\mathbf{F}^p \cong \mathbf{F}; \tag{1.54}$$

$$\mathbf{T}^* \cong \mathbf{T} - \mathbf{B}. \tag{1.55}$$

These approximations carry through the entire integration procedure, reducing the computational complexity of the problem, and give a clearer conceptual understanding of the elastic-plastic decomposition of the deformation gradient. By neglecting elastic deformations, we are also better able to associate the operation of lumping all of the system rotation into the plastic deformation gradient with the notion of affine deformation during plastic flow.

1.4 Identification of Material Properties

In order to successfully implement the constitutive model, the material constants must be appropriately identified. The constants which must be obtained experimentally include those that model the temperature, pressure, strain rate, softening and hardening effects. The necessary experiments are described here, and the constants for PMMA are then determined from such experiments reported in the literature.

1.4.1 Temperature

Temperature affects both components of resistance. It affects the intermolecular resistance explicitly and strongly in the $k\Theta$ term and implicitly since the initial athermal shear resistance, s_0, is dependent upon temperature. Recalling equation (1.20), the temperature dependence of s_0 is proportional to the temperature dependence of the shear modulus which is shown in Figure 1.8 for PMMA. The figure depicts the characteristic large drop in shear modulus at $\Theta_g = 110^oC$. The value for s_0 at $\Theta = 90^oC$ in

the annealed state was computed from the shear modulus and Poisson's ratio at this temperature [14] giving:

$$s_0 = 88.0MPa. \tag{1.56}$$

The explicit temperature dependence of the entropic resistance represented by the back stress tensor, **B**, enters through the rubbery modulus, C^R, which is proportional to temperature, $C^R = nk\Theta$. Here, n is taken to be constant, but, as discussed in section 1.2.5, n evolves with both temperature and back stress.

1.4.2 Pressure

The effect of pressure on yield can be measured by superposing various levels of pressure on stress-strain tests conducted at constant strain rate, either in tension, compression or shear, and recording the peak yield stress. A less extensive method would be to test the material in tension and then in compression since these contain two different pressure levels. The peak yield stress is then plotted against the pressure. The slope of this curve gives the pressure coefficient α. Rabinowitz, Ward, and Perry [8] have conducted the more extensive series of tests on PMMA giving $\alpha = 0.20$.

1.4.3 Strain Rate

The material constants which model the strain rate effects consist of the pre-exponential factor, $\dot{\gamma}_0$,and the lumped parameter, A. There are two different series of tests which can be used to determine these constants. One series which was used by Argon and Bessonov [11] consists of stress-strain tests at a fixed strain rate over a range of temperatures. The second series which we adopt here involves conducting stress-strain tests at a fixed temperature at various levels of strain rate.

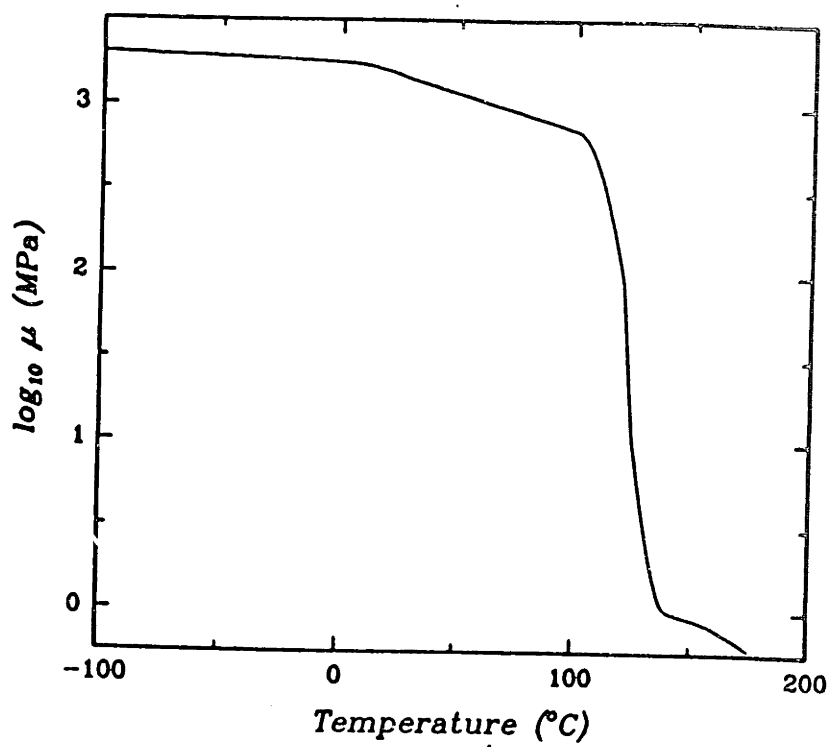

Figure 1.8. Log shear modulus vs Temperature for PMMA [14].

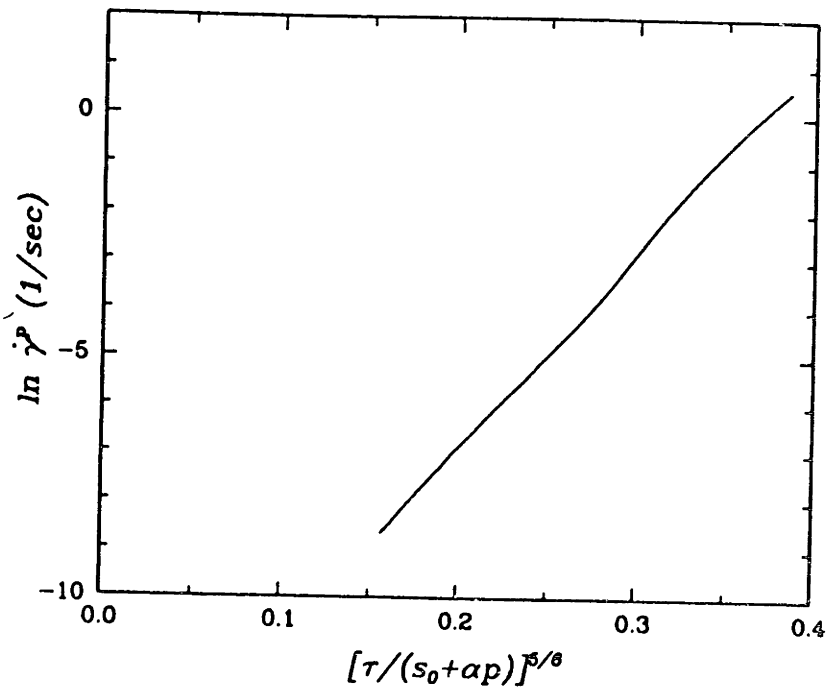

Figure 1.9. Plastic shear strain rate as a function of intermolecular resistance for PMMA at 90° C as computed from the data of reference [12].

In order to determine the constants from the tests at various strain rates, equation (1.47) is first rearranged to be the equation of a line:

$$ln\dot{\gamma}^p = B + C\left(\frac{\tau}{s_0 + \alpha p}\right)^{\frac{5}{6}}; \tag{1.57}$$

$$\text{where : } B = ln\dot{\gamma}_0 - \frac{A}{\Theta}(s_0 + \alpha p), \tag{1.58}$$

$$C = \frac{A}{\Theta}(s_0 + \alpha p). \tag{1.59}$$

Here it is understood that for initial (peak) yield stress, s has yet to evolve substantially from its initial value, s_0. The values at peak yield for τ and $\dot{\gamma}^p$ are used to obtain $ln\dot{\gamma}^p$ *vs.* $\left(\frac{\tau}{s_0+\alpha p}\right)^{\frac{5}{6}}$. The slope and intercept of the resulting line are the values of C and B from which the constants $\dot{\gamma}_0$ and A may be extracted.

The true stress-strain data of Hope, Ward, and Gibson [12] on PMMA at $\Theta = 363K$ for various strain rates (Figure 1.7) are now used to obtain values for $\dot{\gamma}_0$ and A for this material. This data is from tensile tests. Since our equations are in terms of plastic shear strain rates, $\dot{\gamma}^p$, and effective shear stress, τ, the values of $\dot{\epsilon}$ and σ_y, where σ_y is the peak true tensile stress, must first be modified on the basis of a Mises criterion by multiplying and dividing, respectively, by $\sqrt{3}$. Also, since the tests are tensile, there is a pressure component $p = -\frac{1}{3}\sigma_y$ at yield which is taken into account. The resulting data points for $ln\dot{\gamma}^p$ and $\left(\frac{\tau}{s+\alpha p}\right)^{\frac{5}{6}}$ are plotted in Figure 1.9. One can see that they do indeed form a straight line from whose slope and intercept we obtain values for A and $\dot{\gamma}_0$:

$$\dot{\gamma}_0 = 1.13\left(10^{11}\right) sec^{-1}, \tag{1.60}$$

$$A = 167.0^{\circ}K/MPa. \tag{1.61}$$

The fact that this experimental data lies on a straight line gives further support to the Argon model, since it was obtained independently from the theoretical development.

It is also of interest to point out that the Hope, et al. data exhibit the rate effects on terminal hardening at the lower imposed strain rates as discussed in section 1.2.5. As mentioned previously, this effect has not been included in the model and would not have much impact on high deformation rate processes. However, a model of this effect was suggested, and, one can see from Figure 1.7 that at lower strain rates, this phenomenon would have some impact on the level of texture developed in the material.

1.4.4 Strain Softening

This material, PMMA, exhibits a large amount of initial strain softening at $\Theta = 363K$ as is evident from Figure 1.7. It is apparent from this data that the percent softening, $\frac{\sigma_{max}-\sigma_{min}}{\sigma_{max}}$, is independent of strain rate, so, $s_{ss}(\Theta, \dot{\gamma}^p)$ in equation (1.49) will be taken as a function of temperature only. Softening is generally highly dependent on temperature. This effect has been experimentally observed both on the global level by examining stress-strain curves, and on the local level by examining the degree and coarseness of shear band formation in various amorphous polymers at different temperatures [7]. True stress-strain curves illustrating the temperature dependence of strain softening for PMMA are shown in Figure 1.10. It is to be noted that these tests were not conducted at constant strain rate, but at constant displacement rate. Subsequent rate effects, although present due to the inhomogeneous deformation of test specimens, are not apparent in the resulting curves. Therefore, these curves can only give an indication of the trend which strain softening follows with temperature. For temperatures below $90°C$, the percent softening is relatively constant. However, for temperatures above

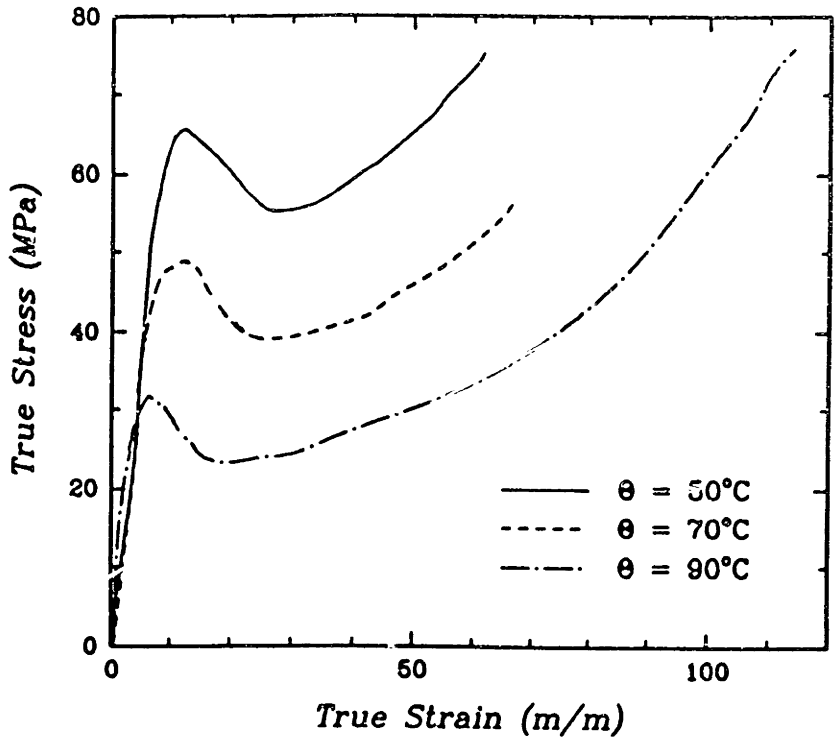

Figure 1.10. Tensile true stress–strain curves for PMMA as a function of temperature. These are constant displacement rate results [15].

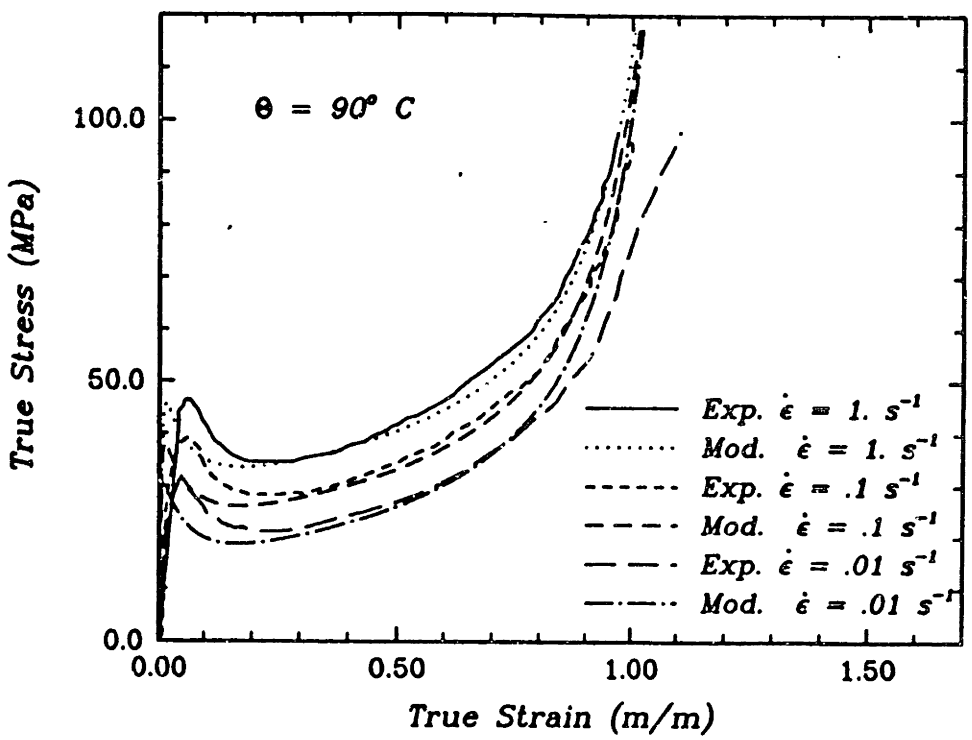

Figure 1.11. Tensile true Stress–strain data on amorphous PMMA: Model Results vs. Experimental Results. Experimental results taken from reference [12].

this range, i.e., as Θ approaches Θ_g, the amount of softening decreases rapidly with increasing temperature. For the extrusion analyses conducted in the following chapter, we are considering the material in the temperature range, $20^oC \leq \Theta \leq 90^oC$, and will therefore take the ratio, s_{ss}/s_0, to be constant. By comparing the maximum yield stress with the minimum yield stress after softening, the ratio, s_{ss}/s_0, was inferred to be:

$$\frac{s_{ss}}{s_0} = 0.875. \tag{1.62}$$

The rate of the yield drop with respect to deformation is measured by h which can be computed by rearranging equation (1.49) and estimating from Figure 1.7 the increment in plastic shear strain, $\Delta\gamma^p$, over which the drop, $\Delta s = s_{ss} - s_0$, occurs:

$$h \approx \frac{\Delta s}{\Delta\gamma^p}\left(\frac{1}{1-\frac{s_0}{s_{ss}}}\right). \tag{1.63}$$

For PMMA at $\Theta = 363K$, h was found to be $900MPa$.

1.4.5 Strain Hardening

The material properties required to model the entropic resistance are the rubbery modulus, C^R, and the number of rigid links between entanglements, N. An approximate value for the rubbery modulus, C^R, may in principle be measured by taking the material to a temperature, Θ_{test}, slightly above Θ_g and testing it in tension at a moderately rapid rate to minimize entanglement drift. The initial slope of the resulting stress-strain curve is C^R at this temperature. The value for C^R at the temperature, Θ, under consideration could be obtained by re-scaling as:

$$C^R(\Theta) = C^R(\Theta_{test}) \times \left(\frac{\Theta}{\Theta_{test}}\right). \tag{1.64}$$

This value will be lower than the actual value at Θ_{test} if Θ_{test} is in the glassy regime. The modulus C^R may also be found by measuring the number of chain segments per unit volume, n, at this temperature with, e.g., analysis of birefringence data, and calculating C^R from $C^R = nk\Theta$. A value for n at $\Theta = 363K$ (Table 1.1) was determined using this method by Kahar, et al. [15] for PMMA:

$$n = 8.4\left(10^{26}\right) m^{-3}, \tag{1.65}$$

from which the rubbery modulus at $\Theta = 363K$ was found to be:

$$C^R = 4.2MPa. \tag{1.66}$$

The number of rigid links between entanglements, N, may be computed from any tensile test taken to the limiting stretch of the material. For the Langevin model used, N is equal to the square of the terminal or locking stretch, λ_L. From Figure 1.7 one can see that locking occurs at a true strain of approximately 1 at strain rates greater than $0.01sec^{-1}$. This corresponds to a locking stretch of $\lambda_L = e \doteq 3$, where e is the base of the natural logarithm, giving:

$$N = \lambda_L^2 = 9. \tag{1.67}$$

All of the required material constants have now been identified.

The true stress-strain results of our model are superposed over the Hope, et al. experimental curves in Figure 1.11 and show very good agreement. The maximum and minimum flow stresses of the constitutive model match the experimental results over the range of imposed strain rates very well, as does the plastic strain increment over which the drop in flow stress occurs. The strain at which the maximum flow stress occurs is slightly off due to some small discrepancy in the elastic moduli. The effect of hardening is also well modelled as is shown by the slope of the stress-strain curves

at the larger stretches and the stretch at which locking occurs. We can see that the strain rate effect of hardening was not accounted for in the model by observing that the theoretical stress-strain curves at the lower strain rates reach terminal locking at the same λ_L as those at the higher strain rates, whereas the experimental curves at the lower rates have an effectively larger locking stretch and smaller slope.

The temperature dependence of the true stress-strain relation at a constant strain rate of $\dot{\epsilon} = 0.005 sec^{-1}$ as predicted by the constitutive model is depicted in Figure 1.12. The experimental curves of Figure 1.10 resulted from testing at a normalized displacement rate of $0.005 sec^{-1}$. Therefore, the peak stresses prior to strain softening of Figure 1.12 may be compared with those of Figure 1.10. The model predictions are found to be in very good agreement with the experimental results. The remainder of the curves are not comparable because the experiments were not conducted at constant strain rate.

1.5 Conclusion

In this chapter, a constitutive model describing the large inelastic deformation of glassy polymers has been developed based on the macromolecular structure of these materials and the corresponding micromechanism of plastic flow. The effects of strain rate, pressure, temperature, true strain softening and strain hardening have been accounted for in this model. The physical mechanism associated with each of these phenomena has been described. The kinematic formulation used to properly account for finite strain and rotation effects has also been detailed, noting that the conceptual complexity of the elastic-plastic decomposition of the deformation gradient is significantly reduced from that of poly-crystalline metals due to the affine molecular deformation that these

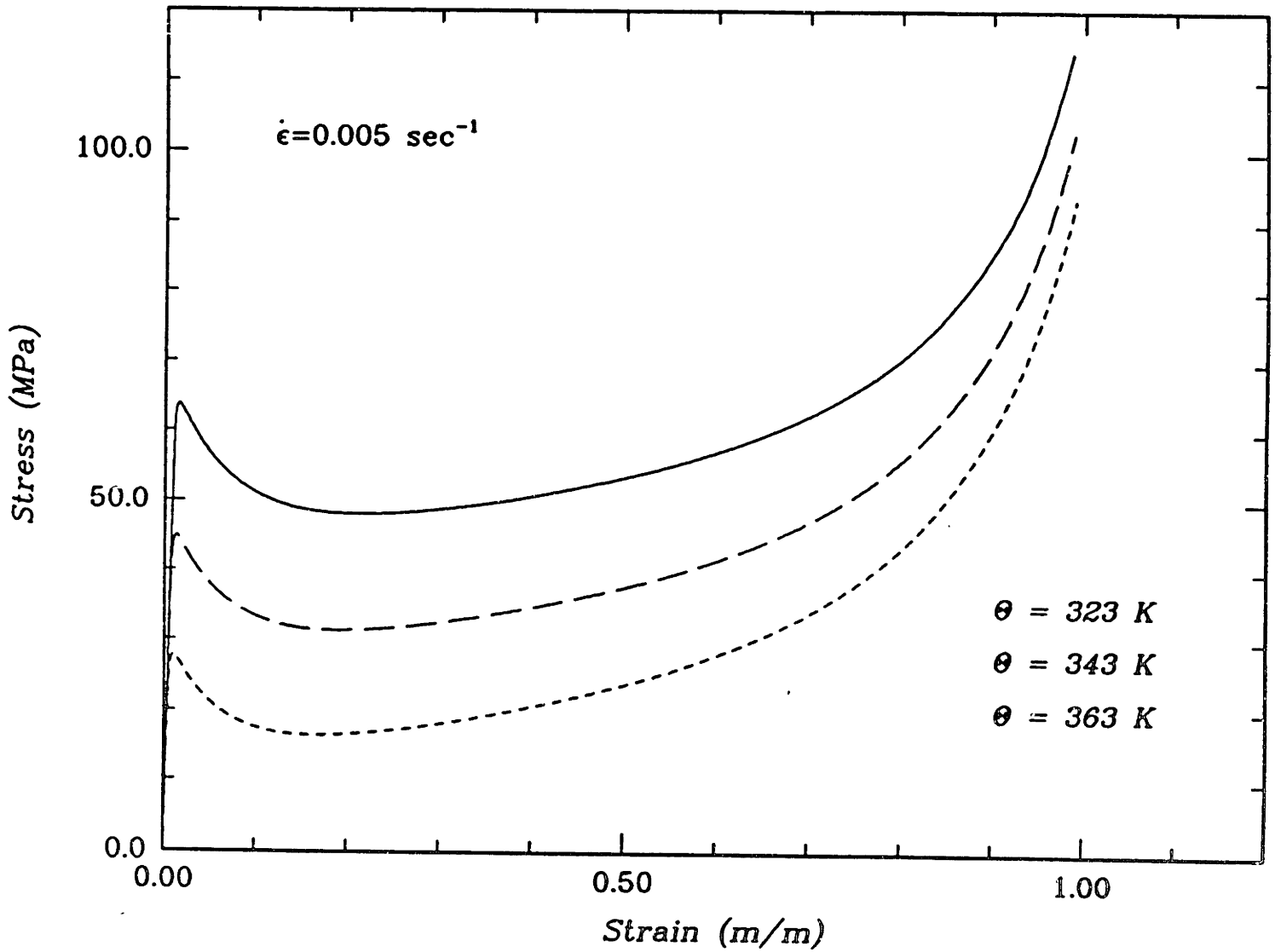

Figure 1.12. Model results for tensile true stress–strain data on glassy PMMA at a constant strain rate of 0.005sec^{-1} as a function of temperature.

polymers exhibit. As an aside, the elastic-plastic decomposition used was also applied to the case of the single crystal in Appendix B in order to demonstrate the general scope of this representation. The commercial glassy polymer PMMA was then successfully modelled with this constitutive formulation. The model was then numerically integrated and incorporated into the general purpose non-linear finite element code ABAQUS enabling the solution of boundary value problems involving inhomogeneous deformations such as the hydrostatic extrusion of glassy polymers analyzed in the next chapter. In Chapter Three, the model will be further modified to include effects of pre-orientation on the material behavior.

Chapter 2

Numerical Simulation of Hydrostatic Extrusion

2.1 Introduction

The manufacturing of products of industrial importance from glassy polymers by warm (near Θ_g) mechanical processes such as extrusion, drawing, and blow moulding usually produces a textured solid containing residual stresses. These processes generally impose very large and inhomogeneous deformations on the polymer making it difficult to predict and/or assess the degree of texture and residual stresses remaining in the products after manufacturing. In this chapter, we will analyze one such mechanical process, hydrostatic extrusion, using the constitutive model of Chapter One which describes the large inelastic deformation of amorphous polymers. The analysis will examine the development of texture in the material during processing, the effect of rate, temperature, pressure, and friction on the processing, as well as unloading effects as the processing nears completion. These results will be compared with experimental results wherever possible.

Oriented polymers may be successfully manufactured by the process of hydrostatic extrusion. This process essentially consists of forcing a continuous billet of material

through an appropriately shaped die via hydrostatically induced pressure. In particular, we will be analyzing the axisymmetric extrusion of a cylindrical billet of the isotropic amorphous polymer polymethylmethacrylate (PMMA) through a conical die, thereby producing a longer cylinder of smaller radius of what has now become oriented PMMA (Figure 2.1). The two major kinematic parameters of the process are the nominal extrusion ratio, R_N, which is the ratio of the cross-sectional area of the cylindrical billet (πR_0^2) to that of the die exit (πR_e^2), and the die angle, α_d, which is the half angle of the conical portion of the die.

Extensive experimental studies on the hydrostatic extrusion of both semi-crystalline and amorphous polymers have been conducted by a research group at the University of Leeds. The results of such experiments on amorphous PMMA are well documented in references [12] and [15]. These experiments cover a wide range of nominal extrusion ratios and examine such features as pressure vs. extrudate velocity, die swell, and shrinkage force. These experimental results will be used as a base for comparison with our numerical results.

The analysis of the extrusion of PMMA will be conducted using the constitutive model developed in Chapter One. This physically-based model accounts for the effects of strain rate, pressure, temperature, strain softening, and strain hardening. The material properties corresponding to these effects as characterized by PMMA's stress-strain curves [12] were identified in section 1.4. This constitutive model has been numerically integrated and incorporated into the finite element code ABAQUS [16] with the user-defined material law option (see Appendix A). This chapter will concentrate on the modelling of the hydrostatic extrusion boundary value problem, the interpretation of the numerical results of this problem, and the examination of the impact of the

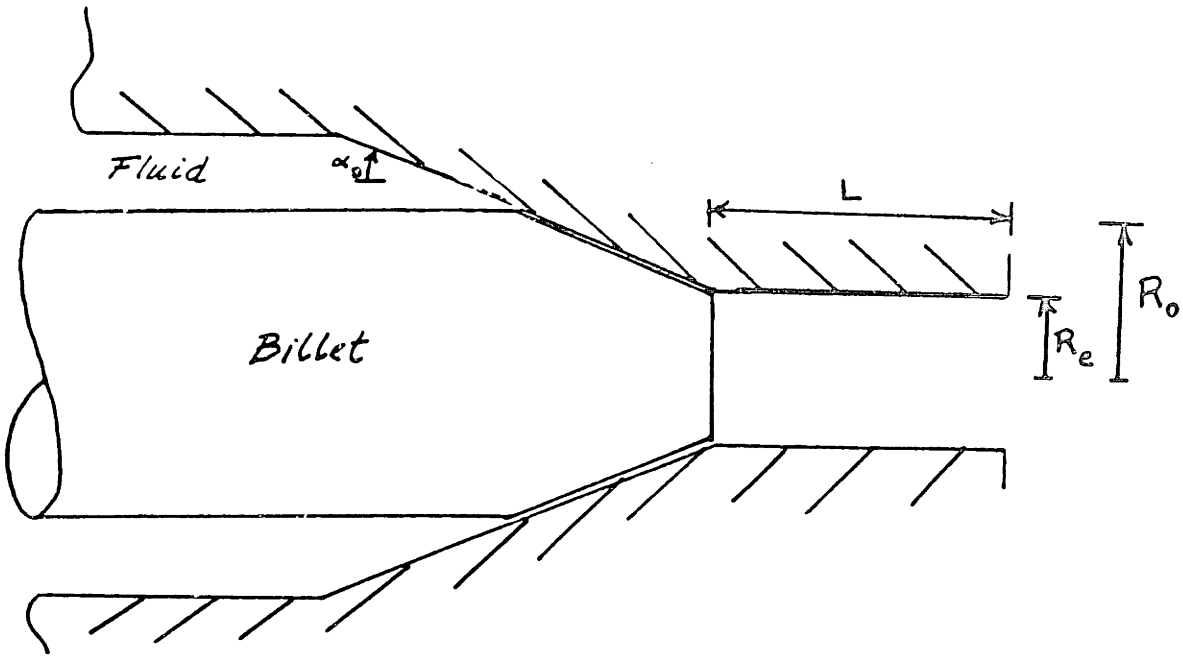

Figure 2.1. Schematic of the process of hydrostatic extrusion of a cylindrical billet through a conical die.

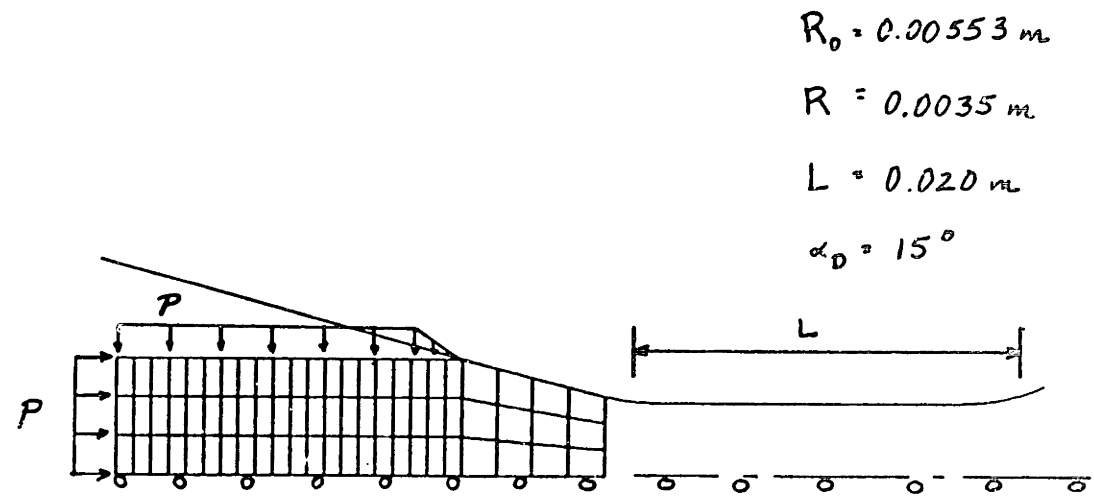

Figure 2.2. Finite element model of the hydrostatic extrusion of PMMA. Nominal extrusion ratio: R_N=2.5.

material behavior and boundary conditions on the results. In particular, the effects of rate, friction and temperature on the process are examined. The numerical results are directly compared with the experimental results of the Leeds University research group. These comparisons will show that our constitutive model can accurately predict the rate and temperature effects of the material behavior, as well as correctly assess the development of texture within the material as it undergoes large inhomogeneous deformation processing.

2.2 Description and Modelling of Boundary Value Problem

The hydrostatic extrusion of solid cylindrical rods of material is schematically illustrated in Figure 2.1. A long cylindrical rod with a "plug" tapered to correspond to the die angle is fitted into the die. A pressure transmitting fluid, castor oil, is then pumped into the apparatus until a relatively constant pressure is attained and the billet is then moving through the die at a relatively constant velocity. The plug at the end of the billet helps to prevent any initial leakage of fluid. The surface of the billet of PMMA has been treated in order to alleviate such processing problems as "stick-slip". The reader is referred to references [12] and [15] for a detailed description of the surface preparation of the material and the set-up of the experimental equipment.

Our analysis of the extrusion process takes full advantage of the axisymmetry of the geometry and boundary conditions. The finite element model for the case of a nominal extrusion ratio of 2.5 is shown in Figure 2.2. The mesh of the billet (Figure 2.2) consists of 8-node, reduced-integration, axisymmetric elements (ABAQUS type CAX8R). The elements are arranged three deep through the radius and are evenly spaced in the axial

direction throughout the cylindrical portion of the billet. The elements in the plug portion of the billet generally have greater axial spacing because they do not undergo as large a deformation as the main portion of the billet. The length of the billet modelled was chosen such that steady state was reached while a significant portion of the billet still remained to enter the die angle region.

The die is modelled as a stationary rigid surface with dimensions corresponding to those of the experimental apparatus:

R_e = exit radius = $0.0035m$;

L = barrel length =$0.20m$;

α_D = die angle = $15°$.

Interface elements (ABAQUS type IRS22A) identify those sections of the billet which may contact the die. As these sections contact the die boundary, a reaction pressure is applied to prevent penetration of the rigid surface. To ease the convergence of the abruptness of this contact problem, an exponential pressure-clearance relationship (see ABAQUS User Manual, p.6.6.24-1) is defined such that the contact pressure is gradually applied beginning at a distance of 0.01mm from the die surface. Analyses are conducted considering both a free-sliding interface between the billet and the die, as well as assuming Coulomb friction between these two bodies. The results of these two boundary conditions are later compared.

All nodes along the axis of symmetry are constrained to have no radial motion. The nodes at the trailing end of the billet are constrained to have the same axial displacement. A pressure boundary condition is applied along the trailing end and side of the billet mesh to simulate the pressure-transmitting fluid. The pressure along the side is gradually tapered to zero as the billet approached contact with the die (see

Figure 2.2). The applied pressure is ramped from zero to a constant value over a time period of 10 seconds. As the trailing end of the billet approaches contact with the die angle region, the boundary condition is switched from one of constant pressure to one of constant displacement rate at the trailing end of the billet. The constant displacement rate applied is that previously obtained at steady state. This boundary condition change is made at this point in the deformation in order to simulate the behavior of an even longer billet of material. If this change had not been made and the same level of pressure had been applied, the billet would have begun to move through the die at a faster rate because there would be less material in contact with the die surface, and, therefore, less resistance to the applied pressure. Since the rate of imposed deformation has a strong impact on the material response, it is important to either keep the velocity constant or use a very long mesh.

The extrusion is carried out at a temperature of $90°C$. Since the processing of the material occurs at relatively low magnitudes of strain rate ($\sim 10^{-3} sec^{-1}$), adiabatic heating effects are negligible, and we can consider the material to deform under isothermal conditions while in the die. However, as the billet exits from the die, it enters an environment at room temperature. After observing the large temperature dependence of the behavior of PMMA as shown in the preceding chapter and reference [13], we considered the temperature change upon exiting an important boundary condition to model. A simple heat transfer analysis considering natural convection boundary conditions was conducted to calculate a suitable temperature profile (Figure 2.3) modelling the cooling down of the extrudate from $90°C$ to $25°C$ as it exits the die (see Appendix C). Analyses for the case of an extrusion ratio of 2.5 are conducted using both this exit temperature profile, as well as isothermal $90°C$ exit conditions. Effects of the exit

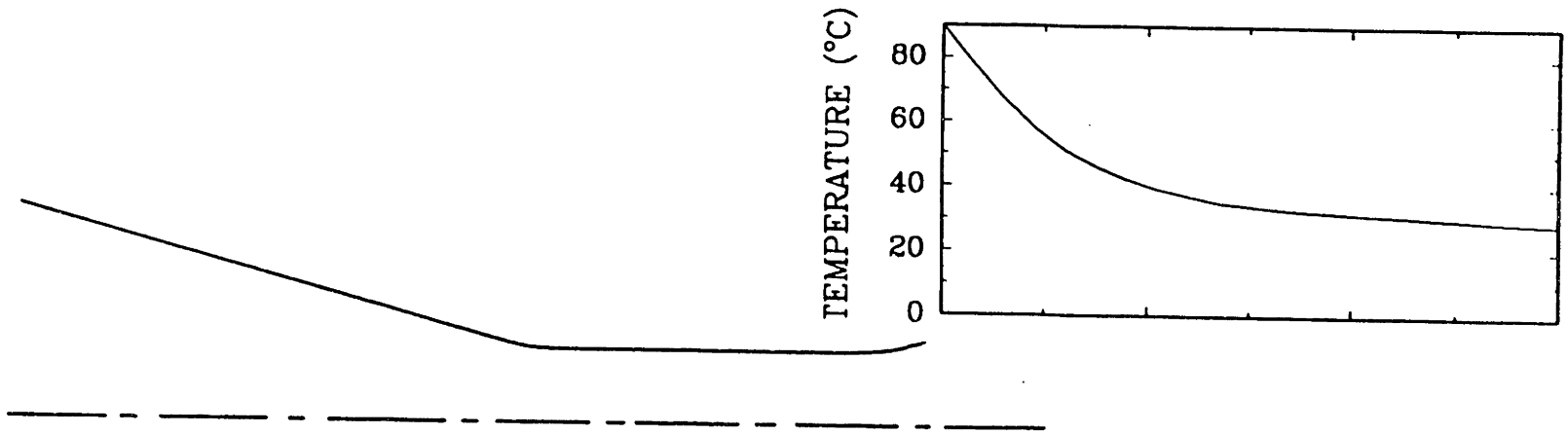

Figure 2.3. Temperature profile of extrudate as it exits the die. Die is represented by the solid line at left.

temperature conditions are found to be important, and are discussed later in this chapter.

2.3 Results

Our numerical analysis of the hydrostatic extrusion process accurately predicts the end state and global response of the material as will be shown by comparisons of the computed texture, back stress tensor, and pressure vs. steady state velocity with experimental results. The analysis also reveals many interesting details of the material behavior during processing while active plastic deformation is occurring. These include the evolution of texture, as well as gradients in strain rate and pressure at different points along the die. Below, we will discuss the response of the material to the processing as it moves through the cone and barrel portions of the die as well as the final state reached after exiting the die.

Three nominal extrusion ratios were analyzed: $R_N = 2.5$, 1.85, and 1.30. The billet of ratio 2.5 was most extensively analyzed. For this case, both sliding and friction interface boundary conditions between the billet and die were considered, as well as unloading at the constant extrusion temperature, $90°C$, and unloading as the extrudate exits the die into a room temperature environment, thereby cooling down to $25°C$. Both the friction and cool-down effects were found to be important. Therefore, the billets of extrusion ratios 1.85 and 1.30 were analyzed considering a friction interface with the die and unloading into a room temperature environment. The billet of nominal ratio 2.5 was also analyzed at two different levels of applied pressure to verify that an appropriate increase in velocity is obtained with an increase in pressure.

2.3.1 Die Swell

The results for the analysis of the billet of nominal extrusion ratio 2.5 with an applied pressure of 65MPa are shown in Figures 2.4 - 2.6. The plots of the deformed billet at various points during the processing (Figure 2.4) illustrate the material moving through the die with the transitional or "plug" section undergoing a lesser deformation than the main cylindrical section of the billet. The cylindrical section is shown as it begins deforming in the conical region of the die, and, then, as it reaches a relatively uniform state of deformation in the barrel region where it experiences shearing along the interface with the die. The material then exits the barrel and the processed deformation partially unloads. This unloading is commonly referred to as die swell which is defined as the fractional increase in the extrudate radius upon exiting the die.

The importance of the temperature boundary condition upon exiting is evident in these plots of the deforming billet as shown by comparing the different increases in radius upon exiting when cool down is, and is not, taken into account (Figures 2.4a and 2.4b). When the extrudate is allowed to exit into an environment of constant temperature, $\Theta = 90°C$, a die swell of 30% is obtained. Whereas, when the extrudate is permitted to cool down to room temperature upon exiting via the temperature profile shown in Figure 2.3, a die swell of 9.5% is obtained. The higher deformation resistance associated with the lower near exit temperatures resulted in the smaller computed die swell. A die swell of ~10% was obtained experimentally [12], indicating the necessity of including the appropriate temperature boundary condition. Our numerically computed die swell of 9.5% for the cool-down temperature distribution assumed is in very good agreement with the experimental result.

One of the reasons for this effect of temperature on die swell is illustrated in the

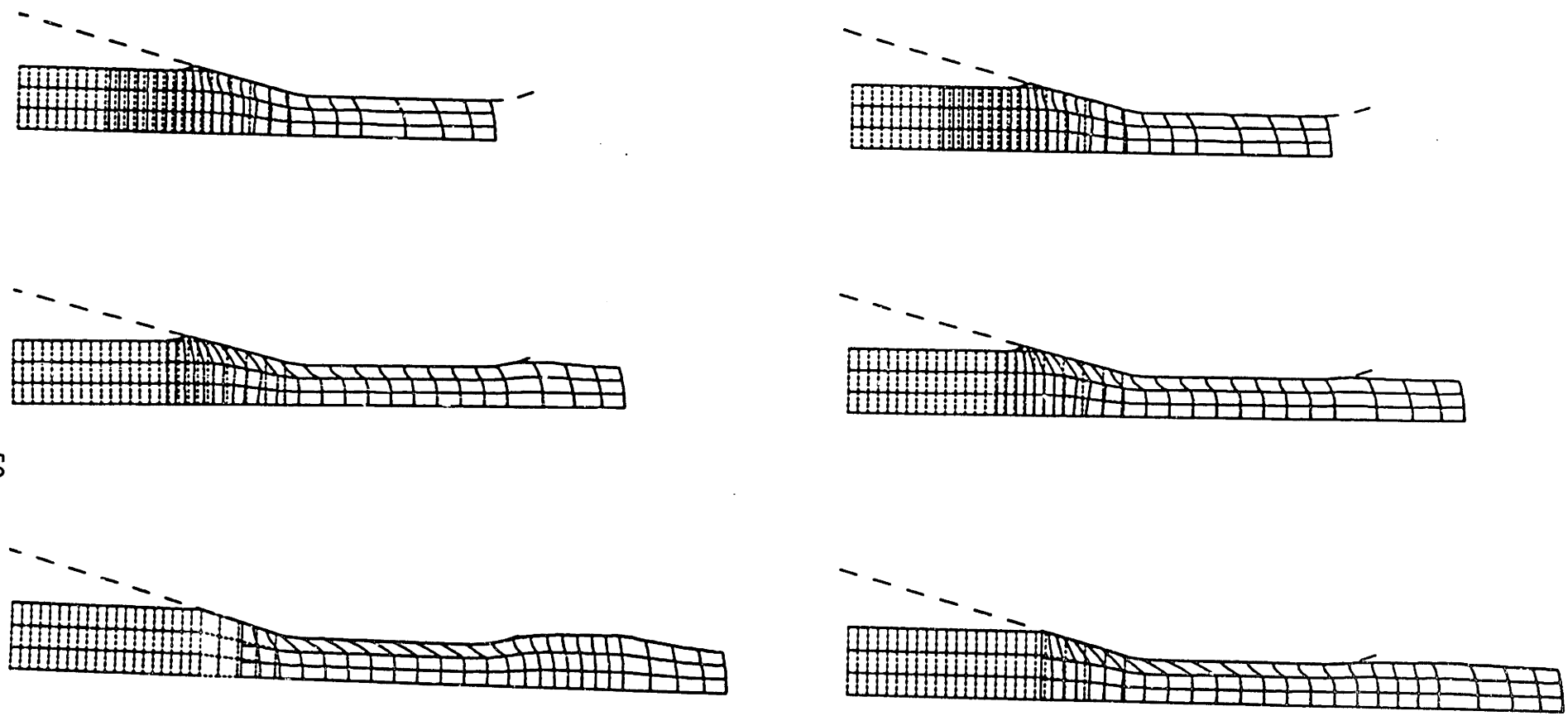

Figure 2.4. Deformation of billet of PMMA, R_N=2.5, at various points during the process considering both isothermal 90°C exit temperature conditions (a) and cool-down from 90°C to 25°C (b). The solid lines represent the deformed mesh; the dashed lines represent the undeformed mesh. Note the difference in die swell.

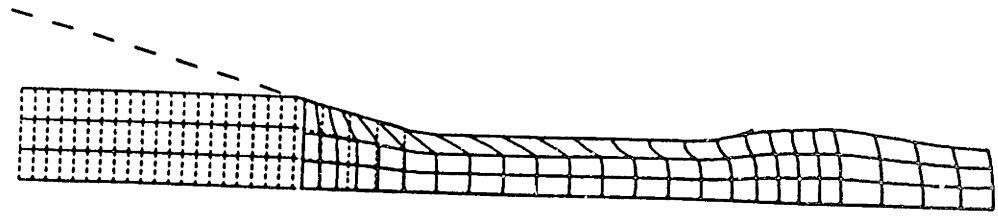

(a) Deformed mesh.

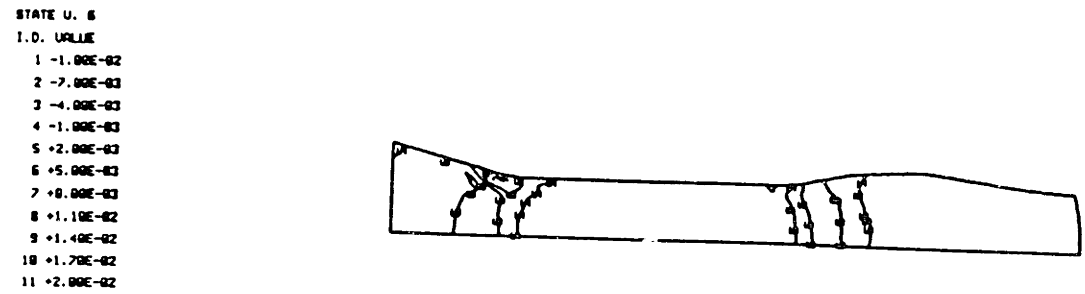

(b) Contour of the plastic strain rate.

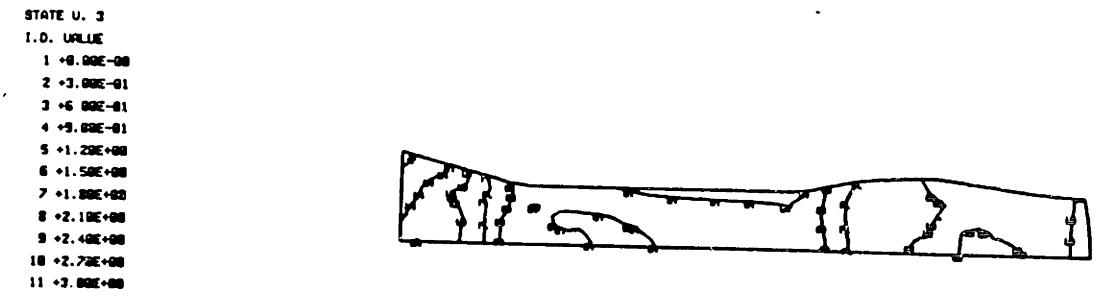

(c) Contour of F^P_{22}.

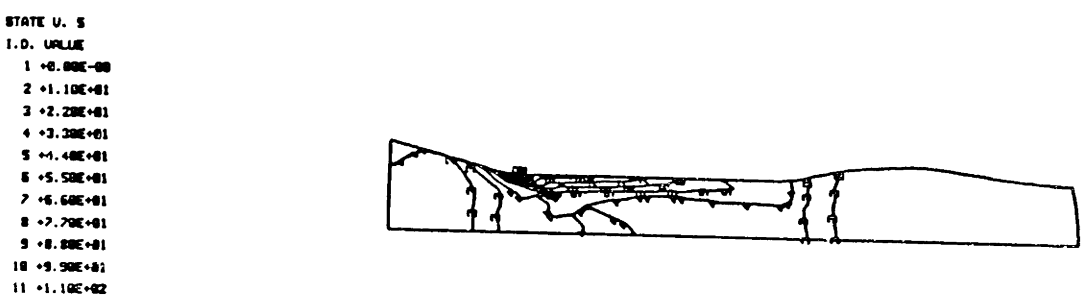

(d) Contour of B_{22}.

Figure 2.5. Results for the hydrostatic extrusion of PMMA, R_N=2.5, considering a frictional interface, α_f=0.20, and isothermal 90°C exit temperature conditions.

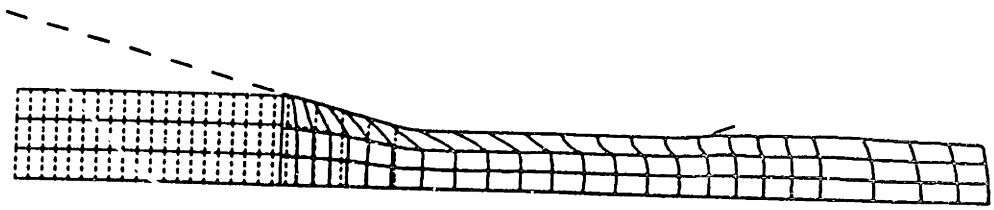

(a) Deformed mesh.

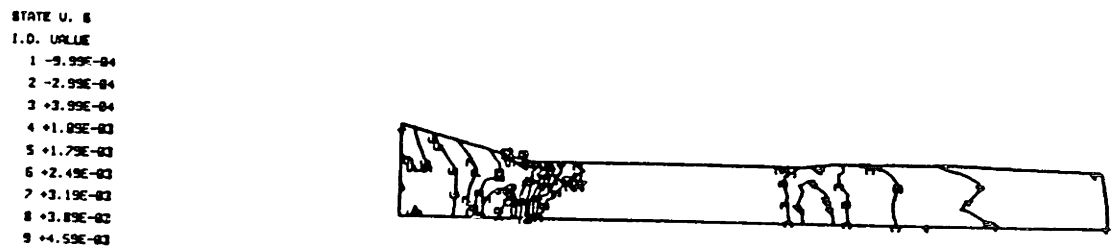

(b) Contour of plastic strain rate.

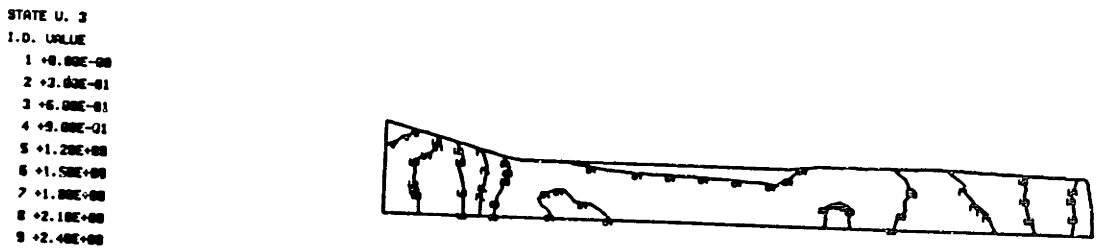

(c) Contour of F^{P}_{22}.

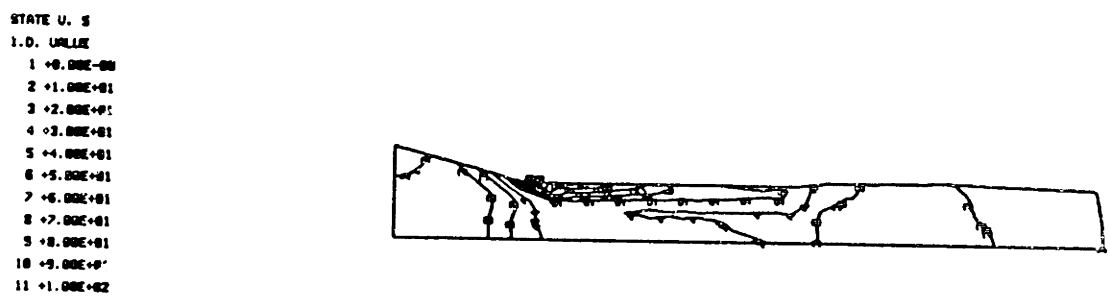

(d) Contour of B_{22}.

Figure 2.6. Results for the hydrostatic extrusion of PMMA, R_N=2.5, considering a frictional interface, α_1=0.20, and an exit temperature profile cooling from 90°C to 25°C.

contour plots of plastic strain rate (Figures 2.5b and 2.6b). Comparing the rate contours in the exit region of the extrudate kept at 90^oC with that cooled to 25^oC, we note that the plastic strain rate for the 90^oC case is four times higher than for the cool-down case. This is due to the strong Bauschinger effect of the material. Figure 2.7 depicts the true stress-strain curve for PMMA as it is homogeneously extended in simple tension at a constant strain rate of $3(10^{-3})sec^{-1}$ to a stretch of 2.5 and then unloaded at this same rate and at a constant temperature of 90^oC, or with simultaneous cooling from 90^oC to 25^oC at a $\dot{\Theta} = 1K/sec$ upon unloading reaching 40^oC at zero stress, then experiencing a small contraction due to the additional 15^oC temperature decrease. Reverse yielding is shown to occur much earlier at the higher temperature leading to the higher plastic strain rates at the die exit and subsequently a less oriented and, thus, softer material. This leads to the larger degree of unloading in the 90^oC case as compared to the cooled down case.

The second reason for this effect of temperature on die swell is due to the elastic thermal expansion/contraction of the material caused by a temperature change. Since we have a decrease in temperature upon exiting the die, the material experiences a contraction of $\alpha_\Theta \Delta\Theta$, where α_Θ is the linear coefficient of thermal expansion which is equal to $2.6(10^{-4})K^{-1}$ at $\Theta \leq \Theta_g$ for PMMA [21]. The overall temperature change of 65^oC gives a diametral contraction of 1.69%. The response occurs simultaneously with the reverse yielding phenomenon described in the previous paragraph. This contribution to the temperature effect on die swell is small compared to that of the reverse yielding as it accounts for only 1.69% of the 20% difference in die swell. The stress-strain curve of Figure 2.7 implicitly includes this thermal response of the material as do our analyses.

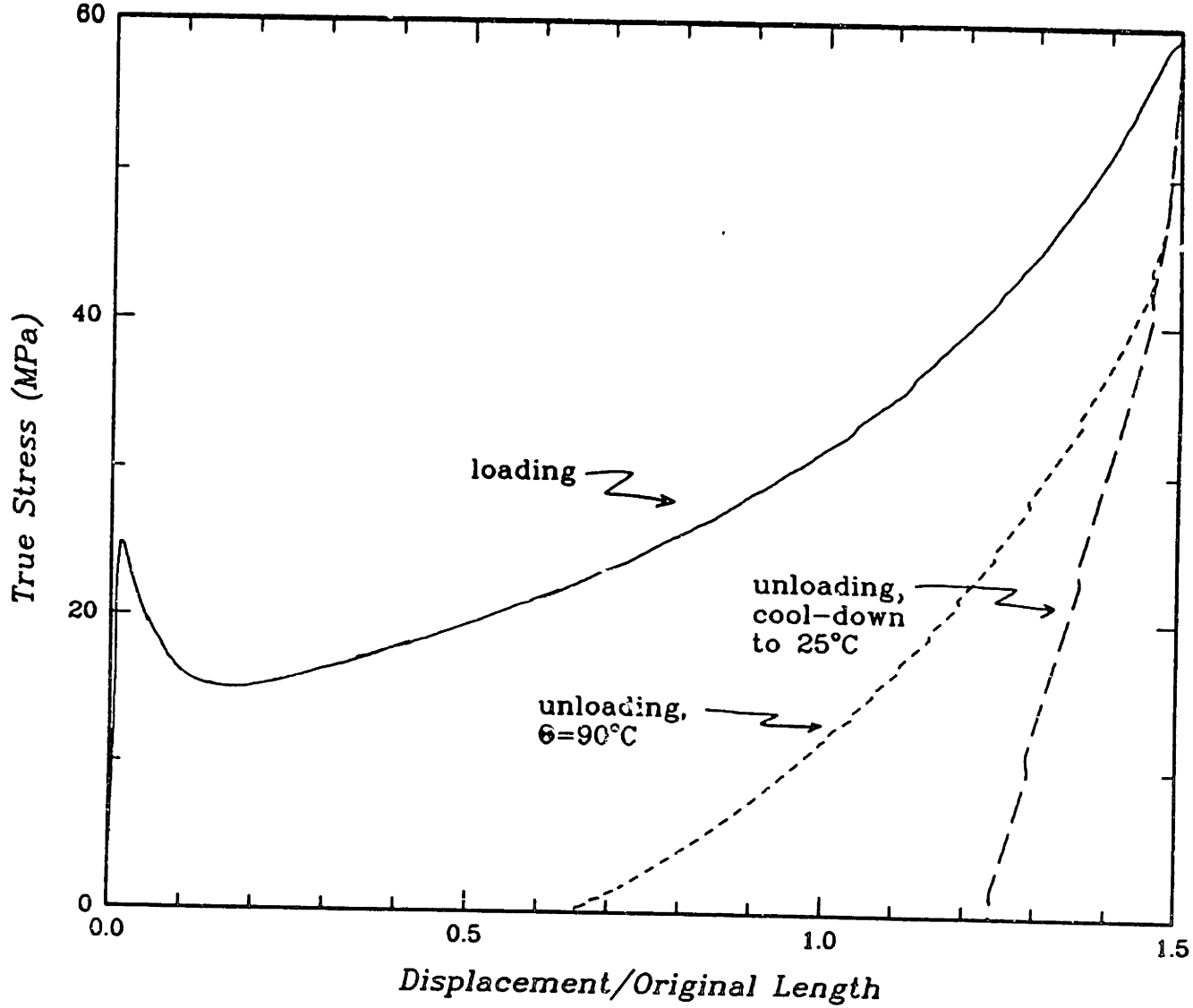

Figure 2.7. Tensile true stress–nominal strain curve for PMMA with loading to a stretch of 2.5 at a true strain rate of 0.003 sec^{-1} and unloading at approximately this rate. Loading is done at Θ=90°C; unloading is done at both 90°C and with simultaneous cooling down at a rate of 1 $K^{-}sec$.

2.3.2 Strain Rate

The plastic strain rate contours also indicate where the active plastic deformation is occurring. This is shown to be in the conical region of the die, with the strongest concentration at the section where the cone meets the barrel. The intense deformation occurring in this section is indicated by the strong concentration of rate contour lines. As mentioned in the preceding paragraph, there is also reverse yielding occurring in the exit region. These plastic strain rates are of an overall lower magnitude than those in the conical region as shown in Figure 2.6b.

The plastic shear strain rate contours shown in Figures 2.5b and 2.6b are of an order of magnitude of $10^{-3}sec^{-1}$. These results were obtained using a Coulomb friction interface boundary condition between the billet and the die. A coefficient of friction, α_f, of 0.20 was used in this analysis. This value is less than the value of 0.40 obtained from experiments of PMMA against steel [22]. The lower value was used to account for the lubrication due to the hydrostatic pressure inducing fluid. The lower value was suggested [12] as being a more realistic value for the conditions of hydrostatic extrusion. When friction effects are neglected and a free sliding interface between the billet and the die is assumed, the plastic strain rates are more than an order of magnitude higher. For an applied pressure of 65MPa and extrusion ratio of 2.5, strain rates of order $10^{-3}sec^{-1}$ are achieved in the experiments as inferred by the die geometry and resulting exit velocity. This indicates the importance of including the friction boundary condition in order to obtain the appropriate rate effect in the analysis. This effect can also be observed by comparing the extrudate velocity obtained for different applied pressures. For the applied pressure of 65MPa, the exit velocity calculated considering a freely sliding interface was ~60mm/min while for a frictional interface

($\alpha_f = 0.20$), it was ~3mm/min. The corresponding experimentally recorded value was between 1mm/min and 2mm/min. For an applied pressure of 75MPa, the calculated exit velocity considering an identical frictional interface was ~15mm/min, while the experimentally recorded value for this pressure level was approximately 6mm/min. Both the analysis and the experiments show the velocity at 75MPa to be approximately five times greater than that at 65MPa. The discrepancy between the absolute values of the numerically obtained pressure-velocity pairs and those obtained experimentally is primarily due to the low value of the coefficient of friction used in the analysis. The use of a slightly higher value for α_f may bring the calculated velocities closer to the experimentally observed values.

2.3.3 Texture

In their experiments, Kahar, et al. [15] made several measurements to quantify the resulting texture in the material: the actual draw ratio, the shrinkage stress, and the birefringence. The actual draw ratio, which differs from the nominal ratio due to die swell, can be predicted from the axial (2,2) component of the plastic deformation gradient, F^p_{22}, of our model. Figure 2.6c shows a contour of F^p_{22} at one point during the processing. In the barrel section, the draw ratio of 2.5 is correctly predicted. Upon exiting, F^p_{22} begins to decrease, reaching a value of 2.05 which corresponds to a die swell of 9.5%. This value, which was discussed earlier, was found to agree well with the experimentally observed die swell of ~10% which corresponds to an actual extrusion ratio of ~2.025. Kahar, et al. found their other two texture measurements, the shrinkage stress and the birefringence, to be directly proportional to one another. The shrinkage stress measurement and its relationship to the back stress tensor of our constitutive model are discussed below.

Amorphous polymers, after large deformations at temperatures below their glass transition temperature, are known to recover their initial undeformed shape when unconstrained and heated to $\Theta \geq \Theta_g$. A set of forces would be required to retain this deformed shape if heated to $\Theta \geq \Theta_g$ (see Figure 1.6). These forces correspond to the back stresses of our model. Kahar, et al. measured the axial component of this force on their extruded samples. This "shrinkage stress" was measured by taking a thin slice of the extruded material, attaching it to an Instron load cell, immersing it in an oil bath at a temperature $\Theta = 116.5^oC$, where $\Theta_g = 110^oC$, and recording the resulting force vs. time. The (2,2) component of the back stress of our model is directly comparable to this shrinkage stress measurement.

Before making the comparison between our back stress and Kahar's shrinkage stress, we note that such an experimental measurement is fraught with problems. The first problem is to separate out that part of the measured stress due to the thermal expansion of the material which occurs while in the test machine grips and heated to $\Theta = 116.5^oC$. Kahar, et al. claim to have accounted for this effect in their experiments. However, if we consider the thermal expansion, the "locked-in" stretch of the material, which is held constant during the test, becomes partly due to expansion and partly due to molecular alignment. Therefore, the stretch due to alignment is less than the observed stretch by an amount equal to $\int \alpha_\Theta d\Theta = 2.6\%$ where $\alpha_\Theta = 2.6(10^{-4})$ for $\Theta \leq \Theta_g$ and $\alpha_\Theta = 5.8(10^{-4})$ for $\Theta \geq \Theta_g$. This would have the net effect of lowering the back stress for that total amount of stretch. A second problem with this measurement is encountered by making the measurement on a thin slice of the extruded sample. Cutting a thin slice of the material would possibly relieve the residual stresses existing in the extrudate. The residual stress state is commented on later and is shown to be

axial. In the extrudate, these stresses satisfy equilibrium and, also, act to balance the existing back stresses to give a zero net plastic strain rate after steady state is reached. If these stresses are relieved, the existing back stresses would then be free to further relax. This again would lead to a lower measure of the back stress. Due to these difficulties, the shrinkage stress is not an accurate measure of the internal resistance of the material. However, it does provide an estimate of the resistance that is worth comparing with our back stress calculation.

Our numerical results of the back stress component and Kahar's experimental results of the shrinkage stress measurement are listed in Table 2.1 for the three extrusion ratios of 1.3, 1.85, and 2.5. Our back stress tensor is a deviatoric measure only. Since the experiments measure both the deviatoric and dilational components, i.e., uniaxial tensile stress, we must first multiply the shrinkage stress by $\frac{2}{3}$ in order to make the comparison with our numerically computed back stress. For the low extrusion ratio of 1.3, good agreement is attained between our calculations and experiment: 3.2MPa vs 1.8MPa. At the higher extrusion ratio of 1.85, the back stress component was predicted to be somewhat higher than that actually observed: 7MPa vs 3.0MPa. These discrepancies are due, in part, to the measurement difficulties discussed above as well as to the fact that these particular extrusions were conducted at low strain rates of order $10^{-3} sec^{-1}$. Our constitutive model currently neglects a certain low strain rate phenomenon which affect the back stress. This phenomenon is discussed in Chapter One and will be briefly elaborated on here. At lower strain rates, there is enough time for a noticable amount of entanglement drift to occur which acts to increase the effective locking stretch of the material. A larger locking stretch will result in a lower back stress at any fixed imposed level of stretch. Therefore, due to this low strain rate

TABLE 2.1

Back Stress Results

Nominal Extrusion Ratio	B_{22} MPa	Shrinkage Stress [15] Measurement, MPa
1.30	3.2	2.7
1.85	7.0	4.5
2.50	16.0	N/A

phenomenon, the network locking stretch becomes effectively larger as plastic strain accumulates with time, making the actual back stress (the measured shrinkage stress) at any fixed level of total deformation lower than that which would be predicted had the process been conducted at a higher rate with a "fixed" locking stretch. Therefore, our computed back stress will be somewhat higher than the actual back stress for these low strain rate extrusions. This is also apparent in Figure 1.7 where the model over-predicts the experimentally obtained stress as larger strains are approached for the low strain rate curves. Also, the measured shrinkage stress is somewhat lower than actual due to the thermal expansion and residual stress relief effects discussed above. All of these effects are enhanced with increasing stretch which explains why we obtain somewhat better agreement at the lower extrusion ratio of 1.3. A shrinkage stress measurement was not available for the ratio of 2.5. However, from the above trend, we can deduce that the numerically computed back stress of 16MPa probably overestimates what would be experimentally measured. Shrinkage stress measurements from extrusions conducted at higher strain rates were not available. For the reasons discussed, our model should give a better assessment for the back stress tensor in a material processed at the higher strain rates.

The evolution of the back stress as the material moves through the die is also interesting to observe. As shown in Figures 2.5d and 2.6d, the back stress begins to develop in the conical region of the die when the material begins deforming. As the material moves through the barrel, a larger back stress develops in the material nearest the die. This is due to the additional surface deformation imposed by the frictional interface with the die. However, we see that as the extrudate exits the die, the material recovers from this effect, and a uniform state of texture is reached demonstrating the

viscoplastic response of the material.

2.3.4 Residual Stresses

A residual stress state is often found to exist in a processed material. This is the case for the PMMA extrudate. There are only negligibly small residual radial, hoop, or shear stresses in the extrudate. However, there does exist a large residual axial stress distribution. Figure 2.8 depicts the axial stress along the center of the specimen, the mid-radial section, and the specimen surface during active processing and after unloading. Peaks in the axial stress occur at the die angle/barrel intersection and the die exit due to the changing geometry. We observe compressive axial stresses along the centerline while the billet is in the die. Upon exiting the die, the centerline axial stress becomes tensile. The reverse is true for the surface where a tensile axial stress occurs in the die and a compressive axial stress after exiting the die. We also note that the modelling of the unloading of the specimen is critical in determining the correct residual stress state. Therefore, the exit temperature conditions are important in this step of the analysis as well as in determining the correct die swell.

2.4 Conclusion

In this chapter, we have analyzed the hydrostatic extrusion of PMMA using the constitutive model of Chapter One which describes the large inelastic deformation of glassy polymers. This particular warm deformation process contains many of the conditions which exist in polymer processing in general and which have a strong impact on the material behavior: time, temperature, pressure, and large imposed deformations. However, this process was still simple enough to be able to perform suitable quantitative

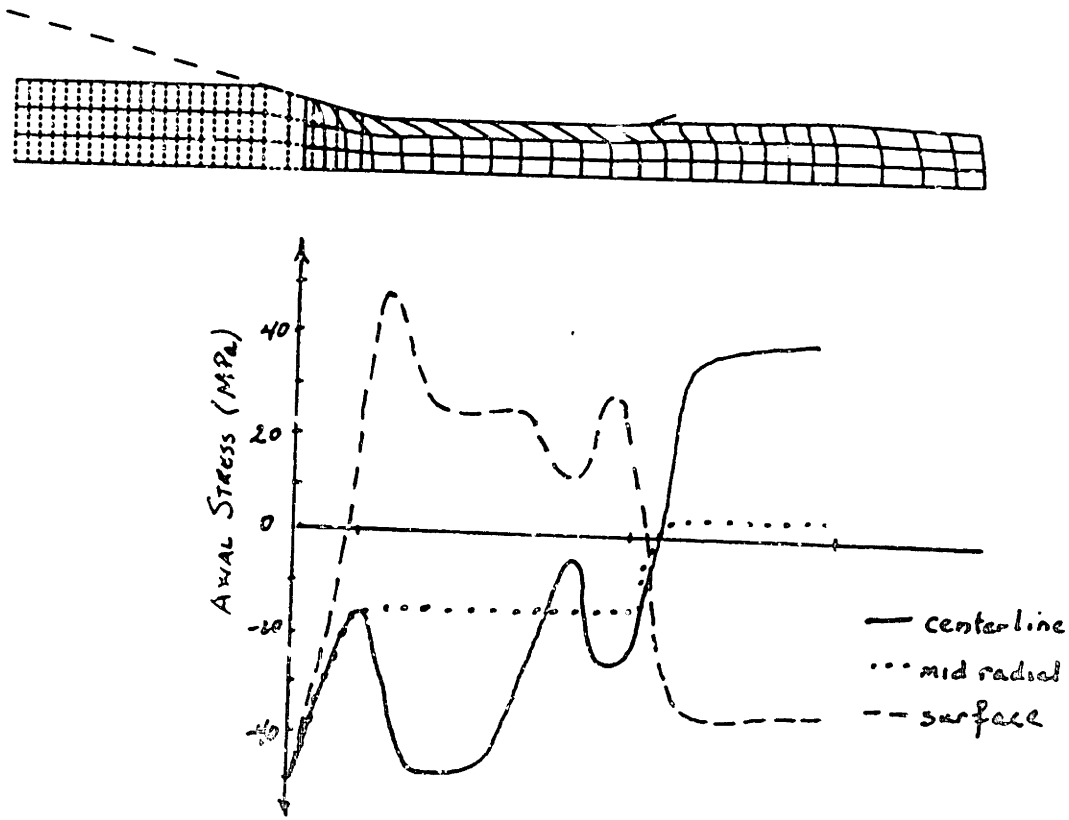

Figure 2.8. Residual axial stress distribution in PMMA extrudate with nominal extrusion ratio of 2.5.

measurements of these effects. Our numerical results for the quantities of die swell, strain rate, pressure vs. velocity, and shrinkage stress were found to satisfactorily predict those same quantities measured in the experiments of the Leeds University group. It was argued that even better agreement with such a low strain rate experiment could be obtained had the additional relaxation phenomenon of entanglement drift been incorporated into the model. This could be done at a future date. We can conclude that our constitutive model can be used with confidence as a predictive tool in the analysis of warm deformation-processing of glassy polymers. In a complicated process, it is often not possible to monitor such items as effects of rate, temperature, pressure and developing texture on the material response, yet knowledge of these quantities may aid in determining the service life of the resulting product. Analyses using our constitutive model would prove very valuable in such a case. Along this line of discussion, it would also be of interest to analyze a pre-textured product's response to loading, i.e. the distribution of texture in the product is known a priori via an experimental measurement such as birefringence. This effect is discussed in the next chapter.

Chapter 3

PREORIENTATION

A product often possesses residual texture which was either incidentally or deliberately acquired during its processing history. This was illustrated in the preceding chapter in the example of the PMMA material sample which was purposely oriented via hydrostatic extrusion. A polymer is frequently preferentially oriented in order to increase its yield strength in specific directions. Examples include the production of high strength fibers in the textile industry and biaxially oriented films in the packaging industry. The response of the textured solid to normal service life loading conditions will differ considerably from that of a product composed of isotropic material. In order to accurately predict the behavior of a textured polymer, a physically sound constitutive model is needed. Here, the model of Chapter One is modified to include the effect of preorientation on subsequent material response. The modified model is then utilized in an analysis of the effect of texture on both homogeneous and localized flow in glassy polymers. These results are compared with trends found by experiments as reported in the literature.

3.1 Modelling Texture

Texture affects both the elastic and the inelastic response of a polymer. However, at large deformations, the effect of texture on the inelastic response far outweighs that on the elastic response especially for amorphous polymers. Hadley [24] has summarized the effect of orientation on the small strain elastic properties of polymers. He reports that, whereas the component of the elastic modulus tensor which relates the applied stress to strain in a simple tensile test, i.e. the Young's modulus for the isotropic case, of some semi-crystalline polymers may increase by as much as an order of magnitude at large draw ratios, the largest increase in the modulus of amorphous polymers was found in PMMA and was only 30% [25]. This increase in elastic modulus with orientation is very small compared to the effect of hardening at large strains and will be neglected in this model for large inelastic deformations. Therefore, for the purposes of this work, only the effect of texture on the inelastic response of the material will be incorporated into the constitutive model.

The effect of texture, i.e., preorientation, on the inelastic response of the material is examined by first considering the effect it has on the two deformation resistances of our model: the intermolecular resistance and the entropic resistance. The intermolecular resistance is intimately related to the elastic moduli. Since we are neglecting the effect of pre-orientation on the elastic properties of the material, we can assume the effect of texture on this first resistance is minimum, and, therefore, negligible. However, we will want to implicitly include effects on this resistance of any aging that occurs subsequent to texture-producing processing. This will be discussed later. The effect of texture on the directional entropic resistance is considerable. It is this resistance that is directly correspondent to the permanent shape change of the material.

Texture may be thought of as an initial permanent shape change which has associated with it an initial entropic resistance. Therefore, before plastic flow commences in a textured polymer, in addition to the intermolecular resistance, an initial entropic resistance must also be overcome. This is why we see elevated levels of tensile "peak yield" stresses in the direction of principal orientation of polymers. The effect of texture on the polymer's inelastic behavior through its impact on the deformation resistances should now be conceptually clear and will now be incorporated into the constitutive model.

The incorporation of preorientation into the model described in Chapter One may be accomplished by first considering the deformation of an initially isotropic body and then considering the similar deformation of an initially oriented body. These deforming bodies are schematically illustrated in Figures 3.1 (a) and (b). The various deformed configurations are described by their appropriate deformation gradients. For the case of the initially isotropic body (Chapter One), the configuration of the undeformed body, B_0, may be described by the identity tensor, $\mathbf{I}$, indicating no texture in the body. This body is then loaded to a new state, B_t, and its deformed configuration may be described by the deformation gradient at this time, $\mathbf{F}_t$. If the body is now unloaded to a stress free state without rotation as described in Chapter One, the unloaded configuration may be described by the plastic deformation gradient, $\mathbf{F}_t^p$. The velocity terms, i.e. the rate of deformation and the spin, from these various configurations are also depicted in the figure. Considering the same loading steps in an initially oriented material, we see the initial configuration of the body, B_0, may now be represented by the tensor $\mathbf{V}^i$ which describes the initial texture of the body. This body is now deformed via $\mathbf{F}_t$, where $\mathbf{F}_t$ describes the applied deformation and can be thought of as a deformation

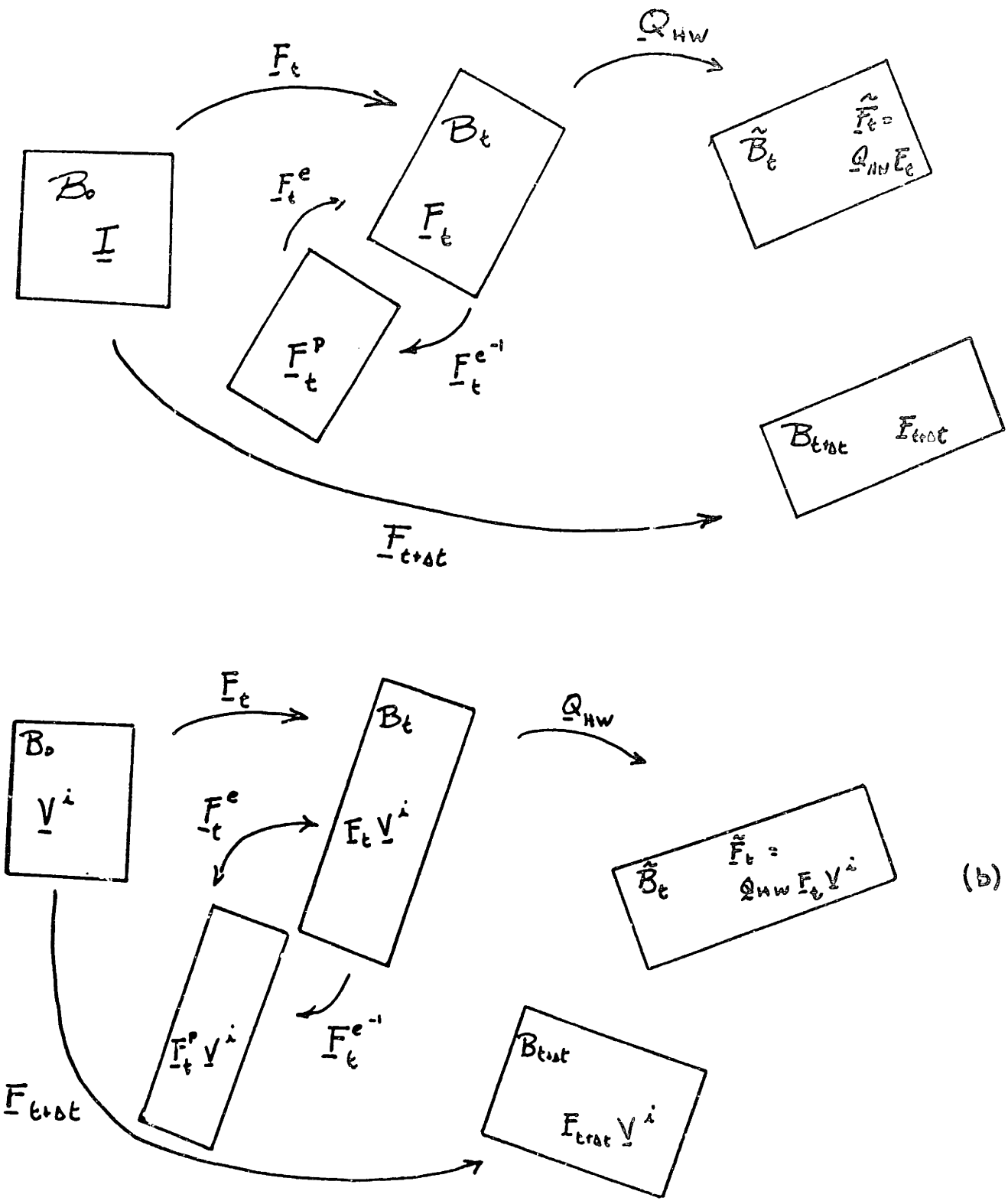

Figure 3.1. (a) Deformation of an initially isotropic body.
(b) Deformation of a pre-oriented body, where the initial texture is described by V^i.

relative to the preoriented state, and its new configuration may be described by $\mathbb{F}_t\mathbb{V}^i$. When the body is unloaded, the resulting configuration is $\mathbf{F}^p_t\mathbb{V}^i$. Therefore, the initial texture $\mathbb{V}^i$ may be interpretted as an initial plastic stretch tensor. The initial condition of texture is incorporated into the model as an initial plastic deformation gradient.

The numerical integration of the original model is described in Appendix A. The effect of the initial condition on this integration is briefly detailed below. The variables are updated by converging on $\mathbf{F}^p_{t+\Delta t}$. The essential equations for the initially isotropic body are summarized below:

$$\begin{aligned}
&\mathbf{F}^p_{t+\Delta t} = \tilde{\mathbf{F}}^p_t + \mathbf{D}^p_{t+\Delta t}\mathbf{F}^p_{t+\Delta t}\Delta t; && (a)\\
&\tilde{\mathbf{F}}^p_t = \mathbf{Q}_{HW}\mathbf{F}^p_t; && (b)\\
&\mathbf{Q}_{HW} = [\mathbf{I} - \tfrac{1}{2}\mathbf{W}\Delta t]^{-1}[\mathbf{I} + \tfrac{1}{2}\mathbf{W}\Delta t]; && (c)\\
&\mathbf{D}^p_{t+\Delta t} = \dot{\gamma}^p_{t+\Delta t}\mathbf{T}^{*\prime}_{t+\Delta t}/\sqrt{2}\tau_{t+\Delta t}; && (d)\\
&\mathbf{T}^*_{t+\Delta t} = \mathbf{T}_{t+\Delta t} - \tfrac{1}{J_{t+\Delta t}}\mathbf{F}^e_{t+\Delta t}\mathbf{B}_{t+\Delta t}\mathbf{F}^e_{t+\Delta t}; && (e)\\
&\mathbf{B}_{t+\Delta t} = f\left(\mathbf{F}^p_{t+\Delta t}\right). && (f)
\end{aligned} \tag{3.1}$$

When the initial condition of texture is included, these equations become:

$$\begin{aligned}
&\mathbf{F}^p_{t+\Delta t}\mathbf{V}^i = \tilde{\mathbf{F}}^p_t\mathbf{V}^i + \mathbf{D}^p_{t+\Delta t}\mathbf{F}^p_{t+\Delta t}\mathbf{V}^i\Delta t; && (a)\\
&\mathbf{D}^p_{t+\Delta t} = \dot{\gamma}^p_{t+\Delta t}\mathbf{T}^{*\prime}_{t+\Delta t}/\sqrt{2}\tau_{t+\Delta t}; && (b)\\
&\mathbf{T}^*_{t+\Delta t} = \mathbf{T}_{t+\Delta t} - \tfrac{1}{J_{t+\Delta t}}\mathbf{F}^e_{t+\Delta t}\mathbf{B}_{t+\Delta t}\mathbf{F}^e_{t+\Delta t}; && (c)\\
&\mathbf{B}_{t+\Delta t} = f\left(\mathbf{F}^p_{t+\Delta t}\mathbf{V}^i\right). && (d)
\end{aligned} \tag{3.2}$$

It is noted that, for this case, $\mathbf{D}^p_{t+\Delta t}$ is the rate of change of shape of the configuration described by the kinematics $\mathbf{F}^p_{t+\Delta t}$ and is in the direction prescribed by $\mathbb{T}^{*\prime} = \mathbb{T}' - (\frac{1}{J}\mathbf{F}^e\mathbf{B}\mathbf{F}^e)'$ where $\mathbf{B}$ is a function of the tensor $\mathbf{F}^p_{t+\Delta t}\mathbf{V}^i$. It is also worth pointing out that $\mathbf{V}^i$ is invertible and, therefore, both sides of equation (2a) may be post-multiplied by $[\mathbf{V}^i]^{-1}$ to give:

$$\left[\mathbf{F}^p_{t+\Delta t}\right] = \left[\mathbf{Q}_{HW}\mathbf{F}^p_t + \mathbf{D}^p_{t+\Delta t}\mathbf{F}^p_{t+\Delta t}\Delta t\right]. \tag{3.3}$$

This shows that the purely kinematic decomposition $\mathbb{F}_{t+\Delta t} = \mathbf{F}^e_{t+\Delta t}\mathbf{F}^p_{t+\Delta t}$ is updated just as in the case with an initial isotropic state except that the tensor $\mathbf{D}^p_{t+\Delta t}$, although

the rate of shape change of the configuration $\mathbf{F}^p_{t+\Delta t}$, accounts for the resistance due to the initial texture, $\mathbf{V}^i$, as well as subsequent texturing from $\mathbf{F}^p_{t+\Delta t}$. The numerical integration procedure is not encumbered by the incorporation of an initial texture.

3.2 Effect of Preorientation on Material Behavior

A polymer's homogeneous and localized flow behavior are both altered by the existence of any initial texture/pre-orientation in the material. During homogeneous deformation, the stress at which active plastic flow begins is affected by both the degree and the orientation of the initial texture. This behavior is examined below with simulated tensile tests. Polymers are also known to exhibit "shear banding", highly localized regions of straining, during plastic flow. Experiments [26, 27, 28] have shown that the direction of shear banding in polymers is affected by the degree and orientation of texture in the material. This behavior is also examined with our model and simulated tensile tests. The numerical results are compared with behavior trends reported in the literature.

3.2.1 Homogeneous Behavior

The effect of orientation on the flow behavior of a homogeneous polymer is now examined. Figure 3.2 depicts the true stress-stretch curve of an initially isotropic amorphous polymer which is loaded, unloaded, and then reloaded without allowing for aging in a simulated plane strain tensile test[1]. The effect of the initial loading, which orients

[1]For illustrative purposes, the material constants obtained for the isotropic PMMA material of Chapter One are used in the numerical analyses of this chapter.

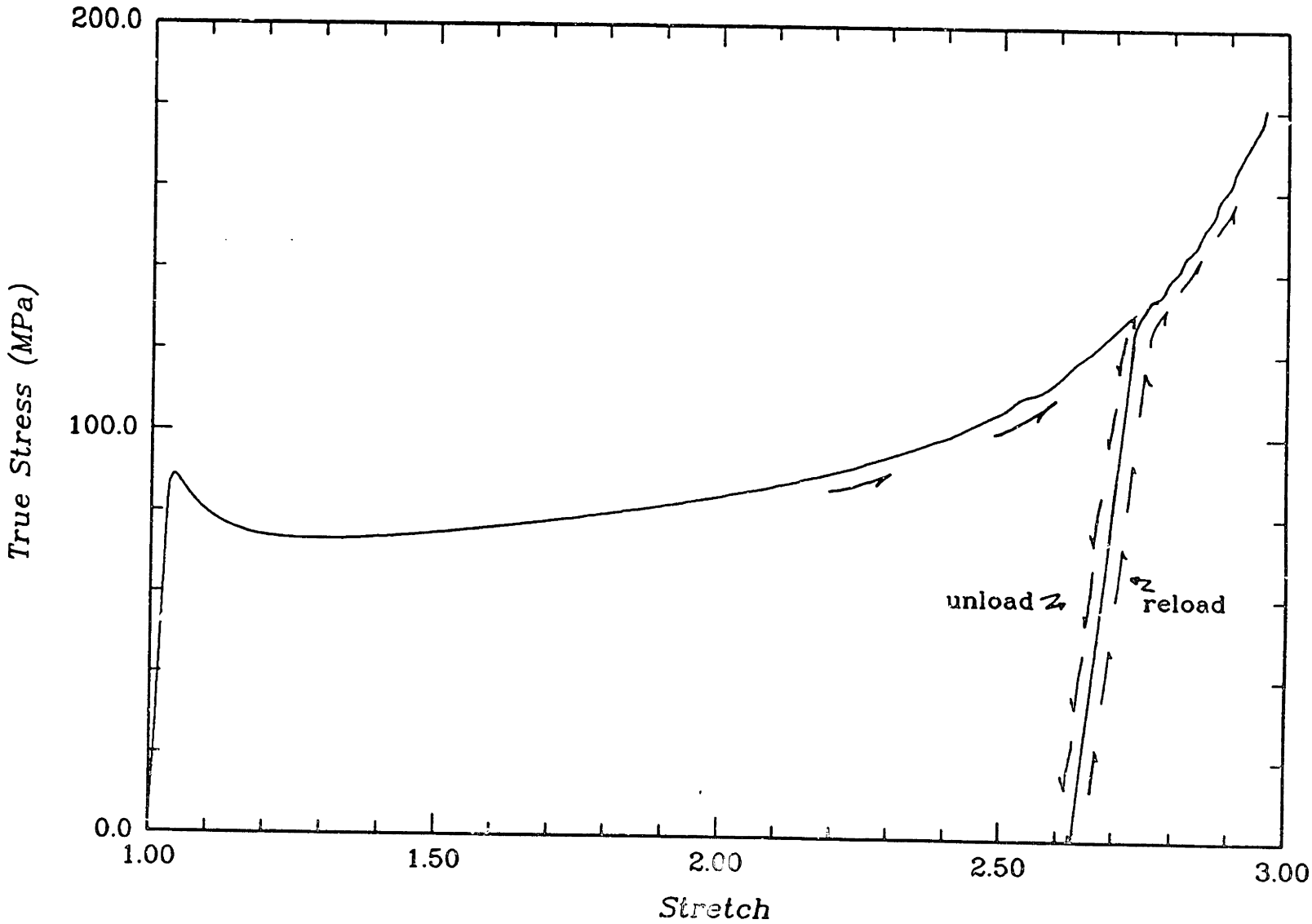

Figure 3.2 Tensile true Stress–stretch curve for PMMA at ϵ=0.01 s^{-1} and Θ=25°C showing loading, unloading, and reloading.

the material, upon the stress level at which subsequent plastic flow commences is apparent upon reloading. It is an oriented, unloaded state such as this that is now our starting point. We first take a brief look at some experimental results from tensile tests on oriented polymers. Secondly, we discuss an anisotropic yield criterion which has been applied to these polymers in the past. Finally, using the constitutive model described earlier, we analyze plastic flow in an oriented glassy polymer under both uni- and biaxial loading conditions.

Previous Work

Tensile tests on thin "plane stress" type specimens of oriented polymers have been conducted by Rider and Hargreaves on amorphous polyvinyl chloride (PVC) [27, 35], by Brown, et al. on semi-crystalline (nearly amorphous) polyethylene terephthalate (PET) [28, 37], and by Duckett, et al. on semi-crystalline polypropylene (PP) [29]. The initial texture of these test specimens may be described by the principal stretches: $\lambda_1 = \lambda$, $\lambda_2 = \lambda_3 = 1/\sqrt{\lambda}$, where λ is often called the initial draw ratio (IDR). The orientation of the texture of a specimen when tested in simple tension is given by its initial draw direction (IDD) which is the angle, θ, that the first principal stretch makes with the tensile axis (Figure 3.3). Results of the yield stress [2] of the above materials with given IDRs as a function of IDD when tested in tension at a fixed displacement rate are shown in Figure 3.4. These materials exhibit a significant drop in the peak stress as the principal stretch ratios leave the tensile axis followed by a gradual levelling off of this stress after an IDD of approximately 60°. Brown, et al. and Rider and Hargreaves then used their data to determine the coefficients for Hill's yield criterion for anisotropic

[2] Here, we use the term yield stress to describe either i) the peak stress before softening, if softening occurs; or, ii) the stress at the point where the tangents to the elastic and hardening portions of stress-strain curve intersect.

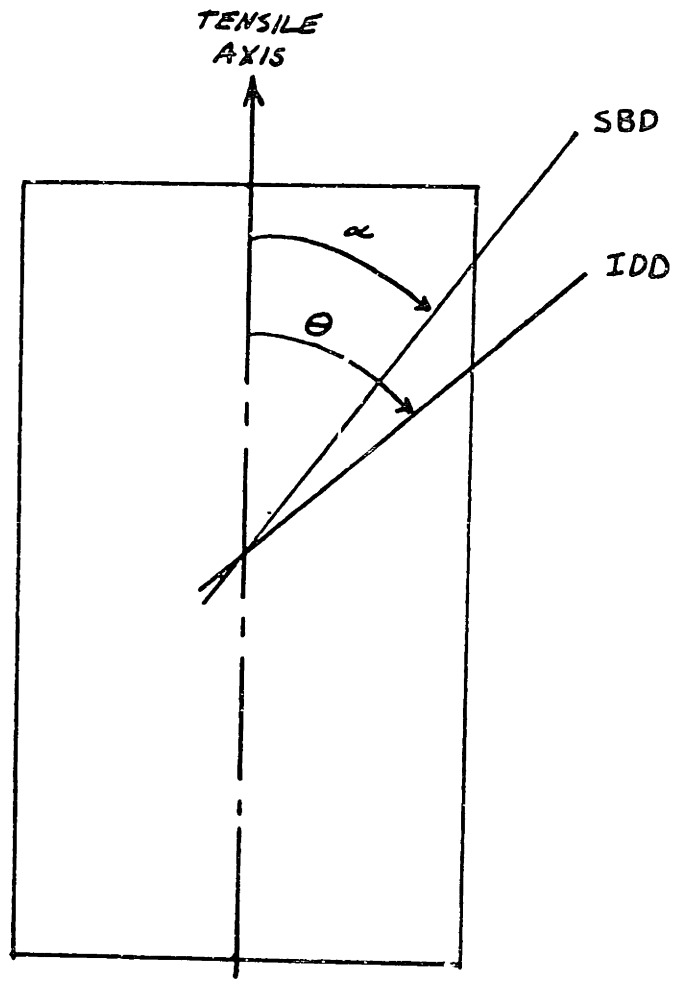

Figure 3.3. Schematic of a pre-textured tensile specimen. The angle between the tensile axis and the initial draw direction (IDD) is given by Θ. The angle between the tensile axis and the shear band (SBD) is given by α.

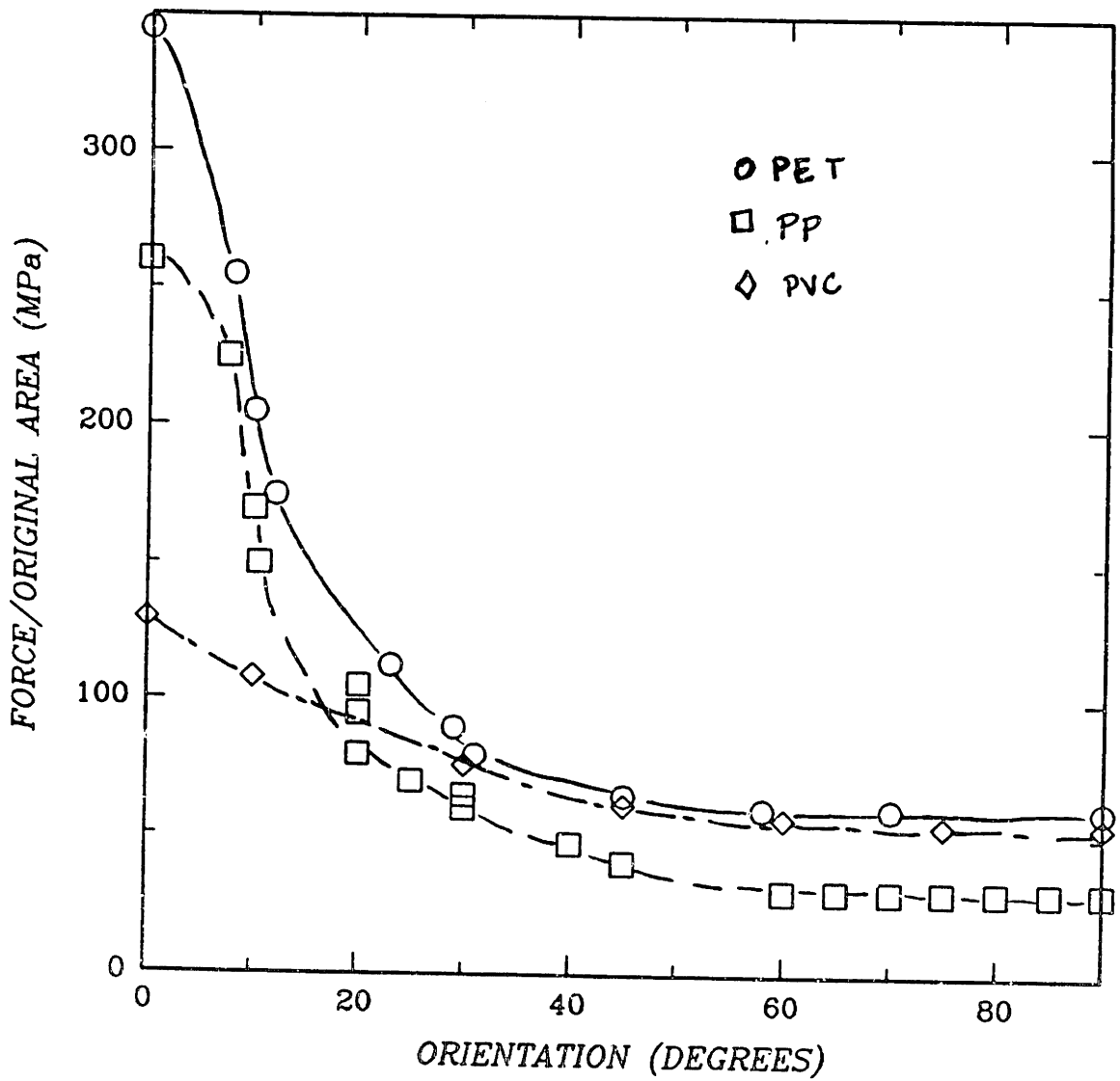

Figure 3.4. Nominal tensile yield stress as a function of orientation for highly oriented PET [3.14] and PP [3.3], and for PVC of IDR=3.3 3.4 .

materials [38] which is discussed next.

A criterion for yield for materials which have been preferentially oriented, e.g. by strain hardening, such that they retain three mutually orthogonal planes of symmetry has been proposed by Hill [38]. The yield surface, which reduces to the Mises yield surface when anisotropy vanishes, is given by:

$$F(\sigma_{yy}-\sigma_{zz})^2+G(\sigma_{zz}-\sigma_{xx})^2+H(\sigma_{xx}-\sigma_{yy})^2+2L\sigma_{yz}^2+2M\sigma_{zx}^2+2N\sigma_{xy}^2=1, \quad (3.4)$$

where σ_{ij} represent the stress components, the directions x, y, and z represent the three mutually orthogonal planes of symmetry, and the constants F, G, H, L, M, and N represent the square of the inverse of the yield strength under the appropriate normal and shear loading conditions. Hill's criterion requires identical yield points in tension and compression. This criterion was applied to the PET and PVC experiments discussed above. The symmetry of the pre-orienting process where the resulting principal stretch ratios were as given earlier: $\lambda_x=\lambda$, $\lambda_y=\lambda_z=1/\sqrt{\lambda}$, implies that the Hill coefficients G and H are equivalent. Due to the loading in these experiments, values for L and M are not required. Constants for the three remaining Hill coefficients F, G, and N were obtained with the data from the 0°, 45°, and 90° IDD tests. The resulting curves were found to predict the yield at all IDDs very well. These investigators noted that oriented PET and PVC behave differently in tension and compression, exhibiting a Bauschinger effect as well as pressure dependent yield. These effects are not accounted for in the Hill Criterion. Therefore, both Rider and Hargreaves and Brown, et al. modified the criterion to include a scalar internal stress, or back stress, b, which lumps the Bauschinger and pressure effects together. The modified criterion reads as follows:

$$H(\sigma_{zz}-b-\sigma_{yy})^2+F(\sigma_{yy}-\sigma_{xx})^2+G(\sigma_{xx}-\sigma_{zz}+b)^2+2N\sigma_{xy}^2+2L\sigma_{yz}^2+2M\sigma_{zx}^2=1. \quad (3.5)$$

Brown, et al. also conducted tests in simple shear on their material. The modified criterion was found to give good agreement with the shear data as well as the tensile data. We note that the material constants F, G, N and b are for a given initial draw ratio, as well as at a given strain rate and temperature. Once these material constants have been evaluated for the desired IDR, yield can be predicted for a multiaxial state of stress for a material with that initial texture. As an example, we obtain the biaxial yield loci at various IDDs for PVC at an IDR of 3.7, a temperature of $25°C$, and a displacement rate of 1 cm/min where the gauge length was 8 mm. The constants are given as $F = 2.4(10^{-2})\frac{mm^4}{kg^2}$, $H = 0.41(10^{-2})\frac{mm^4}{kg^2}$, $N = 4.8(10^{-2})\frac{mm^4}{kg^2}$, and $b = 4.0\frac{kg}{mm^2}$ [27]. The calculated yield loci are shown in Figure 3.5. If one is relying on this yield criterion to predict the yield behavior as a function of the initial texture in the material, a matrix of the material parameters F, G, H, L, M, N, and b must be assembled by conducting numerous experiments at every IDR. Furthermore, these coefficients are valid only for cases of stretches in ratio $\lambda:\frac{1}{\sqrt{\lambda}}:\frac{1}{\sqrt{\lambda}}$. Below, we discuss the prediction of uni- and multi-axial yield of oriented glassy polymers with the constitutive model of this thesis which is based on material properties from a set of experiments on the material in the isotropic state alone.

Constitutive Model Results

Here, we simulate plane strain tensile tests on oriented PMMA where the initial texture was obtained, for example, *via* a plane strain extrusion process, such that the texture may be described by the principal stretch ratios: $\lambda_1 = \lambda$, $\lambda_2 = 1/\lambda$, and $\lambda_3 = 1.0$, where λ is the IDR. We measure the effect the amount of texture and the orientation of the texture have on the flow behavior of the material by "testing" samples of various initial principal stretch ratios in uniaxial tension and biaxial tension/compression at

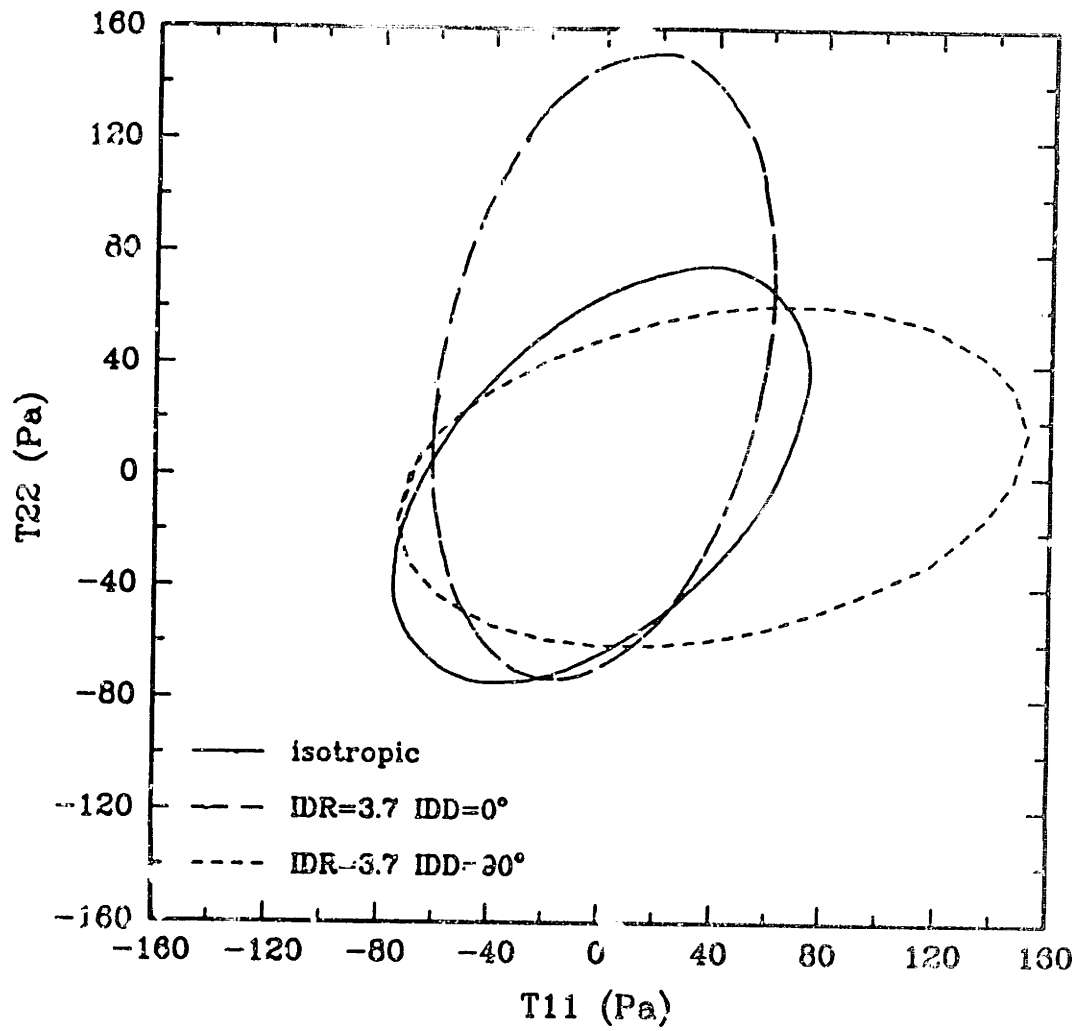

Figure 3.5. Biaxial yield locus for PVC in the isotropic state and at an IDR of 3.7 and IDDs of θ = 0° and 90° as computed with the Mises criterion (isotropic state) and Hill criterion with Rider and Hargreaves experimental data.

a number of different IDDs. The samples of material are assumed to have been given enough time to have aged after their initial processing and prior to their tensile testing. This means that any softening that occurred during the processing which produced the textured material has been negated (see section 1.2.4). This is reflected in the model by using an appropriate initial condition on the intrinsic yield strength. Here, we assume the material to be fully aged, so the value for s_0 of the initially isotropic material is used. Therefore, the material again softens. The orientation and texture effects are examined by comparing the stress state at which the material begins to flow at a fixed temperature and strain rate.

For the case of plane strain tension, we compare the peak flow stress prior to softening of the IDRs of $\lambda = 1.0$, 1.5, 2.0, 2.25, and 2.5, where the locking stretch of the material is $\lambda_L = 3.0$, over an orientation range of $\theta = 0°$ to $\theta = 90°$ and at a constant normalized displacement rate of 0.01 sec^{-1} and a constant temperature of $25°C$. A one 8-node plane strain reduced integration element (ABAQUS type CPE8R) model was used in the simulation. The boundary conditions (see Figure 3.6) consisted of fixing the nodes along the bottom of the mesh in the y-direction, the center node of both the top and bottom surface was fixed in the x-direction, and the nodes along the top surface were displaced in the y-direction as the loading condition. Before continuing, we note here that such homogeneous deformation does not actually occur in these materials after yielding because of the large tendency for deformation to localize. This is discussed in the next section. We conduct these tests to obtain the values at which plastic flow begins at a given strain rate as a function of IDR and IDD. The computed peak stresses as a function of IDR and IDD are plotted in Figure 3.7. The impact of orientation is found to increase greatly as we approach initial textures near the locking

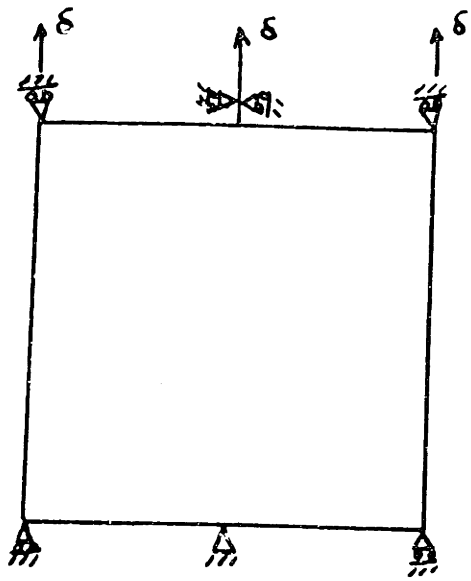

Figure 3.6. Finite element mesh with boundary conditons for plane strain tensile test simulation.

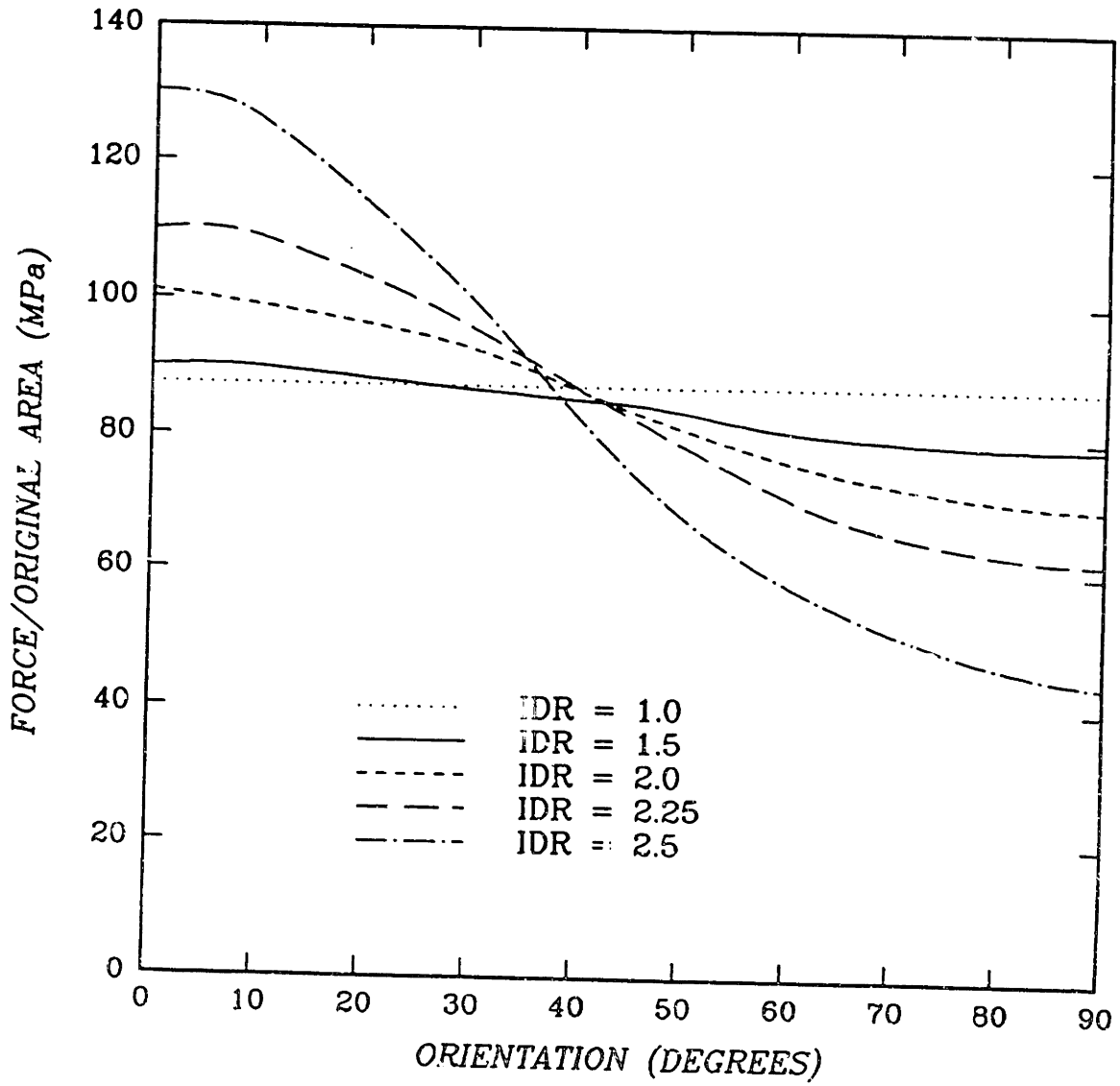

Figure 3.7. Computed peak flow stress as a function of orientation for various initial draw ratios (IDR) for PMMA at Θ=25°C.

regime, i.e. at stretch ratios greater than 2.0. This, of course, is due to the dramatic increase in the back stress as the locking stretch is approached. We also note that these curves pass through the isotropic "yield" point prior to an orientation of 45°. By examining the flow condition for plane strain tension at a fixed strain rate and temperature and neglecting pressure effects, we see the back stress acts to decrease the flow stress for the case of plane strain prior to an IDD of 45°. We approximate τ to be $[\frac{1}{2}(\mathbf{T}' - \mathbf{B})^2]^{\frac{1}{2}}$, where:

$$\mathbf{T} = \begin{matrix} 0 & 0 & 0 \\ 0 & \sigma & 0 \\ 0 & 0 & -\frac{\sigma}{2} \end{matrix} \tag{3.6}$$

and

$$\mathbf{B} = \begin{matrix} cos\theta & sin\theta & 0 & -b & 0 & 0 & cos\theta & -sin\theta & 0 \\ -sin\theta & cos\theta & 0 & 0 & b & 0 & sin\theta & cos\theta & 0 \\ 0 & 0 & 1 & 0 & 0 & 0 & 0 & 0 & 1 \end{matrix} \tag{3.7}$$

The flow condition is:

$$\tau = s[1 - \frac{\Theta}{As} ln \frac{\dot{\gamma}_0}{\dot{\gamma}^p}]^{\frac{s}{6}}, \tag{3.8}$$

which is constant for a given strain rate and temperature. The athermal shear strength, s, is taken to be s_0. Incorporating equations (3.6) and (3.7) into (3.8) gives:

$$\frac{1}{4}\sigma^2 + b^2(cos^2\theta - sin^2\theta)^2 - b\sigma(cos^2\theta - sin^2\theta) + 4b^2 sin^2\theta cos^2\theta = \tau^2. \tag{3.9}$$

For the case of $\Theta = 45°$, the tensile flow stress is $\sigma = 2\sqrt{\tau^2 - b^2}$. Therefore, at an IDD of 45°, the flow stress will be less than the isotropic stress. This decrease in flow stress increases with IDR as shown in Figure 3.7. These model results for the larger stretch ratios compare well with the trends found in the experiments discussed earlier.

As an exercise, we found it interesting to take the set of the above simulations for the IDR of 2.5 past yield to a nominal strain of 30%. The engineering stress-strain curve

for the IDD range of $0° \leq \Theta \leq 90°$ are shown in Figure 3.8. These curves illustrate the strong dependence of material response on orientation for not only the initial flow stress but, also, all subsequent behavior. We compared the engineering stress-nominal strain curves rather than the true stress-strain curves because, even with this supposedly "homogeneously" applied deformation the material is unable to respond as such when aligned off-axis because of its asymmetry. This response is clearly seen in plots of the deformed one-element mesh over the tested IDD range (Figure 3.9). Those cases with a principal stretch parallel with the tensile axis, i.e., the material is symmetrically aligned with respect to the tensile axis, deform in homogeneous tension. When the material is initially aligned off-axis, the solid shears as well as deforms in tension. In other words, with this one element model, we are picking up the inherent tendency of the material to localize into shear bands without any effort to initiate localization. This phenomenon is discussed in greater detail in section 3.2.2.

This same "material" is examined under biaxial loading conditions for various IDRs and IDDs. Biaxial yield loci are computed for a fixed shear strain rate of 0.01 sec^{-1} and temperature of $25°C$ with and without pressure dependence of flow in order to better illustrate the preorientation dependence alone. The biaxial yield locus for isotropic PMMA with and without pressure effects (Figure 3.10) is used as a base for comparison of orientation effects on the yield loci. This diagram shows the effect of pressure on the yield surface where the solid withstands larger stresses under compressive loading than under tensile loading before yielding. PMMA is particularly pressure sensitive with $\alpha_p = 0.2$ as reported earlier in section 1.4.2. The effect of material preorientation on the yield locus is illustrated in Figures 3.11 - 3.14 for the IDR of 2.0, 2.25, 2.5, and 2.60, respectively. We observe a small effect at the low IDR of $\lambda = 2.0$ and a noticably

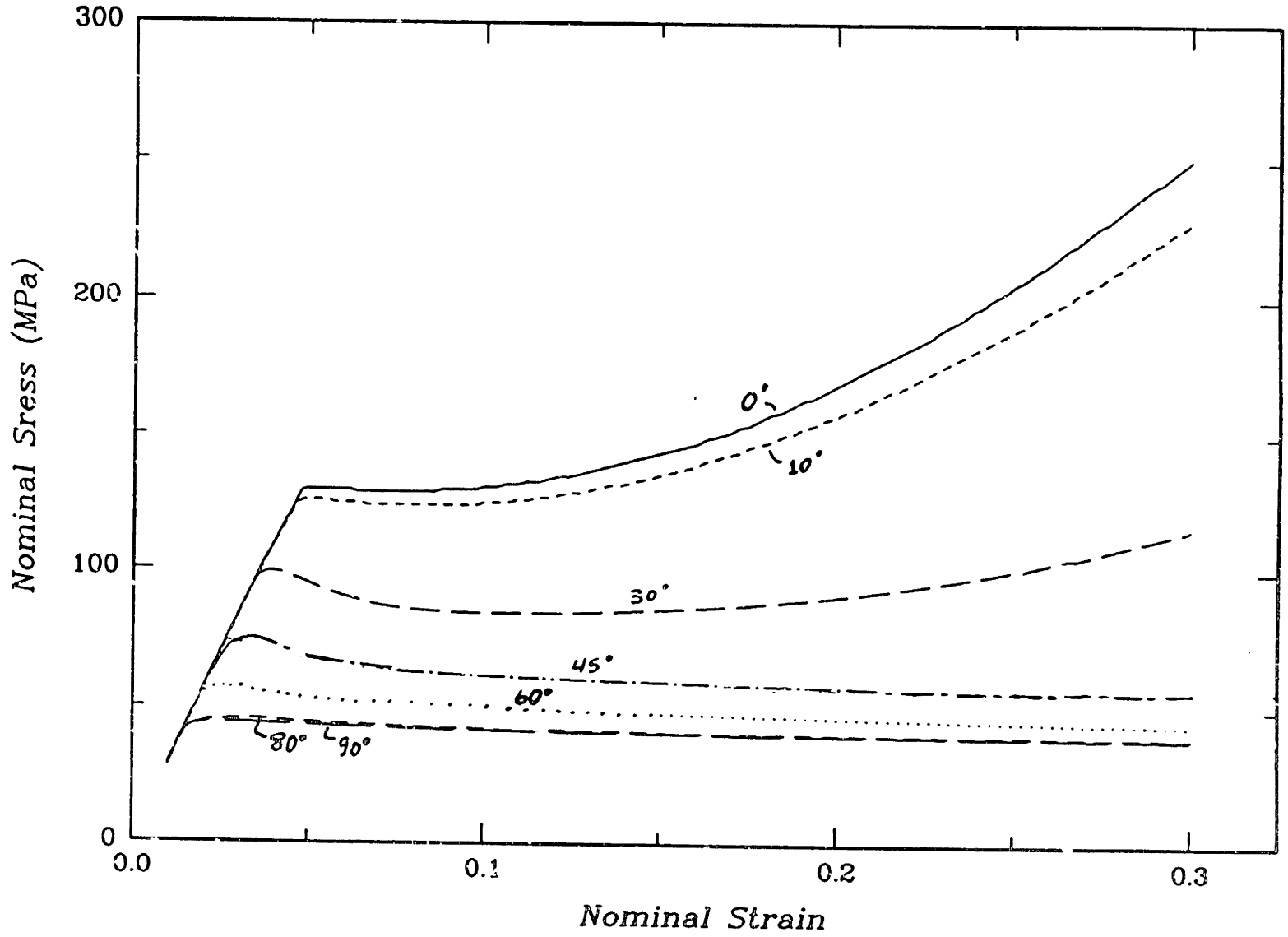

Figure 3.8. Nominal stress-nominal strain curves for oriented PMMA, R=2.5, over a range of IDDs.

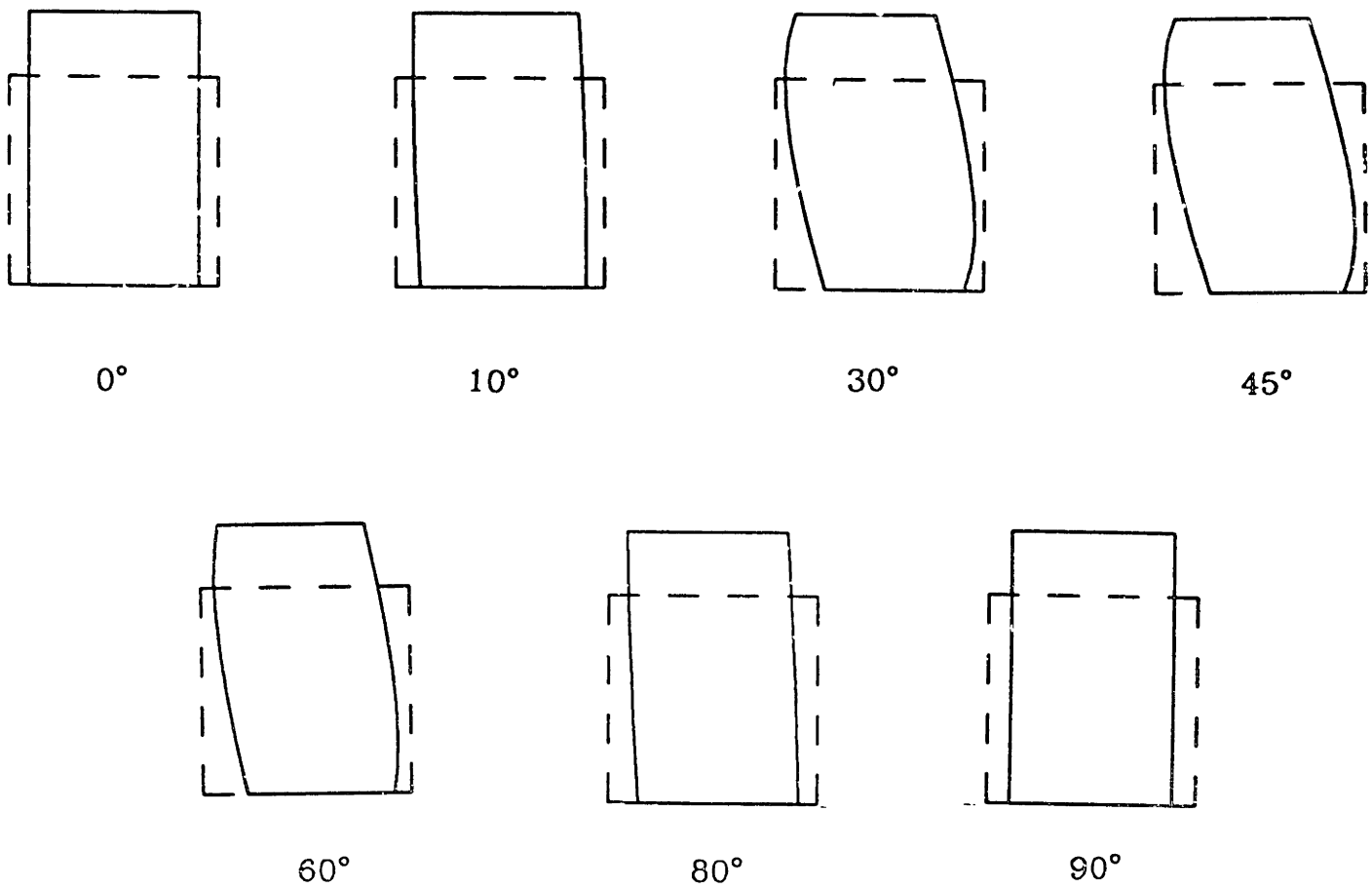

Figure 3.9. Plots of the deformed one-element meshes after a nominal strain of 30 for oriented PMMA, IDR=2.5, over a range of IDDs. The shearing of the cases aligned off-axis is apparent.

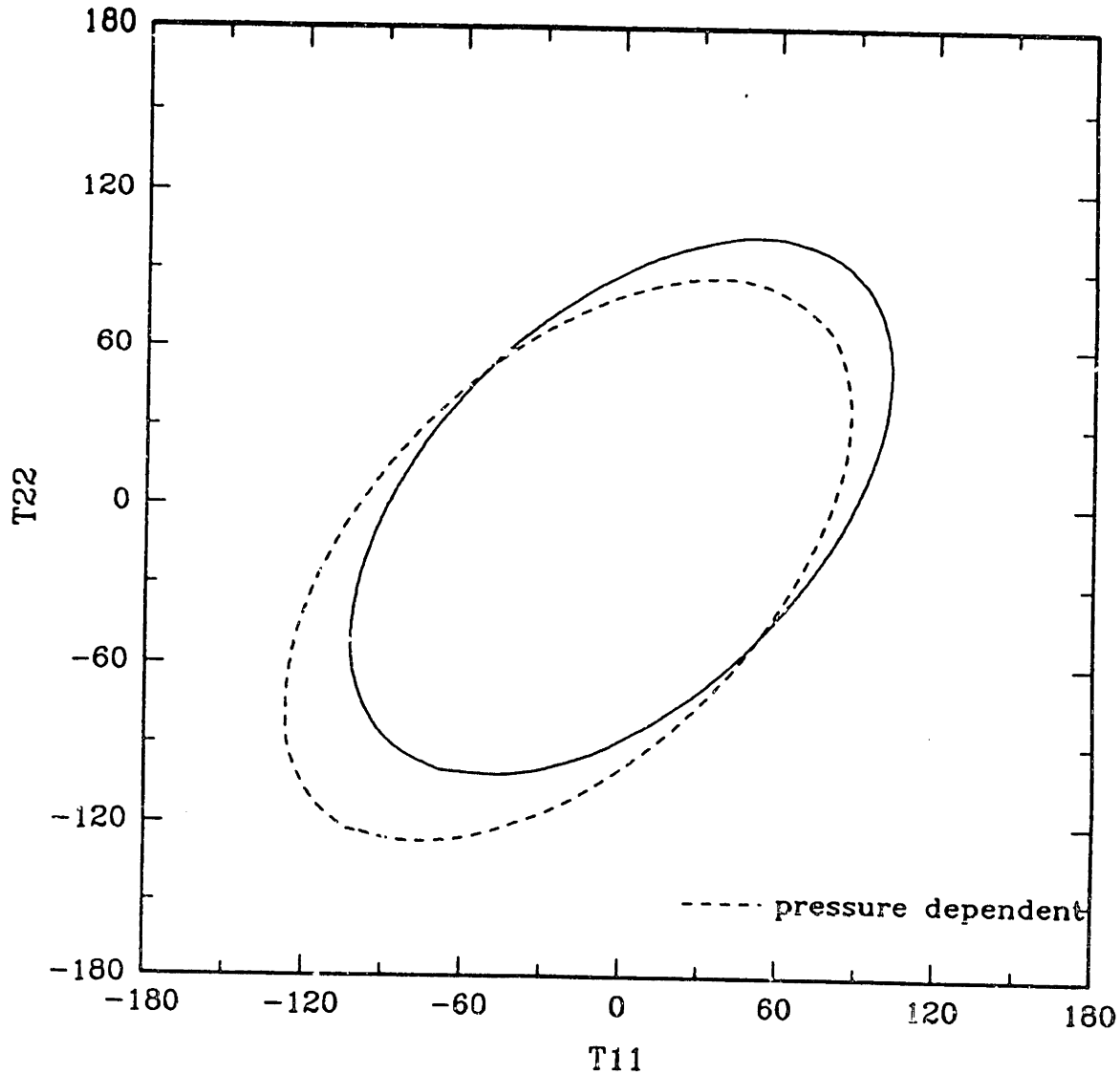

Figure 3.10. Biaxial yield locus for isotopic PMMA at fixed strain rate of 0.01 and temperature of 25°C, with and without pressure dependence.

larger effect at the higher draw ratios. Aligning the IDR with the T11 or T22 axis causes the yield locus to move along the corresponding axis of alignment without changing size. This demonstrates the kinematic hardening response of the model. Orienting the IDR at an off-axis angle, i.e. $0° < \theta < 90°$, shifts the yield locus along both stress axes as well as shrinking the locus in size. The shifting and shrinking of the locus is, of course, symmetric about the $\theta = 45°$ orientation which has the smallest locus. Pressure affects the yield loci of the oriented material just as it did the isotropic material, slightly elongating each locus and shifting it towards the bottom left quadrant of the plot where the compressive stresses are highest. The orientation effect on the peak yield stress of uniaxial tests may be extracted from these plots by identifying the value along the T22 axis of the pressure dependent loci for each IDR and IDD. These values correspond to those reported in Figure 3.5. The biaxial loci illustrate the dramatic effect of both the initial texture and orientation of texture on the flow behavior of amorphous polymers under a multiaxial stress state. Our model also applies to any triaxial loading condition. However, the effect is easier to demonstrate as well as visualize in two dimensions as done here. Recall that the biaxial yield loci were at a fixed strain rate and temperature. The material model includes these effects and, therefore, can handle more general and inhomogeneous loading conditions. This is done below by investigating the effect of orientation on shear banding in glassy polymers.

3.2.2 Localized Flow

Many different types of materials are known to experience shear localization during plastic flow. The occurrence of this phenomenon in ductile metals, single crystals, and geological materials has been reviewed by Rice [30]. Shear localization is a phenomenon

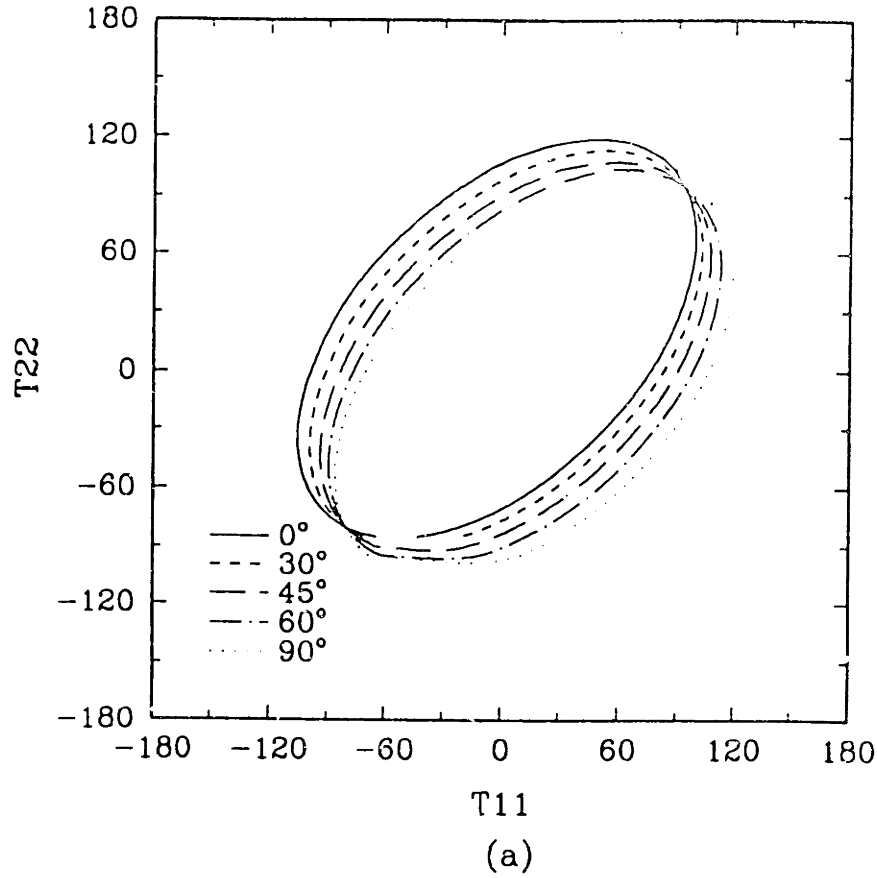

(a)

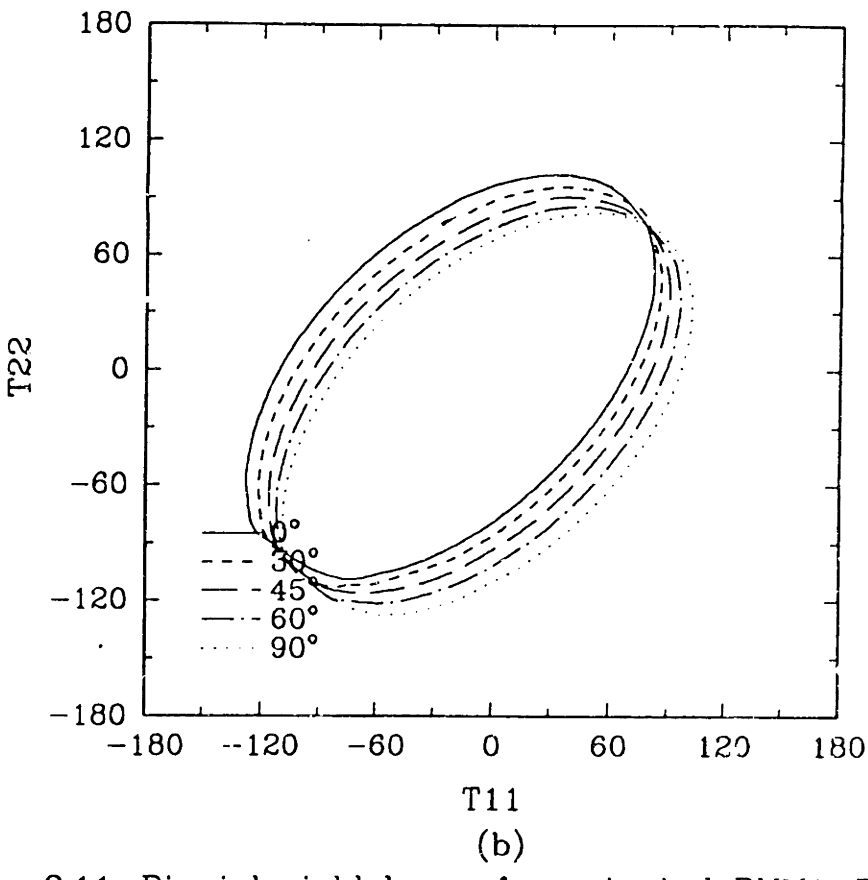

(b)

Figure 3.11. Biaxial yield locus for oriented PMMA, R=2.0, at fixed strain rate = 0.01 and for various orientations with the 2 axis, with (b) and without (a) pressure dependence.

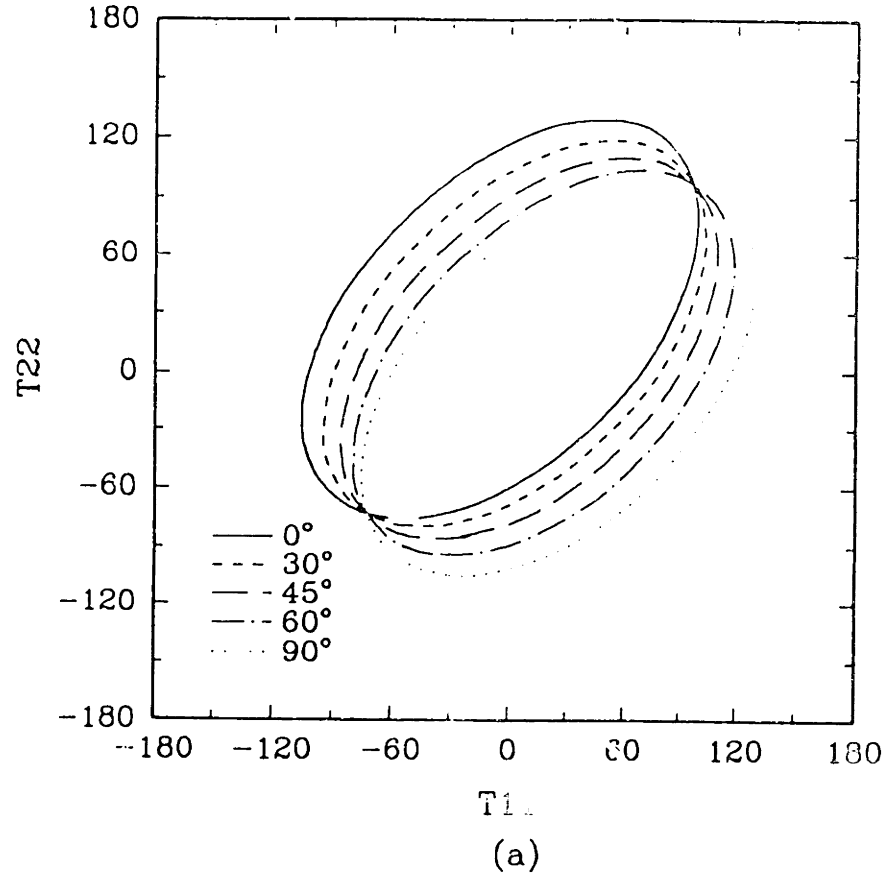

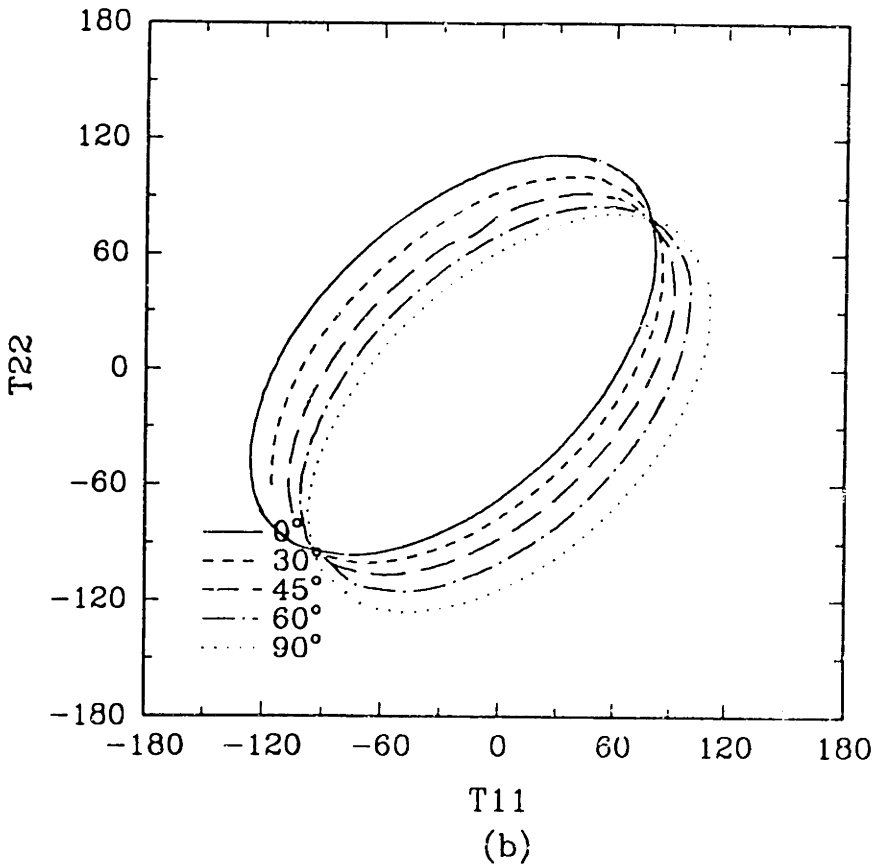

Figure 3.12. Biaxial yield locus for oriented PMMA, R=2.25, at fixed strain rate = 0.01 and for various orientations with the 2 axis, with (b) and without (a) pressure dependence.

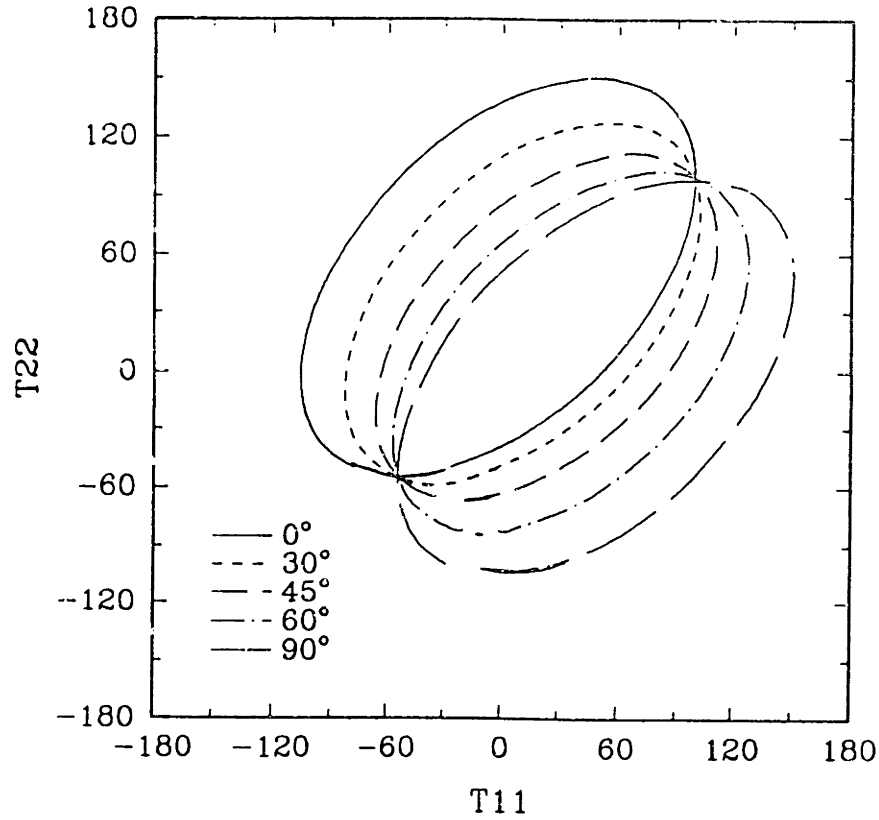

(a)

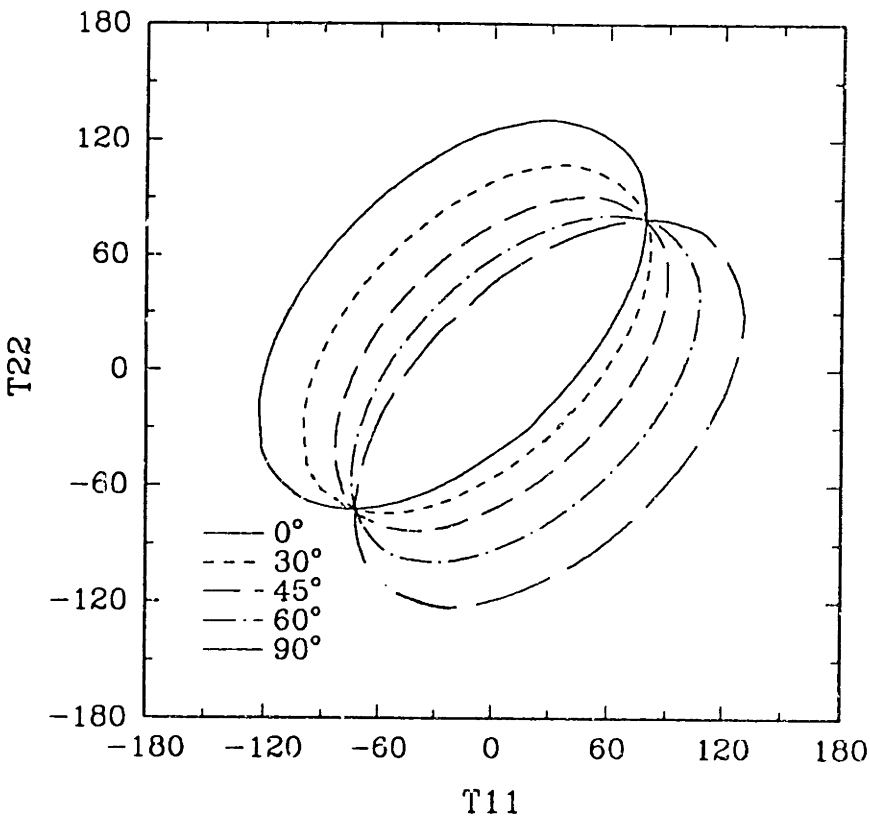

(b)

Figure 3.13. Biaxial yield locus for oriented PMMA, R=2.5, at fixed strain rate = 0.01 and for various orientations with the 2 axis, with (b) and without (a) pressure dependence.

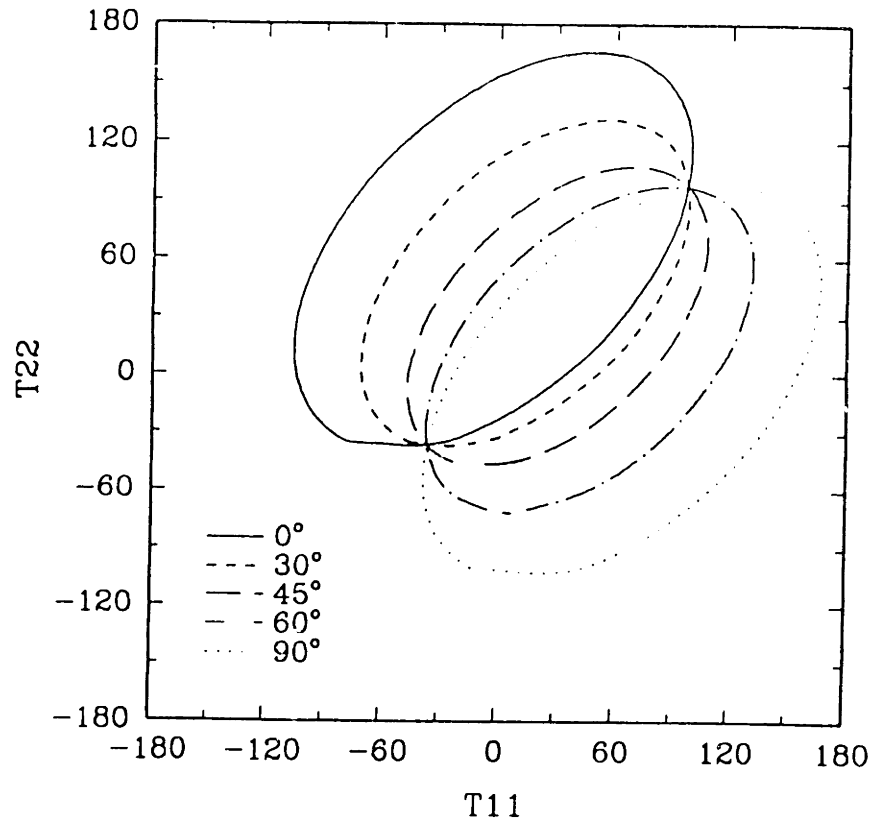

(a)

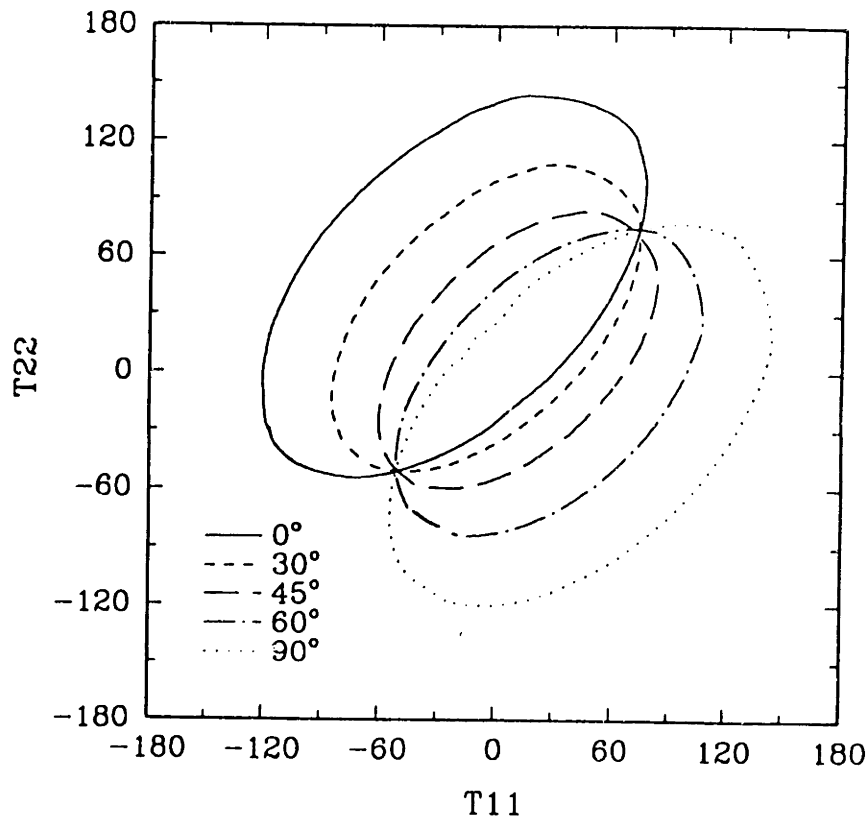

(b)

Figure 3.14. Biaxial yield locus for oriented PMMA, R=2.6, at fixed strain rate = 0.01 and for various orientations with the 2 axis, with (b) and without (a) pressure dependence.

which is of great interest to study because it affects such a broad spectrum of materials and can have a marked impact on all subsequent deformation in the material, often leading to fracture. An analytical solution for the conditions necessary for localization to occur and the directions along which the resulting bands will propagate has been obtained via a bifurcation analysis for various isotropic material models for the rate-independent case [30, 31] and a linear perturbation stability analysis for the rate-dependent case [32]. Finite element analysis may also be used to predict the direction of shear banding after artificially initiating localization with either a material or geometric imperfection [33].

Localization in Pre-Oriented Polymers

Experiments on pre-oriented polymers have shown that shear localization is affected by both the degree and orientation of the material's initial texture. This effect has been examined experimentally by Duckett [26] and Brown and Ward [28] in the fully oriented semi-crystalline polymer PET below its Θ_g, by Duckett, et al. [29] in the highly oriented semi-crystalline polymer PP above its Θ_g, and by Rider and Hargreaves [27] in the amorphous polymer PVC. In these experiments, textured polymers were tested at various IDDs (and various IDRs for the PVC case) in simple tension. The resulting shear band direction (SBD) was recorded. This direction is given by the angle α shown in Figure 3.3. The experiments on the semi-crystalline polymer sheets showed the SBD to be closer to the tensile axis than the IDD except for IDDs of $\theta \leq 16^o$ in which cases shear banding was difficult to observe, i.e. homogeneous deformation was obtained. These results are shown in Figures 3.15 and 3.16. Rider and Hargreaves' plots of the SBD as a function of IDD of PVC at various draw ratios are shown in Figure 3.17.

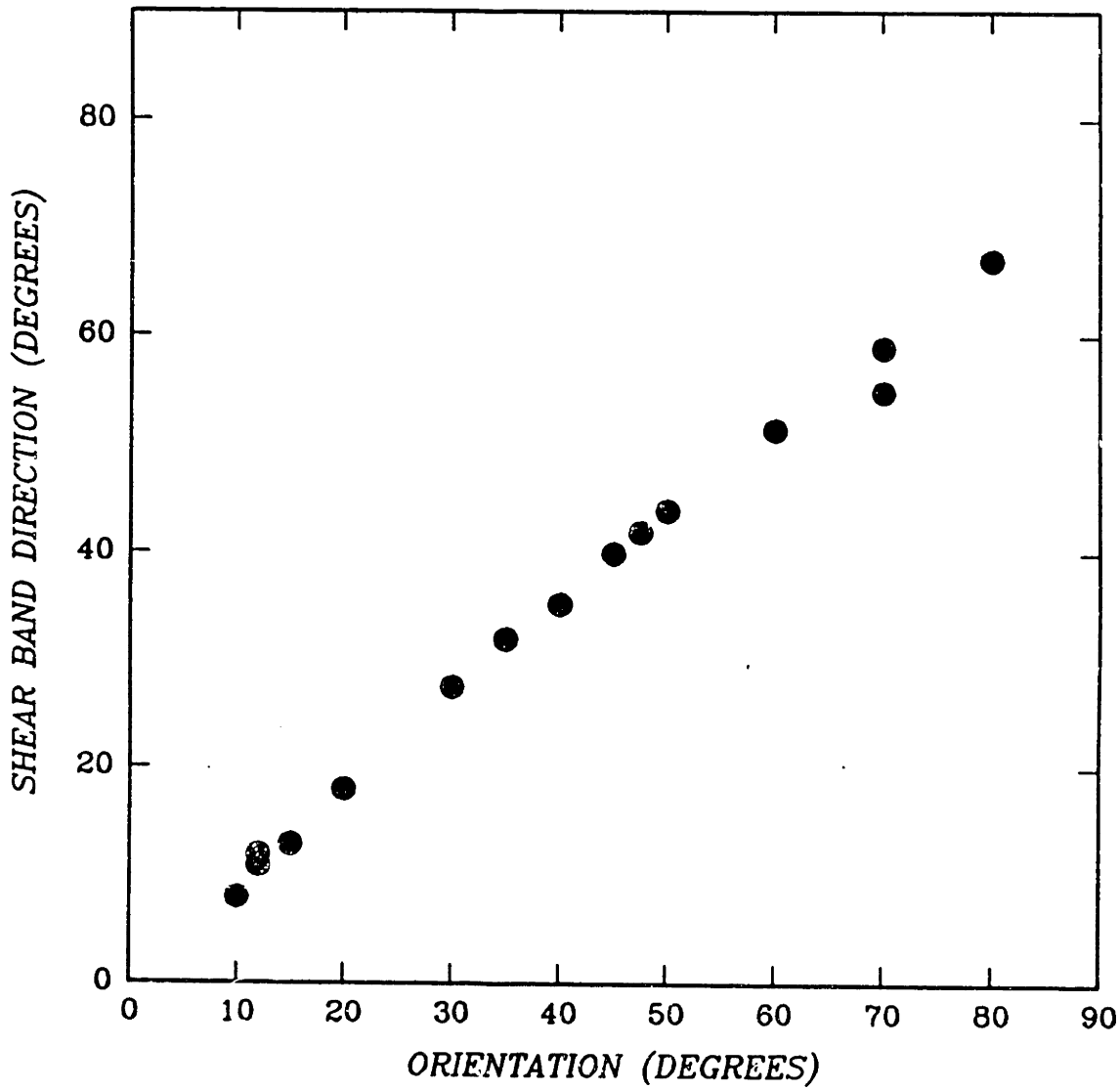

Figure 3.15. Brown and Ward experimental results for shear band direction as a function of orientation for fully oriented sheets of semi-crystalline PET [3.5].

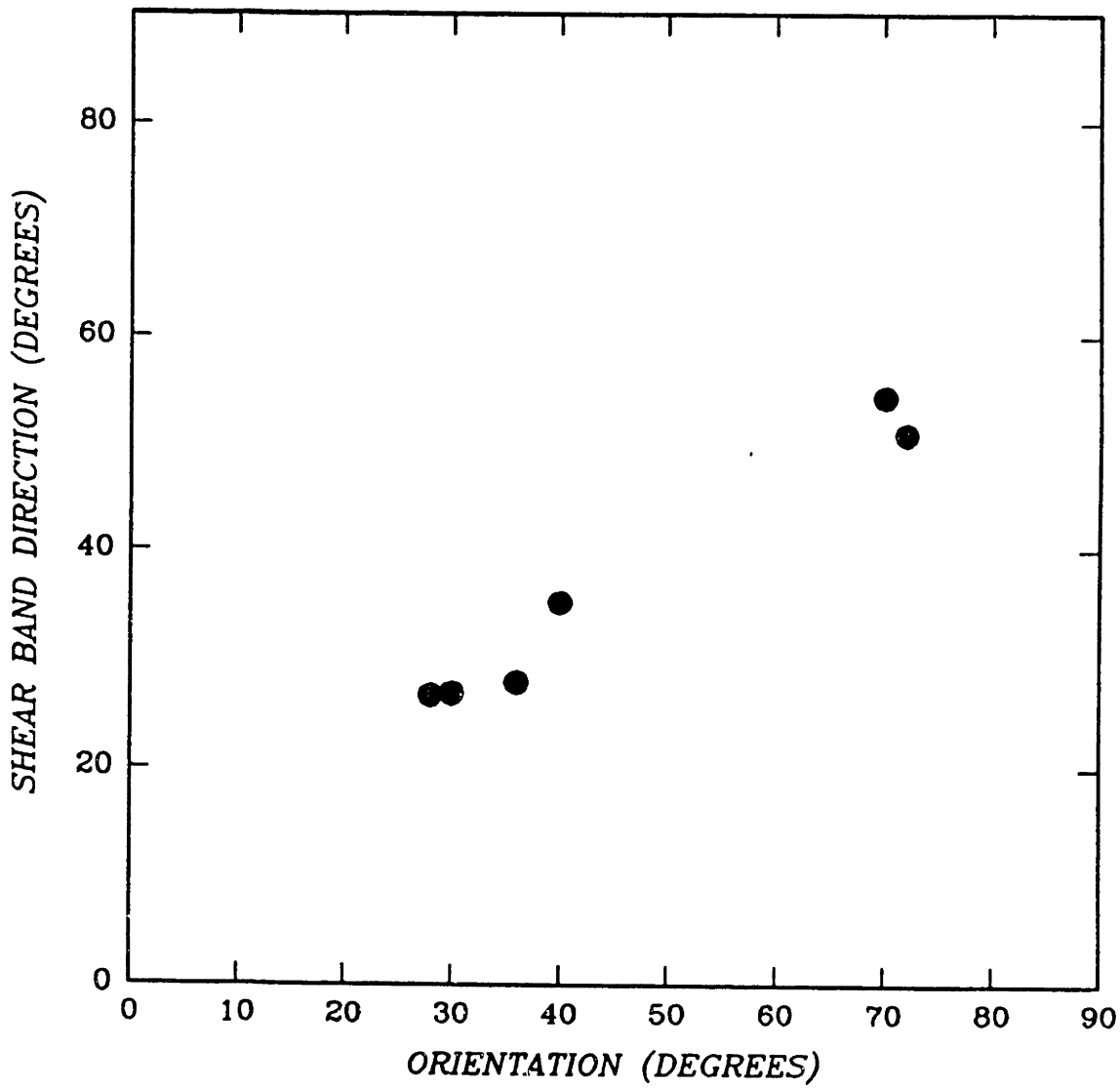

Figure 3.16. Duckett, et al. experimental results for shear band direction as a function of orientation for highly oriented sheets of semi-crystalline polypropylene tested in tension [3.6].

The data is from tensile tests on thin sheets which have been oriented such that the principal stretch ratios are given by: $\lambda_1 = \lambda$, $\lambda_2 = \lambda_3 = 1/\sqrt{\lambda}$. This experimental data indicate that the SBD depends on the specific material, the initial draw ratio, and the orientation. As the IDR increases, its impact on the direction of shear localization with orientation becomes stronger, especially as the locking stretch ratio is neared. This shows that the SBD is dependent on both material and IDR, i.e. the effect of IDR on the material response is relative to the locking stretch of the specific material. We can see these effects in the amorphous PVC data where the IDR has a very large impact on the SBD as a function of orientation. Figure 3.17 shows that at a low IDR, the SBD is not significantly impacted by the IDD, and the SBD becomes a strong function of the IDD as the IDR increases and approaches the effective locking stretch of the material.

These investigators [26, 28, 29] have been able to analytically predict the direction of shear banding in these polymers with reasonable accuracy by using Hill's anisotropic theory of yield and the Levy-Mises equations for plastic straining modified for an anisotropic material with orthorhombic symmetry. These equations are given by:

$$\begin{aligned} d\epsilon^p_{xx} &= [H(\sigma_{xx} - \sigma_{yy}) + G(\sigma_{xx} - \sigma_{zz})]d\Lambda, \\ d\epsilon^p_{yy} &= [F(\sigma_{yy} - \sigma_{zz}) + H(\sigma_{yy} - \sigma_{xx})]d\Lambda, \\ d\epsilon^p_{zz} &= [G(\sigma_{zz} - \sigma_{xx} + F(\sigma_{zz} - \sigma_{yy})]d\Lambda, \\ d\gamma^p_{xy} &= N\sigma_{xy}d\Lambda, \end{aligned} \tag{3.10}$$

where $d\epsilon^p_{ij}$ is the plastic strain increment, σ_{ij} is the stress, and $d\Lambda$ is a constant, and x is the direction parallel to the IDD. For the experimental tensile tests, we had G=H and $\sigma_{zz} = 0$. Thus, these equations reduce to:

$$\begin{aligned} d\epsilon^p_{xx} &= [2G\sigma_{xx} - G\sigma_{yy}]d\Lambda, \\ d\epsilon^p_{yy} &= [(F+G)\sigma_{yy} - G\sigma_{zz}]d\Lambda, \\ d\epsilon^p_{zz} &= -[G\sigma_{xx} + F\sigma_{yy}]d\Lambda, \\ d\gamma_{xy} &= N\sigma_{xy}d\Lambda. \end{aligned} \tag{3.11}$$

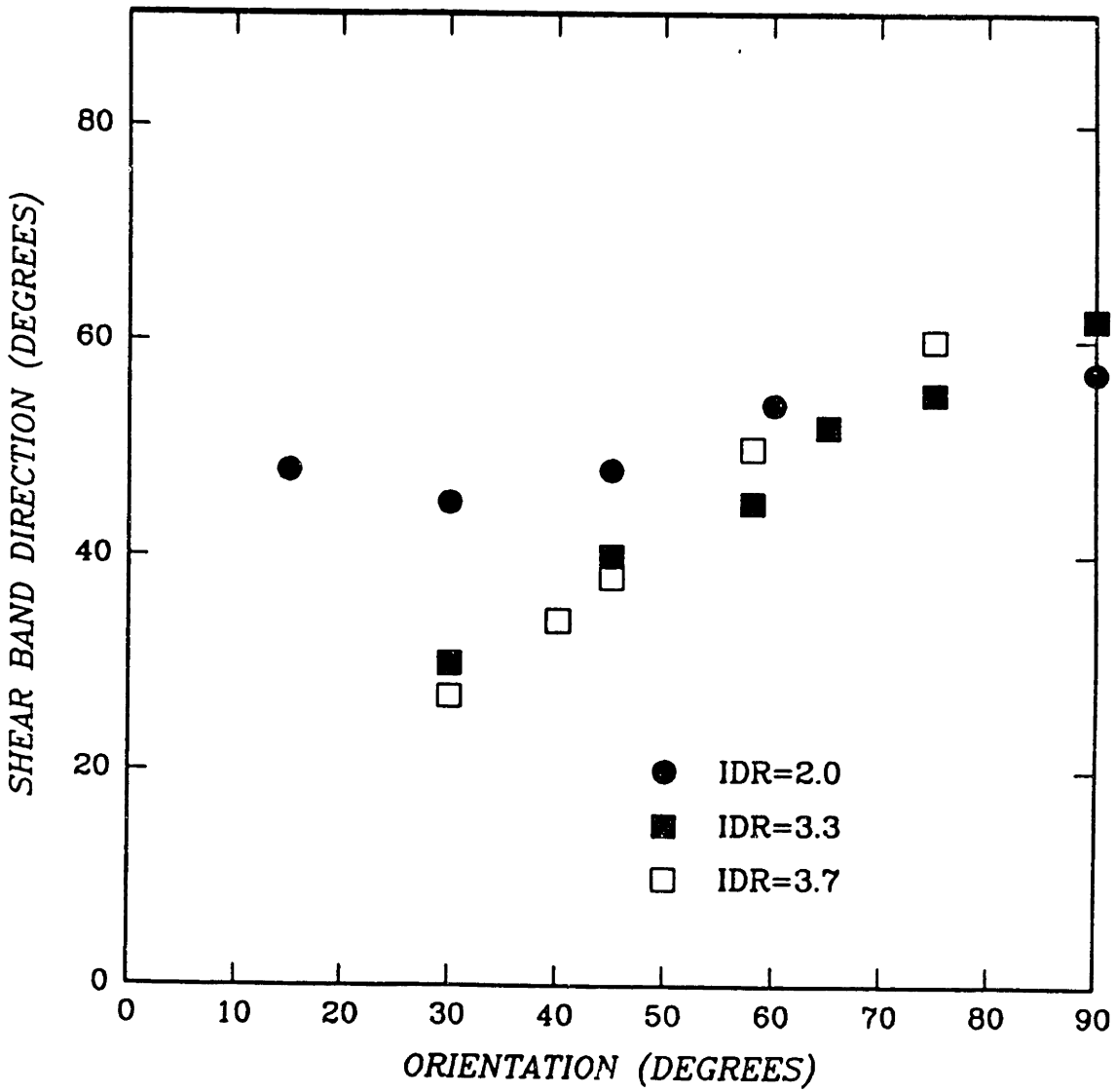

Figure 3.17. Rider/Hargreaves experimental results for shear band direction as a function of orientation for various draw ratios in amorphous PVC. This data was from plane stress tensile tests [3.4].

To determine the SBD from these equations we assume that all active plastic deformation is concentrated within the shear band. Therefore, the shear band direction must be common to both the plastically deforming material within the band and the less intensely deforming bulk of the specimen. This requires a zero value for the normal component of plastic straining in the direction of the band. Equations (3.11) written in a frame rotated an angle β from the IDD become:

$$\begin{aligned} d\tilde{\epsilon}^p_{xx} &= d\epsilon^p_{xx}cos^2\beta + d\epsilon^p_{yy}sin^2\beta + 2d\gamma^p_{xy}sin\beta cos\beta, \\ d\tilde{\epsilon}^p_{yy} &= d\epsilon^p_{xx}sin^2\beta + d\epsilon^p_{yy}cos^2\beta - 2d\gamma^p_{xy}sin\beta cos\beta, \\ d\tilde{\epsilon}^p_{zz} &= d\epsilon^p_{zz}, \\ d\tilde{\gamma}^p_{xy} &= -(d\epsilon^p_{xx} - d\epsilon^p_{yy})sin\beta cos\beta + d\gamma^p_{xy}(cos^2\beta - sin^2\beta). \end{aligned} \tag{3.12}$$

If we say β defines the angle of the shear band, then $d\tilde{\epsilon}^p_{xx}$ must equal zero. This gives the following quadratic equation for the $tan\beta$:

$$d\epsilon^p_{yy}tan^2\beta + 2d\gamma^p_{xy}tan\beta + d\epsilon^p_{zz} = 0.0. \tag{3.13}$$

Therefore, we obtain two directions for the formation of a shear band. These predicted directions agreed well with the experimental data and were further improved upon by using the Hill criterion as modified with a scalar back stress which was described earlier. We emphasize that using this method requires experimentally obtaining the Hill coefficients and the scalar back stress at each draw ratio. In the analysis below, we compute the effect of texture and orientation on the direction of subsequent shear localization in an oriented glassy polymer with a model based on its isotropic behavior and given its initial draw ratio and direction. The model does not require any further property measurements on the oriented polymer itself.

Once the material has localized and a prominent shear band forms, the material within the band reorients toward the tensile axis. This phenomenon has been observed in PET [28], PP [29], and PVC [36] by examining the deformed material with a polarizing microscope. The extinction direction corresponds to the max refractive index which

is parallel to the principal draw direction. The extinction direction in the band was found to be different from that of the bulk material. The extinction direction within the band rotated from the IDD towards the tensile axis by an angle $(\theta - \bar{\theta})$, where $\bar{\theta}$ is the angle the principal draw ratio within the band now makes with the tensile axis. The experimental results for the semi-crystalline polymers PET and PP are listed in Table 3.1. This data shows that the material within the band reorients towards the axis. Brown and Ward also had additional results showing that the greater the amount of applied tensile deformation, the greater the amount of reorientation. This was more clearly demonstrated by Rider and Hargreaves in their results on PVC shown in the plots of Figure 3.18. These plots show the orientation of the material within the band with respect to the tensile axis, $\bar{\theta}$, as a function of the applied nominal stretch ratio. We note that the local stretch in the shear band would be much greater due to the localization of the deformation in the region. The orientation at $\lambda = 1.0$ is the IDD. These results indicate the material within the band continues to reorient as it is stretched until the orientation direction is parallel with the tensile axis. Rider and Hargreaves results also demonstrate that the reorientation occurs faster, i.e. at lower stretch ratios, when the IDR is smaller. This, of course, is due to the fact that there is less re-orienting to accomplish. Our analysis below will examine the phenomenon of reorientation with the shear band.

Numerical Simulation of Localization

The case of a plane strain tensile test of oriented PMMA at room temperature is analyzed here using the constitutive model of Chapter One as modified in section 3.1. We are interested in obtaining the effect of material orientation on the direction of

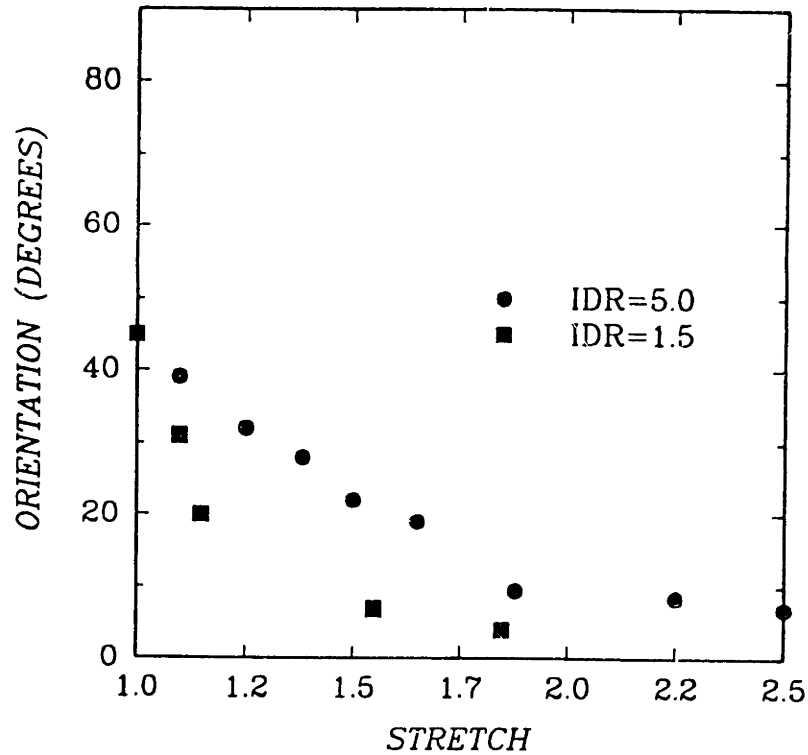

(a)

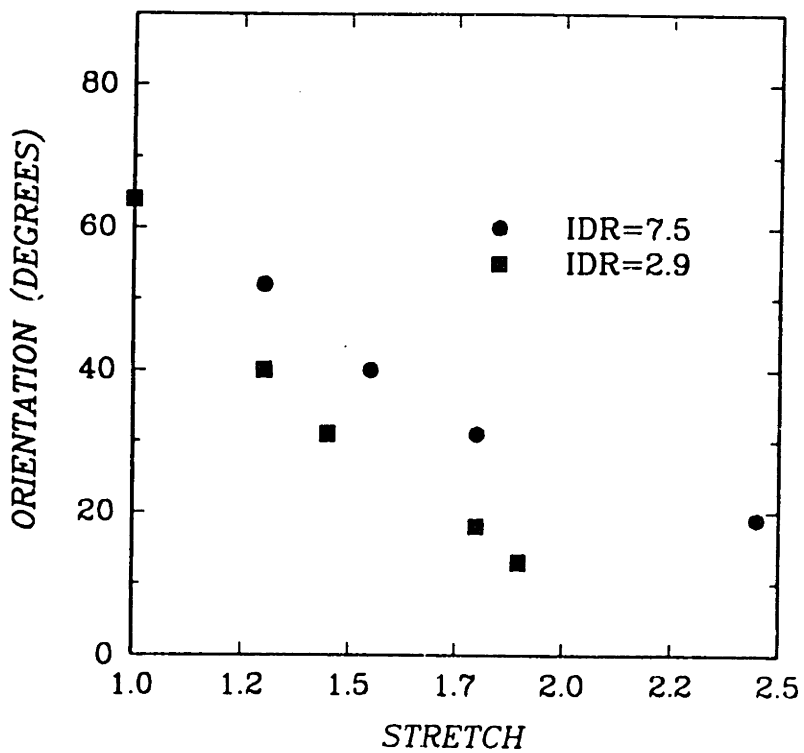

(b)

Figure 3.18. Rider/Hargreaves experimental results for material orientation within shear band as a function of stretch for (a) IDRs of 5.0 and 1.5 given an IDD of 45°, and (b) IDRs of 7.5 and 2.9 given an IDD of 64°.

shear banding in amorphous polymers. A relatively coarse mesh of 4-node plane strain elements (ABAQUS type CPE4) is used in the finite element analysis. This element is the Nagtegaal, et al constant dilation 4 node element where the shear and pressure terms are integrated separately to prevent "locking" of the mesh. We note that a sharper shear band would be picked up with a finer mesh and/or a mesh of quadrilateral elements composed of constant strain triangle (CST) elements. The element size defines the minimum possible thickness of the band. Therefore, an analysis with a finer mesh of 4-node elements could result in a narrower shear band. The shear band will form along element boundaries. The CST mesh formation provides a greater freedom for the deformation to localize because of the larger number and direction of element boundaries. If one is interested in obtaining a narrow band, and the direction of the band is known *a priori*, then one could tailor a CST mesh to accurately pick up the localized straining. For the purposes of this analysis, the coarse unbiased mesh of quadrilateral elements shown in Figure 3.19 will suffice in the prediction of the direction of shear banding. However, it may result in an artificially broad shear band.

For the case of plane strain tensile testing of a preoriented polymer, the problem becomes asymmetric with respect to the tensile axis when the principal direction of orientation is aligned at some angle with respect to the tensile axis. This was shown in the discussion on the simulation of "homogeneous" deformation of oriented polymers. The asymmetry of the problem permits a model of one-half of the test specimen to be used with appropriate boundary conditions. The asymmetry is due to the material orientation. This condition is enforced by constraining the nodes on the bottom of the mesh on either side of the specimen center to displace in equal and opposite x and y directions. Due to the material orientation, shear band formation in the central portion

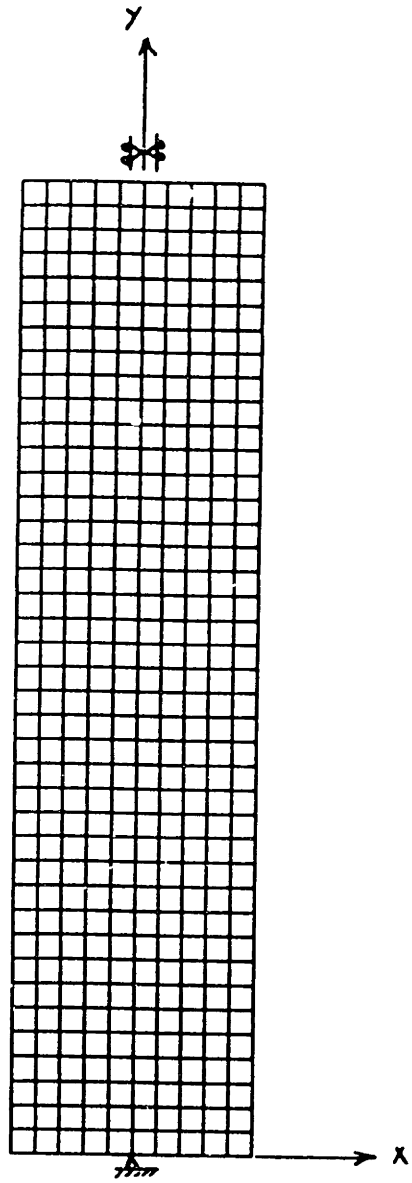

Figure 3.19. Finite element model of one-half of a plane strain tensile test specimen. Boundary conditions consist of constraining nodes on either side of the specimen center along the bottom surface of the mesh to displace in equal and opposite x- and y-directions. The nodes along the top surface are constrained to remain on a straight line. The top center node is constrained in the x-direction.

of the specimen may result in rotation of the specimen. We permit this to occur by constraining the nodes along the top of the mesh to remain on a straight line but give them the freedom to contract as well as pivot about the center node of this surface. This would be equivalent to loading the specimen in a pinned grip. The center node of the bottom surface of the mesh is constrained in the x- and y-directions. The center node of the top surface of the mesh is constrained in the x-direction and displaced in the y-direction for our loading condition. The half-length of the specimen was chosen to be four times the width in order to allow the shear band to grow along a straight path until reaching a free surface.

The shear band is initiated in the center of the specimen by making the two bottom center elements of the mesh softer than the remainder of the mesh. This is done by assigning these elements a lower value for the material property of the athermal shear resistance, s_0=105MPa, than the rest of the elements of the mesh which are assigned s_0=112MPa. This causes a shear band to emanate from this point once the material begins to flow. Different values of s_0 were tried on these two elements in a test case to ascertain its effect on the resulting shear band direction. It was found to have no effect.

The analysis is conducted on a mathematical model with the same material constants as determined in Chapter One for PMMA which has been oriented to varying levels of texture such that the principal values of the initial textures are given by: $\lambda_1 = \lambda$, $\lambda_2 = 1/\lambda$, $\lambda_3 = 1.0$, where λ is the initial draw ratio and λ_3 coincides with the plane strain direction of the "test". The material is then "tested" in plane strain tension at the initial draw ratios of $\lambda = 2.0$, 2.25, and 2.50, and the initial draw directions of $\theta = 0°$, $30°$, $45°$, $60°$, and $90°$. The direction of shear banding is obtained by

examining contours of the plastic strain rate where regions of intense plastic straining indicate the development of a shear band. The angle that these regions make with the tensile axis gives the direction of banding.

The contour plots of plastic strain rate for the above tensile tests are shown in Figures 3.20 - 3.22. Two bands of concentrated straining initially form in each sample. These bands are at approximately 90° to one another with possibly a few degrees difference [34] due to the pressure dependent yield of the polymer which is included in the constitutive model. One can see how the angle at which the shear band forms with respect to the tensile axis, α, changes with both initial draw ratio and direction. These results are more concisely summarized in Figure 3.23. These numerical results demonstrate that as the IDR approaches the locking regime, where the locking stretch of PMMA is 3.0, the dependence of the shear band direction on orientation becomes more acute. This follows the trends found in experiments discussed earlier which showed that the more highly textured the polymer, the greater is the dependence of shear band formation on orientation.

Another interesting result of the numerical analysis is illustrated in Figure 3.24. This figure shows the contours of plastic strain rate as deformation progresses for the cases where the IDR is initially oriented with the tensile axis. For the high draw ratio of 2.5, we see the material at first begins to localize into symmetric 45° shear bands; however, the straining soon becomes uniform throughout the test specimen. This was also observed in the experiments on highly oriented semi-crystalline PET where clearly defined shear bands were not observed at orientations of $\theta < 15°$. Duckett, et al. did not comment on any test they may have conducted at 0° orientation on polypropylene. Rider and Hargreaves did not obtain distinct banding for $\lambda = 2.0$ and

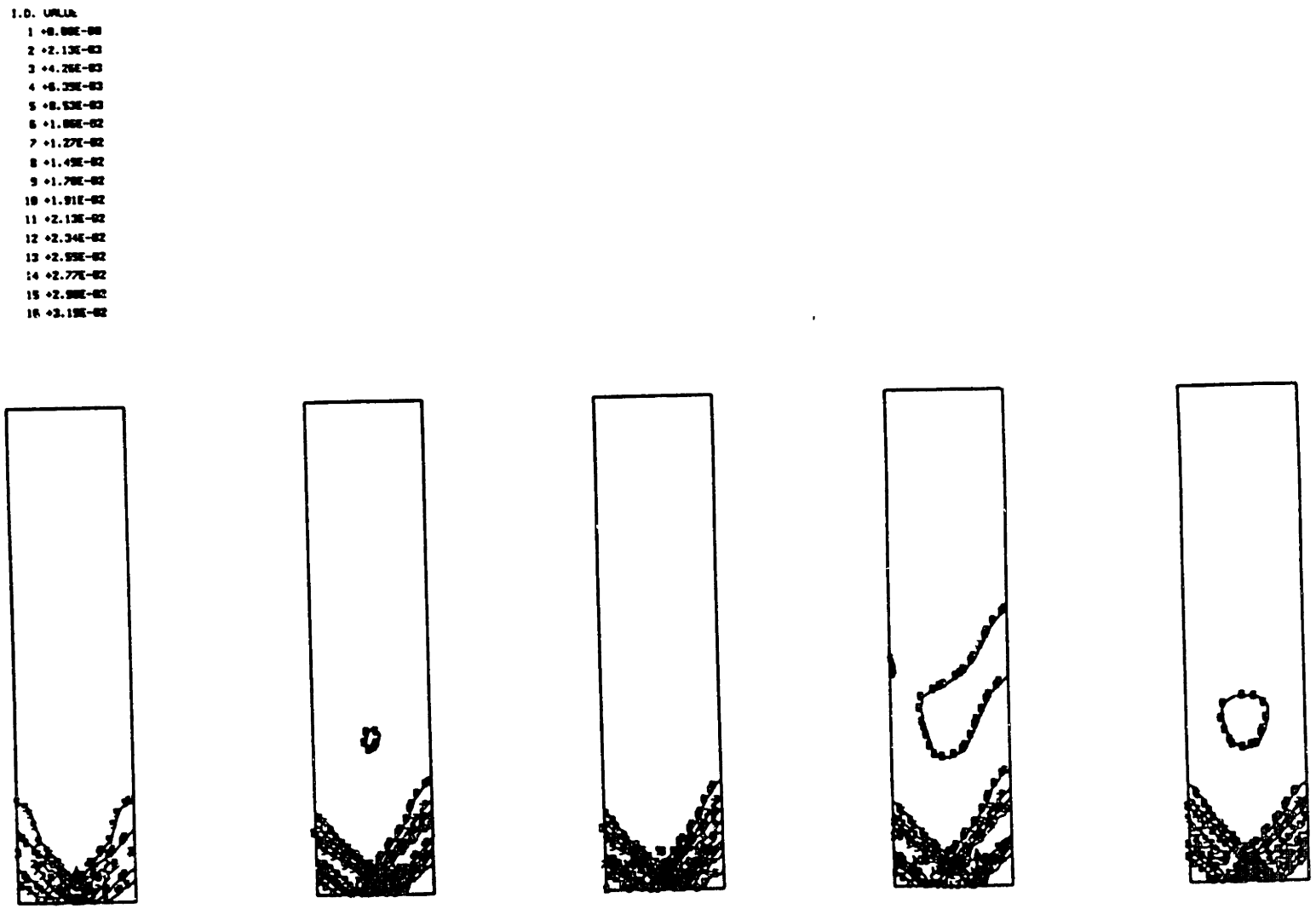

Figure 3.20. Contour plots of the plastic strain rate for the initial draw ratio of 2.0 at initial draw directions of Θ = 0°, 30°, 45°, 60°, and 90°.

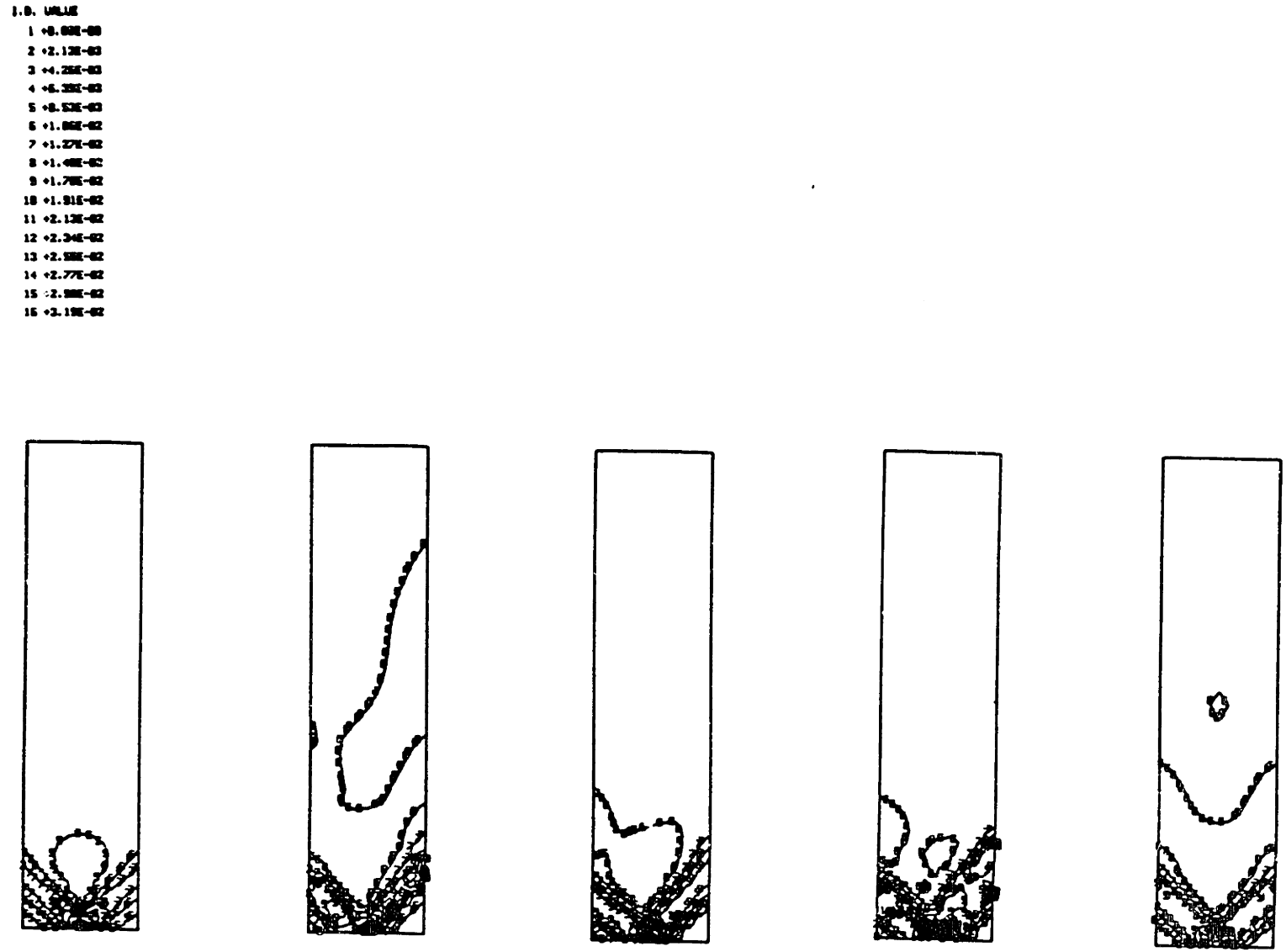

Figure 3.21. Contour plots of the plastic strain rate for the initial draw ratio of 2.25 at initial draw directions of Θ = 0°, 30°, 45°, 60°, and 90°.

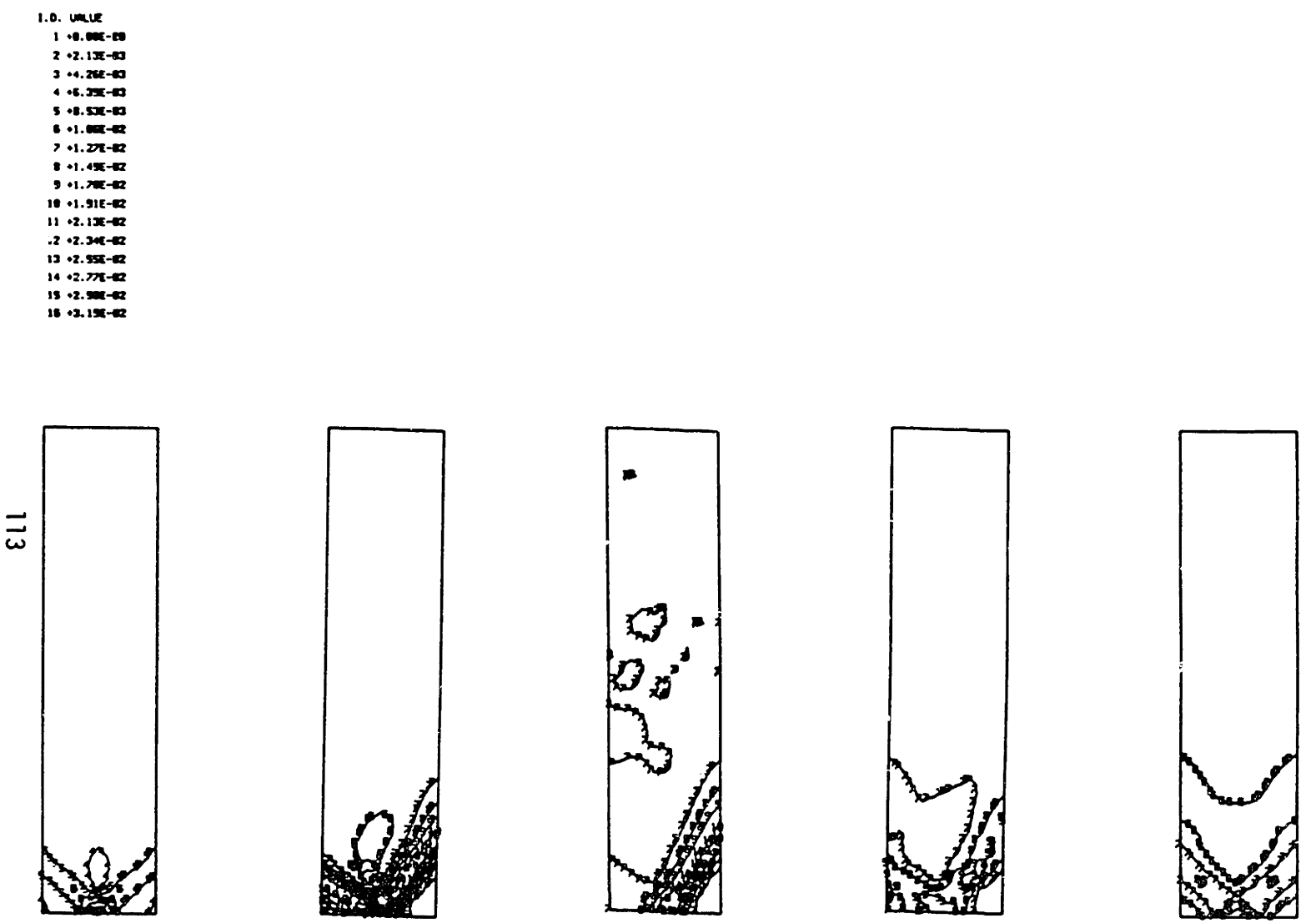

Figure 3.22. Contour plots of the plastic strain rate for the initial draw ratio of 2.5 at initial draw directions of Θ = 0°, 30°, 45°, 60°, and 90°.

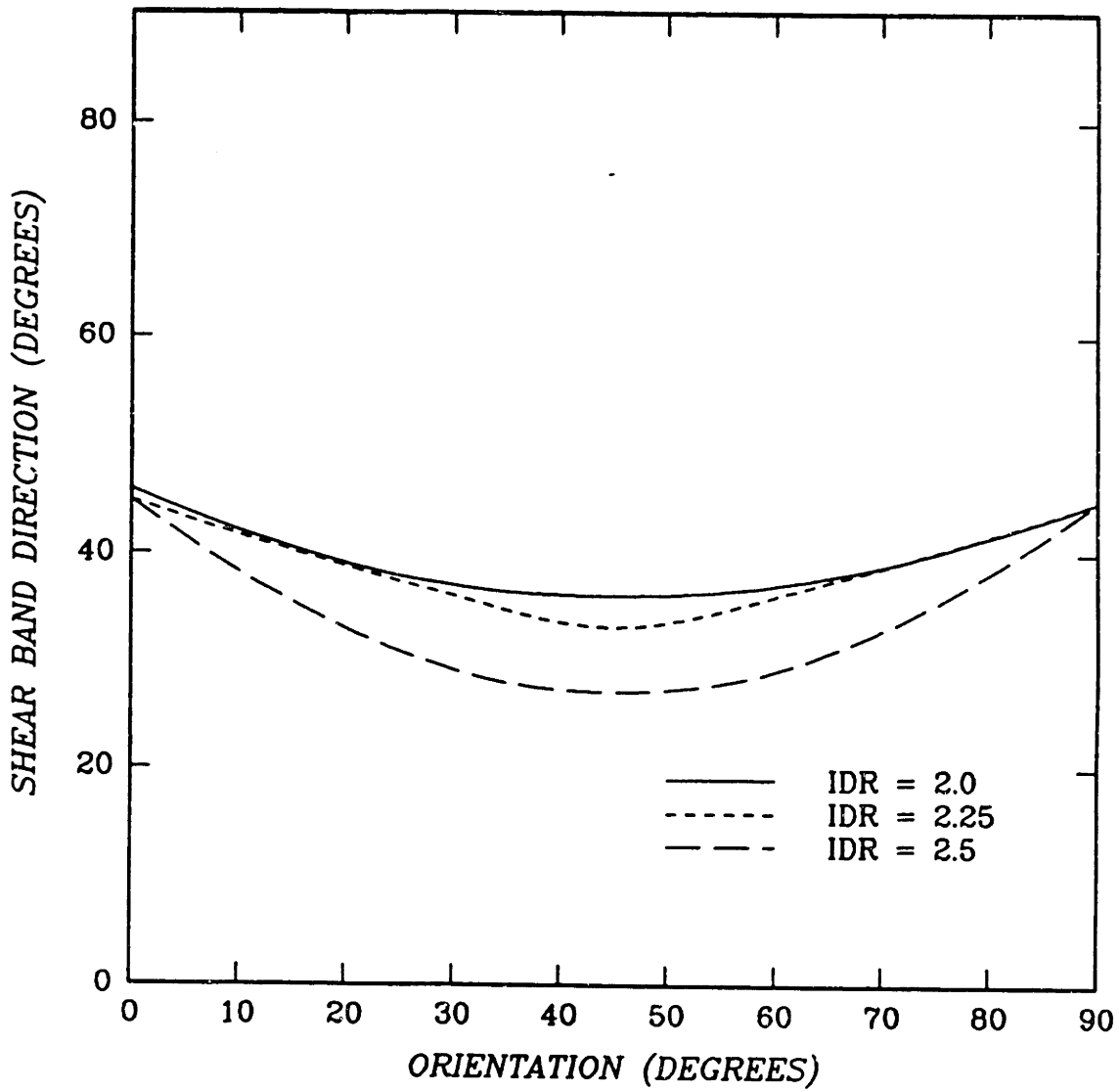

Figure 3.23. Shear band direction as a function of orientation for various initial draw ratios in PMMA. These results were computed from simulated plane strain tensile tests.

$\theta = 0°$ or $\lambda = 3.3$ and $\theta = 0°, 15°$ in their PVC samples. It appears that they did not test the highest draw ratio at these orientations for this reason. The absence of shear banding in these experimental cases as well as the numerical simulations at 0° orientation can be explained in terms of a Considere stability analysis. In the isotropic material, necking occurs in the Considere construction at the point when the slope of the stress-strain curve equals the stress, σ, divided by the stretch, λ, or $\frac{d\sigma}{d\lambda} = \frac{\sigma}{\lambda}$. Stability is regained and cold-drawing begins at a second Considere point. The highly preoriented material which is aligned with the tensile axis is essentially at a state past the second Considere point and in the middle of a stable cold-drawing mode which even the artificial initiation of localization cannot supersede. Referring to the stress-stretch curve for isotropic PMMA, our material of IDR=2.5 is past this second Considere point whereas the lower IDR of 2.25 is before but near this point. Therefore, we can expect the material with IDR=2.5 to continue in the stable drawing mode and the material with IDR=2.25 to require a greater amount of applied strain before localization disappears and stable cold-drawing takes over. This is exactly what was predicted with the model as illustrated in Figure 3.24 which demonstrates that a larger applied stretch was needed before homogeneous drawing occurred in the material with an IDR of 2.25 than in the material with an IDR of 2.5. Our model correctly predicts this continued drawing.

It is also of interest to observe the development of a shear band in those cases where the IDR is aligned asymmetrically about the tensile axis. The case of an IDR of λ=2.5 and and IDD of θ= 30° was chosen to examine this development. Figures 3.25 and 3.26 depict the contour plots of plastic shear strain rate and plots of the deformed mesh as deformation progresses for this case. The plots of the deforming mesh show the

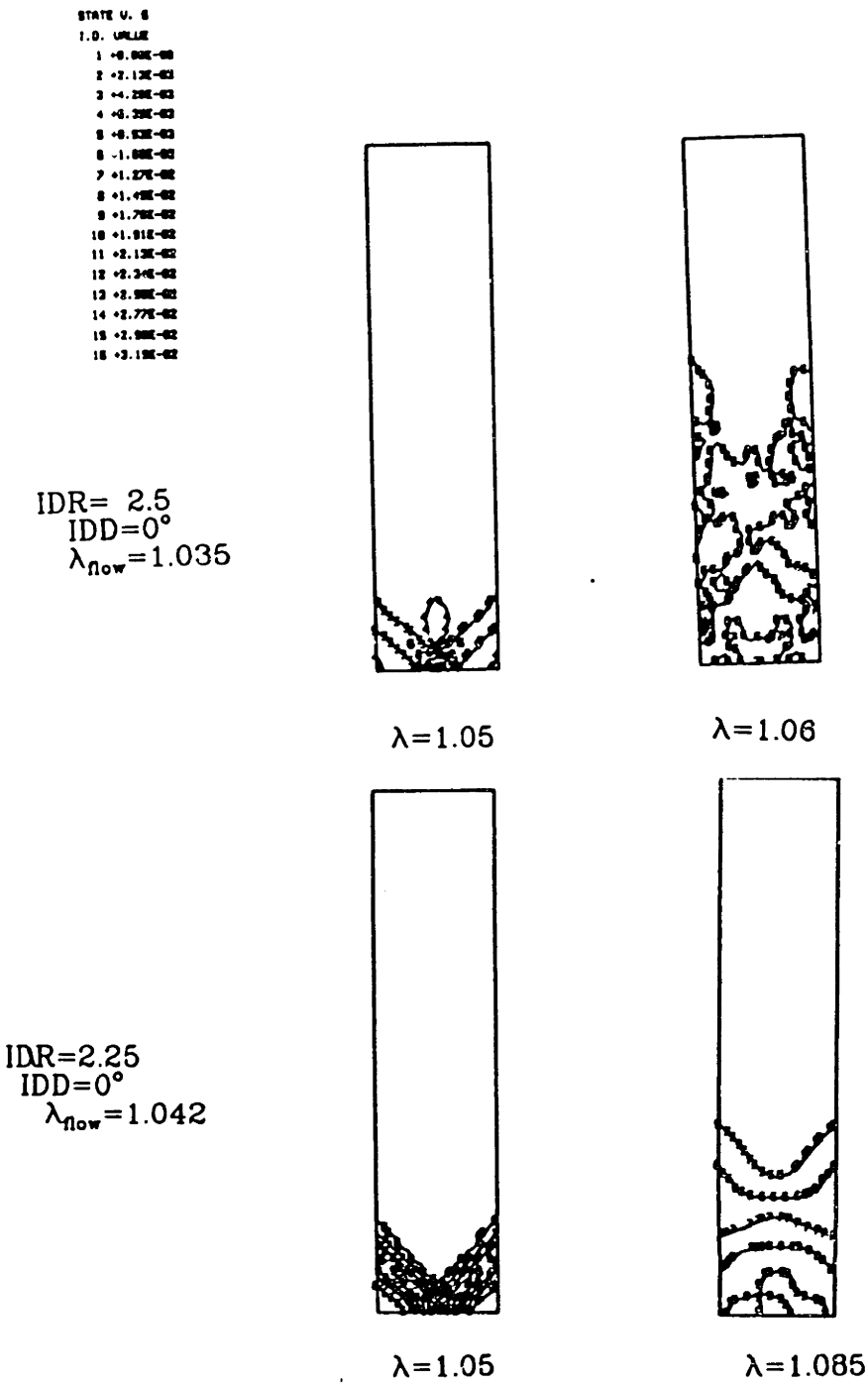

Figure 3.24. Contours of plastic shear strain rate for an IDD of 0° and IDRs of 2.25 and 2.5 for PMMA at different applied stretches. Note that homogeneous deformation (cold drawing of sample) is obtained at a lower stretch ratio for the higher IDR. λ_{flow} is the stretch at which flow begins.

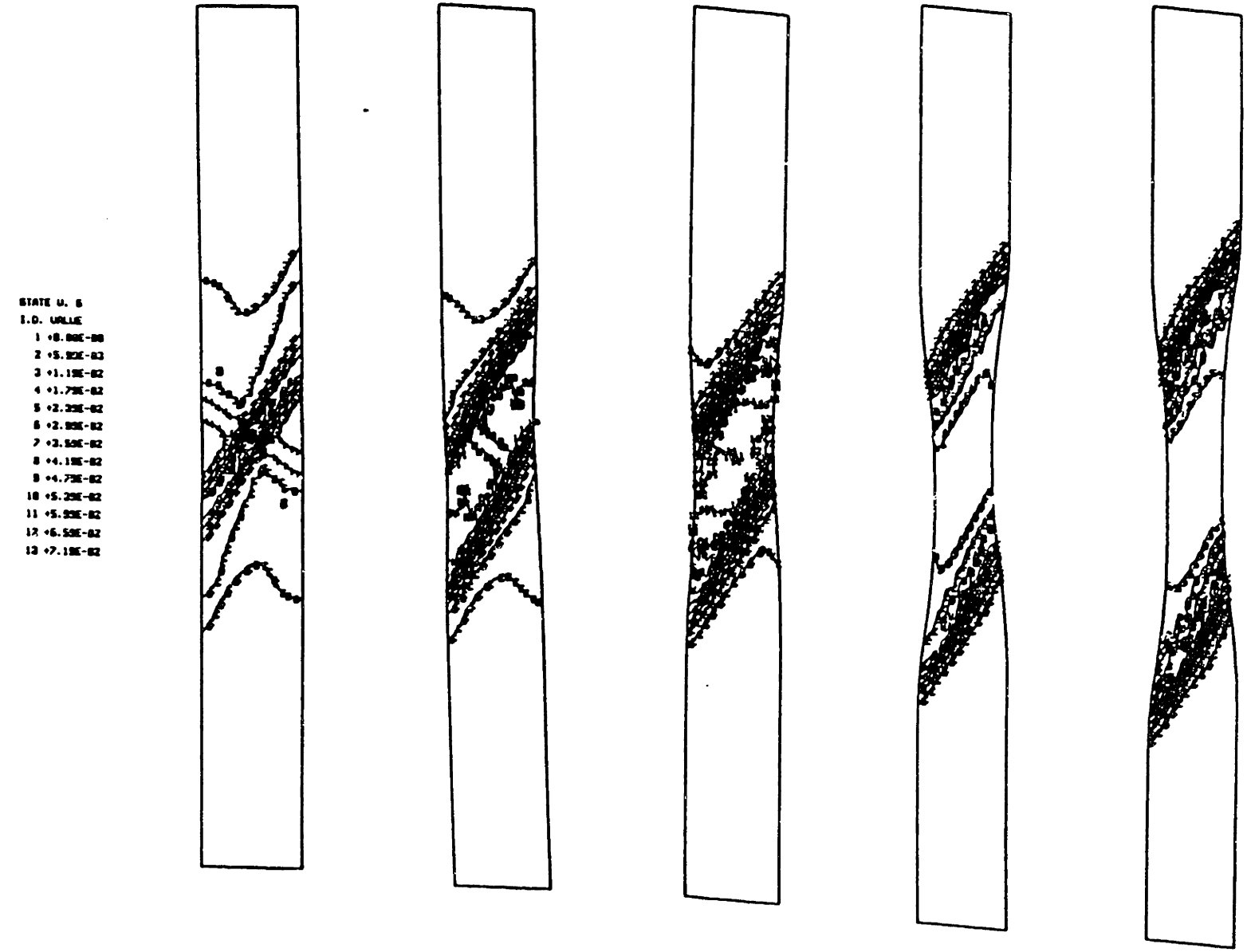

Figure 3.25. Contour plots of plastic shear strain rate as a function of deformation for the case of an IDR of λ=2.5 and an IDD of Θ=30°.

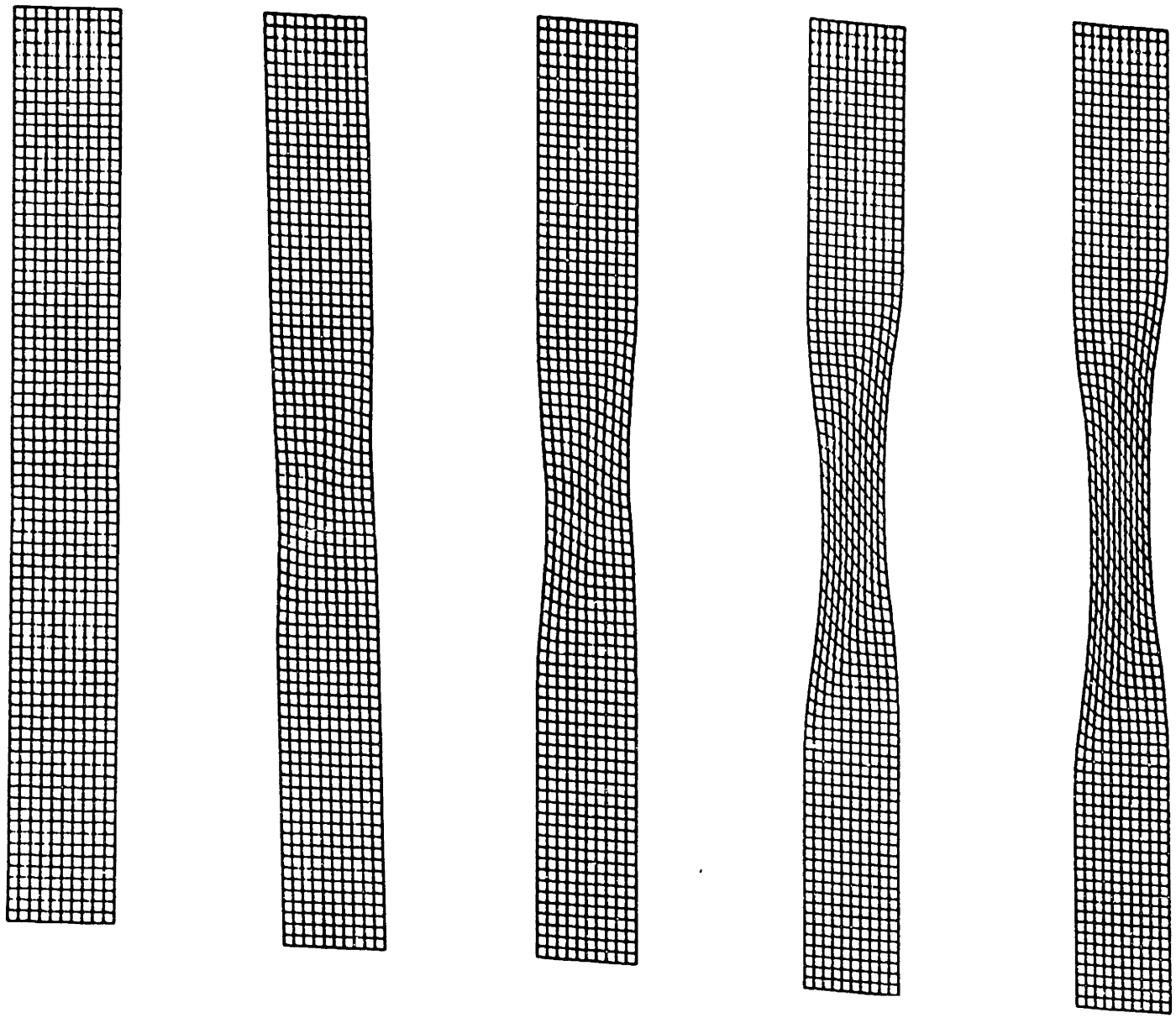

Figure 3.26. Plots of the mesh as deformation progresses clearly clearly illustrating the development of a shear band for the case of an IDR of $\lambda = 2.5$ and an IDD of $\Theta = 30^{o}$.

deformation to be concentrated in a shear band. The material asymmetry also causes a slight shearing of the bulk of the specimen. A similar response was obtained earlier in our one-element tensile test simulation of section 3.2.1. The plastic shear strain rate contours illustrate the increase in intensity of straining within the band with deformation where the plastic shear strain rate is as much as five times greater than the applied nominal tensile strain rate of $0.01 sec^{-1}$. The rate contours for the case of $\theta = 30^{o}$ also show the broadening of the band where the region of highest shear strain rate moves away from the center of the specimen. This indicates that the material near the specimen center, where the shear band initially formed, is now essentially "locked". Therefore, active plastic deformation spreads up (and down) the specimen, thus, broadening the band. We also observe two concentrated bands of intense straining in the initial stages of deformation. However, as deformation progresses, one band disappears, and we eventually form a single distinct shear band through the first and third quadrants of the specimen, where the IDD is also through these quadrants. This is what is generally observed in the "plane stress" experiments also. However, the second band which appeared in the initial stages of our numerical analysis is, on occassion, the shear band which forms in the experiments. We note that direct comparisons between our plane strain numerical results and the "plane stress" experimental results cannot be made due to the different nature of the tests.

We were also able to predict the reorientation of the material within the band. The amount of reorientation was found to depend on the applied deformation. Figure 3.27 depicts the reorientation of the material within the band for the cases of and IDR of 2.5 and IDDs of 30^{o} and 45^{o} as a function of the applied stretch. We note here that the applied stretch (nominal) is relative to the total specimen length of 8.0 units,

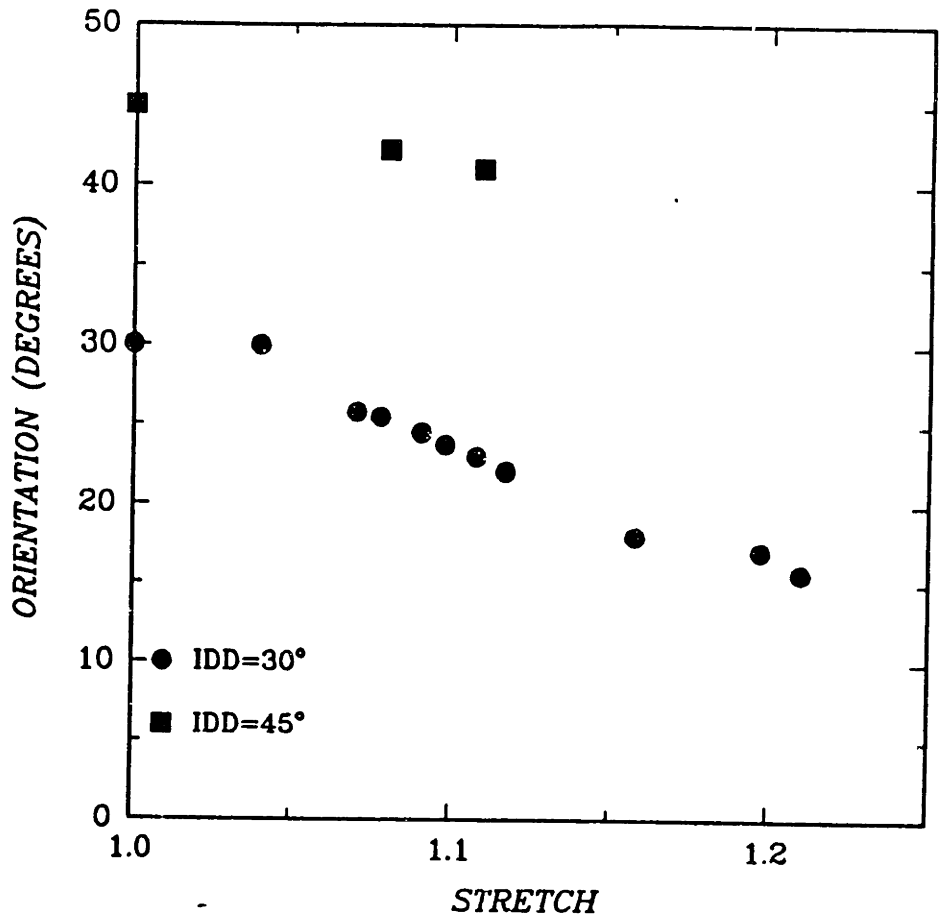

Figure 3.27. Numerical results for material orientation within the shear band as a function of stretch for an IDR of 2.5 and IDDs of 30° and 45° for PMMA.

whereas the active plastic deformation occurs over a gauge length of approximately 2.6 units. We see the material reorients toward the tensile axis by a greater amount as the applied tensile stretch increases. These results are in accord with those found in the experiments discussed earlier.

3.3 Conclusion

In this chapter, the effect of preorientation on the inelastic deformation behavior of glassy polymers was examined. This effect was incorporated into the constitutive model of Chapter One. This model was subsequently used in conjunction with the finite element method to analyze the homogeneous and localized flow of oriented glassy polymers. Comparing the results of our numerical simulations to trends found in similar experiments, we found that our model correctly predicts the flow behavior in simple homogeneous tension and biaxial tension/compression, as well as the direction of shear banding during localized flow and associated material reorientation within the band. The numerical analyses did not require any further experimental material property identification beyond the isotropic material properties and the initial texture.

Chapter 4

Discussion

A physically-based constitutive model describing the large inelastic deformation of glassy polymers at finite strains was developed in this thesis. The model was then numerically integrated and incorporated into an existing non-linear finite element code, ABAQUS. This enabled the numerical simulation of the hydrostatic extrusion of PMMA. The model was then further refined to include the effect of an existing initial orientation in the material. The effect of preorientation on the subsequent inhomogeneous inelastic response of this material was then examined.

The development of the constitutive model was based on the macromolecular structure of a glassy polymer and the primary micromechanism responsible for plastic flow associated with this structure. These materials are seen as overcoming two physically distinct sources of resistance before large strain inelastic flow may occur. Prior to initial yield, the material must exceed an isotropic resistance to deformation due to intermolecular interaction. Once inelastic flow has commenced, molecular alignment occurs, altering the configurational entropy of the material. This is the second source of deformation resistance. Documented experiments indicate that strain rate, temperature, pressure and softening affect the intermolecular resistance. These effects were incorporated into a micromechanical model of the intermolecular resistance. The

modelling of true strain softening lead to a scalar state variable representation of the athermal yield strength of the material. The entropic hardening of the material is due to the developing molecular orientation in the material. This resistance takes the form of a back stress tensor and is a state function of the plastic shape change of the material. The resulting material law was incorporated into a continuum model encompassing finite strain and rotation effects. The material properties needed in this model were then systematically obtained for the glassy polymer PMMA from experimental data found in the polymer literature. Tensile tests were then performed with the model over a range of strain rates. The model results were found to be in very good agreement with experiments.

After the numerical implementation of the constitutive model into a finite element code, the simulation of the hydrostatic extrusion of PMMA was performed. The numerical results for the quantities of die swell, strain rate, pressure vs velocity, and shrinkage stress were found to satisfactorily predict those same quantities measured in the corresponding experiments conducted at Leeds University. The simulation was also able to monitor the development of texture, identify regions of high strain rate during processing, and determine residual stresses which set in after processing. We can conclude that our constitutive model may be used with confidence as a predictive tool in the analysis of more complicated manufacturing processes where it may not be possible to experimentally measure or monitor the above effects. This could be a powerful tool in the design of warm mechanical processes because it would eliminate much of the costly trial and error procedure of process design which would be replaced by the numerical simulation of possible designs. The simulations would be able to monitor the state of the material during processing, identify trouble points in the process design,

as well as predict the state of the end product.

The resulting product of the extrusion discussed above contained a state of residual texture. Such is the case for most manufactured polymeric products, where texture is acquired either incidently or deliberately during processing. The effect of texture, i.e. preferred directions of orientation, on subsequent inelastic flow of the solid was incorporated into the constitutive model. Preoriented polymers are known to exhibit highly localized flow in the form of very distinct shear bands. This behavior was successfully simulated with the modified constitutive model. Previous models of yield (strictly rate-independent) in oriented polymers used a modified Hill yield criterion, requiring the experimental determination of several additional properties for every state of preorientation. The model proposed in this thesis does not require any further experimental material property identification beyond the isotropic material properties and the initial texture. This model would be a powerful tool in the analysis of preoriented glassy polymeric products.

Future work along this line of research of glassy polymers would focus on further refinements to the constitutive model and more experimental testing. A model for the rate and temperature effects on the back stress was proposed in this thesis in the form of an evolution equation for the number of rigid links between entanglements. Before implementation of this model refinement, a systematic set of experiments needs to be identified and conducted in order to properly define the properties needed in the evolution equation. Experimental data is also required to determine an appropriate function for aging to complete the evolution equation for the athermal shear resistance. We recognize that good experimental data is essential for the development of any constitutive model. Data was available in the literature to identify trends in the inelastic

behavior of glassy polymers in general. Specific data was found on PMMA for all of the effects currently included in the model. This is not the case for all glassy polymers. Therefore, the experimental generation of a data base of material properties is needed. It would also be of interest to experimentally examine shear localization in oriented polymers and then simulate the identical experiments with the model to further verify its validity.

Bibliography

[1] Haward, R.N. and G. Thackray, Proc. Royal Soc., 1968, **302**, p.453.

[2] Argon, A.S., Phil. Mag., 1973, **28**, p.39.

[3] Parks, D.M., Argon, A.S., and B. Bagepalli, "Large Elastic-Plastic Deformation of Glassy Polymers", MIT Program in Polymer Science and Technology Report, October, 1984.

[4] Fardshisheh, F. and E.T. Onat, **Problems in Plasticity**, ed. A. Sawczuk, Noordhoff, Leyden, 1972, p.89.

[5] Wang, M.C. and E.J. Guth, J. Chem. Phys., 1952, **20**, p.1144.

[6] Haward, R.N., Coll. and Poly. Sci., 1980, **258**, No. 6, p.42.

[7] Haward, R.N., **The Physics of Glassy Polymers**, App. Sci. Pub., Essex, England, 1973.

[8] Rabinowitz, S., Ward, I.M., and J.S.C. Perry, J. Mat. Sci., 1970, **5**, p.29.

[9] Spitzig, W.A. and O. Richmond, Poly. Engr. Sci., 1979, **19**, p.1129.

[10] Sauer, J.A., Pae, K.D., and S.K. Bhateja, J. Macromol. Sci.-Phys., 1973, **B8**, p.631.

[11] Argon, A.S. and M.I. Bessonov, Phil. Mag., 1977, **35** p.917.

[12] Hope, P.S., Ward, I.M., and A.G. Gibson, J. Mat. Sci., 1980, **15**, p.2207.

[13] Hope, P.S., Duckett, R.A., and I.M. Ward, J. App. Poly. Sci., 1980, **25**, p. 1373.

[14] Ferry, J.D., **Viscoelastic Properties of Polymers**, J. Wiley and Sons, N.Y, 1962.

[15] Kahar, N., Duckett, R.A., and I.M. Ward, Polymer, 1978, **19**, p.136.

[16] Hibbitt, H.D., Nuc. Engr. Design, 1984, **77**, p.271. Also, ABAQUS User Manual, HKS, Inc., Providence, RI.

[17] Argon, A.S., Megusar, J., and N.J. Grant, *Scripta Met*, **19**, 1985, p.591.

[18] Rivlin, R.S., Thomas, A.G., *Eng. Frac. Mech.*, **18**, 1983, p.389.

[19] Green, M.S., Tobolsky, A.V., *J. Chem. Phys.*, **14**, 1946, p.80.

[20] James, H.M., Guth, E., *J. Chem. Phys.*, **11**, 1943, p.455.

[21] Brandrup, J., Immergut, E.H., eds., **Polymer Handbook**, Wiley and Sons, NY, 1975.

[22] Weast, R.C., **Handbook of Chemistry and Physics**, Chem. Rubber Co., Cleveland, 1973.

[23] Treloar, L.R.G., **The Physics of Rubber Elasticity, Third Ed.**, Clarendon, Oxford, 1975.

[24] Hadley, D.W., *Small Strain Elastic Properties*, Ch. 9 of **Structure and Properties of Oriented Polymers**, ed. Ward, I.M., App. Sci. Pub. Ltd., London, 1975.

[25] Wright, H., Faraday, C.S.N., White, E.F.T., and Treload, L.R.G., *J. Phys. D*, **4**, 1971, p.2002.

[26] Duckett, R.A., *Anisotropic Yield Behavior*, Ch. 11 of **Structure and Properties of Oriented Polymers**, ed. Ward, I.M., App. Sci. Pub. Ltd., London, 1975.

[27] Rider, J.G., Hargreaves, E., *J. Pol. Sci., Part A-2*,**7**, 1969, p.829.

[28] Brown, N., Ward, I.M., *Phil. Mag.*, **18**, 1968, p.961.

[29] Duckett, R.A., Goswami,B.C., Ward, I.M., *J. Poly. Sci., Pol. Phys. Ed.*, **10**, 1972, p.2167.

[30] Rice, J.R., **Proceedings of the 14th International Congress of Theoretical and Applied Mechanics, Vol. I**, p.207, North-Holland, Amsterdam, 1976.

[31] Rudnicki, J.W., Rice, J.R., *J. Mech. Phys. Solids*,**23**, 1975, p.371.

[32] Anand, L., Kim, K.H., Shawki, T.G., 1986, submitted to *J. Mech. Phys. Sol.*.

[33] Tvergaard, V., Needleman, A., Lo, K.K., *J. Mech. Phys. Solids*, **29**, 1981, p.115.

[34] Anand, L., Spitzig, W.A., *Acta Met.*, **30**, 1982, p.553.

[35] Rawson, F.F. and Rider, J.G.,*J. Poly. Sci., Part C*, No. 33, 1971, p.87.

[36] Rider, J.G., Hargreaves, E., *J. Phys. D: App. Phy.*, **3**, 1970, p.993.

[37] Brown, N., Duckett, R.A., Ward, I.M., *Phil. Mag.*, **18**, 1968, p. 483.

[38] Hill, R., **The Mathematical Theory of Plasticity**, Oxford University Press, Oxford, 1983, p.318.

[39] Lee, E.H.,*ASME Jnl. App. Mech.*, **36**, 1969, p.1.

[40] Loret, B., *Mech. of Mat.*, **2**, 1983, p.287.

[41] Asaro, R.J., *Micromechanics of Crystals and Polycrystals*, in **Advances in Applied Mechanics, Vol. 23**, 1983, Academic Press, NY.

[42] Asaro, R.J., Needleman, A., *Acta Met.*, **33**, 1985, p.923.

[43] Onat, E.T., *Representation of Inelastic Behavior in the Presence of Anisotropy and Finite Deformations*, Ch. 5 of **Recent Advances in Creep and Fracture of Engineering Materials and Structures**, 1982, Pineridge Press, Swansea, U.K.

[44] Anand, L., *Int. Jnl. of Plast.*, **1**, 1985, p.213.

[45] Dafalias, Y.F., *ASME Jnl. App. Mech.*, **52**, 1985, p.825.

[46] Pierce, D., Asaro, R.J., Needleman, A., *Acta Met.*, **31**, 1983, p.1951.

[47] Chapman, A.J., **Heat Transfer**, MacMillan Pub. Co., 1974.

[48] Schramm, R.E., Clark, A.F., Reed, R.P., eds., **NBS Monograph 132**, US Gov. Print. Off., Washington, 1973.

[49] Hughes, T.J.R., Winget, J., *Int. J. Num. Meth. Eng.*, **15**, 1980, p.1862.

[50] Kramer, E.J., *J. App. Phys.*, **41**, 1970, p.4327.

[51] Nagtegaal, J.C., Parks, D.M., Rice, J.R., *Comp. Meth. Appl. Mech. Eng.*, 4, 1974, p.153.

[52] Havner, K.S., **Mechanics of Solids: The Rodney Hill 60th Ann. Vol.**, p.265, eds. Hopkins, H.G., Sewell, M.J., Pergamon Press, 1982.

[53] Pierce, D., Shih, C.F., Needleman, A., *Comp. and Struc.*, 18, 1984, p.875.

Appendix A

Numerical Implementation of Constitutive Model

The constitutive model detailed in this thesis has been incorporated into the general-purpose non-linear finite element code ABAQUS [16]. This code permits the user the flexibility of specifying his own constitutive law through a "user material" subroutine option. The user is provided with the deformation gradient, $\mathbf{F}_t$, the Kirchhoff stress tensor, $\mathbf{S}_t$, and any user-defined state variables; in our case, the intrinsic yield strength, s_t, and the back stress tensor, $\mathbf{B}_t$, at the beginning of an increment. An estimate for the kinematic solution for the increment is provided with the deformation gradient at $t + \Delta t$, $\mathbf{F}_{t+\Delta t}$. In his user material subroutine, UMAT, the user must update the stress tensor and any other state variables. For this particular material model, we begin with the state of the material at time t: ($\mathbf{S}_t$, s_t, $\mathbf{B}_t$). We note that, numerically, due to our unique $\mathbf{F} = \mathbf{F}^e\mathbf{F}^p$ decomposition where $\mathbf{F}^{eT} = \mathbf{F}^e$, $\mathbf{F}_t^e$ can be found from $\mathbf{S}_t$ and, therefore, $\mathbf{F}_t^p$ is also known. Since the back stress is uniquely related to the plastic deformation gradient, $\mathbf{B}_t$ is also known. Therefore, we can find the complete state of the material $(\mathbf{S}, s, \mathbf{B})$ simply by knowing $(\mathbf{F}, \mathbf{S}, s)$ and it is not necessary to store $\mathbf{B}_t$. With this knowledge and the kinematics $\mathbf{F}_{t+\Delta t}$, we can integrate our constitutive equations

to obtain the state of the material at time $t + \Delta t$: $(\mathbf{S}_{t+\Delta t}, s_{t+\Delta t}, \mathbf{B}_{t+\Delta t})$. After the integration of the material state is successfully completed, the Jacobian, or the change in the increment in Kirchhoff stress with respect to a virtual change in the increment in strain, must be computed. This quantity is needed in ABAQUS in its overall Newton scheme to achieve a more accurate assessment of the kinematics. In order to obtain optimum convergence, the Jacobian should be 100% consistent with the integration operator. However, in our case the stress and back stress are computed from the total quantities of the elastic and plastic deformation gradients, respectively. The Jacobian is computed from incremental quantities which are needed in the integration of state. Thus, it was found to be easier to obtain a Jacobian derived from the rate quantities associated with the increment rather than an increment in the total quantities which must be converged upon in the actual integration scheme. This appendix will discuss the numerical integration of the material state and the computation of the Jacobian. A listing of the resulting FORTRAN program UMAT written to be used in conjunction with ABAQUS is also included at the end of this appendix.

A.1 Numerical Integration of State

In our integration of state, we first note that this is a large deformation analysis, and, therefore, we must account for any effects finite rotations may have on the integration. This is done by using an algorithm developed by Hughes and Winget [49] which is, in a certain sense, objective with respect to large rotations. In this algorithm, the state at time t is rotated to an intermediate configuration from which the material response of the stress increment is computed:

$$\begin{array}{ll} \mathbf{T}_{t+\Delta t} = \tilde{\mathbf{T}} + \Delta\mathbf{T}; & (a) \\ \tilde{\mathbf{T}} = \mathbf{Q}_{HW}\mathbf{T}_t\mathbf{Q}_{HW}^T; & (b) \\ \mathbf{Q}_{HW} = [\mathbf{I} - \frac{1}{2}\mathbf{W}\Delta t]^{-1}[\mathbf{I} + \frac{1}{2}\mathbf{W}\Delta t]; & (c) \\ \Delta\mathbf{T} = \mathcal{L}^e[(\mathbf{D} - \mathbf{D}^p)\Delta t]; & (d) \end{array} \tag{A.1}$$

where $\mathbf{W}\Delta t$ is, in fact, a function of $\mathbf{F}_{t+\Delta t}$ and $\mathbf{F}_t$:

$$\mathbf{W} = skew[\frac{\mathbf{F}_{t+\Delta t} - \mathbf{F}_t}{\Delta t}][\frac{\mathbf{F}_{t+\Delta t} + \mathbf{F}_t}{2}]^{-1}. \tag{A.2}$$

The stress tensor passed into the UMAT subroutine through the ABAQUS interface is the rotated stress tensor, $\tilde{\mathbf{S}} = J\tilde{\mathbf{T}}$. The tilde is used to signify a quantity at time t rotated to this intermediate state. The orthogonal transformation of the tensors $\mathbf{T}, \mathbf{F}, \mathbf{F}^e, \mathbf{F}^p$ are taken as :

$$\begin{array}{lll} \mathbf{T} & \rightarrow & \mathbf{Q}\mathbf{T}\mathbf{Q}^T, \quad (a) \\ \mathbf{F} & \rightarrow & \mathbf{Q}\mathbf{F}, \quad (b) \\ \mathbf{F}^e & \rightarrow & \mathbf{Q}\mathbf{F}^e\mathbf{Q}^T, \quad (c) \\ \mathbf{F}^p & \rightarrow & \mathbf{Q}\mathbf{F}^p. \quad (d) \end{array} \tag{A.3}$$

The stress tensor has been transformed to the intermediate configuration before entering UMAT; however, the deformation gradient, $\mathbf{F}_t$, has not been rotated. Therefore, the first step in the integration is to rotate $\mathbf{F}$, $\mathbf{F}^e$, $\mathbf{F}^p$ to the intermediate configuration via the transformation rule of (A.3). With all of the tensor quantities appropriately transformed, we now compute the material response portion of the stress increment.

An implicit integration scheme is used to obtain the new state and converge on $\mathbf{F}^p_{t+\Delta t}$. Therefore, we begin by iterating on $\mathbf{F}^p_{t+\Delta t}$ to achieve the final state:

$$\mathbf{F}^{pi+1}_{t+\Delta t} = \tilde{\mathbf{F}}^p_t + \dot{\mathbf{F}}^{pi}_{t+\Delta t}\Delta t, \tag{A.4}$$

where $\tilde{\mathbf{F}}^p_t$ is the plastic deformation gradient at time t rotated by the Hughes-Winget(HW) rotation matrix, $\mathbf{Q}_{HW}$, to the intermediate configuration:

$$\tilde{\mathbf{F}}^p_t = \mathbf{Q}_{HW}\mathbf{F}^p_t. \tag{A.5}$$

The superscripts i and $i+1$ denote the iteration number for this variable. The values for all variables at the first iteration are taken to be their values at time t. An expression for the change in plastic deformation gradient, $\dot{\mathbf{F}}^p_{t+\Delta t}\Delta t$, is found by beginning with the definition of the plastic velocity gradient:

$$\mathbf{L}^p = \dot{\mathbf{F}}^p \mathbf{F}^{p-1} = \mathbf{D}^p + \mathbf{W}^p, \tag{A.6}$$

or,

$$\dot{\mathbf{F}}^p = \left(\mathbf{D}^p + \mathbf{W}^p\right) \mathbf{F}^p. \tag{A.7}$$

We note here that $\mathbf{W}^p = \mathbf{W} - \mathcal{W}\left(\mathbf{D} + \mathbf{D}^p\right)$ and the rotation resulting from the spin $\mathbf{W}$ has been accounted for in the HW intermediate rotation on $\mathbf{F}^p_t$. Therefore, for our integration purposes $\mathbf{W}^p = -\mathcal{W}\left(\mathbf{D} + \mathbf{D}^p\right)$. We make a further observation by noting that $\mathcal{W}$ is of order ϵ^e, and, therefore, $\mathbf{W}^p$ is of order $\epsilon^e(\mathbf{D} + \mathbf{D}^p)$. For problems of interest, terms of order ϵ^e are negligible compared to terms of order unity and will, in general, be neglected in both the numerical updating of variables as well as the calculation of the Jacobian which is discussed later in this appendix. Therefore, we may neglect the term $\mathbf{W}^p$ with respect to the $\mathbf{D}^p$ term in equation (A.7) remembering that the "W-portion" of $\mathbf{W}^p$ is already accounted for in the $\tilde{\mathbf{F}}^p_t$ term. The equation to update $\mathbf{F}^p_{t+\Delta t}$ is now given by:

$$\mathbf{F}^{p(i+1)} = \tilde{\mathbf{F}}^p_t + \mathbf{D}^{p(i)} \mathbf{F}^{p(i)} \Delta t, \tag{A.8}$$

where, for convenience, the subscripts $t + \Delta t$ have been dropped and will be used only if needed for clarity.

The rate of plastic deformation at time $t + \Delta t$ must now be found and is calculated by:

$$\mathbf{D}^p = \dot{\gamma}^p \mathbf{N}, \tag{A.9}$$

where the tensor direction N is given by:

$$\begin{aligned} \mathbf{N} &= \mathbf{T}^{*\prime}/\sqrt{2}\tau, \\ \tau &= \sqrt{\tfrac{1}{2}\mathbf{T}^{*\prime}\mathbf{T}^{*\prime}}, \\ \mathbf{T}^{*\prime} &= \left(\mathbf{T} - \tfrac{1}{J}\mathbf{F}^e\mathbf{B}\mathbf{F}^e\right)', \end{aligned} \tag{A.10}$$

and the plastic shear strain rate is given by:

$$\dot{\gamma}^p = \dot{\gamma}_0 exp\left[-\frac{A}{\Theta}(s+\alpha p)\left(1-\left(\frac{\tau}{s+\alpha p}\right)^{\frac{s}{q}}\right)\right]. \tag{A.11}$$

The intrinsic shear strength, s, must simultaneously be updated as follows:

$$s_{t+\Delta t}^{(i+1)} = s_t + \dot{s}_{t+\Delta t}^{(i)} \Delta t, \tag{A.12}$$

where,

$$\dot{s}_{t+\Delta t}^{(i+1)} = h\left(1 - \frac{s_{t+\Delta t}^{(i)}}{s_{ss}}\right)\dot{\gamma}_{t+\Delta t}^{p(i)}. \tag{A.13}$$

The pressure is obtained from the stress tensor:

$$p = -\frac{1}{3} tr\,(\mathbf{T}). \tag{A.14}$$

The above equations are all needed to calculate $\mathbf{D}^p$ at each iteration. After the new guess for the plastic deformation gradient, $\mathbf{F}^{p(i+1)}$, is computed, the corresponding elastic deformation gradient is found from:

$$\mathbf{F}^{e(i+1)} = \mathbf{F}[\mathbf{F}^{p(i+1)}]^{-1} \tag{A.15}$$

The Cauchy stress tensor is then computed:

$$\mathbf{T}^{(i+1)} = \frac{1}{J}\mathcal{L}^e\left[ln\mathbf{F}^{e(i+1)}\right]. \tag{A.16}$$

Then the back stress tensor:

$$\mathbf{B}^{(i+1)} = f(\mathbf{V}^{p(i+1)}), \tag{A.17}$$

and, from the above, the driving stress tensor is found:

$$\mathbf{T}^{\prime(i+1)} = \left[\mathbf{T}^{(i+1)} - \frac{1}{J}\mathbf{F}^{e(i+1)}\mathbf{B}^{(i+1)}\mathbf{F}^{e(i+1)}\right]^{\prime}, \tag{A.18}$$

and the effective equivalent shear stress:

$$\tau^{(i+1)} = \sqrt{\frac{1}{2}\mathbf{T}^{\prime(i+1)}\mathbf{T}^{\prime(i+1)}}. \tag{A.19}$$

The plastic shear strain rate, $\dot{\gamma}^p$, and the intrinsic shear strength, s, are now computed from equations (A.11-A.13). The new rate of plastic deformation is now found and used in equation (A.8) and the procedure repeats itself. At the beginning of each iteration, the new tensor $\mathbf{F}^{p(i+1)}$ is compared with the "old" or previous tensor, $\mathbf{F}^{p(i)}$. When all components are within a tolerance of 0.0001 of their previous values, we have converged on the new state of the material. This generally takes less than 6 iterations. If more iterations are required for convergence, the increment is started over with a smaller time step.

After the new state of the material is successfully computed, the Jacobian must be calculated and passed back to ABAQUS. This tensor is used in the main program to determine the kinematical correction to the virtual work equilibrium for the next iteration and is, therefore, an important factor in increasing the rate of convergence of the problem.

In the computation of the Jacobian for this constitutive model, liberal use is made of the assumption that the elastic strains are small in order to simplify the format of the Jacobian.

A.2 Computation of the Jacobian

The Jacobian, J, is the fourth order tensor obtained by finding the change in the increment in Kirchhoff stress, $\mathbf{S} = J\mathbf{T}$, with respect to a virtual change in the increment in strain:

$$J = \frac{\partial \triangle \mathbf{S}}{\partial \triangle \epsilon}. \tag{A.20}$$

We note that the increment in strain over a step in time, $\triangle t$, is essentially equal to the rate of deformation multiplied by the length of the time increment, $\mathbf{D}\triangle t$. Therefore, the Jacobian can be found by computing:

$$J = \frac{\partial \triangle \mathbf{S}}{\partial \mathbf{D} \triangle t}. \tag{A.21}$$

We begin the calculation of this quantity by recognizing that the increment in Kirchhoff stress can be broken down into its deviatoric and dilatational components:

$$\triangle \mathbf{S} = 2\mu \left[\mathbf{D}\triangle t - \mathbf{D}^p \triangle t\right] + \left[K tr(\mathbf{D}\triangle t) - 3K\alpha_\theta \triangle \Theta\right]\mathbf{1}, \tag{A.22}$$

where, μ is the shear modulus; K is the bulk modulus; α_θ is the linear coefficient of thermal expansion; $\mathbf{D}\triangle t$ is the increment in strain; and $\mathbf{D}^p \triangle t$ is the increment in plastic strain. We will derive the Jacobian in a manner similar to the forward gradient scheme of reference [53].

Working on the deviatoric portion, we can write:

$$(\mathbf{D}\triangle t)' = \frac{1}{2\mu}\triangle \mathbf{S}' + \mathbf{D}^p \triangle t. \tag{A.23}$$

The amount of plastic strain over the increment, $\mathbf{D}^p \triangle t$, may be approximated as:

$$\mathbf{D}^p \triangle t = \left[\mathbf{D}^p_t + d\mathbf{D}^p\right] \triangle t, \tag{A.24}$$

where $\mathbf{D}_t^p$ is the rate of plastic deformation at time t, and $d\mathbf{D}^p$ is the change in this rate over the increment. The quantity $d\mathbf{D}^p$ may be found by invoking the chain rule of differentiation on the expression for $\mathbf{D}^p$. We first recall this expression for $\mathbf{D}^p$ to be:

$$\mathbf{D}^p = \dot{\gamma}^p \mathbf{N}, \tag{A.25}$$

which, in expanded form, is:

$$\mathbf{D}^p = \dot{\gamma}_0 exp\left[-\frac{A}{\Theta}(s+\alpha p)\left[1-\left(\frac{\tau}{s+\alpha p}\right)^{\frac{5}{6}}\right]\right]\frac{\mathbf{T}^{*\prime}}{\sqrt{2}\tau}. \tag{A.26}$$

The change in this rate is then found to be:

$$d\mathbf{D}^p = d\dot{\gamma}^p \mathbf{N} + \dot{\gamma}^p d\mathbf{N}, \tag{A.27}$$

where the change in the direction, $d\mathbf{N}$, is given by:

$$d\mathbf{N} = [I - \mathbf{N}\otimes\mathbf{N}]\frac{1}{\sqrt{2}\tau} d\mathbf{T}^{*\prime}, \tag{A.28}$$

and the change in the plastic shear strain rate, $d\dot{\gamma}^p$, is found by:

$$d\dot{\gamma}^p = \frac{\partial\dot{\gamma}^p}{\partial\tau}d\tau + \frac{\partial\dot{\gamma}^p}{\partial p}dp + \frac{\partial\dot{\gamma}^p}{\partial s}ds + \frac{\partial\dot{\gamma}^p}{\partial\Theta}d\Theta. \tag{A.29}$$

Equation (A.29) is now examined term by term. The first term, $\frac{\partial\dot{\gamma}^p}{\partial\tau}d\tau$, is given by:

$$C_1 \equiv \frac{\partial\dot{\gamma}^p}{\partial\tau} = \dot{\gamma}^p \frac{5}{6}\frac{A}{\Theta}\left(\frac{\tau}{s+\alpha p}\right)^{-\frac{1}{6}}, \tag{A.30}$$

$$d\tau = \frac{1}{2\tau}\mathbf{T}^{*\prime}\cdot d\mathbf{T}^{*\prime}. \tag{A.31}$$

The second term, $\frac{\partial\dot{\gamma}^p}{\partial p}dp$, is given by:

$$C_2 \equiv \frac{\partial\dot{\gamma}^p}{\partial p} = \dot{\gamma}^p \frac{A}{\Theta}\alpha\left[-1+\frac{1}{6}\left(\frac{\tau}{s+\alpha p}\right)^{\frac{5}{6}}\right], \tag{A.32}$$

$$dp = -Ktr(d\mathbf{D}\Delta t) + 3K\alpha_\theta d\Delta\Theta. \tag{A.33}$$

The third term, $\frac{\partial \dot{\gamma}^p}{\partial s} ds$, is given by:

$$C_3 \equiv \frac{\partial \dot{\gamma}^p}{\partial s} = \dot{\gamma}^p \frac{A}{\Theta} \left[-1 + \frac{1}{6} \left(\frac{\tau}{s + \alpha p} \right)^{\frac{5}{6}} \right], \tag{A.34}$$

where ds is found from equation (A.13) giving:

$$ds = \left[1 + \frac{h \dot{\gamma}^p \Delta t}{s_{ss}} \right]^{-1} \left[h \left(1 - \frac{s}{s_{ss}} \right) d\dot{\gamma}^p \Delta t \right]. \tag{A.35}$$

The fourth term, $\frac{\partial \dot{\gamma}^p}{\partial \Theta} d\Theta$, is given by:

$$C_4 \equiv \frac{\partial \dot{\gamma}^p}{\partial \Theta} = \dot{\gamma}^p \left[\frac{A}{\Theta^2} (s + \alpha p) \left[1 - \left(\frac{\tau}{s + \alpha p} \right)^{\frac{5}{6}} \right] - \frac{A}{\Theta} \left[1 - \frac{1}{6} \left(\frac{\tau}{s + \alpha p} \right)^{\frac{5}{6}} \right] \frac{\partial s}{\partial \Theta} \right], \tag{A.36}$$

where $d\Theta$ is a load increment. An increment in temperature due to adiabatic heating at large strain rates is incorporated in a separate version of the UMAT. After incorporating equations (A.31-A.38) into equation (A.30), we obtain:

$$d\dot{\gamma}^p = C_5 \left[C_1 \frac{1}{2\tau} \mathbf{T}^{*\prime} \cdot d\mathbf{T}^{*\prime} - C_2 K \mathbf{I} \cdot \mathbf{D} \Delta t + C_4 d\Theta \right], \tag{A.37}$$

where,

$$C_5 = \left[1 - C_3 \left(1 - \frac{h \dot{\gamma}^p \Delta t}{s_{ss}} \right)^{-1} h \left(1 - \frac{s}{s_{ss}} \right) \Delta t \right]^{-1}. \tag{A.38}$$

Substituting equations (A.28) and (A.37) into equation (A.27), an expression for $d\mathbf{D}^p$ is now obtained:

$$d\mathbf{D}^p = \frac{1}{\sqrt{2}} \left[\frac{\dot{\gamma}^p}{\tau} I + \left(C_5 C_1 - \frac{\dot{\gamma}^p}{\tau} \right) \mathbf{N} \otimes \mathbf{N} \right] d\mathbf{T}^{*\prime} + \left[C_5 C_2 dp + C_5 C_4 d\Theta \right] \mathbf{N}. \tag{A.39}$$

We calculate the change in the driving stress state, $d\mathbf{T}^{*\prime}$, from equation (A.10c) which gives:

$$d\mathbf{T}^{*\prime} = \frac{1}{J} \left[d\mathbf{S}^{\prime} - \mathbf{F}^e d\mathbf{B} \mathbf{F}^e + O(d\epsilon^e) \right] - \frac{1}{J} \mathbf{D} \Delta t \mathbf{T}^{*\prime}. \tag{A.40}$$

An expression for $d\mathbf{B}$ is now needed and may be approximated as $\dot{\mathbf{B}} \Delta t$, where $\dot{\mathbf{B}}$ is given by:

$$\dot{\mathbf{B}} = \mathbf{B}^{\nabla} - \mathbf{W}^{p}\mathbf{B} + \mathbf{B}\mathbf{W}^{p}, \tag{A.41}$$

and $\mathbf{B}^{\nabla}$ is given by:

$$\mathbf{B}^{\nabla} = \mathcal{L}^{R}\left[\mathbf{D}^{p}\right], \tag{A.42}$$

where $\mathcal{L}^{R}$ is the fourth order hardening modulus tensor derived from our back stress definition and defined in reference [3]. It is now noted that we are incrementing from the the HW intermediate state and, therefore, have already accounted for the rotational portion of $d\mathbf{B}$ due to the spin $\mathbf{W}$. We also neglect terms of order ϵ^{e}, thus finding the portion $\mathcal{W}\left(\mathbf{D}+\mathbf{D}^{p}\right)$ of the rotation to make a negligible contribution to the integration as discussed earlier. Therefore, $d\mathbf{B}$ may be approximated by:

$$d\mathbf{B} \simeq \mathbf{B}^{\nabla}\Delta t \simeq \mathcal{L}^{R}\left[\mathbf{D}^{p}\Delta t\right] \simeq \mathcal{L}^{R}\left[\mathbf{D}_{t}^{p} + d\mathbf{D}^{p}\right]\Delta t. \tag{A.43}$$

Incorporating these equations for $d\mathbf{T}^{*\prime}$ and $d\mathbf{B}$ into the expression for $d\mathbf{D}^{p}$ and neglecting terms of order ϵ^{e} compared to unity, we obtain:

$$\begin{aligned} &d\mathbf{D}^{p} = \\ &\mathcal{F}\left[d\mathbf{S}' - \mathcal{L}^{R}\left[\mathbf{D}_{t}^{p} + d\mathbf{D}^{p}\right]\Delta t - \mathbf{I}\cdot\mathbf{D}\Delta t\mathbf{T}^{*\prime}\right] \\ &+\left(C_{5}C_{2}dp + C_{5}C_{4}d\Theta\right)\mathbf{N}; \end{aligned} \tag{A.44}$$

where,

$$\mathcal{F} = \frac{1}{\sqrt{2}J}\left[\frac{\dot{\gamma}^{p}}{\tau}I + \left(C_{5}C_{1} - \frac{\dot{\gamma}^{P}}{\tau}\right)\mathbf{N}\otimes\mathbf{N}\right]; \tag{A.45}$$

or,

$$\begin{aligned} &d\mathbf{D}^{p} = \\ &K^{-1}\mathcal{F}\left[d\mathbf{S}' - \mathcal{L}^{R}\left[\mathbf{D}_{t}^{p}\Delta t\right] - \mathbf{I}\cdot\mathbf{D}\Delta t\mathbf{T}^{*\prime}\right] \\ &+K^{-1}\left(C_{5}C_{2}dp + C_{5}C_{4}d\Theta\right)\mathbf{N}; \end{aligned} \tag{A.46}$$

where,

$$K = \left[I + \mathcal{F}\mathcal{L}^{R}\Delta t\right]. \tag{A.47}$$

This expression for $d\mathbf{D}^p$ is now substituted into equation (A.23) for $(\mathbf{D}\Delta t)'$:

$$\begin{aligned}
&(\mathbf{D}\Delta t)' = \\
&\tfrac{1}{2\mu}\Delta\mathbf{S}' + \mathbf{D}_t^p\Delta t \\
&+K^{-1}\tfrac{1}{\sqrt{2}J}\left[\tfrac{\dot\gamma^p\Delta t}{\tau}I + \left(C_5C_1\Delta t - \tfrac{\dot\gamma^p\Delta t}{\tau}\right)\mathbf{N}\otimes\mathbf{N}\right]\left[\Delta\mathbf{S}' - \mathcal{L}^R\left[\mathbf{D}_t^p\Delta t\right] - \mathbf{I}\cdot\mathbf{D}\Delta t\mathbf{T}^{*\prime}\right] \\
&+K^{-1}\left(C_5C_2\Delta t dp + C_5C_4\Delta t\Delta\Theta\right)\mathbf{N}.
\end{aligned} \tag{A.48}$$

Premultiplying both sides of the preceding equation and rearranging terms as well as dropping higher terms, such as terms of order $(\Delta\epsilon^p)^2$, an expression for $\mathbf{T}^{*\prime}\cdot\Delta\mathbf{S}'$ is obtained:

$$\begin{aligned}
&\mathbf{T}^{*\prime}\cdot\Delta\mathbf{S}' = \\
&m\mathbf{T}^{*\prime}\cdot(\mathbf{D}\Delta t)' - m\mathbf{D}_t^p\Delta t \\
&-\tfrac{1}{\sqrt{2}J}mC_5C_1\Delta t\mathbf{T}^{*\prime}\cdot\left[-\mathcal{L}^R\left[\mathbf{D}_t^p\Delta t\right] - \mathbf{T}^{*\prime}\otimes\mathbf{ID}\Delta t\right] \\
&-m\left(C_5C_2\Delta t dp + C_5C_4\Delta t d\Theta\right)\mathbf{T}^{*\prime}\cdot\mathbf{N},
\end{aligned} \tag{A.49}$$

where,

$$m = \left[\frac{1}{2\mu} + \frac{1}{\sqrt{2}J}C_5C_1\Delta t\right]^{-1} = \frac{2J\mu}{J + \sqrt{2}\mu C_5C_1\Delta t}. \tag{A.50}$$

These equations are now used to obtain an expression for the increment in the deviatoric portion of the Kirchoff stress, $\Delta\mathbf{S}'$, with respect to the deviatoric portion of the strain increment, $(\mathbf{D}\Delta t)'$:

$$\begin{aligned}
&\Delta\mathbf{S}' = \\
&2\bar\mu\left[I - \sqrt{2}\mu g\mathbf{N}\otimes\mathbf{N}\right](\mathbf{D}\Delta t)' \\
&+2\bar\mu\left[I - (\cdots)\mathcal{L}^R\right]\mathbf{D}_t^p\Delta t \\
&+2\bar\mu\left[\tfrac{\dot\gamma^p\Delta t}{J}I + \tau g\mathbf{N}\otimes\mathbf{N}\right]\mathbf{N}\otimes\mathbf{ID}\Delta t \\
&-2\bar\mu\left(C_5C_2\Delta t dp + C_5C_4\Delta t d\Theta\right)\left[I - \sqrt{2}\mu g\mathbf{N}\otimes\mathbf{N}\right]\mathbf{N},
\end{aligned} \tag{A.51}$$

where,

$$g = \frac{C_5C_1\Delta t - \frac{\dot\gamma^p\Delta t}{\tau}}{J + \sqrt{2}\mu C_5C_1\Delta t} \tag{A.52}$$

and,

$$2\bar\mu = \frac{2J\tau\mu}{J\tau + \sqrt{2}\mu\dot\gamma^p\Delta t}. \tag{A.53}$$

Now adding the dilatational portion of the stress increment by referring to equation (A.22) , we obtain:

$$\begin{aligned}
&\triangle \mathbf{S} = \\
&2\bar{\mu}\mathbf{D}\triangle t + \left(K - \tfrac{2}{3}\bar{\mu}\right)\mathbf{I}\otimes\mathbf{I}\mathbf{D}\triangle t - 3K\alpha_\theta d\Theta\mathbf{I} \\
&+\left[I - (\cdots)\mathcal{L}^R\right]\mathbf{D}^p_t\triangle t \\
&-2\sqrt{2}\bar{\mu}\mu g\mathbf{N}\otimes\mathbf{N}\mathbf{D}\triangle t \\
&+2\bar{\mu}\left[\tfrac{\dot{\gamma}^p\triangle t}{J}I + \tau g\mathbf{N}\otimes\mathbf{N}\right]\mathbf{N}\otimes\mathbf{I}\mathbf{D}\triangle t \\
&-2\bar{\mu}\left(-C_5C_2\triangle tK\mathbf{I}\cdot\mathbf{D}\triangle t + C_5C_4\triangle t d\Theta\right)\left[I - \sqrt{2}\mu g\mathbf{N}\otimes\mathbf{N}\right]\mathbf{N}.
\end{aligned} \tag{A.54}$$

Finally, for the Jacobian, we obtain:

$$\begin{aligned}
&J \equiv \tfrac{\partial\triangle\mathbf{S}}{\partial\mathbf{D}\triangle t} \\
&= 2\bar{\mu}I + \left(K - \tfrac{2}{3}\bar{\mu}\right)\mathbf{I}\otimes\mathbf{I} - A\mathbf{N}\otimes\mathbf{N} + B\mathbf{N}\otimes\mathbf{I},
\end{aligned} \tag{A.55}$$

where,

$$A = 2\sqrt{2}\bar{\mu}\mu g, \tag{A.56}$$

$$B = 2\bar{\mu}\left[\frac{\dot{\gamma}^p\triangle t}{J} + C_5C_2\triangle tK + g\left(\tau - \sqrt{2}\mu C_5C_2\triangle tK\right)\right]. \tag{A.57}$$

A.3 Listing of UMAT Subroutine

The above integration scheme and Jacobian for the constitutive model describing the large inelastic deformation of amorphous polymers has been coded into a FORTRAN program to be used in conjunction with the finite element code ABAQUS [16]. The following pages contain a listing of that program. Those subroutines of ABAQUS which were modified in order to obtain the Hughes-Winget rotation matrix and the deformation gradient at the beginning and end of the increment for each material point are also listed. These were from ABAQUS version 4.5-159.

```
      SUBROUTINE UMAT(STRESS,STATEV,DDSDDE,SSE,SPD,SCD,STRAN,
     1 DSTRAN,TIME,DTIME,TEMP,DTEMP,PREDEF,DPRED,MATERL,NDI,NSHR,
     2 NTENS,NSTATV,PROPS,NPROPS,COORDS)
        IMPLICIT REAL*8(A-H,O-Z)
        DIMENSION STRESS(NTENS),STATEV(NSTATV),DDSDDE(NTENS,NTENS),
     1  STRAN(NTENS),DSTRAN(NTENS),PREDEF(1),DPRED(1),PROPS(NPROPS)
     2  , COORDS(3)
       DIMENSION RSTR(3,3),SIGB(3,3),TF(3,3),TSIG(3,3),TFE(3,3),
     1 TFP(3,3),TSIGB(3,3),TSGSTP(3,3),TDP(3,3),TDTSTP(3,3),
     2 TDTF(3,3),TDTFE(3,3),TDTFP(3,3),TDTSIG(3,3),TDTSGB(3,3)
       COMMON/CERROR/RESMAX(30),JNREMX(30),ERRMAX(2),CETOL,CSLIM,
     1  CEMAX,PCTOL,TLIMIT,PSUBIN,RESMIN,DUMAX(30),JNDUMX(30),ERRPRE,
     2  UDELSS,PTOL,AMTOL,DMKET,DMRETL,SIGTOL,DSIGMX,UTOL,UMAX,U4MAX,
     3  VMAX,V4MAX,AMAX,A4MAX,TMAX,EPPMAX,RMAX,R4MAX,NGOPEN,NGCLOS,
     4  ROTTOL,ROTFAC,JRIKND,NINOCS,RIKUB,RIKUMX,RIKMU,RIKLAM,RIKDLA,
     5  RIKRO,RIKOLD,RIKLMX,QMAX,DUMAXP,STRRAT,PCUT,RIKDLO
        COMMON/ROTSTR/RSTR
        COMMON/DEFGRAD/TDTF,TF
        COMMON/MECHPROP/EYONG,GNU,N,CR,ALF
        COMMON/RATE/A1,GAMDOT0
        COMMON/RATEPROP/RATEC1,RATEC2,RATEC3
        COMMON/SOFT/S0,SSS,H,ST
        COMMON/TOL/EMAX,ETOL
        COMMON/TEMPER/TEMPG,XM1,XM2,XX1,XX2,XY1,XY2,XX3,RSG
        COMMON/TEMP11/XTEMP,XDTEMP,TEMPTDT,TEMP0,TALF
        DATA RSTR/1.D0,0.D0,0.D0,0.D0,1.D0,0.D0,0.D0,0.D0,1.D0/
C***************************************************************
C
C  THIS UMAT IS FOR THE LARGE INELASTIC DEFORMATION OF GLASSY POLYMERS
C  AND ACCOUNTS FOR RATE, TEMPERATURE, PRESSURE, TRUE STRAIN-SOFTENING
C  AND STRAIN HARDENING EFFECTS.
C
C  ALL SUBROUTINES WERE WRITTEN BY MARY BOYCE UNLESS OTHERWISE
C  DESIGNATED TO BE WRITTEN BY BHARAT BAGEPALLI
C
C***************************************************************
C  MATERIAL PROPERTIES
C************************
C PROPS(1)=COEFFICIENT OF THERMAL EXPANSION=TALF
C PROPS(2)=POISSON'S RATIO
C PROPS(3)=CR=nKT
C PROPS(4)=N
C PROPS()=GAMDOT0
C PROPS(6)=A OF GAMDOTP=GAMDOT0*EXP( (A/TEMP)*S(1-(TAU/S)**(5/6)))
C PROPS(7)=PERCENT DIFFERENCE IN INTRINSIC YIELD STRENGTH = RATIO OF
C              SSS TO S0
C PROPS(8)=H COEFFICIENT OF EVOLUTION EQUATION FOR S;
C              SDOT=H*(1-S/SSS)*GAMDOTP
C PROPS(9)=PRESSURE COEFFICIENT OF PRESSURE DEPENDENT YIELD = ALF
C            SIGMAY=SIGMAY0+ALF*PRESSURE
C PROPS(10)=TEMP0=ORIGINAL TEMP
C
C***************************************************************
        XTEMP=TEMP
        XDTEMP=DTEMP
        TALF=PROPS(1)
        RMTEMP=298.D0
        TEMP0=PROPS(10)
        TEMPTDT=TEMP+DTEMP
        EMAX=0.D0
        ETOL=2.D0*CETOL
        N=IDNINT(PROPS(4))
        CR=PROPS(3)*TEMPTDT/TEMP0
```

```
      GNU=PROPS(2)
      EN=PROPS(4)
C*************************************
C  TEMPERATURE DEPENDENCE OF SHEAR MODULUS AND INTRINSIC YIELD
C  STRENGTH: PROPERTIES AND LINE EQUATION FOR POLYCARBONATE
C       IF ABSOLUTE TEMPTDT LT XX2  THEN
C          LOG(SHEAR MODULUS)= XM1*(TEMPTDT-XX1)+XY1
C       IF ABSOLUTE TEMPTDT GT XX1 BUT LT XX3
C          LOG(SHEAR MODULUS)= XM2*(TEMPTDT-XX2)+XY2
C       IF ABSOLUTE TEMPTDT GT XX3
C          LOG(SHEAR MODULUS)= XY2
C       XX2=TEMP  IMMEDIATELY(~15DEGREES) BEFORE TG
C       XX3=TEMP  IMMEDIATELY(~15DEGREES) AFTER TG
C
C       RSG=RATIO OF ORIGINAL ROOM TEMP INTRINSIC YIELD STRENGTH TO
C                ROOM TEMP SHEAR MODULUS
C*************************************
C PC TEMPERATURE PROPERTIES
C
CTEMPG=423D0
CXM1=-7.4835E-04
CXX1=158D0
CXY1=3.D0
CXM2=-.0938D0
CXX2=408D0
CXY2=2.813D0
CXY3=0D0
CXX3=438.D0
CRSG=0.11D0
C
C END OF PC PROPERTIES
C
C PMMA TEMPERATURE PROPERTIES
C
      TEMPG=383.D0
      XM1=-1.7974D-03
      XX1=363.D0
      XY1=2.89D0
      XM2=-5.69D-02
      XX2=373.D0
      XY2=2.845D0
      XX3=423.D0
      XY3=0.D0
      RSG=0.113D0
C
      IF(TEMPTDT.LT.XX2) SHR =  10**
     1   (XM1*(TEMPTDT-XX1)+XY1)
      IF(TEMPTDT.GE.XX2.AND.TEMPTDT.LT.XX3) SHR =
     1       10** (XM2*(TEMPTDT-XX2)+XY2)
      IF(TEMPTDT.GE.XX3) SHR = 10**XY3
      EYONG=2.D0*(1.D0+GNU)*SHR
C*************************************************************************
C RATE PROPERTIES
C*********************
C PROPS(5)=GAMDOT0
C PROPS(6)=A
C PROPS(7)=S0
C  where,
C   DP=GAMDOT0*EXP(-A1*S(1-((TAU/S)**(5/6)))*TSGSTP/(SQRT(2)*TAU)
C RATEC1=GAMDOT0*EXP(-A1*S)/SQRT(2)
C RATEC2=EXP(A1*S)
C RATEC3=5/6
C SO... DP=RATEC1*RATEC2**((TAU/S)**C3)*TSGSTP/TAU
```

```
C*****************************************************************
      GAMDOT0=PROPS(5)
      A1=PROPS(6)/TEMPTDT
C*****************************************************************
C SOFTENING PROPERTIES
C*************************
C S0=PROPS(7)-INITIAL INTRINSIC YIELD
C SSS=PROPS(8)-INTRINSIC YIELD AT STEADY STATE
C H=COEFFICIENT OF SOFTENING EVOLUTION LAW, WHERE DS/DT=H(1-S/SSS)GAMDOT
C ALF=COEFFICIENT FOR PRESSURE EFFECT ON INTRINSIC YIELD
C*****************************************************************
      S0=RSG*SHR
      SSS=PROPS(7)*S0
      H= PROPS(8)
      ALF=PROPS(9)
C*********************************************
C  ST = INTRINSIC YIELD AT TIME T
C*********************************************
      ST=STATEV(1)
      IF(TIME.EQ.0.D0) ST=S0
C*********************************************
C  P0 = PRESSURE AT TIME T
C*********************************************
      P0= - ( STRESS(1)+STRESS(2)+STRESS(3) )/3.D0
      RATEC1=GAMDOT0*DEXP(-A1*(ST+ALF*P0))/DSQRT(2.D0)
      RATEC2=DEXP(A1*(ST+ALF*P0))
      RATEC3=5.D0/6.D0
      SRT3=2.D0 / DSQRT(3.D0)
C
C CONVERT STRESS VECTOR TO MATRIX FORM
C
        TSIG(1,1)=STRESS(1)
        TSIG(2,2)=STRESS(2)
        TSIG(3,3)=STRESS(3)
        TSIG(1,2)=STRESS(4)
        TSIG(2,1)=STRESS(4)
        DO 2 I=1,2
        TSIG(I,3)=0.D0
        TSIG(3,I)=0.D0
    2   CONTINUE
C*****************************************************************
C   CHECK TO SEE THAT INTERMEDIATE ROTATION WAS COMPUTED IN MAIN PART
C   OF ABAQUS ( IN CURRENT VERSION, THIS IS NOT ALWAYS DONE ON FIRST
C   INCREMENT ). IF IT WAS NOT, THEN COMPUTE IT.
C*****************************************************************
      DO 3 I=1,3
    3 IF(RSTR(I,I).NE.1.D0) GO TO 6
      CALL ROTATE(RSTR,TSIG,TDTF,TF,DTIME)
    6 CONTINUE
C*****************************************************************
C GIVEN TF, TSIG AND RSTR COMPUTE INTERMEDIATE VALUES OF TFP AND TDP
C*****************************************************************
      CALL INITFP(RSTR,TF,TSIG,TFP,TDP,TAU0,P0)
C*****************************************************************
C       RESET INCREMENTAL ROTATION MATRIX TO IDENTITY
C*****************************************************************
       DO 8 I=1,3
       DO 8 J=1,3
      RSTR(I,J)=0.D0
      IF(I.EQ.J)RSTR(I,J)=1.D0
   8   CONTINUE
C*****************************************************************
C COMPUTE THE NEW STATE OF MATERIAL AT T+DTIME GIVEN THE TIME INCREMENT,
```

```
C TDP,TFP, AND TDTF
C*****************************************************************
        CALL NEWSTATE(DTIME,TDP,TFP,TDTF,TDTFE,TDTFP,TDTSIG,
     1  TDTSGB,TDTSTP,TAU,TDTS,PRES)
        IF(EMAX.GE.ETOL) THEN
          CEMAX=EMAX
          GO TO 207
        END IF
C*****************************************************************
C
C GIVEN THE NEW STATE, COMPUTE THE JACOBIAN (DDSDDE) NEEDED TO
C RETURN TO ABAQUS
C
C*****************************************************************
        CALL JACOB(TDTF,TDTSIG,TDTSTP,TAU,DTIME,DDSDDE,TDTS)
C*****************************************************************
C
C       SET THE UPDATED STRESS TO VECTOR FORM TO RETURN TO ABAQUS
C
C*****************************************************************
        STRESS(1)=TDTSIG(1,1)
        STRESS(2)=TDTSIG(2,2)
        STRESS(3)=TDTSIG(3,3)
        STRESS(4)=TDTSIG(1,2)
C*****************************************************************
C
C DEFINE STATE VARIABLES TO BE PRINTED OUT.  IN THIS CASE, THE PLASTIC
C DEFORMATION GRADIENT
C
C*****************************************************************
        STATEV(1)=TDTS
        STATEV(2)=TDTFP(1,1)
        STATEV(3)=TDTFP(2,2)
        STATEV(4)=TDTFP(1,2)
        STATEV(5)=TDTSGB(2,2)
C*****************************************************************
C
C CALCULATE ERROR PARAMETER FOR VISCO OPTION
C
C*****************************************************************
        GG1= STATEV(6)
        GG2 = RATEC1 * RATEC2** ( (TAU/(TDTS+ALF*PRES))**RATEC3 )
        STATEV(6)=GG2
        CEMAX= DTIME * DABS((GG1-GG2)) / SRT3
        DEPM=0.005D0
        DEP=DSQRT(2.D0)*GG2*DTIME
        RDEP=DEP/DEPM
        RCE=CEMAX/CETOL
        IF(RDEP.GT.RCE) CEMAX=RDEP*CETOL
C*****************************************************************
  207   RETURN
        END
C
        SUBROUTINE ROTATE(RSTR,TSIG,TDTF,TF,DTIME)
C*****************************************************************
C THIS SUBROUTINE COMPUTES THE INTERMEDIATE ROTATION MATRIX AND ROTATES
C THE STRESS TENSOR TO THIS INTERMEDIATE STATE
C*****************************************************************
        IMPLICIT REAL*8 (A-H,O-Z)
       DIMENSION RSTR(3,3),TSIG(3,3),TF(3,3),TDTF(3,3),FDOT(3,3),
     1 EL(3,3),X(3,3),W(3,3)
C************************
C COMPUTE TDTF INVERSE
```

```
C************************
      CALL INVRS(TDTF,X)
C************************
C COMPUTE FDOT
C************************
        DO 10 I=1,3
        DO 10 J=1,3
10    FDOT(I,J) = (TDTF(I,J)-TF(I,J))
C*****************************************
C COMPUTE THE VELOCITY GRAD = FDOT * F INVERSE
C*****************************************
      CALL MATMUL(FDOT,X,EL,3,3,3)
C*********************************************************
C COMPUTE THE HUGHES-WINGET INTERMEDIATE ROTATION MATRIX  *
C RSTR = (I-W*DTIME/2)INVERSE  * (I + W*DTIME/2)          *
C*********************************************************
        DO 20 I=1,3
        DO 20 J=1,3
      W(I,J) = (EL(I,J)-EL(J,I))/4.D0
      X(I,J)= -W(I,J)
      IF(I.EQ.J) X(I,J) = 1.D0 +X(I,J)
20    IF(I.EQ.J) W(I,J) = 1.D0 +W(I,J)
      CALL INVRS(X,EL)
      CALL MATMUL(EL,W,RSTR,3,3,3)
        DO 30 I=1,3
        DO 30 J=1,3
30    EL(I,J)=RSTR(J,I)
C*********************************************
C ROTATE THE STRESS TENSOR TO INTERMEDIATE STATE *
C TSIG = (RSTR TRANSPOSE) * TSIG * RSTR          *
C*********************************************
      CALL MATMUL(EL,TSIG,X,3,3,3)
      CALL MATMUL(X,RSTR,TSIG,3,3,3)
      RETURN
      END
      SUBROUTINE INITFP(RSTR,TF,TSIG,TFP,TDP,TAU,PRES)
C*****************************************************************
C THIS SUBROUTINE OBTAINS THE INITIAL CONDITIONS NEEDED TO       *
C UPDATE ALL THE VARIABLES.  THE VARIABLES NEEDED FOR THE        *
C ITERATION SCHEME ARE TFP AND TDP                               *
C*****************************************************************
      IMPLICIT REAL*8 (A-H,O-Z)
      DIMENSION RSTR(3,3),TF(3,3),TSIG(3,3),TFP(3,3),TDP(3,3)
     1 ,XTF(3,3),TFE(3,3),TSIGB(3,3),TSGSTP(3,3)
      COMMON/SOFT/SO,SSS,H,ST
      COMMON/TEMP11/TEMP,DTEMP,TEMPTDT,TEMP0,TALF
C**********************************
C OBTAIN THE DETERMINANT OF TF     *
C**********************************
      DT=TF(3,3)*(TF(1,1)*TF(2,2)-TF(1,2)*TF(2,1))
C**********************************
C ROTATE TF TO THE INTERMEDIATE STATE  *
C**********************************
      CALL MATMUL(RSTR,TF,XTF,3,3,3)
        DO 10 I=1,3
        DO 10 J=1,3
10    TF(I,J)=XTF(I,J)
C************************************************
C OBTAIN TFE FROM TSIG (THE INTERMEDIATE STRESS)  *
C************************************************
      CALL FESIG(TSIG,TFE,DT)
C*****************************************************************
C COMPUTE THE REMAINING VARIABLES                                 *
```

```
C       SUB UPDATE CALCULATES ALL REMAINING VARIABLES IF GIVEN TF,TFE,  *
C          AND TSIG                                                     *
C*************************************************************************
        CALL UPDATE(TF,TFE,TFP,TDP,TSIG,TSIGB,TSGSTP,TAU,ST,PRES)
C*************************************************************************
        RETURN
        END
C
        SUBROUTINE UPDATE(UF,UFE,UFP,UDP,USIG,USIGB,USGSTP,UTAU,SIM1
     1  ,PRES)
C*************************************************************************
C THIS SUBROUTINE CALCULATES UFP,UDP,USIGB,USGSTP,UTAU GIVEN UFE,UF,USIG
C*************************************************************************
        IMPLICIT REAL*8 (A-H,O-Z)
        DIMENSION UF(3,3),UFE(3,3),UFP(3,3),UDP(3,3),USIG(3,3)
     1  ,USIGB(3,3),USGSTP(3,3),X(3,3)
        COMMON/RATEPROP/C1,C2,C3
        COMMON/RATE/A1,GAMDOT0
        COMMON/MECHPROP/EYONG,GNU,N,CR,ALF
        COMMON/TOL/EMAX,ETOL
C**********************************
C       COMPUTE UFP FROM UFE,UF    *
C**********************************
        RT2=DSQRT(2.D0)
        CALL INVRS(UFE,X)
        CALL MATMUL(X,UF,UFP,3,3,3)
        CALL NORMFP(UFP)
        IF(EMAX.GE.ETOL) GO TO 25
C**************************************
C  COMPUTE THE BACKSTRESS FROM UFP    *
C**************************************
        CALL SIGMAB(UFP,USIGB)
C*********************************************
C  COMPUTE SIGSTRPRIME FROM USIG AND USIGB   *
C*********************************************
        CALL SIGSTR(USIG,USIGB,UFE,USGSTP)
C****************
C COMPUTE TAU    *
C****************
        CALL MATMUL(USGSTP,USGSTP,X,3,3,3)
        UTAU=DSQRT((X(1,1)+X(2,2)+X(3,3))/2.0D0)
C*************************************************************************
C CHECK THAT TAU IS NOT ZERO, IN OTHER WORDS, CHECK THAT THE
C PLASTIC RATE OF DEFORMATION IS NOT ZERO AND NEEDS TO BE CALCULATED.
C
              IF(UTAU.LT.5.D-03)THEN
          UTAU=0.D0
          DO 11 I=1,3
          DO 11 J=1,3
   11     UDP(I,J)=0.D0
          GO TO 25
       ENDIF
   12    CONTINUE
C END OF CHECK
C*************************************************************
C
C*****************************************
C COMPUTE PLASTIC RATE OF DEFORMATION     *
C*****************************************
C
        C1=GAMDOT0*DEXP(-A1*(SIM1+ALF*PRES))/RT2
        C2=DEXP(A1*(SIM1+ALF*PRES))
        GAMP=(C1*C2**((UTAU/(SIM1+ALF*PRES))**C3))/UTAU
```

```
            DO 20 I=1,3
            DO 20 J=1,3
   20     UDP(I,J)=GAMP*USGSTP(I,J)
C*****************************************************************
   25     CONTINUE
          RETURN
          END
C
          SUBROUTINE NEWSTATE(DTIME,TDP,TFP,TDTF,TDTFE,TDTFP,
     1    TDTSIG,TDTSGB,TDTSTP,TAU,S,PRES)
C*****************************************************************
C THIS ROUTINE COMPUTES THE STATE OF THE BODY AT TIME T+DTIME     *
C WITH A IMPLICIT  SCHEME WHICH CONVERGES  ON FP                  *
C                                                                 *
C*****************************************************************
          IMPLICIT REAL*8 (A-H,O-Z)
          DIMENSION TDP(3,3),TFP(3,3),TDTF(3,3),TDTFE(3,3),TDTFP(3,3),
       2  TDTSIG(3,3),TDTSGB(3,3),TDTSTP(3,3),X(3,3),XIN(3,3),TDTDP(3,3)
          COMMON/SOFT/S0,SSS,H,ST
          COMMON/TOL/EMAX,ETOL
          COMMON/TEMPER/TEMPG,XM1,XM2,XX1,XX2,XY1,XY2,XX3,RSG
          COMMON/TEMP11/TEMP,DTEMP,TEMPTDT,TEMP0,TALF
          EMAX=0.D0
C*********************************************
C TOLE IS THE TOLERANCE FOR TDTFP TO CONVERGE ON
C*********************************************
          TOLE=0.00010D0
C************************
C  INITIAL CONDITIONS    *
C************************
          DO 10 I=1,3
          DO 10 J=1,3
          TDTDP(I,J)=TDP(I,J)
   10     TDTFP(I,J)=TFP(I,J)
          S=ST
          IF(TEMPTDT.LT.XX2) S=ST*10**(XM1*DTEMP)
          IF(TEMPTDT.GE.XX2.AND.TEMPTDT.LT.XX3) S=ST*10**(XM2*DTEMP)
          NI=0
          DET=TDTF(3,3)*(TDTF(1,1)*TDTF(2,2)-TDTF(1,2)*TDTF(2,1))
C********************
C START ITERATIONS    *
C********************
 1000   CONTINUE
          NI=NI+1
          IF(NI.GT.6) THEN
            EMAX=ETOL
            GO TO 2000
          END IF
C
C COMPUTE TDTFP FROM TFP AND TDTDP
C
C STORE TDTFP FROM PREVIOUS ITERATION IN X FOR COMPARISON
C
             DO 40 I=1,3
             DO 40 J=1,3
   40     X(I,J)=TDTFP(I,J)
C*****************************************************************
C      UPDATE   FP :
C        TDTFP(i) = TFP + DTIME * TDTDP(i-1) *TDTFP(i-1)
C*****************************************************************
          CALL MATMUL(TDTDP,TDTFP,XIN,3,3,3)
          DO 20 I=1,3
          DO 20 J=1,3
```

```
   20   TDTFP(I,J) = TFP(I,J) + DTIME * XIN(I,J)
        CALL NORMFP(TDTFP)
        IF(EMAX.GE.ETOL) GO TO 2000
C*****************
C COMPUTE TDTFE  *
C*****************
        CALL INVRS(TDTFP,XIN)
        CALL MATMUL(TDTF,XIN,TDTFE,3,3,3)
C******************
C SYMMETRIZE TFE  *
C******************
          DO 60 I=1,3
          DO 60 J=1,3
  60    XIN(I,J)=(TDTFE(I,J)+TDTFE(J,I))/2.D0
          DO 70 I=1,3
          DO 70 J=1,3
   70   TDTFE(I,J)=XIN(I,J)
C**************************
C COMPUTE STRESS FROM TFE  *
C**************************
        CALL SIGMA(TDTFE,TDTSIG)
        PRES= - ( TDTSIG(1,1)+TDTSIG(2,2)+TDTSIG(3,3))/3.D0
C*****************************************
C COMPUTE REMAINING TERMS WITH SUB UPDATE  *
C*****************************************
      CALL UPDATE(TDTF,TDTFE,TDTFP,TDTDP,TDTSIG,TDTSGB,TDTSTP,TAU,S
     1 ,PRES)
C*************************************************************
C  UPDATE THE INTRINSIC YIELD WHICH MAY BE MODIFIED DUE TO   *
C  STRAIN SOFTENING                                          *
C*************************************************************
        ERR=DABS((S-SSS)/SSS)
        IF(ERR.LT.0.001D0) GO TO 49
        CALL SOFTEN(S,TAU,TDTSTP,TDTDP,DTIME,PRES)
        IF(EMAX.GE.ETOL) GO TO 2000
C*************************************************************
C CHECK FOR CONVERGENCE ON TDTFP                             *
C  (THIS CHECK IS ON INDIVIDUAL COMPONENTS OF TDTFP)          *
C*************************************************************
  49    DO 50 I=1,3
        DO 50 J=1,3
        X(I,J)=X(I,J)-TDTFP(I,J)
        IF(DABS(X(I,J)).GT.TOLE) GO TO 51
   50   CONTINUE
        GO TO 2000
   51    GO TO 1000
 2000   RETURN
        END
C
        SUBROUTINE SOFTEN(S,TAU,TDTSTP,TDTDP,DTIME,PRES)
C*********************************************************************
C  THIS ROUTINE CALCULATES THE MODIFIED INTRINSIC YIELD STRENGTH OF THE
C  MATERIAL DUE TO STRAIN SOFTENING OF THE MATERIAL
C*********************************************************************
        IMPLICIT REAL*8 (A-H,O-Z)
        DIMENSION TDTSTP(3,3),TDTDP(3,3)
        COMMON/RATE/A1,GAMDOT0
        COMMON/RATEPROP/C1,C2,C3
        COMMON/SOFT/S0,SSS,H,ST
        COMMON/MECHPROP/EYONG,GNU,N,CR,ALF
        COMMON/TOL/EMAX,ETOL
        COMMON/TEMP11/TEMP,DTEMP,TEMPTDT,TEMP0,TALF
        COMMON/TEMPER/TEMPG,XM1,XM2,XX1,XX2,XY1,XY2,XX3,RSG
```

```
      RT2=DSQRT(2.D0)
      NT=0
      STT=ST
      IF(TEMPTDT.LT.XX2) STT=ST*10**(XM1*DTEMP)
      IF(TEMPTDT.GE.XX2.AND.TEMPTDT.LT.XX3) STT=ST*10**(XM2*DTEMP)
      GP=C1*C2**( (TAU/(S+ALF*PRES))**C3 )
      GG=GP*RT2
    5 NT=NT+1
      IF(NT.GT.7) THEN
        EMAX=ETOL
        GO TO 25
      ENDIF
      SN=S
      HH=H*GG*DTIME
      S=SSS*(STT+HH)/(SSS+HH)
      ERR=DABS((S-SN)/SN)
      IF(ERR.LT.0.001D0) GO TO 25
      C1=GAMDOT0*DEXP(-A1*(S+ALF*PRES))/RT2
      C2=DEXP(A1*(S+ALF*PRES))
      GP=C1*C2**((TAU/(S+ALF*PRES))**C3)
      GG=GP*RT2
      GP=GP/TAU
      DO 10 I=1,3
      DO 10 J=1,3
   10 TDTDP(I,J)=GP*TDTSTP(I,J)
      GO TO 5
   25 RETURN
      END
C
      SUBROUTINE JACOB(TF,TSIG,TSGSTP,TAU,DTIME,DDSDDE,TDTS)
C*****************************************************************
C THIS ROUTINE CALCULATES THE JACOBIAN NEEDED TO RETURN TO ABAQUS
C*****************************************************************
      IMPLICIT REAL*8 (A-H,O-Z)
      DIMENSION TF(3,3),TSIG(3,3),TSGSTP(3,3),DDSDDE(4,4),TERM1(4)
     1 ,X(3,3)
      COMMON/RATE/RA1,GAMDOT0
      COMMON/SOFT/S0,SSS,H,ST
      COMMON/RATEPROP/RC1,RC2,RC3
      COMMON/MECHPROP/EYONG,GNU,N,CR,ALF
C
      G=EYONG/(2.D0*(1.D0+GNU))
      BULK=EYONG/(3.D0*(1.D0-2.D0*GNU))
      RT2=DSQRT(2.D0)
      SM=(TSIG(1,1)+TSIG(2,2)+TSIG(3,3))/3.D0
      PRES=-SM
      DEP=DTIME*RT2*RC1*RC2**((TAU/(TDTS+ALF*PRES))**RC3)
C************************
C CHECK FOR ELASTICITY   *
C************************
      IF(DEP.GT.1.D-05) GO TO 3
      GO TO 100
C  END OF CHECK
    3 DET=TF(3,3)*(TF(1,1)*TF(2,2)-TF(1,2)*TF(2,1))
C************************************
C PARAMETERS TO BE USED FREQUENTLY   *
C************************************
      HH=H*DEP
      TT1=TAU/(TDTS+ALF*PRES)
      T1=TT1**RC3
      T2=TT1**(1.D0/6.D0)
      T2=1.D0/T2
      TM1=RA1*(1.D0-T1/6.D0)
```

```
      TM2=SSS+HH
C COMPUTE BETA
      BETA=1.D0+SSS*HH*TM1*(1.D0-(ST+HH)/TM2)/TM2
      BETA=1.D0/BETA
C COMPUTE THE PARTIAL OF GAMP*DT  WRT TAU
      DGPDTA=DEP*RA1*T2
C COMPUTE THE PARTIAL OF GAMP*DT WRT PRES
      DGPDP=-DEP*TM1*ALF
C COMPUTE THE OFTEN USED ZETA
      ZETA=(BETA*DGPDTA - DEP/TAU)/RT2
C COMPUTE THE OFTEN USED ETA
      ETA= 1.D0 + RT2*G*BETA*DGPDTA
      ETA=1.D0/ETA
C COMPUTE ZETA*ETA
      ZN=ZETA*ETA
C COMPUTE THE "MODIFIED" SHEAR MODULUS
      JT=DET*TAU
      GBAR=G*JT/(JT+RT2*G*DEP)
C COMPUTE GBAR*ZETA*ETA
      GBZN=GBAR*ZN
      T3=RT2*TAU
C*****************************************************************
C WITH ABOVE VALUES, COMPUTE THE VARIOUS COEFFICIENTS FOR THE JACOBIAN
C*****************************************************************
C
      A=2.D0*GBAR
C
      B=BULK-A/3.D0
C
      C=4.D0*GBZN*G
C
      EE=2.D0*GBZN*T3
C
      F=A*BETA*DGPDP*BULK
C
      Q=F*ZN*2.D0*G/DET
C
      P=A*DEP/T3
C
      EFQ=EE + F - Q
C*****************************************************************
C PUT IT ALL TOGETHER INTO THE JACOBIAN
C*****************************************************************
      DO 15 I=1,3
      DO 15 J=1,3
   15 X(I,J)=TSGSTP(I,J)/T3
        DO 20 I=1,3
   20 TERM1(I)=EFQ*X(I,I)+P*TSGSTP(I,I)+B
      TERM1(4)= EFQ*X(1,2) + P*TSGSTP(1,2)
C DIAGONAL TERMS
        DO 30 I=1,3
   30 DDSDDE(I,I)= A + TERM1(I) - C*X(I,I)**2
C OFF-DIAGONAL TERMS
        DO 40 I=2,3
      DDSDDE(1,I)= - C*X(I,I)*X(1,1)
   40 DDSDDE(I,1)=DDSDDE(1,I)
      DDSDDE(2,3)= - C*X(2,2)*X(3,3)
      DDSDDE(3,2)=DDSDDE(2,3)
        DO 50 I=1,3
        DO 50 J=1,3
      IF(I.NE.J) DDSDDE(I,J)=DDSDDE(I,J)+TERM1(I)
   50 CONTINUE
C ROW AND COLUMN 4 TERMS
```

```
          DO 60 I=1,3
          DDSDDE(I,4)= - C*X(I,I)*X(1,2)
   60     DDSDDE(4,I)=DDSDDE(I,4) + TERM1(4)
          DDSDDE(4,4)= - C*X(1,2)**2 + A/2.D0
          GO TO 500
C*****************
C IF ELASTIC      *
C*****************
  100     CONTINUE
          AA=BULK+4.D0*G/3.D0
          BB=BULK-2.D0*G/3.D0
          DO 110 I=1,3
          DO 110 J=1,3
          IF(I.EQ.J) DDSDDE(I,J)=AA
  110     IF(I.NE.J) DDSDDE(I,J)=BB
          DDSDDE(4,4)=G
  500     RETURN
          END
C
C  TO GET EL(1,1), EL(2,2)
C
      SUBROUTINE EL11(S1,S3,BITA1,BITA3,A)
C  S1,S3 FROM SUBROUTINE PLSTR
C  BITA1,BITA3 FROM SUBROUTINE LINV
      IMPLICIT REAL*8(A-H,O-Z)
        COMMON/MECHPROP/EYONG,GNU,N,CR,ALF
C************************************
C THIS ROUTINE WRITTEN BY BAGE?ALLI
C************************************
      EN=N
      D=DSQRT(EN)
      AA1=S1/D
      AA3=S3/D
      A=S1*BITA1+S3*BITA3
      IF(AA1.LT..95D0) A1=D*(1.D0/BITA1**2-1.D0/(DSINH(BITA1))**2)
      IF(AA1.GE..95D0) A1=D*(1.D0/BITA1**2)
      IF(AA3.LT..95D0) A2=(S3**2)/(D*(1/BITA3**2-
     +1/(DSINH(BITA3))**2))
      IF(AA3.GE..95D0) A2=(S3**2)*D/BITA3**2
      A=(A+(S1**2)/A1 +A2)*CR
C A =EL(1,1) WITH S1,S3; A=EL(2,2) WITH S2,S3
      RETURN
      END
C
C   TO GET TFE IN TERMS OF TSIG
C
      SUBROUTINE FESIG(TSIG,TFE,DT)
      IMPLICIT REAL*8(A-H,O-Z)
      DIMENSION TFE(3,3),TSIG(3,3),R1(3,3),R2(3,3),R3(3,3)
        COMMON/MECHPROP/EYONG,GNU,N,CR,ALF
        COMMON/TEMP11/TEMP,DTEMP,TEMPTDT,TEMP0,TALF
C************************************
C THIS ROUTINE WRITTEN BY BAGE?ALLI
C************************************
C
C GIVEN TSIG, OBTAIN TFE
C
      A1=(1.D0+GNU)/EYONG
      A2=GNU/EYONG
      DO 10 I=1,3
      DO 10 J=1,3
        R1(I,J)=0.D0
 10       IF(I.EQ.J) R1(I,J)=1.D0
```

```
      A3=TSIG(1,1)+TSIG(2,2)+TSIG(3,3)
      DO 20 I=1,3
      DO 20 J=1,3
 20      TFE(I,J)=(TSIG(I,J)*A1-A2*R1(I,J)*A3)*DT
      B1=.5D0*(TSIG(1,1)+TSIG(2,2))
      B2=.5D0*(TSIG(1,1)-TSIG(2,2))
      B3=TSIG(1,2)
      S1=B1+DSQRT(B2**2+B3**2)
      S2=B1-DSQRT(B2**2+B3**2)
      S3=TSIG(3,3)
      B2=B2*2.D0
      B3=2.D0*B3
      IF(B3.EQ.0.0.AND.B2.EQ.0.0) THEN
      THETA=0.0
      GO TO 9990
      ENDIF
      THETA=DATAN2(B3,B2)
      THETA=.5D0*THETA
 9990  CC1=DCOS(THETA)
      SS1=DSIN(THETA)
      DO 30 I=1,3
      DO 30 J=1,3
 30      R2(I,J)=0.D0
      R2(1,1)=CC1
      R2(2,2)=CC1
      R2(1,2)=-SS1
      R2(2,1)=SS1
      R2(3,3)=1.D0
      CALL MATMUL(TFE,R2,R3,3,3,3)
      R2(2,1)=-SS1
      R2(1,2)=SS1
      CALL MATMUL(R2,R3,TFE,3,3,3)
C
      DO 11 I=1,3
      DO 11 J=1,3
 11      R1(I,J)=0.D0
      R1(1,1)=DEXP(TFE(1,1))
      R1(2,2)=DEXP(TFE(2,2))
      R1(3,3)=DEXP(TFE(3,3))
      DO 31 I=1,3
      DO 31 J=1,3
 31      R2(I,J)=0.D0
      R2(1,1)=CC1
      R2(2,2)=CC1
      R2(1,2)=SS1
      R2(2,1)=-SS1
      R2(3,3)=1.D0
      CALL MATMUL(R1,R2,R3,3,3,3)
      R2(2,1)=SS1
      R2(1,2)=-SS1
      CALL MATMUL(R2,R3,R1,3,3,3)
        TT=TALF3(TEMP-TEMP0)
      DO 41 I=1,3
      DO 41 J=1,3
         TFE(I,J)=.5D0*(R1(I,J)+R1(J,I))
 41   IF(I.EQ.J) TFE(I,J)=TFE(I,J)+TT
C
      RETURN
      END
C  TO OBTAIN BITA=L-INVERSE(S/SQRT(N)),WITH COSH(BITA)-1/BITA=S/SQRT(N)=L(BITA)
C
      SUBROUTINE LINV(S,N,BITA)
      IMPLICIT REAL*8(A-H,O-Z)
```

```
C*****************************************
C THIS ROUTINE WRITTEN BY BAGEPALLI
C*****************************************
      TOLHI=.001
      TOLLO=.001
      EN=N
        DEN=DSQRT(EN)
      AA=S/DEN
      AA1=1.D0/DEN
      B=1.D0
      IF(AA.LE..4D0.AND.AA.GT.AA1) B=1.D0
      IF(AA.LE..6D0.AND.AA.GT..4D0) B=2.D0
      IF(AA.LE..8D0.AND.AA.GT..6D0) B=3.D0
      IF(AA.LE..9D0.AND.AA.GT..8D0) B=4.D0
      IF(AA.LE..92D0.AND.AA.GT..9D0) B=5.D0
      IF(AA.LE..95D0.AND.AA.GT..92D0) B=8.D0
      IF(AA.LE..97D0.AND.AA.GT..95D0) B=12.D0
      IF(AA.LE..975D0.AND.AA.GT..97D0) B=25.D0
      IF(AA.LE..98D0.AND.AA.GT..975D0) B=44.D0
      IF(AA.LE..99D0.AND.AA.GT..98D0) B=60.D0
      IF(AA.LE.1.D0.AND.AA.GT..99D0) B=90.D0
      IF(AA.GT.1.D0.AND.AA.LT.1.2D0) THEN
      B=100.D0
      S=.999999*DEN
      ENDIF
      IF(AA.GT.1.2D0) THEN
      WRITE(6,9999) AA
 9999     FORMAT(' SUBROUTINE LINV, STRETCH EXEEDS SQRT(N) ',F10.5)
      CALL XIT
      ENDIF
 10       F=(1.D0/DTANH(B)-1.D0/B)-S/DEN
      IF(AA.LT..945D0) FP=(1.D0/(B*B)-1.D0/(DSINH(B))**2)
      IF(AA.GE..945D0) FP=1.D0/(B*B)
      BP=B-F/FP
      E0=DABS(BP-B)
      E1=DABS(B)
      E2=E0/E1
      B=BP
      IF(AA.GE..95) THEN
      IF(E2.GT.TOLHI) GO TO 10
      GO TO 40
      ENDIF
      IF(E2.GT.TOLLO) GO TO 10
  40    BITA=B
C       WRITE(6,*) S,BITA
      RETURN
      END
C
C SUBROUTINE TO MULTIPLY MATRICES A(I,K)*B(K,J)=C(I,J)
C
      SUBROUTINE MATMUL(A,B,C,NRA,NCA,NCB)
C NRA,NCA=#ROWS,#COLUMNS IN A;NCB=#COLUMNS IN B
C
      IMPLICIT REAL*8(A-H,O-Z)
      DIMENSION A(NRA,NCA),B(NCA,NCB),C(NRA,NCB)
       DO 10 I=1,NRA
      DO 10 J=1,NCB
      C(I,J)=0.D0
      DO 10 K=1,NCA
  10      C(I,J)=A(I,K)*B(K,J) + C(I,J)
      RETURN
      END
C
```

```
C   TO NORMALIZE TFP=1/CUBRT(DET(TFP))*TFP
C
      SUBROUTINE NORMFP(TFP)
      IMPLICIT REAL*8(A-H,O-Z)
      DIMENSION TFP(3,3)
        COMMON/TOL/EMAX,ETOL
      D1=(TFP(1,1)*TFP(2,2)-TFP(1,2)*TFP(2,1))*TFP(3,3)
      IF(D1.LE.0.D0) THEN
      WRITE(6,9989)
 9989     FORMAT(' SUBROUTINE NORMFP ; VALUES OF DET(FP) AND FP ARE',
     1  2E13.6,  '  THE TIME STEP WILL BE REDUCED ')
      WRITE(6,*) D1,TFP
        EMAX=2.D0*ETOL
        GO TO 11
      ENDIF
      D3=1.D0/3.D0
      D3=D1**D3
         DO 10 I=1,3
         DO 10 J=1,3
  10  TFP(I,J)=   TFP(I,J)/D3
  11  RETURN
      END
C
C  TO OBTAIN PLASTIC STRETCHES AND ROTATION VECTORS: LAMBDAP(I,J);R(I,J)
C
      SUBROUTINE PLSTR(F,S1,S2,S3,C,S)
C  S(I)=PRINCIPAL STRETCHES;C,S= COS(THETA), SIN(THETA)
C
      IMPLICIT REAL*8(A-H,O-Z)
      DIMENSION F(3,3),A(3,3),B(3,3),CC(3,3),V(3,3),R(3,3)
C*********************************
C THIS ROUTINE WRITTEN BY BAGEPALLI
C*********************************
      DO 11 I=1,3
      DO 11 J=1,3
  11      A(I,J)=F(J,I)
      CALL MATMUL(F,A,B,3,3,3)
      S3=(B(1,1)+B(2,2))*0.5
      S2=((B(1,1)-B(2,2))*0.5)**2+B(1,2)**2
      S2=DSQRT(S2)
      S1=S3+S2
      S2=S3-S2
      S3=DSQRT(B(3,3))
      S1=DSQRT(S1)
      S2=DSQRT(S2)
      S4=2*B(1,2)
      S5=B(1,1)-B(2,2)
      IF(S4.EQ.0.D0.AND.S5.EQ.0.D0) THETA=0.D0
      IF(S4.EQ.0.D0.AND.S5.EQ.0.D0) GO TO 25
      THETA=DATAN2(S4,S5)
      THETA=THETA*0.5D0
  25      C=DCOS(THETA)
      S=DSIN(THETA)
      DO 10 I=1,3
      DO 10 J=1,3
      V(I,J)=0.D0
      R(I,J)=0.D0
      A(I,J)=0.D0
  10      B(I,J)=0.D0
      A(1,1)=1.D0/S1
      A(2,2)=1.D0/S2
      A(3,3)=1.D0/S3
      V(1,1)=S1
```

```
      V(2,2)=S2
      V(3,3)=S3
      B(1,1)=C
      B(2,2)=C
      B(2,1)=-S
      B(1,2)=S
      B(3,3)=1.D0
      CALL MATMUL(A,B,CC,3,3,3)
      CALL MATMUL(V,B,R,3,3,3)
      B(1,2)=-S
      B(2,1)=S
      CALL MATMUL(B,CC,A,3,3,3)
      CALL MATMUL(B,R,V,3,3,3)
      CALL MATMUL(A,F,R,3,3,3)
      RETURN
      END
C
```

```
C TO GET SIGMA(I,J) IN TERMS OF TFE(I,J)
C
      SUBROUTINE SIGMA(TFE,TSIG)
C
C DT IS DETERMINANT OF F
C
      IMPLICIT REAL*8(A-H,O-Z)
      DIMENSION TFE(3,3),TSIG(3,3),A(3,3),B(3,3)
        COMMON/MECHPROP/EYONG,GNU,N,CR,ALF
        COMMON/TEMP11/TEMP,DTEMP,TEMPTDT,TEMP0,TALF
      CALL PLSTR(TFE,S1,S2,S3,C,S)
      DO 10 I=1,3
      DO 10 J=1,3
      A(I,J)=0.0
  10      B(I,J)=0.0
      A(1,1)=DLOG(S1)
      A(2,2)=DLOG(S2)
      A(3,3)=DLOG(S3)
      S4=A(1,1)+A(2,2)+A(3,3)
      S5=EYONG/(1.D0+GNU)
      S6=S5*GNU/(1.D0-2.D0*GNU)
      S6=S6*S4
      A(1,1)=A(1,1)*S5+S6
      A(2,2)=A(2,2)*S5+S6
      A(3,3)=A(3,3)*S5+S6
      B(1,1)=C
      B(2,2)=C
      B(3,3)=1.D0
      B(1,2)=S
      B(2,1)=-S
      CALL MATMUL(A,B,TSIG,3,3,3)
      B(1,2)=-S
      B(2,1)=S
      CALL MATMUL(B,TSIG,A,3,3,3)
      DT=(TFE(1,1)*TFE(2,2)-TFE(1,2)**2)*TFE(3,3)
       TT=EYONG*TALF*(TEMPTDT-TEMP0)/(1.D0-2.D0*GNU)
      DO 20 I=1,3
      DO 20 J=1,3
        IF(I.EQ.J) A(I,J)=A(I,J)-TT
 20      TSIG(I,J)=A(I,J)/DT
      RETURN
      END
C  TO GET TSIGB(I,J) IN TERMS OF TFP(I,J)
C
      SUBROUTINE SIGMAB(TFP,TSIGB)
      IMPLICIT REAL*8(A-H,O-Z)
      DIMENSION TFP(3,3),TSIGB(3,3),A(3,3),B(3,3),
     +CC(3,3),DD(3,3)
        COMMON/MECHPROP/EYONG,GNU,N,CR,ALF
C*********************************
C THIS ROUTINE WRITTEN BY BAGEPALLI
C*********************************
      CALL PLSTR(TFP,S1,S2,S3,C,S)
      DO 10 I=1,3
      DO 10 J=1,3
      A(I,J)=0.0
 10      B(I,J)=0.0
      CALL LINV(S1,N,BITA1)
      CALL LINV(S2,N,BITA2)
      CALL LINV(S3,N,BITA3)
        EN=N
      D1=1/1.5D0
      D2=1/3.D0
```

```
        CCR=CR*DSQRT(EN)/3.D0
C
      A(1,1)=CCR*(S1*BITA1*D1-(S2*BITA2+S3*BITA3)*D2)
      A(2,2)=CCR*(S2*BITA2*D1-(S3*BITA3+S1*BITA1)*D2)
      A(3,3)=CCR*(S3*BITA3*D1-(S1*BITA1+S2*BITA2)*D2)
C
      B(1,1)=C
      B(2,2)=C
      B(1,2)=S
      B(2,1)=-S
      B(3,3)=1.0
      CALL MATMUL(A,B,DD,3,3,3)
      B(1,2)=-S
      B(2,1)=S
      CALL MATMUL(B,DD,TSIGB,3,3,3)
      RETURN
      END
C
C  TO OBTAIN SIGMA-STAR(I,J)PRIME
C
      SUBROUTINE SIGSTR(TSIG,TSIGB,TFE,TSGSTP)
C  TSGSTP(I,J) IS THE OUTPUT=SIGMA-STAR(I,J)PRIME
C
      IMPLICIT REAL*8(A-H,O-Z)
      DIMENSION TSIG(3,3),TSIGB(3,3),TFE(3,3),TSGSTP(3,3),
     +B(3,3),C(3,3)
      CALL MATMUL(TSIGB,TFE,C,3,3,3)
      CALL MATMUL(TFE,C,B,3,3,3)
 11      FORMAT(3X,3F10.4)
      DETFE=((TFE(1,1)*TFE(2,2)-TFE(1,2)**2)*TFE(3,3))
      DO 10 I=1,3
      DO 10 J=1,3
 10     C(I,J)=TSIG(I,J)-B(I,J)/DETFE
        CM=(C(1,1)+C(2,2)+C(3,3))/3.D0
      DO 20 I=1,3
      DO 20 J=1,3
        TSGSTP(I,J)=C(I,J)
 20     IF(I.EQ.J) TSGSTP(I,J)=TSGSTP(I,J)-CM
      RETURN
      END
        SUBROUTINE INVRS(A,B)
        IMPLICIT REAL*8 (A-H,O-Z)
        DIMENSION A(3,3),B(3,3)
        DO 10 I=1,3
        DO 10 J=1,3
 10     B(I,J)=0.D0
        BB=A(1,1)*A(2,2)-A(1,2)*A(2,1)
        B(1,1)=A(2,2)/BB
        B(2,2)=A(1,1)/BB
        B(2,1)=-A(2,1)/BB
        B(1,2)=-A(1,2)/BB
        B(3,3)=1.D0/A(3,3)
        RETURN
        END
C
      SUBROUTINE ROTSIG(S,A,SPRIME,LSIG)
      IMPLICIT REAL*8(A-H,O-Z)
      DIMENSION S(1),A(3,3),SPRIME(1)
C
      COMMON/CEL/LELOP,JETP,JETP1,KEL,KINTK,KINTL,KINTSL,KSPT,NEMCRD,
     1 JINTYP,JEXTYP,JEXTY2,JLIB,NAN24,MDOF,MCRD,
     1 NNODE,NNODU,NTENS,NDI,NSHR,NPR,NINTK,NINTM,NINTSL,NINTLL,NMP,
     4 NPARS,NSHL,NBM,NELZM,NINTTS,NEINT,NDOFEL,JUNSYM,NEGEOM,
```

```
     5 LNODEK,NNODEP,LBASIS,NNODET,NTENST,NTDOFN,LLUMPM,NOFFT,NNCOI,
     1 NSPT,NNOD2,NNOD3,NNOD4,NTDOFE,KSPTT,NINR,NEMB
      COMMON/CONSTS/PI,SIN60,COS60,KCROS2(3),KCROS3(3),ZERO,LZERO,ONE,
     1 ONE,TWO,HALF,ABIG,ASMALL,BCBIG,LOCSHR(2,3),THIRD,PRECIS
     2,BLANK
C
C*****************************************************************
C
C THIS IS AN ABAQUS SUBROUTINE MODIFIED BY BOYCE TO OBTAIN ADDITIONAL
C INFORMATION NEEDED IN UMAT. MODIFICATIONS ARE SURROUNDED BY C****LINES
C
C*****************************************************************
C
C  LSIG=1  - STRESS
C  LSIG=2  - ENG. STRAIN
C LSIG=1 OR 2 PLUS 10 INDICATES REPLACE S WTIH SPRIME
C*********************************
C RSTR IS THE INTERMEDIATE ROTATION FROM T TO T+DT
      DIMENSION                    RSTR(3,3)
      COMMON/ROTSTR/RSTR
C*********************************
      LSIG1=LSIG-(LSIG/10)*10
      IF (NDI.EQ.0) GO TO 50
      DO 20 K1=1,NDI
      TERM=ZERO
      DO 5 K2=1,NDI
      TERM=TERM+A(K1,K2)*A(K1,K2)*S(K2)
    5 CONTINUE
      IF(NSHR.EQ.0) GO TO 15
      K3=NDI
      TERM1=ZERO
      DO 10 K2=1,NSHR
      K3=K3+1
      K4=LOCSHR(1,K2)
      K5=LOCSHR(2,K2)
      TERM1=TERM1+A(K1,K4)*A(K1,K5)*S(K3)
   10 CONTINUE
      IF(LSIG1.EQ.1)TERM1=TWO*TERM1
      TERM=TERM+TERM1
   15 CONTINUE
      SPRIME(K1)=TERM
   20 CONTINUE
   50 CONTINUE
      IF(NSHR.EQ.0) GO TO 100
      K1=NDI
      DO 70 K11=1,NSHR
      K1=K1+1
      K2=LOCSHR(1,K11)
      K3=LOCSHR(2,K11)
      TERM=ZERO
      IF(NDI.EQ.0) GO TO 60
      DO 55 K4=1,NDI
      TERM=TERM+A(K2,K4)*A(K3,K4)*S(K4)
   55 CONTINUE
      IF(LSIG1.EQ.2)TERM=TWO*TERM
   60 CONTINUE
      TERM1=ZERO
      K4=NDI
      DO 65 K41=1,NSHR
      K4=K4+1
      K5=LOCSHR(1,K41)
      K6=LOCSHR(2,K41)
      TERM1=TERM1+(A(K2,K5)*A(K3,K6)+A(K2,K6)*A(K3,K5))*S(K4)
```

```
   65 CONTINUE
      TERM=TERM+TERM1
      SPRIME(K1)=TERM
   70 CONTINUE
  100 CONTINUE
      IF(LSIG1.EQ.LSIG)GO TO 200
      DO 110 K1=1,NTENS
      S(K1)=SPRIME(K1)
  110 CONTINUE
  200 CONTINUE
C*************************************
       IF(LSIG.NE.11) GO TO 300
       DO 270 II=1,3
       DO 270 JJ=1,3
       RSTR(II,JJ)=A(II,JJ)
  270  CONTINUE
C*************************************
  300  CONTINUE
      RETURN
      END
      SUBROUTINE LSOL8V(XX1,GX1,ANORMI,EXPU,MNCRDX,ANDR,MNRLX,EMCRD,
     1EMCD0,DVRED,GEOM,EU,EPAR,EJAC,EDU)
      IMPLICIT REAL*8(A-H,O-Z)
      DIMENSION XX1(3,3),GX1(2,2),ANORMI(1),EXPU(MNCRDX,1),ANDR(MNRLX,1)
     1,EMCRD(2),EMCD0(1),DVRED(8),GEOM(1),EJAC(3,3),EDU(1),EU(1),EPAR(2)
C
      COMMON/CDV/DV,DVDV0
      COMMON/CEL/LELOP,JETP,JETP1,KEL,KINTK,KINTL,KINTSL,KSPT,NEMCRD,
     1 JINTYP,JEXTYP,JEXTY2,JLIB,NAN24,MDOF,MCRD,
     1 NNODE,NNODU,NTENS,NDI,NSHR,NPR,NINTK,NINTM,NINTSL,NINTLL,NMP,
     4 NPARS,NSHL,NBM,NELZM,NINTTS,NEINT,NDOFEL,JUNSYM,NEGEOM,
     5 LNGDEK,NNODEP,LBASIS,NNODET,NTENST,NTDOFN,LLUMPM,NOFFT,NNODI,
     1 NSPT,NNOD2,NNOD3,NNOD4,NTDOFE,KSPTT,NINR,NBMB
      COMMON/CGAUSS/GAUSP2(2),GAUSW2(2),GAUSP3(3),GAUSW3(3),
     1 GAUSP4(4),GAUSW4(4),GAUSP5(5),GAUSW5(5),GAUSP6(6),GAUSW6(6),
     2 GAUSP7(7),GAUSW7(7),GAUSP8(8),GAUSW8(8),GAUSP9(9),GAUSW9(9)
     3,OGASP2
      COMMON/CNS/INCRD,INU,INDU,INC,INRRES,INV,INA,INT,
     1 INDI,INDI1,IHAF,INSRES,IPORES,INFREF,INSREF,INEIG,INCC
      COMMON/CONSTS/PI,SIN60,COS60,KCROS2(3),KCROS3(3),ZERO,LZERO,LONE,
     1 ONE,TWO,HALF,ABIG,ASMALL,BCBIG,LOCSHR(2,3),THIRD,PRECIS
     2,BLANK
      COMMON/CONTRO/LINITL,LARGE,LINEAR,LCRELP,LDYN,LHEAT,LSTAT,
     1 LOK,LEFOND,LMOLOD,LMASS,LREST,LFILE,LUNSYM,LPPOPN,LMODST,
     2 LELMOD,LCORT,LTRAMA,LEIGEN,NRHSV,LMESSG,LLHS,LLHSK,LLHSM,
     3 LRHS,LSTRN,LINMAT,LGAPFL,LMDBW,LSUPGN,LGAPS,LGAPEL,LSHELL,
     4 LSUPEL,LGBO,LCONS,LSSS,LSS1,LEXTRP,LDYNC,LEIPRE,LCTU,LPROC,
     5 LADDM,LDAA,LSOLID,LRIKS,LREBAR,LSUBMX,LREBAS,LRHSI,LHYBBM,
     6 LBQUIL,LSTEND,LWPEN,LPORPS,LWPENE,LNOSTP,LSBQU,LAUTO,LITFRE,
     7 LITFRP,LGAPPR,LHYBOK,LMODYN,NRHSI,NRHSP,LCOMPD,LPOUT,LSTRNE
     8 ,LREBA1
      COMMON/COUNT/KINC,MINC,KITER,MITER,PATIME,ATIME,DATIME,
     1 CTIME,DCTIME,DTIME,DDTIME,HTIME,DHTIME,DDTPRE,DATPRE,HTIM1,
     2 DHTIM2,EXFAC,KSTEP,KCUTS,MCUTS,NUMBER,LSHAF1,LCUTBK,DTNEWS,
     3 KITGEN,KMDINC,TTIME,DTMIN,DTMAX,MITEIG,MITXXX,STIME,DSTIME
     4,TPREV,TNEW,TOLD,TEND
C*********************************************************
       DIMENSION TDTF(3,3),TF(3,3),GXHAT(3,3),EMCRDT(3)
       COMMON/DEFGRAD/TDTF,TF
       COMMON/VI/EMCRDT
C*********************************************************
C
C*********************************************************
```

```
C
C THIS IS AN ABAQUS SUBROUTINE MODIFIED BY BOYCE TO OBTAIN
C ADDITIONAL INFORMATION NEEDED IN UMAT
C
C*************************************************************
      NGEOM=5
      ISPACE=0
      IF(NINTK.NE.NINTM) GO TO 150
CHECKED FOR 1ST ORDER ELEMENTS
      IF(NNODI.GT.4) GO TO 100
      IF(KINTK.NE.1) GO TO 100
      DO 50 KINR=1,NINR
      I11=(KINR-1)*NNOD3
      DO 10 K1=1,2
      DO 8 K2=1,2
      TERM=ZERO
C*******************************
        GXHAT(K1,K2)=ZERO
C*******************************
      I1=I11+K2*NNODI
      DO 5 KNODE=1,NNODI
      I1=I1+1
C*******************************
        KEDU=2*(KNODE-1)+K1
        GXHAT(K1,K2)=GXHAT(K1,K2)+ANORMI(I1)*(EXPU(K1,KNODE)-EDU(KEDU))
C*******************************
      TERM=TERM+ANORMI(I1)*EXPU(K1,KNODE)
    5 CONTINUE
      GX1(K1,K2)=TERM
    8 CONTINUE
   10 CONTINUE
      CALL ASET(XX1,ZERO,9)
      I1=(KINR-1)*NGEOM
      DO 20 K1=1,2
      DO 18 K2=1,2
      I1=I1+1
      DO 15 K3=1,2
      XX1(K3,K1)=XX1(K3,K1)+GX1(K3,K2)*GEOM(I1)
C*******************************************
        TF(K3,K1)=TF(K3,K1)+GXHAT(K3,K2)*GEOM(I1)
C*******************************************
   15 CONTINUE
   18 CONTINUE
   20 CONTINUE
      XX1(3,3)=ONE
C**************
        TF(3,3)=ONE
C**************
      IF(NPARS.NE.0) GO TO 40
      R=ZERO
      BIGR=ZERO
      IF(NNODI.NE.4) GO TO 30
C************
        RT=ZERO
C************
      DO 25 KNODE=1,NNODI
      R=R+EXPU(1,KNODE)
C****************
        RT=RT+EXPU(1,KNODE)-ELU(2*KNODE-1)
C****************
      BIGR=BIGR+ANDR(INCRD,KNODE)
   25 CONTINUE
C****************
```

```
        TF(3,3)=RT/BIGR
C***************
      GO TO 39
   30 CONTINUE
      I1=(KINR-1)*NNOD3
      DO 35 KNODE=1,NNODI
      I1=I1+1
      R=R+ANORMI(I1)*EXPU(1,KNODE)
      BIGR=BIGR+ANORMI(I1)*ANDR(INCRD,KNODE)
   35 CONTINUE
C***************
        TF(3,3)=EMCRDT(1)/BIGR
C***************
   39 CONTINUE
      XX1(3,3)=R/BIGR
   40 CONTINUE
C***************
        CALL ACOPY(XX1,TDTF,9)
C***************
      DET=XX1(1,1)*XX1(2,2)-XX1(1,2)*XX1(2,1)
      DVRED(KINR)=DET
      DO 43 K1=1,2
      DO 42 K2=1,2
      EJAC(K1,K2)=ZERO
      GX1(K1,K2)=ZERO
      I2=I11+NNODI*K2
      I3=K1
      DO 41 KNODE=1,NNODI
      I2=I2+1
      GX1(K1,K2)=GX1(K1,K2)+ANORMI(I2)*(EXPU(K1,KNODE)-HALF*EDU(I3))
      EJAC(K1,K2)=EJAC(K1,K2)+ANORMI(I2)*EDU(I3)
      I3=I3+2
   41 CONTINUE
   42 CONTINUE
   43 CONTINUE
      DET=GX1(1,1)*GX1(2,2)-GX1(1,2)*GX1(2,1)
      DET=ONE/DET
      TEMP=GX1(1,1)
      GX1(1,1)=GX1(2,2)*DET
      GX1(1,2)=-GX1(1,2)*DET
      GX1(2,1)=-GX1(2,1)*DET
      GX1(2,2)=TEMP*DET
      DO 46 K1=1,2
      DO 45 K2=1,2
      XX1(K1,K2)=ZERO
      DO 44 K3=1,2
      XX1(K1,K2)=XX1(K1,K2)+EJAC(K1,K3)*GX1(K3,K2)
   44 CONTINUE
   45 CONTINUE
   46 CONTINUE
      XX1(3,3)=ZERO
      IF(NPARS.NE.0) GO TO 49
      DR=ZERO
      R=ZERO
      IF(NNODI.NE.4) GO TO 48
      I1=1
      DO 47 KNODE=1,NNODI
      R=R+EXPU(1,KNODE)-HALF*EDU(I1)
      DR=DR+EDU(I1)
      I1=I1+2
   47 CONTINUE
      GO TO 480
   48 CONTINUE
```

```
      I1=1
      I2=I11
      DO 470 KNODE=1,NNODI
      I2=I2+1
      R=R+ANORMI(I2)*(EXPU(1,KNODE)-HALF*EDU(I1))
      DR=DR+ANORMI(I2)*EDU(I1)
      I1=I1+2
  470 CONTINUE
  480 CONTINUE
      XX1(3,3)=DR/R
   49 CONTINUE
      K1=NINR+KINR
      DVRED(K1)=XX1(1,1)+XX1(2,2)
      DO 490 K1=1,2
      DO 489 K2=1,2
      TERM=ZERO
      I1=I11+NNODI*K2
      DO 485 KNODE=1,NNODI
      I1=I1+1
      TERM=TERM+ANORMI(I1)*EXPU(K1,KNODE)
  485 CONTINUE
      GX1(K1,K2)=TERM
  489 CONTINUE
  490 CONTINUE
      DET=GX1(1,1)*GX1(2,2)-GX1(1,2)*GX1(2,1)
      DET=ONE/DET
      TEMP=GX1(1,1)
      GX1(1,1)=GX1(2,2)*DET
      GX1(1,2)=-GX1(1,2)*DET
      GX1(2,1)=-GX1(2,1)*DET
      GX1(2,2)=TEMP*DET
      I1=2*(NINR+(KINR-1)*NNODI)+1
      J1=I11+NNODI
      DO 495 KNODE=1,NNODI
      I1=I1+1
      I2=I1+NNODI
      J1=J1+1
      J2=J1+NNODI
      DVRED(I1)=ANORMI(J1)*GX1(1,1)+ANORMI(J2)*GX1(2,1)
      DVRED(I2)=ANORMI(J1)*GX1(1,2)+ANORMI(J2)*GX1(2,2)
  495 CONTINUE
   50 CONTINUE
  100 CONTINUE
      ISPACE=NINR
      IF(NNODI.GT.4) GO TO 150
      IF(NNODI.EQ.4) GO TO 120
      KH=(KINTK-1)/3+1
      KG=KINTK-(KH-1)*3
      G=GAUSP3(KG)*OGASP2
      H=GAUSP3(KH)*OGASP2
      XM1=(ONE-G)*(ONE-H)
      XM2=(ONE+G)*(ONE-H)
      XM3=(ONE-G)*(ONE+H)
      XM4=(ONE+G)*(ONE+H)
      XJ0=XM1*DVRED(1)+XM2*DVRED(2)+XM3*DVRED(3)+XM4*DVRED(4)
      XJ0=XJ0*.25
      TERM=XM1*DVRED(5)+XM2*DVRED(6)+XM3*DVRED(7)+XM4*DVRED(8)
      I1=1+2*NINR
      DVRED(I1)=.25*TERM
      I1=1+2*(NINR+NNODI)
      I111=2*NNODI
      DO 110 K1=1,2
      I1=1+2*(NINR+NNODI)+(K1-1)*NNODI
```

```
      I2=1+2*NINR+(K1-1)*NNODI
      DO 105 KNODE=1,NNODI
      I1=I1+1
      I2=I2+1
      TERM=XM1*DVRED(I2)+XM2*DVRED(I2+I111)+XM3*DVRED(I2+2*I111)+
     1XM4*DVRED(I2+3*I111)
      DVRED(I1)=.25*TERM
  105 CONTINUE
  110 CONTINUE
      GO TO 150
  120 CONTINUE
      XJ0=DVRED(1)
      DVRED(3)=DVRED(2)
      I1=3
      I2=11
      DO 124 K1=1,2
      DO 122 KNODE=1,NNODI
      I1=I1+1
      I2=I2+1
      DVRED(I2)=DVRED(I1)
  122 CONTINUE
  124 CONTINUE
  150 CONTINUE
      I11=(ISPACE+KINIK-1)*NNOD3
      DO 170 K1=1,2
      DO 160 K2=1,2
      TERM=ZERO
C*****************
        GXHAT(K1,K2)=ZERO
C*****************
      I1=I11+K2*NNODI
      DO 155 KNODE=1,NNODI
      I1=I1+1
C******************
        KEDU=2*(KNODE-1)+K1
        GXHAT(K1,K2)=GXHAT(K1,K2)+ANORMI(I1)*(EXPU(K1,KNODE)-EDU(KEDU));
C******************
      TERM=TERM+ANORMI(I1)*EXPU(K1,KNODE)
  155 CONTINUE
      GX1(K1,K2)=TERM
  160 CONTINUE
  170 CONTINUE
C***************
        CALL ASET(TF,ZERO,9)
C***************
      CALL ASET(XX1,ZERO,9)
      I1=(ISPACE+KINIK-1)*NGBOM
      DO 190 K1=1,2
      DO 180 K2=1,2
      I1=I1+1
      DO 175 K3=1,2
      XX1(K3,K1)=XX1(K3,K1)+GX1(K3,K2)*GBOM(I1)
C***************
        TF(K3,K1)=TF(K3,K1)+GXHAT(K3,K2)*GBOM(I1)
C**************
  175 CONTINUE
  180 CONTINUE
  190 CONTINUE
      XX1(3,3)=ONE
C************
        TF(3,3)=ONE
C*************
      IF(NPARS.EQ.0) XX1(3,3)=EMCRD(1)/EMCD0(1)
```

```
C**************
        IF(NPARS.EQ.0) TF(3,3)=EMCRDT(1)/EMCD0(1)
C***************
      IF(NNODU.EQ.NNODI) GO TO 63
      I1=NNODI*2+1
      XX1(3,3)=ONE+(-(EMCRD(1)-ANDR(INCRD,NNODI+1))*EU(I1+2)+
     1(EMCRD(2)-ANDR(INCRD+1,NNODI+1))*EU(I1+1)+EU(I1))/EPAR(2)
   63 CONTINUE
C***************
        CALL ACOPY(XX1,TDTF,9)
C*************
      VRATIO=ONE
C PLANE STRESS ASSUMED INCOMPRESSIBLE
      TERM=ONE
      IF(NDI.EQ.2) GO TO 200
      TERM=(XX1(1,1)*XX1(2,2)-XX1(1,2)*XX1(2,1))*XX1(3,3)
      VRATIO=TERM
      VRATIO=DMAX1(VRATIO,.1D0)
      VRATIO=DMIN1(VRATIO,10.D0)
      DVDV0=VRATIO
      DV=DV*VRATIO
  200 CONTINUE
      IF(NINITK.NE.NINITM) GO TO 220
      TERM=VRATIO/TERM
      TERM=DSIGN(DABS(TERM)**THIRD,TERM)
      DO 210 K1=1,2
      DO 210 K2=1,2
      XX1(K1,K2)=XX1(K1,K2)*TERM
  210 CONTINUE
  220 CONTINUE
      TERM=GX1(1,1)*GX1(2,2)-GX1(1,2)*GX1(2,1)
      IF(TERM.GT.ZERO)GO TO 230
      LOK=0
      LOUTBK=1
  230 CONTINUE
      TERM=ONE/TERM
      IF(NDI.EQ.2) XX1(3,3)=TERM
      TEMP=GX1(1,1)
      GX1(1,1)=GX1(2,2)*TERM
      GX1(1,2)=-GX1(1,2)*TERM
      GX1(2,1)=-GX1(2,1)*TERM
      GX1(2,2)=TEMP*TERM
      RETURN
      END
      SUBROUTINE LSOL81(ANORMI,EXPU,ANDR,XX1,EJAC,MNCRDX,MNRLX,
     1EINTS,EPAR,EMCRD,EN,GEOM,GX1,EDU,EMCD0,EBASIS,DUDX,DVRED,EU)
      IMPLICIT REAL*8(A-H,O-Z)
      DIMENSION ANORMI(1),EXPU(MNCRDX,8),ANDR(MNRLX,8),XX1(3,3),
     1EJAC(3,3),EINTS(1),EPAR(2),EMCRD(3),EN(8),GEOM(1),GX1(2,2),EU(1)
     2,EDU(1),EMCD0(3),EBASIS(9),DUDX(3,3),DVRED(1)
      DIMENSION LOCNOD(4)
C
      COMMON/CDV/DV,DVDV0
      COMMON/CEL/LELOP,JETP,JETP1,KEL,KINITK,KINITL,KINTSL,KSPT,NEMCRD,
     1 JINTYP,JEXTYP,JEXTY2,JLIB,NAN24,MDOF,MCRD,
     1 NNODE,NNODU,NTENS,NDI,NSHR,NPR,NINITK,NINITM,NINTSL,NINITLL,NMP,
     4 NPARS,NSHL,NBM,NELZM,NINITS,NEINT,NDOFEL,JUNSYM,NEGEOM,
     5 LNODEK,NNODEP,LBASIS,NNODET,NTENST,NTDOFN,LLUMPM,NOFFT,NNODI,
     1 NSPT,NNOD2,NNOD3,NNOD4,NTDOFE,KSPTT,NINR,NBMB
      COMMON/CNS/INCRD,INU,INDU,INC,INRRES,INV,INA,INT,
     1 INDI,INDI1,IHAF,INSRES,IPORES,INFREF,INSREF,INEIG,INCC
      COMMON/CONSTS/PI,SIN60,COS60,KCROS2(3),KCROS3(3),ZERO,LZERO,LONE,
     1 ONE,TWO,HALF,ABIG,ASMALL,BCBIG,LOCSHR(2,3),THIRD,PRECIS
```

```
     2,BLANK
      COMMON/CONTRO/LINITL,LARGE,LINEAR,LCREEP,LDYN,LHEAT,LSTAT,
     1 LOK,LEPOND,LMOLOD,LMASS,LREST,LFILE,LUNSYM,LPPOPN,LMODST,
     2 LELMOD,LCORT,LTRAMA,LEIGEN,NRHSV,LMESSG,LLHS,LLHSK,LLHSM,
     3 LRHS,LSTRN,LINMAT,LGAPFL,LMDBW,LSUPGN,LGAPS,LGAPEL,LSHELL,
     4 LSUPEL,LGBO,LCONS,LSSS,LSS1,LEXTRP,LDYNC,LEIPRE,LCTU,LPROC,
     5 LADDM,LDAA,LSOLID,LRIKS,LREBAR,LSUBMX,LREBAS,LRHSI,LHYBBM,
     6 LEQUIL,LSTEND,LWPEN,LPORPS,LWPENE,LNOSTP,LSBQU,LAUTO,LITFRE,
     7 LITFRP,LGAPPR,LHYBOK,LMODYN,NRHSI,NRHSP,LCOMPD,LPOUT,LSTRNE
     8 ,LREBA1
      COMMON/COUNT/KINC,MINC,KITER,MITER,FATIME,ATIME,DATIME,
     1 CTIME,DCTIME,DTIME,DDTIME,HTIME,DHTIME,DDTPRE,DATPRE,HTIM1,
     2 DHTIM2,EXFAC,KSTEP,KOUTS,MOUTS,NUMBER,LSHAF1,LOUTBK,DTNEWS,
     3 KITGEN,KMDINC,TTIME,DTMIN,DTMAX,MITEIG,MITXXX,STIME,DSTIME
     4,TPREV,TNEW,TOLD,TEND
C*************************
      DIMENSION TDTF(3,3),TF(3,3),GXHAT(3,3),EMCRDT(3)
      COMMON/DEFGRAD/TDTF,TF
      COMMON/VI/EMCRDT
C*****************************************************************
C
C THIS IS AN ABAQUS SUBROUTINE MODIFIED BY BOYCE TO OBTAIN
C ADDITIONAL INFORMATION NEEDED IN UMAT
C
C*****************************************************************
C
      DATA LOCNOD/1,2,4,3/
C
      IINT=NNOD3*(KINTK-1)
      NGEOM=5
      IGBO=(KINTK-1)*NGEOM
      IF(NINTK.NE.NINTM) GO TO 5
      IINT=IINT+NNOD3*NINR
      IGBO=IGBO+NINR*NGEOM
    5 CONTINUE
      I1=IINT
      DO 10 KNODE=1,NNODI
      I1=I1+1
      EINTS(KNODE)=ANORMI(I1)
      EN(KNODE)=ANORMI(I1)
   10 CONTINUE
      DO 20 K1=1,2
      EMCRD(K1)=ZERO
      EMCD0(K1)=ZERO
        EMCRDT(K1)=ZERO
      I1=INCRD-1+K1
      DO 15 KNODE=1,NNODI
C*************************
        EMCRDT(K1)=EMCRDT(K1)+EN(KNODE)*(EXPU(K1,KNODE)-
     1  EDU(2*KNODE+K1-2))
C*************************
      EMCRD(K1)=EMCRD(K1)+EN(KNODE)*EXPU(K1,KNODE)
      EMCD0(K1)=EMCD0(K1)+EN(KNODE)*ANDR(I1,KNODE)
   15 CONTINUE
   20 CONTINUE
      EMCRD(3)=ZERO
      EMCD0(3)=ZERO
      DO 22 K1=1,9
      EBASIS(K1)=ZERO
   22 CONTINUE
      EBASIS(1)=ONE
      EBASIS(5)=ONE
      EBASIS(9)=ONE
```

```
      I1=IGEO+NGEOM
      DV=GEOM(I1)
      IF(LARGE.NE.0) GO TO 40
      I1=IGEO
      DO 25 K1=1,4
      I1=I1+1
      GX1(K1,1)=GEOM(I1)
   25 CONTINUE
      GO TO 100
   40 CONTINUE
      CALL LSOL8V(XX1,GX1,ANORMI,EXPU,MNCRDX,ANDR,MNRLX,EMCRD,
     1EMCDO,DVRED,GEOM,EU,EPAR,EJAC,EDU)
  100 CONTINUE
      I1=NNODI
      J1=IINT+NNODI
      DO 120 KNODE=1,NNODI
      I1=I1+1
      I2=I1+NNODI
      J1=J1+1
      J2=J1+NNODI
      EINTS(I1)=ANORMI(J1)*GX1(1,1)+ANORMI(J2)*GX1(2,1)
      EINTS(I2)=ANORMI(J1)*GX1(1,2)+ANORMI(J2)*GX1(2,2)
  120 CONTINUE
      IF(LARGE.EQ.0) GO TO 301
      DO 210 K1=1,2
      DO 205 K2=1,2
      EJAC(K1,K2)=ZERO
      GX1(K1,K2)=ZERO
      I2=IINT+NNODI*K2
      I3=K1
      DO 202 KNODE=1,NNODI
      I2=I2+1
      GX1(K1,K2)=GX1(K1,K2)+ANORMI(I2)*(EXPU(K1,KNODE)-HALF*EDU(I3))
      EJAC(K1,K2)=EJAC(K1,K2)+ANORMI(I2)*EDU(I3)
      I3=I3+2
  202 CONTINUE
  205 CONTINUE
  210 CONTINUE
      DET=GX1(1,1)*GX1(2,2)-GX1(1,2)*GX1(2,1)
      DET=ONE/DET
      TEMP=GX1(1,1)
      GX1(1,1)=GX1(2,2)*DET
      GX1(1,2)=-GX1(1,2)*DET
      GX1(2,1)=-GX1(2,1)*DET
      GX1(2,2)=TEMP*DET
      DO 240 K1=1,2
      DO 235 K2=1,2
      DUDX(K1,K2)=ZERO
      DO 232 K3=1,2
      DUDX(K1,K2)=DUDX(K1,K2)+EJAC(K1,K3)*GX1(K3,K2)
  232 CONTINUE
  235 CONTINUE
  240 CONTINUE
      DUDX(3,3)=ZERO
      IF(NNODU.EQ.NNODI) GO TO 255
      X=-ANDR(INCRD,NNODI+1)
      Y=-ANDR(INCRD+1,NNODI+1)
      DO 253 KNODE=1,NNODI
      X=X+EN(KNODE)*(EXPU(1,KNODE)-EDU(2*KNODE-1))
      Y=Y+EN(KNODE)*(EXPU(2,KNODE)-EDU(2*KNODE))
  253 CONTINUE
      I1=2*NNODI+1
      TMDT=ONE+(-X*(EU(I1+2)-EDU(I1+2))+
```

```
     1Y*(EU(I1+1)-EDU(I1+1))+EU(I1)-FDU(I1))/EPAR(2)
      TMDT=XX1(3,3)/TMDT
      IF(TMUT.GT.ASMALL) GO TO 254
      DUDX(3,3)=ZERO
      LOK=0
      LCUTEK=1
      GO TO 255
  254 CONTINUE
      DUDX(3,3)=DLOG(TMDT)
  255 CONTINUE
      IF(NPARS.NE.0) GO TO 300
      IF(NNODI.NE.4)GO TO 260
      DR=ZERO
      R=ZERO
      I1=1
      DO 250 KNODE=1,NNODI
      R=R+EXPU(1,KNODE)-HALF*EDU(I1)
      DR=DR+EDU(I1)
      I1=I1+2
  250 CONTINUE
      GO TO 280
  260 CONTINUE
      DR=ZERO
      R=ZERO
      I1=1
      DO 270 KNODE=1,NNODI
      R=R+EN(KNODE)*(EXPU(1,KNODE)-HALF*EDU(I1))
      DR=DR+EN(KNODE)*EDU(I1)
      I1=I1+2
  270 CONTINUE
  280 CONTINUE
      DUDX(3,3)=DR/R
  300 CONTINUE
  301 CONTINUE
      IF(JINTYP.NE.4002) GO TO 990
      DO 310 K1=1,NNODI
      EINTS(K1)=ZERO
  310 CONTINUE
      EINTS(LOCNOD(KINTK))=ONE
  990 CONTINUE
      RETURN
      END
```

Appendix B

Kinematics of Finite Strain

In the incorporation of the proposed material law for amorphous polymers into a 3-D continuum model encompassing finite strain effects, the multiplicative decompositition of the deformation gradient into elastic and plastic components as originally proposed by Fardshisheh and Onat [4] and Lee [39] was used. This decomposition obtains the plastic deformation gradient, $\mathbf{F}^p$, by elastically unloading without rotation to a stress free state. This operation lumps all of the material rotation into the plastic deformation gradient and enforces symmetry upon the elastic deformation gradient, $\mathbf{F}^e$. This decomposition has the advantage of being unique. In the case of amorphous polymers, this also has the advantage of providing a physically understandable interpretation of the material behavior under imposed deformations. This is due to the assumption that the basic molecular structure of the polymer plastically deforms affinely. However, in the more widely researched area of metallic materials, and, in particular, of single crystals, this decomposition does not provide as convenient a conceptual framework of the deformation of crystalline materials as used by Asaro and others [41, 42, 46]. This is because the basic crystal lattice structure does not deform affinely, and the rotation of the lattice structure is perceived to be an elastic deformation as will be discussed

later. Other decompositions, in particular, that used by Asaro [41], have been used to describe the deformation of single crystals with success. For purposes of notational distinction, the two representations discussed in this appendix will be referred to as the "Asaro" and "Onat" representations. The basic framework of the Asaro representation works well for single crystals and has also been extended to polycrystalline materials [40, 44].

The topic of the representation of inelastic material behavior under finite strains and rotations has been the subject of much debate in the recent plasticity literature [39, 40, 41, 44, 44, 45]. It is not attempted to review this extensive topic here. However, the representation applied to the constitutive model presented in this thesis, the Onat representation, is also general enough to apply to other material models although it has not been carried out to completion on a practical problem to the author's present knowledge. Here, it will be demonstrated that the elastic-plastic decomposition of the deformation gradient and its associated rate kinematics proposed by Onat is indeed general enough to apply to the deformation of single crystals. In this representation, the orientation of the lattice is kept track of by updating corresponding tensor state variables. The Onat representation is shown to be more cumbersome for the case of single crystals than that used by Asaro. However, the point to be made is that the Onat representation is general enough to encompass constitutive laws for materials other than amorphous polymers and happens to be a relatively simple way of representing the large inelastic deformation of amorphous polymers because of the nature of the structure of these materials. The problem of the single crystal was chosen to demonstrate the generality of the Onat representation because of the community "acceptance" of the Asaro representation of this problem.

This appendix will first review the basic kinematics of the Onat representation and the Asaro representation. Second, the problem of the deformation of a "planar" single crystal containing a primary and a conjugate slip system will be examined. A solution as published by Asaro [41] will be presented as will the corresponding solution obtained using the Onat representation. The two solutions will be shown to yield identical results.

B.1 Kinematics

The basic kinematics of the Onat and Asaro representations of inelastic behavior under finite strains and rotations are presented. Terms which are specifically Onat terms will be right-subscripted with an O; terms which are specifically Asaro terms will be right-subscripted with an A. Terms which are common to both, such as the deformation gradient, $\mathbf{F}$, and the velocity gradient, $\mathbf{L}$, will not be subscripted.

Some basic kinematic definitions and terminology are now given. In general, a material point in its original undeformed configuration will be represented by $\mathbf{X}$. The same material point in the deformed configuration will be represented by $\mathbf{x}$. The deformation gradient, $\mathbf{F}$,is given by:

$$\mathbf{F} = \nabla_{\mathbf{X}}\mathbf{x}. \tag{B.1}$$

The velocity gradient, $\mathbf{L}$, is given by:

$$\mathbf{L} = \nabla_{\mathbf{x}}\mathbf{v} = \dot{\mathbf{F}}\mathbf{F}^{-1} = \mathbf{D} + \mathbf{W}; \tag{B.2}$$

where $\mathbf{D}$, the rate of deformation, is the symmetric part of $\mathbf{L}$, and $\mathbf{W}$, the spin, is the anti-symmetric part of $\mathbf{L}$.

B.1.1 Basic Kinematics of Onat Representation

Multiplicative Decomposition of the Deformation Gradient

$$\mathbf{F} = \mathbf{F}_O^e \mathbf{F}_O^p \tag{B.3}$$

$$\mathbf{F}_O^{eT} = \mathbf{F}_O^e \tag{B.4}$$

where $\mathbf{F}_O^e$ is the symmetric elastic deformation gradient, and $\mathbf{F}_O^p$ is the plastic deformation gradient obtained by elastic unloading without rotation to a stress free state.

Velocity Gradient

$$\begin{aligned} &\mathbf{L} = \dot{\mathbf{F}}\mathbf{F}^{-1} = \mathbf{D} + \mathbf{W}; \\ &\mathbf{L} = \dot{\mathbf{F}}_O^e \mathbf{F}_O^{e-1} + \mathbf{F}_O^e \dot{\mathbf{F}}_O^p \mathbf{F}_O^{p-1} \mathbf{F}_O^{e-1}; \\ &\mathbf{L}_C^p = \dot{\mathbf{F}}_O^p \mathbf{F}_O^{p-1} = \mathbf{D}_O^p + \mathbf{W}_O^p; \end{aligned} \tag{B.5}$$

where $\mathbf{L}_O^p$ is the Onat plastic velocity gradient which is in the unloaded configuration, $\mathbf{F}_O^p$; $\mathbf{D}_O^p$ is the rate of deformation of the unloaded configuration which must be constitutively prescribed; and $\mathbf{W}_O^p$ is the plastic spin which is algebraically prescribed due to the symmetry restriction on $\mathbf{F}_O^e$. This is shown immediately below:

$$\begin{aligned} &\dot{\mathbf{F}}_O^e = (\mathbf{D} + \mathbf{W})\mathbf{F}_O^e - \mathbf{F}_O^e(\mathbf{D}_O^p + \mathbf{W}_O^p), \\ &\text{and,} \\ &\dot{\mathbf{F}}_O^e = (\dot{\mathbf{F}}_O^e)^T = \mathbf{F}_O^e(\mathbf{D} - \mathbf{W}) - (\mathbf{D}_O^p - \mathbf{W}_O^p)\mathbf{F}_O^e; \\ &\text{or,} \\ &(\mathbf{D} + \mathbf{D}_O^p)\mathbf{F}_O^e - \mathbf{F}_O^e(\mathbf{D} + \mathbf{D}_O^p) = \mathbf{F}_O^e(\mathbf{W}_O^p - \mathbf{W}) - (\mathbf{W}_O^p - \mathbf{W})\mathbf{F}_O^e; \end{aligned} \tag{B.6}$$

therefore, $\mathbf{W}_O^p$ falls out algebraically to be:

$$\mathbf{W}_O^p = \mathbf{W} - \mathcal{W}_O[\mathbf{D} + \mathbf{D}_O^p]; \tag{B.7}$$

where $\mathcal{W}_O$ is a fourth order tensor which is a function of $\mathbf{F}_O^e$ and is of order elastic strain. Therefore, $\mathbf{W}_O^p$ must not be constitutively prescribed.

B.1.2 Basic Kinematics of Asaro Representation

Multiplicative Decomposition of the Deformation Gradient

$$\mathbf{F} = \mathbf{F}_A^* \mathbf{F}_A^p \tag{B.8}$$

$$\mathbf{F}_A^* = \mathbf{F}_A^e \mathbf{F}_A^R \tag{B.9}$$

where $\mathbf{F}_A^p$ is the deformation gradient due to plastic slip; $\mathbf{F}_A^R$ is the residual rotation of the lattice; and $\mathbf{F}_A^e$ is the elastic deformation gradient. In other terms, the gradient $\mathbf{F}_A^*$ accounts for the stretching and rotation of the lattice and $\mathbf{F}_A^p$ accounts for plastic shearing on the crystal slip planes.

Velocity Gradient

$$\begin{aligned} &\mathbf{L} = \dot{\mathbf{F}}\mathbf{F}^{-1} = \mathbf{D} + \mathbf{W}; \\ &\mathbf{L} = \dot{\mathbf{F}}_A^* \mathbf{F}_A^{*-1} + \mathbf{F}_A^* \dot{\mathbf{F}}_A^p \mathbf{F}_A^{p-1} \mathbf{F}_A^{*-1}; \\ &\mathbf{L}_A^p = \mathbf{F}_A^* \dot{\mathbf{F}}_A^p \mathbf{F}_A^{p-1} \mathbf{F}_A^{*-1} = \mathbf{D}_A^p + \mathbf{W}_A^p; \end{aligned} \tag{B.10}$$

where $\mathbf{L}_A^p$ is the Asaro plastic velocity gradient which is in the deformed configuration, $\mathbf{F}$, (note that it is in a different configuration than the Onat plastic velocity gradient); $\mathbf{D}_A^p$ and $\mathbf{W}_A^p$ are the rate of plastic deformation and the plastic spin, respectively. These last two terms must both be constitutively prescribed in this formulation. This is done immediately below.

Constitutive Law for $\mathbf{D}_A^p$ and $\mathbf{W}_A^p$

A crystal slip system may be defined by the dyadic $\mathbf{s}^\alpha \otimes \mathbf{m}^\alpha$, where the vector $\mathbf{s}^\alpha$ lies along the α slip plane and the vector $\mathbf{m}^\alpha$ is perpendicular to this slip plane. The plastic velocity gradient in the Asaro unloaded configuration is given by $\tilde{\mathbf{L}}_A^p = \dot{\mathbf{F}}_A^p \mathbf{F}_A^{p-1}$. This is constitutively obtained by the summation of the rate of plastic straining, $\dot{\gamma}^\alpha$, of each slip system $(\mathbf{s}^\alpha \otimes \mathbf{m}^\alpha)$:

$$\tilde{\mathbf{L}}_A^p = \sum_\alpha \dot{\gamma}^\alpha \mathbf{s}^\alpha \otimes \mathbf{m}^\alpha. \tag{B.11}$$

The plastic velocity gradient in the loaded configuration is obtained by convecting the slip system to this configuration:

$$\mathbf{s}^{*\alpha} \otimes \mathbf{m}^{*\alpha} = \mathbf{F}_A^* \mathbf{s}^\alpha \otimes \mathbf{F}_A^* \mathbf{m}^\alpha. \tag{B.12}$$

This gives the following:

$$\mathbf{L}_A^p = \sum_\alpha \dot{\gamma}^\alpha \mathbf{s}^{*\alpha} \otimes \mathbf{m}^{*\alpha}. \tag{B.13}$$

The rate of plastic deformation and the plastic spin in the loaded and unloaded configurations may be obtained by first decomposing the plastic slip direction tensors $\mathbf{s}^\alpha \otimes \mathbf{m}^\alpha$ and $\mathbf{s}^{*\alpha} \otimes \mathbf{m}^{*\alpha}$ into their symmetric and antisymmetric parts:

$$\begin{aligned}
\tilde{\mathbf{S}}^\alpha &= \tfrac{1}{2}(\mathbf{s}^\alpha \otimes \mathbf{m}^\alpha + \mathbf{m}^\alpha \otimes \mathbf{s}^\alpha); \\
\tilde{\mathbf{A}}^\alpha &= \tfrac{1}{2}(\mathbf{s}^\alpha \otimes \mathbf{m}^\alpha - \mathbf{m}^\alpha \otimes \mathbf{s}^\alpha); \\
\mathbf{S}^\alpha &= \tfrac{1}{2}(\mathbf{s}^{*\alpha} \otimes \mathbf{m}^{*\alpha} + \mathbf{m}^{*\alpha} \otimes \mathbf{s}^{*\alpha}); \\
\mathbf{A}^\alpha &= \tfrac{1}{2}(\mathbf{s}^{*\alpha} \otimes \mathbf{m}^{*\alpha} - \mathbf{m}^{*\alpha} \otimes \mathbf{s}^{*\alpha});
\end{aligned} \tag{B.14}$$

This gives:

$$\begin{aligned}
\mathbf{D}_A^p &= \textstyle\sum_\alpha \dot{\gamma}^\alpha \mathbf{S}^\alpha; \\
\mathbf{W}_A^p &= \textstyle\sum_\alpha \dot{\gamma}^\alpha \mathbf{A}^\alpha; \\
\tilde{\mathbf{D}}_A^p &= \textstyle\sum_\alpha \dot{\gamma}^\alpha \tilde{\mathbf{S}}^\alpha; \\
\tilde{\mathbf{W}}_A^p &= \textstyle\sum_\alpha \dot{\gamma}^\alpha \tilde{\mathbf{A}}^\alpha.
\end{aligned} \tag{B.15}$$

The rates $\mathbf{D}_A^p$ and $\mathbf{W}_A^p$ have now been constitutively prescribed in terms of the plastic strain rates of the individual slip systems. Later in this appendix, the specific problem considering a planar single crystal with two slip systems and a constitutive law for $\dot{\gamma}^\alpha$ will be presented. For the present, we can see that Asaro's representation can appropriately account for the material and lattice deformation of the crystal. The lattice orientation is properly monitored because the plastic spin is constitutively obtained.

In the current context of the Onat representation, there is no room for monitoring the orientation of the crystal lattice. Therefore, another item must be added to this basic framework. Onat has shown theoretically that his representation can accommodate

the internal state and orientation of a material element by the updating of appropriate scalar and tensor state variables [43]. Here, we will carry out this theorem for the practical problem of the planar single crystal. This will be done by first finding the relationship between Onat's and Asaro's representations.

The relationship between Onat's decomposition and Asaro's decomposition is found by first pictorially examining a body as it goes from its original undeformed configuration to a deformed configuration as shown in Figure B1. Here, the "unloaded" states as defined by Onat's $\mathbf{F}_O^p$ and Asaro's $\mathbf{F}_A^p$ are also depicted. In order to account for the lattice orientation in the Onat representation, an appropriate tensor state variable must be constitutively updated. This can be done by finding the relationship between Asaro's unloaded configuration, which is a stress free state containing no lattice deformation or changes in orientation, and Onat's unloaded configuration which is a stress free state (no lattice deformation) that contains any changes in lattice orientation.

Once again, we examine Asaro's elastic-plastic decomposition of the deformation gradient, $\mathbf{F} = \mathbf{F}_A^* \mathbf{F}_A^p$. The lattice deformation gradient, $\mathbf{F}_A^*$, may be broken down into its left stretch and rotation tensors via the polar decomposition theorem to give:

$$\begin{aligned} \mathbf{F}_A^* &= \mathbf{V}^* \mathbf{R}^*; \\ \mathbf{F} &= \mathbf{V}^* \mathbf{R}^* \mathbf{F}_A^p; \end{aligned} \tag{B.16}$$

where $\mathbf{V}^*$ is the symmetric tensor which describes the elastic stretch of the material. Onat has shown that the decomposition $\mathbf{F} = \mathbf{F}_O^e \mathbf{F}_O^p$, where $\mathbf{F}_O^e$ is a symmetric stretch tensor, yields a unique $\mathbf{F}_O^e$. Therefore, since both $\mathbf{V}^*$ and $\mathbf{F}_O^e$ describe the elastic stretch incurred by the solid, we must conclude that:

$$\mathbf{V}^* = \mathbf{F}_O^e. \tag{B.17}$$

In other words, if we elastically unload to a stress-free configuration via $\mathbf{F}_O^{e-1} = \mathbf{F}_O^{e-T}$,then $\mathbf{F}_O^e$ is unique. Therefore, if we elastically unload to a stress-free state via

$\mathbf{V}^{*-1}$, it must be the same stress-free state described by $\mathbf{F}^p_O$. The rotation matrix $\mathbf{R}^{*T}$ keeps us in an unloaded stress-free configuration and simply rotates the lattice to its appropriate stress-free configuration which would be its initial undeformed configuration. Therefore, we obtain:

$$\begin{aligned} &\mathbf{F}^p_O = \mathbf{R}^* \mathbf{F}^p_A; \\ &\text{or, alternatively,} \\ &\mathbf{F}^p_A = \mathbf{R}^{*T} \mathbf{F}^p_O; \end{aligned} \tag{B.18}$$

where $\mathbf{R}^*$ is the rotation tensor which defines the lattice orientation. We may account for the lattice orientation using the Onat representation by observing that the slip system convects from the reference configuration to Onat's unloaded configuration via $\mathbf{R}^*$:

$$\mathbf{s}^\alpha_O \otimes \mathbf{m}^\alpha_O = \mathbf{R}^* \mathbf{s}^\alpha \otimes \mathbf{R}^* \mathbf{m}^\alpha. \tag{B.19}$$

The tensor $\mathbf{s}^\alpha_O \otimes \mathbf{m}^\alpha_O$ represents the slip system in Onat's unloaded configuration and may be decomposed into symmetric and antisymmetric parts:

$$\mathbf{S}^\alpha_O = \frac{1}{2}[\mathbf{s}^\alpha_O \otimes \mathbf{m}^\alpha_O + \mathbf{m}^\alpha_O \otimes \mathbf{s}^\alpha_O]; \tag{B.20}$$

$$\mathbf{A}^\alpha_O = \frac{1}{2}[\mathbf{s}^\alpha_O \otimes \mathbf{m}^\alpha_O - \mathbf{m}^\alpha_O \otimes \mathbf{s}^\alpha_O]; \tag{B.21}$$

The tensors $\mathbf{S}^\alpha_O$ and $\mathbf{A}^\alpha_O$ are the state variables needed in the Onat representation. The rate of change of these state variables is found to be given by:

$$\dot{\mathbf{S}}^\alpha_O = [\dot{\mathbf{R}}^* \mathbf{R}^{*T}] \mathbf{S}^\alpha_O + \mathbf{S}^\alpha_O [\dot{\mathbf{R}}^* \mathbf{R}^{*T}]^T; \tag{B.22}$$

$$\dot{\mathbf{A}}^\alpha_O = [\dot{\mathbf{R}}^* \mathbf{R}^{*T}] \mathbf{A}^\alpha_O + \mathbf{A}^\alpha_O [\dot{\mathbf{R}}^* \mathbf{R}^{*T}]^T; \tag{B.23}$$

where $\dot{\mathbf{R}}^* \mathbf{R}^{*T}$ is shown below to be the lattice spin.

We had previously obtained the velocity gradient in terms of Asaro's decomposition to be:

$$\mathbf{L} = \dot{\mathbf{F}}_A^* \mathbf{F}_A^{*-1} + \mathbf{F}_A^* \dot{\mathbf{F}}_A^p \mathbf{F}_A^{p-1} \mathbf{F}_A^{*-1}. \tag{B.24}$$

By substituting in $\mathbf{F}_A^* = \mathbf{V}^* \mathbf{R}^*$ and $\mathbf{V}^* = \mathbf{F}_O^e$, we obtain:

$$\mathbf{L} = \dot{\mathbf{F}}_O^e \mathbf{F}_O^{e-1} + \mathbf{F}_O^e \dot{\mathbf{R}}^* \mathbf{R}^{*T} \mathbf{F}_O^{e-1} + \mathbf{F}_O^e \mathbf{R}^* \dot{\mathbf{F}}_A^p \mathbf{F}_A^{p-1} \mathbf{R}^{*T} \mathbf{F}_O^{e-1}. \tag{B.25}$$

However, we also know that:

$$\mathbf{L} = \dot{\mathbf{F}}_O^e \mathbf{F}_O^{e-1} + \mathbf{F}_O^e \dot{\mathbf{F}}_O^p \mathbf{F}_O^{p-1} \mathbf{F}_O^{e-1}. \tag{B.26}$$

This leads to:

$$\mathbf{L}_O^p = \dot{\mathbf{F}}_O^p \mathbf{F}_O^{p-1} = \dot{\mathbf{R}}^* \mathbf{R}^{*T} + \mathbf{R}^* \tilde{\mathbf{L}}_A^p \mathbf{R}^{*T}. \tag{B.27}$$

A physical interpretation of this equation is that the $\mathbf{R}^* \tilde{\mathbf{L}}_A^p \mathbf{R}^{*T}$ term rotates the velocity gradient of the Asaro unloaded configuration (see Figure B1) into Onat's unloaded configuration. The $\dot{\mathbf{R}}^* \mathbf{R}^{*T}$ term accounts for the rate of this rotation and is the spin of the lattice. In other words, $\mathbf{R}^*$ is effectively a time-dependent observer transformation relating the two different elastically unloaded configurations, c.f. B.18. Since symmetric and anti-symmetric tensors remain as such under an orthogonal transformation and since $\mathbf{R}^*$ is an orthogonal tensor, we can conclude that:

$$\begin{aligned} &\mathbf{W}_O^p = \dot{\mathbf{R}}^* \mathbf{R}^{*T} + \mathbf{R}^* \tilde{\mathbf{W}}_A^p \mathbf{R}^{*T}; \\ &\text{and,} \\ &\mathbf{D}_O^p = \mathbf{R}^* \tilde{\mathbf{D}}_A^p \mathbf{R}^{*T}. \end{aligned} \tag{B.28}$$

These tensors may also be expressed in terms of the slip systems in Onat's unloaded state to be:

$$\mathbf{W}_O^p = \dot{\mathbf{R}}^* \mathbf{R}^{*T} + \sum_\alpha \dot{\gamma}^\alpha \mathbf{A}_O^\alpha; \tag{B.29}$$

and

$$\mathbf{D}_O^p = \sum_\alpha \dot{\gamma}^\alpha \mathbf{S}_O^\alpha. \tag{B.30}$$

Therefore, the lattice spin, $\dot{\mathbf{R}}^*\mathbf{R}^{*T}$, is given by:

$$\mathbf{\Omega}_L \equiv \dot{\mathbf{R}}^*\mathbf{R}^{*T} = \mathbf{W}_O^p - \sum_\alpha \dot{\gamma}^\alpha \mathbf{A}_O^\alpha. \tag{B.31}$$

Equations (B22), (B23), and (B30) may then be used to update the state via, for example, a simple forward Euler integration scheme:

$$(\mathbf{S}_O^\alpha)_{t+\Delta t} = (\mathbf{S}_O^\alpha)_t + (\dot{\mathbf{S}}_O^\alpha)_t \Delta t; \tag{B.32}$$

$$(\mathbf{A}_O^\alpha)_{t+\Delta t} = (\mathbf{A}_O^\alpha)_t + (\dot{\mathbf{A}}_O^\alpha)_t \Delta t. \tag{B.33}$$

The state variables $\mathbf{S}$ and $\mathbf{A}$ may also be updated via an incremental orthogonal transformation corresponding to $\mathbf{\Omega_L}\Delta t$, where the corotational rates of $\mathbf{S}$ and $\mathbf{A}$ are given by:

$$\mathbf{S}^\square = \dot{\mathbf{S}} - \mathbf{\Omega}_L\mathbf{S} + \mathbf{S}\mathbf{\Omega}_L = 0, \tag{B.34}$$

$$\mathbf{A}^\square = \dot{\mathbf{A}} - \mathbf{\Omega}_L\mathbf{A} + \mathbf{A}\mathbf{\Omega}_L = 0, \tag{B.35}$$

and the "intermediate" rotation, $\mathbf{Q}$, must therefore satisfy [54]:

$$\dot{\mathbf{Q}} = \mathbf{\Omega}_L\mathbf{Q}, \tag{B.36}$$

$$\mathbf{Q}(0) = \mathbf{I}, \tag{B.37}$$

or $\mathbf{Q} = exp(\mathbf{\Omega}_L\Delta t)$. The state variables $\mathbf{S}$ and $\mathbf{A}$ are then updated via:

$$(\mathbf{S})_{t+\Delta t} = \mathbf{Q}(\mathbf{S})_t\mathbf{Q}^T, \tag{B.38}$$

$$(\mathbf{A})_{t+\Delta t} = \mathbf{Q}(\mathbf{A})_t\mathbf{Q}^T. \tag{B.39}$$

The preceding equations are easier to visualize if we simplify to the case of no elastic stretching, i.e., $\mathbf{F}_O^e = \mathbf{V}^* = \mathbf{I}$. In this case, Onat's expressions become:

$$
\begin{aligned}
\mathbf{F} &= \mathbf{F}_O^p; \\
\mathbf{L} &= \mathbf{L}_O^p; \\
\mathbf{D} &= \mathbf{D}_O^p = \textstyle\sum_\alpha \dot{\gamma}^\alpha \mathbf{S}_O^\alpha; \\
\mathbf{W} &= \mathbf{W}_O^p; \\
\mathbf{\Omega}_L &= \mathbf{W} - \textstyle\sum_\alpha \dot{\gamma}^\alpha \mathbf{A}_O^\alpha.
\end{aligned}
\tag{B.40}
$$

Asaro's expressions become:

$$
\begin{aligned}
\mathbf{F} &= \mathbf{R}^* \mathbf{F}_A^p; \\
\mathbf{L} &= \dot{\mathbf{R}}^* \mathbf{R}^{*T} + \mathbf{R}^* \dot{\mathbf{F}}_A^p \mathbf{F}_A^{p-1} \mathbf{R}^{*T}; \\
\mathbf{D} &= \mathbf{R}^* \tilde{\mathbf{D}}_A^p \mathbf{R}^{*T}; \\
\mathbf{W} &= \dot{\mathbf{R}}^* \mathbf{R}^{*T} + \mathbf{R}^* \tilde{\mathbf{W}}_A^p \mathbf{R}^{*T}.
\end{aligned}
\tag{B.41}
$$

B.2 Example Problem: Planar Single Crystal

We now examine the problem of the planar single crystal with two shear slip systems and no elastic stretching. This problem has been solved by Pierce, Asaro, and Needleman [46]. This solution will be repeated here. A solution for this same problem using Onat's method will also be presented.

We begin with some definitions of basic parameters to be used in the problem as illustrated in Figure B2. The primary and conjugate slip systems are defined by the vector pairs $(\mathbf{s}^p, \mathbf{m}^p)$ and $(\mathbf{s}^c, \mathbf{m}^c)$, respectively. The position of the primary system is given by the angle ϕ clockwise from the axis of imposed tensile deformation, $\mathbf{e}_2$. The position of the conjugate system is given by the angle ψ counterclockwise from the axis of imposed tensile deformation, $\mathbf{e}_2$. Initial conditions on these angles were taken to be: $\phi(0) = 40^o$ and $\psi(0) = 20^o$. The angle β in the figure describes the orientation of the lattice with initial condition of $\beta(0) = 0$. Therefore, the lattice orientation tensor $\mathbf{R}^*$ is found to be:

$$
\mathbf{R}^* = \begin{matrix} cos\beta & -sin\beta \\ sin\beta & cos\beta \end{matrix}
\tag{B.42}
$$

The rate of plastic shear straining on the primary and conjugate slip systems is given by $\dot{\gamma}^p$ and $\dot{\gamma}^c$, respectively. The visco-plastic constitutive law for these $\dot{\gamma}^\alpha$ is given by the power-law relation:

$$\dot{\gamma}^\alpha = \dot{a}^\alpha \left(\frac{\tau^\alpha}{g^\alpha}\right)^m ; \tag{B.43}$$

where $\dot{a}^\alpha$ is a parameter such that $\dot{a}^\alpha = \dot{\gamma}^\alpha$ when $\tau^\alpha = g^\alpha$; τ^α is the resolved shear stress on that slip system; g^α represents the internal structure of the material and may evolve with strain hardening; and m indicates the rate sensitivity of the material. The internal structure is taken to evolve according to:

$$\dot{g}^\alpha = \sum h_{\alpha\beta}\dot{\gamma}^\beta ; \tag{B.44}$$

where $h_{\alpha\beta}$ is a hardness slope natrix and therefore accounts for latent as well as self strain hardening. For this example, we take:

$$\begin{array}{ll} h_{pc} = q h_{pp}; & h_{cp} = q h_{cc}; \\ h_{pp} = h; & h_{cc} = h; \end{array} \tag{B.45}$$

where,

$$h = h_0 sech^2 \left(\frac{h_0(\gamma^p + \gamma^c)}{\tau_s - \tau_0}\right); \tag{B.46}$$

where $h_0 = 8.9\tau_0$ and $\tau_s = 1.8\tau_0$ for aluminum 2.8 wt.% copper alloys and $1.0 \leq q \leq 1.4$ [46].

B.2.1 Solution Using Asaro's Representation

The relevant material law information has now been given and we now move onto the solution of pulling this single crystal in tension along the x_2 axis. Since we are pulling in simple tension, points which lie along the x_2 axis will remain along this axis giving:

$$\mathbf{F} \cdot \mathbf{e}_2 = \lambda \mathbf{e}_2 \tag{B.47}$$

where λ is the stretch in this direction. Using Asaro's representation this results in:

$$tan\beta = F^p_{A12}/F^p_{A22} \tag{B.48}$$

and

$$\dot{\beta} = cos^2\beta \left[\frac{\dot{F}^p_{A12}}{F^p_{A22}} - \frac{F^p_{A12}\dot{F}^p_{A22}}{F^{p2}_{A22}} \right]; \tag{B.49}$$

where $\dot{\mathbf{F}}^p_A$ is obtained from:

$$\dot{\mathbf{F}}^p_A = [\dot{\gamma}^p \mathbf{s}^p \mathbf{m}^p + \dot{\gamma}^e \mathbf{s}^e \mathbf{m}^e] \mathbf{F}^I_A. \tag{B.50}$$

These equations together with the resolved shear stresses:

$$\begin{aligned} \tau^p &= \tfrac{\sigma}{2} sin\,(2\phi - 2\beta)\,; \\ \tau^e &= \tfrac{\sigma}{2} sin\,(2\psi - 2\beta)\,; \end{aligned} \tag{B.51}$$

are used to update the state of the material. The orientation of the lattice, β, as a function of the amount of plastic strain on the primary system was found for the following three cases (all with $\dot{a} = 10^{-2}$): $m = 50$, $q = 1.4$; $m = 50$, $q = 1.0$; $m = 10$, $q = 1.0$. The results are shown in Figure B3 and were originally calculated by Pierce, et al [46]. The short FORTRAN program written to do the above calculations is included in section B3.1.

B.2.2 Solution Using Onat Representation

This problem may also be solved using Onat's representation and including the lattice orientation as a state variable. This can be done by integrating equations (B22) and (B23) as suggested in section B1.2.

Since we are considering an elastically rigid single crystal, $\mathbf{F}^e_O = \mathbf{I}$, Onat's plastic deformation gradient is equal to the total deformation gradient:

$$\mathbf{F}_O^p = \mathbf{F}. \tag{B.52}$$

Similarly, Onat's plastic spin is equal to the total spin:

$$\mathbf{W}_O^p = \mathbf{W} = skew[\dot{\mathbf{F}}\mathbf{F}^{-1}] = skew[\dot{\mathbf{F}}_O^p\mathbf{F}_O^{p-1}]. \tag{B.53}$$

This spin does not account for the lattice orientation. The lattice spin is given by:

$$\mathbf{\Omega}_L \equiv \dot{\mathbf{R}}^*\mathbf{R}^{*T} = [\mathbf{W}_O^p - \dot{\gamma}^p\mathbf{A}_O^p - \dot{\gamma}^c\mathbf{A}_O^c]. \tag{B.54}$$

The lattice orientation may then be updated with equations (B.32) and (B.33) or (B.34 - B.38). with the initial conditions:

$$(\mathbf{S}_O^\alpha)_{t=0} = \frac{1}{2}[\mathbf{s}^\alpha \otimes \mathbf{m}^\alpha + \mathbf{m}^\alpha \otimes \mathbf{s}^\alpha], \tag{B.55}$$

$$(\mathbf{A}_O^\alpha)_{t=0} = \frac{1}{2}[\mathbf{s}^\alpha \otimes \mathbf{m}^\alpha - \mathbf{m}^\alpha \otimes \mathbf{s}^\alpha], \tag{B.56}$$

Since this is a 2-D problem, the lattice orientation may be given by the angle β:

$$\beta = tan^{-1}\frac{R_{21}^*}{R_{22}^*}. \tag{B.57}$$

These equations together with the constitutive laws (B.43 - B.46) stated earlier are used to update the state of the material. The FORTRAN program written to do the above calculations is included in section B3.2. The solution for the lattice orientation, β, as a function of the plastic strain on the primary slip system, γ^p, was found for the same three cases as the Asaro solution. The results are plotted against the Asaro results in Figure B3 and are noted to be identical.

It is important to note that the solution processes using the two different representations are very similar. However, they are operationally different in the manner in which the lattice orientation is taken into account. The kinematics of the Asaro elastic-plastic decomposition of the deformation gradient specifically includes the lattice orientation.

The Onat kinematical decomposition is more general and does not explicitly contain the lattice orientation which must be implicitly retained and "constitutively" updated as a tensor state variable. Therefore, this representation requires an additional tensor to properly describe the material behavior of a single crystal. However, in this case, the Onat representation only had one tensor in the decomposition $\mathbf{F} = \mathbf{F}_O^p$. Therefore, both representations would require the same storage space during numerical integration.

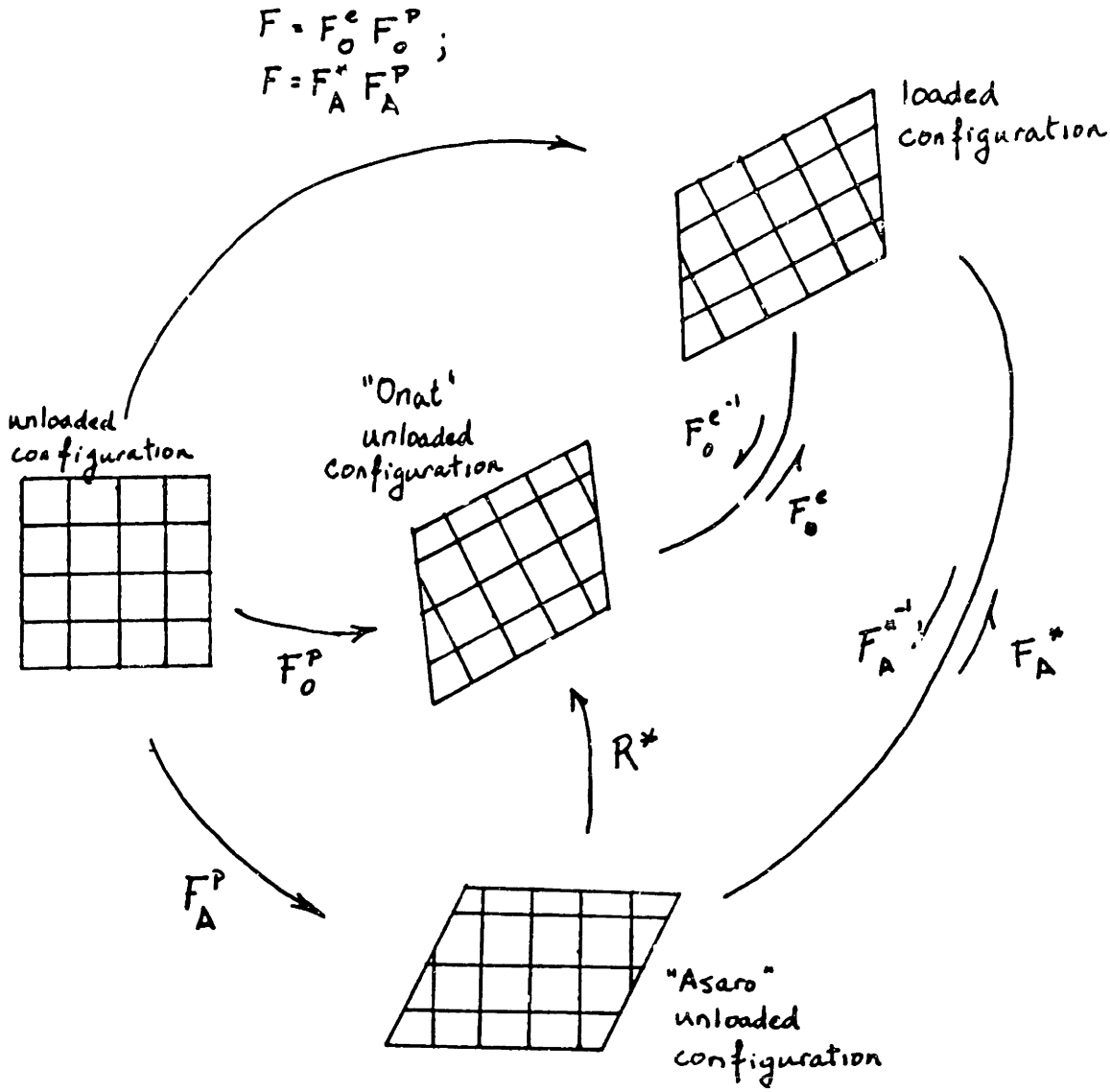

Figure B1. Schematic of a deforming body depicting the "unloaded" states as described by the "Asaro" and "Onat" representations.

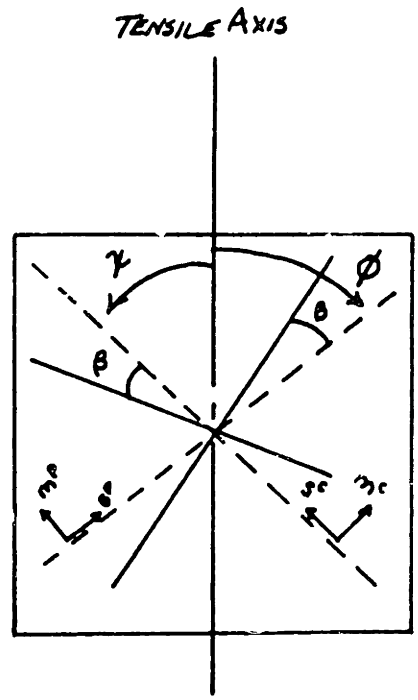

Figure B2. Schematic of the planar single crystal containing two slip systems. The primary and conjugate systems are depicted with respect to the tensile load axis.

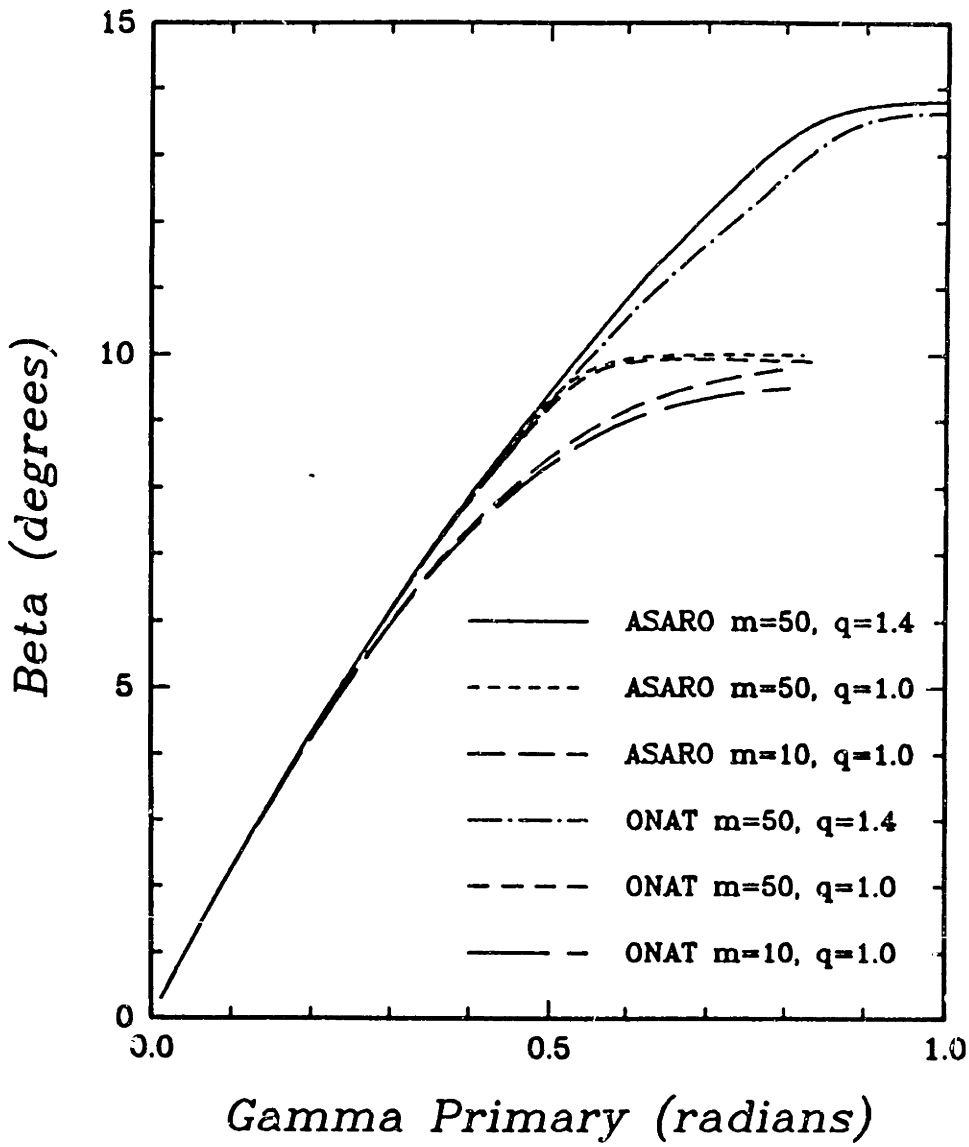

Figure B3. Lattice orientation, β, as a function of the amount of plastic strain on the primary slip system for the three cases of: m=50, q=1.4; m=50, q=1.0; and m=10, q=1.0 as computed using the Asaro and Onat representations.

Appendix C

Extrusion Exit Temperature Profile

In the hydrostatic extrusion process of this paper, the extrudate exits the die, where all processing was conducted isothermally at $90°C$, into a room temperature environment. The cooling of the extrudate from the $90°C$ processing temperature to the $25°C$ room temperature depends on the thermal properties of the material, the dimensions of the extrudate, and the velocity at which it enters the room. We first note that the radius of the extrudate is only 0.0035m, i.e. it is a very slender cylinder. Therefore, a very good estimate of the exit temperature profile can be found from a 1-D heat transfer analysis. We also note that the exit velocity is very small, $\sim$1mm/min, for the extrusion analyzed in this paper. Therefore, we may neglect any effects of forced convection. We see that we are now left with the standard fin problem of steady state heat conduction [47]. We will interpret the steady state temperature at a distance, x, along the fin to be the temperature of the extrudate after exiting that distance from the die. Our governing equations begin with the conservation of energy which requires the heat entering a differential element of the fin to be equal to the heat leaving that element:

$$q_{cond_{in}} = q_{cond_{out}} + q_{conv}. \tag{C.1}$$

This results in the following differential equation for the temperature, Θ:

$$k\frac{d^2\Theta}{dx^2} - \frac{2h}{R}(\Theta - \Theta_\infty) = 0, \tag{C.2}$$

where, k is the thermal conductivity of the material, h is the heat transfer or film coefficient, R is the extrudate radius, and Θ_∞ is the ambient temperature. The boundary conditions require:

$$\Theta(x = 0) = \Theta_0 = 90°C; \tag{C.3}$$

$$\Theta(x = \infty) = \Theta_\infty = 25°C. \tag{C.4}$$

These conditions give the following temperature distribution:

$$\Theta = \Theta_\infty + (\Theta_0 - \Theta_\infty)\, exp\left[-\sqrt{\frac{2h}{Rk}}x\right]. \tag{C.5}$$

If we include effects of axial convection, we must include an additional heat flux due to the rate of change of internal energy of a volume element, q_{c_p}:

$$q_{c_p} = \rho\pi R^2 dx c_p \frac{d\Theta}{dt}; \tag{C.6}$$

where, ρ is the material density, c_p is the specific heat per unit mass of the material, and t is time. Invoking the chain rule, we may write:

$$\frac{d\Theta}{dt} = v\frac{d\Theta}{dx}; \tag{C.7}$$

where, v is the velocity of the extrudate. This modifies the governing equation to read:

$$k\frac{d^2\Theta}{dx^2} - \frac{2h}{R}(\Theta - \Theta_\infty) = \rho c_p v\frac{d\Theta}{dx}, \tag{C.8}$$

which gives a temperature distribution of:

$$\Theta = \Theta_\infty + (\Theta_0 - \Theta_\infty)\, exp\left[-\left[\sqrt{\left(\frac{\rho v c_p}{2k}\right)^2 + \frac{2h}{Rk}} - \frac{\rho v c_p}{2k}\right]x\right]. \tag{C.9}$$

The exit temperature profile was also approximated with a finite element heat transfer analysis considering a long slender rod of length L at an initial temperature of $90°C$. The temperature at one end was held constant at $90°C$, and the rod was permitted to cool through natural convection for a time period equal to $t = L/v$.

The exit temperature profiles obtained from equations (C.5), (C.9), and the finite element analysis are shown in Figure C1. Values for the thermal properties used were as follows:

$$k = 0.193 W/m - K; \tag{C.10}$$

$$\rho = 1.2(10^3) kg/m^3; \tag{C.11}$$

$$c_p = 1300 J/kg - K; \tag{C.12}$$

$$h = 10 W/K - m^2. \tag{C.13}$$

The values for the thermal conductivity and the density were for PMMA [21] A value for the specific heat of PMMA was not available. Therefore, this was approximated by using the value for polycarbonate [48]. The heat transfer coefficient is for a medium in air [47]. The distribution from the finite element analysis was used as the exit temperature profile in the extrusion analysis. The distribution which includes axial convection was computed after the extrusion analyses were completed. Therefore, even though this distribution is likely the most accurate of the three, it was not used.

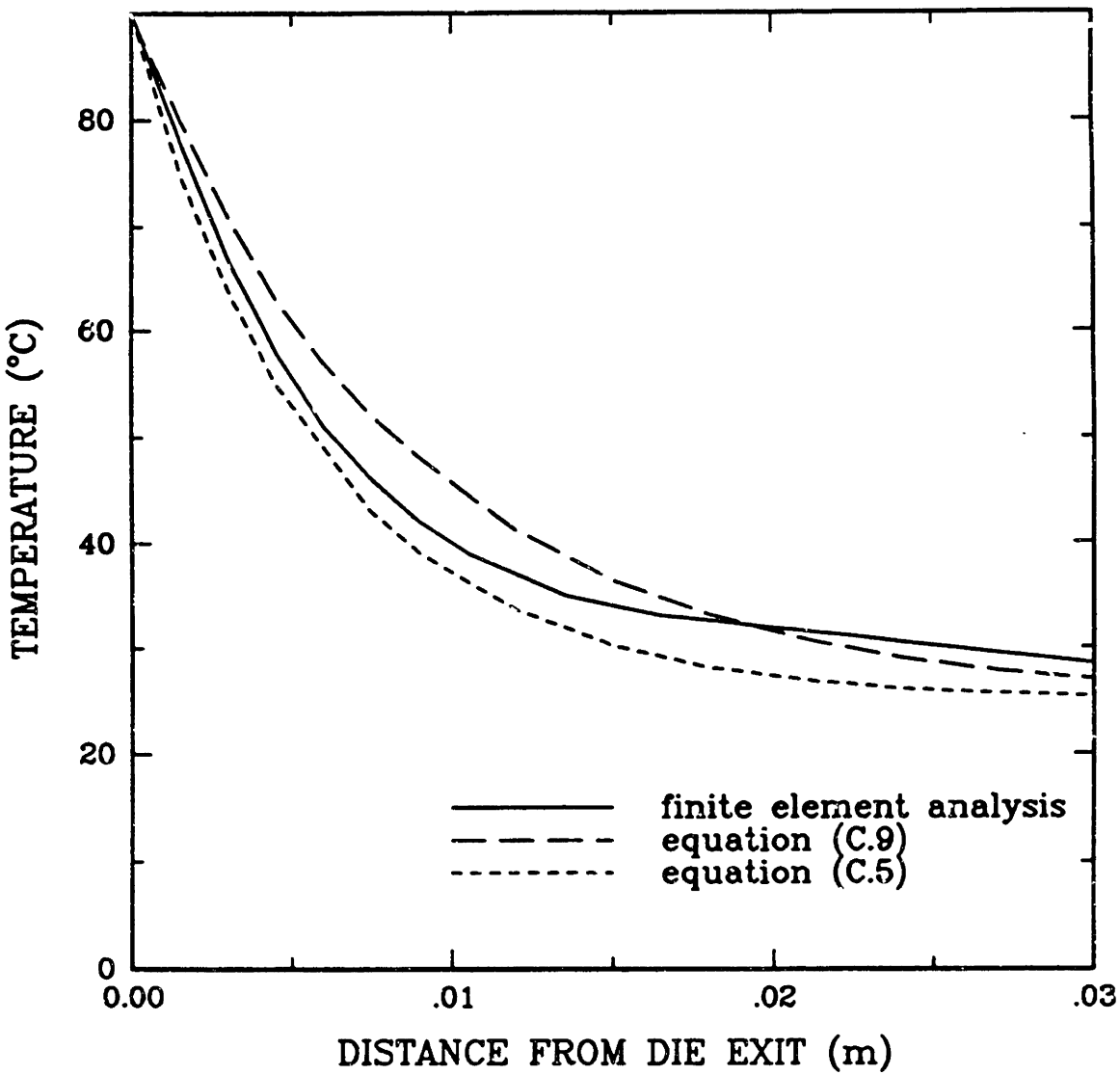

Figure C1. Extrudate exit temperature profile from equation (C.5), equation (C.9), and the finite element analysis.